Development of optical pH nanosensors for biological insights into the intracellular trafficking of nanomedicines

Arpan Desai

Thesis submitted to the University of Nottingham for the degree of Doctor of Philosophy

July 2014

I. Abstract

The field of nanomedicine has progressed to a stage where a diverse set of materials are available for controlling how a drug is delivered in the body. Although these materials can be engineered to overcome many of the obstacles associated with drug delivery, the complexity of cellular trafficking mechanisms means controlling intracellular delivery remains a major challenge. The primary portal for the cellular internalisation of nanomedicines is endocytosis, which involves transport through a network of highly complex intracellular compartments undergoing a dynamic process of acidification. As a result, nanoparticle-based pH sensors offer a new perspective from which to investigate this process.

In this study, ratiometric polyacrylamide pH nanosensors were utilised to probe fundamental aspects of intracellular trafficking with the view of developing biological insights to aid the rational design of nanomedicines. Nanosensors were fabricated with a dynamic range covering the entire range of the endocytic pathway (4.0 – 7.5), with sizes between 50 and 100 nm. Endocytic uptake of nanosensors was induced in four different cell types (HeLa, 3T3, MRC-5 and JAWS II) by increasing the surface charge on the nanosensor. Dynamic pH measurements were found to be highly sensitive to experimental methodology for performing ratiometric measurements, particularly image analysis. Consequently an optimised procedure for performing ratiometric measurements was developed, and subsequently validated by correlating pH measurements with intracellular location using 3D structured illumination microscopy (3D-SIM).

Application of pH nanosensors in studies investigating fundamental aspects of intracellular trafficking resulted in three key findings: 1) HeLa, 3T3 and JAWS II cells process material in different ways with respect to the extent and rate of acidification in endocytic organelles, 2) surface charge does not affect the final intracellular location of polyacrylamide nanoparticles internalised by endocytosis, and 3) lipid-mediated transfection of siRNA is associated with a greater degree of lysosomal disruption compared to cationic polymer-mediated transfection, with the former observed to show increased toxicity. These findings represent biological insights, which can be utilised to provide a rational basis for tailoring the response of pH-sensitive nanomedicines to a specific cell type, tuning the physicochemical properties of a material for more efficient intracellular trafficking and optimising siRNA formulations for endo-lysosomal release.

II. Acknowledgements

Firstly, I would like to thank all those at the University of Nottingham who have supported this work. Thank you to Dr Jonathan Aylott who has given me the opportunity to work under his supervision. I gratefully acknowledge his continued intellectual input, enthusiasm and encouragement over the past four years. I am particularly grateful to him for the universal support I have received in all my endeavours in my time at Nottingham, both academic and non-academic. I also gratefully acknowledge Dr Anna Grabowska and Dr Duncan Henderson for their valuable contributions to the project.

I wish to thank all the members of the Aylott Group, in particular Dr Veeren Chauhan, Andrea Lavado, Leigh-Anne Carroll, Arran Basra and Dr Rosie Adsley for making D38 a great environment to work in. I have also been fortunate to be a part of the LBSA and AstraZeneca Doctoral Training Centre for Targeted Therapeutics. Thank you to all those who have helped make these excellent groups, in which to conduct my research. Additionally, I would like to acknowledge AstraZeneca and the EPSRC for funding this project.

Secondly, I would like to thank Professor Frank Caruso for the opportunity to work in his research group at the University of Melbourne. Thank you to Dr Angus Johnston and Dr Annie Yan for useful discussions during my time in Melbourne. Thank you to Tim Esler for help with MATLAB and Ben Hibbs for technical assistance with 3D-SIM microscopy. I acknowledge the BESTS and Universitas 21 scholarship schemes at the University of Nottingham, which helped fund this visit.

Thirdly, I wish to acknowledge all my friends and family. Thank you to all those who have made Nottingham such a great place to live and work for the past four years. I will always be indebted to my grandparents and brothers, Bhavik and Jaideep, who have given me unconditional support, for which I am truly grateful. I would also like to express my gratitude to my fiancée, Geeta, for always believing in me.

Finally, thank you to my parents, who have given me everything in life, this thesis is dedicated to you.

III. Contents

IV. List of Figures and Tables

Chapter 1 Introduction

Chapter 2 Design, synthesis and characterisation of optical pH nanosensors for measurement in the endocytic pathway

Chapter 3 Development and optimisation of methodology for ratiometric measurements

Chapter 4 Optical pH nanosensors for measurement in the endocytic pathway: Delivery, validation and measurement

Chapter 5 Application of pH nanosensors for biological insights into the intracellular trafficking of nanomedicines

Chapter 6 Conclusions and Future work

V. List of Abbreviations

2D	Two dimensional
3D	Three dimensional
5(6)-FAM	5-(and-6)-carboxyfluorescein
5(6)-FAM-SE	5-(and-6)-carboxyfluorescein, succinimidyl ester
ACTA	3- (acrylamidopropyl)-trimethylammonium chloride
AFM	Atomic Force Microscopy
AMPA	N-(3-aminopropyl) methacrylamide hydrochloride
AOT	bis(2-ethylhexyl) sulfosuccinate
AP-2	Clathrin Adapter Protein 2
APS	Ammonium persulfate
APTES	Aminopropyltriethoxysilane
BCECF	2',7'-bis(2-carboxyethyl)-5(6)-carboxyfluorescein
BODIPY	4,4-difluoro-4-bora-3a,4a-diaza-s-indacene
CDCF	5(6)-carboxydichlorofluorescein
CLSM	Confocal Laser Scanning Microscopy
DC	Dendritic Cell
DLS	Dynamic Light Scattering
DMEM	Dulbecco's Modified Eagle Medium
DMSO	Dimethylsulfoxide
DNA	Deoxyribonucleic acid
EDTA	Ethylenediaminetatraacetic acid
FBS	Fetal Bovine Serum
FITC	Fluorescein isothiocyanate
FLIM	Fluorescence-Lifetime Imaging Microscopy
FRET	Förster resonance energy transfer
GFP	Green Fluorescent Protein
GM-CSF	Granulocyte Macrophage Colony Stimulating Factor
HeLa	Henrietta Lacks, human epithelial cervical cancer cells
MTS	(3-(4,5-dimethylthiazol-2-yl)-5-(3-carboxymethoxyphenyl)-2-(4-sulfophenyl)-2H-tetrazolium)
NA	numerical aperture
NADH	Nicotinamide Adenine Dinucleotide plus Hydrogen
NADPH	Nicotinamide Adenine Dinucleotide plus Hydrogen Phosphate
NAS	N-acryloxysuccinimide

NIBS	Non Invasive Back Scatter
NIH	National Institutes of Health
NS_{ds}	Dual-sensitive polyacrylamide nanosensor
NS_{end}	Endosome-sensitive polyacrylamide nanosensor
NS_{esc}	Escape-sensitive polyacrylamide nanosensor
NSOM	Near-field Scanning Optical Microscopy
OG	Oregon Green
PAA	Polyacrylamide
PALM	Photoactivated Localization Microscopy
PBS	Phosphate Buffered Saline
PCC	Pearson's Correlation Coefficient
PDMA	Polydecylmethacrylate
PDMPA	Poly(2-amino-2-methylpropyl)acrylamide
PEBBLE	Probes Encapsulated By Biologically Localized Embedding
PeT	Photoinduced electron Transfer
PFA	Paraformaldehyde
PMT	Photomultiplier tube
PSF	Point Spread Function
QD	Quantum Dot
RBL	Rat Basophilic Leukaemia
RNA	Ribonucleic acid
RPMI	Roswell Park Memorial Institute
S/N	Signal to Noise
SEM	Scanning Electron Microscopy
SFV	Semliki Forest Virus
SIM	Structured Illumination Microscopy
siRNA	Short Interfering Ribonucleic acid
SNARF	Seminaphtharhodafluor
STED	Stimulated Emission Depletion Microscopy
STORM	Stochastic Optical Reconstruction Microscopy
TAMRA	6-carboxytetramethylrhodamine
TAMRA-SE	6-carboxytetramethylrhodamine, succinimidyl ester
TAT	Transactivator of Transcription
TEMED	Tetramethylethylenediamine
TIRF	Total Internal Reflectance Microscopy

Chapter 1 Introduction

1.1 Nanomedicine

1.1.1 Introduction to targeted drug delivery

Over a 100 years ago a Nobel Prize winning German physician and scientist named Paul Ehrlich, pioneered the theory that the most effective way to treat a disease is to target drugs to the entity in the body causing the disease, in this way he envisioned medicines as "magic bullets"[1]. Ehlirch's early work on how chemical dyes interact with cells led to the discovery that the cellular interactions between a cell and chemical compound are governed by their respective chemical composition. His later work in the field of immunology, based on the identification of "side-chains" or receptors on the cell surface led him to reason that if a drug could be attached to a chemical entity, which has high affinity to a receptor, then this was a way of directing a drug to a target[1]. He exploited this idea to found the field of chemotherapy for cancer, demonstrating the concept of medicines as "magic bullets"[1]. Targeted therapeutics, such as this have the advantage of attacking the cause of a disease whilst bypassing healthy tissues, reducing the chances of unfavourable side effects, as well as lowering the amount of drug required to treat a disease. Increasing the precision with which drugs are delivered is a way of producing safer more cost effective medicines. As a result, 100 years on from Ehlirch's discoveries, researchers are still working to realise his vision.

The work in this thesis is primarily concerned with drugs, which have intracellular targets. This represents a diverse range of therapeutic agents including proteins, nucleic acids and small molecules, however achieving "magic bullet" delivery of drugs to an intracellular target in the way Ehlirch envisioned is a challenging task. Several obstacles exist on the journey a drug will take from the point at which it is administered to the point it reaches its target (**Figure 1.1**). The first obstacle encountered is dependent on the route of administration, which could be intravenous, oral, inhaled or intraperitoneal injection. For example if the drug is delivered through an oral route, it must be resistant to the harsh acidic conditions in the early stages of the gastrointestinal tract. Assuming the drug reaches the systemic circulation, it must avoid clearance mechanisms, recognition by the immune system, aggregation with serum proteins and enzymatic degradation[2]. The drug is then required to move through the capillary endothelium to the reach the target tissue. This presents a significant challenge as for most organs, with the exception of the liver, spleen and some tumours, molecules or particles greater than 5 nm in diameter will not freely pass through the capillary wall[3].

Once in the tissues the drug is required to distribute through a dense extracellular matrix comprising polysaccharides and fibrous proteins, again avoiding recognition by the immune system[4]. Finally the drug must be taken up into target cells and trafficked to the correct intracellular location[5].

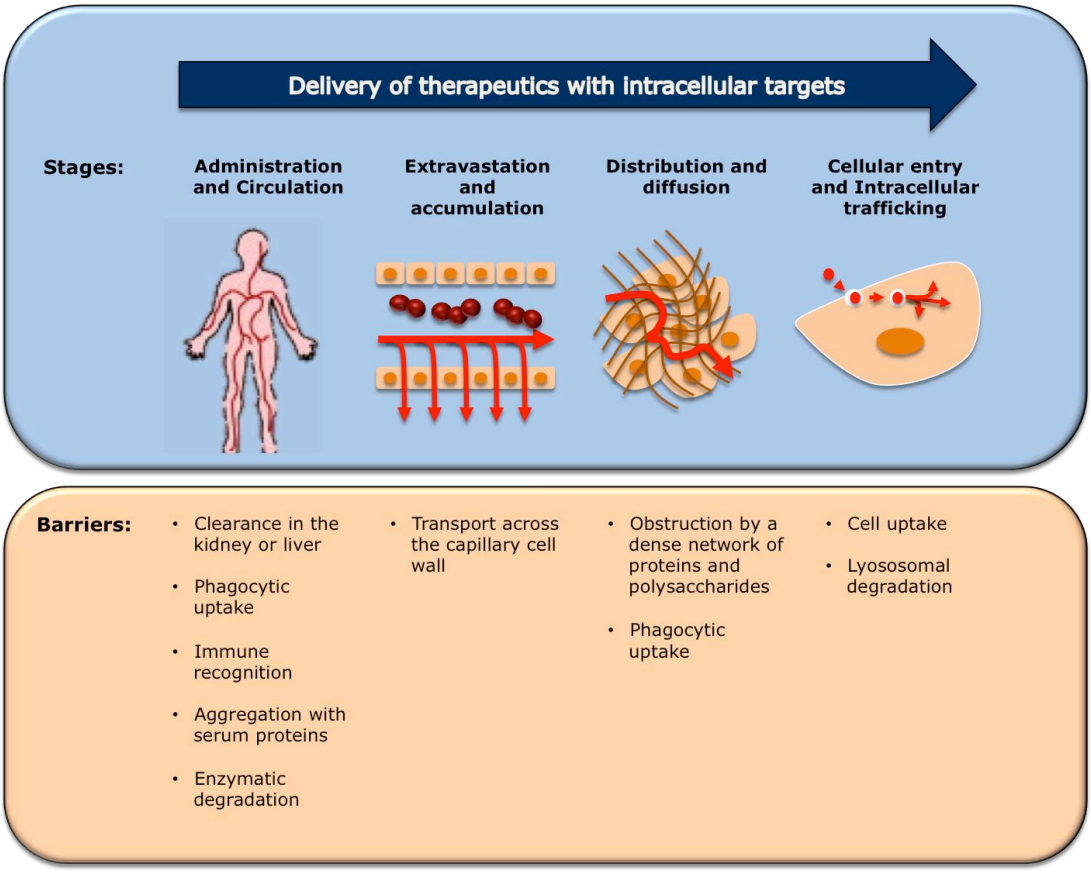

Figure 1.1 *Overview of the stages and barriers involved in intracellular drug delivery.*

Delivering drugs to intracellular targets, as "magic bullets" is a multifaceted challenge, which cannot often be met by a drug substance alone. This has led to the development of nano-sized vehicles for delivering drugs to their targets (nanomedicines). The majority of these are based on polymer-drug conjugates and liposomes, the first reports of which came in 1950s and 1960s respectively[6]. The first polymer-drug conjugate to gain regulatory approval was a polyethylene glycol (PEG) –L-asparaginase conjugate developed in 1994 for the treatment of leukaemia[7], whilst the first liposomal formulation to gain approval was Doxil, in 1995, a liposomal formulation incorporating doxorubicin for the treatment of Kaposi's sarcoma[8]. Since then, ground-breaking advances in nanotechnology have led to the development of evermore sophisticated multifunctional nanomedicines capable of simultaneously addressing the challenges of drug delivery (see reviews[6,9,10]) (**Figure 1.2**). There are now 40 nanoparticle based

medicines currently in clinical use with many more in late clinical development[11]. The development of nanomedicines has been driven by advances in our fundamental understanding of how nanomaterials interact within biological systems, however many questions regarding how these materials behave inside cells still remain unanswered.

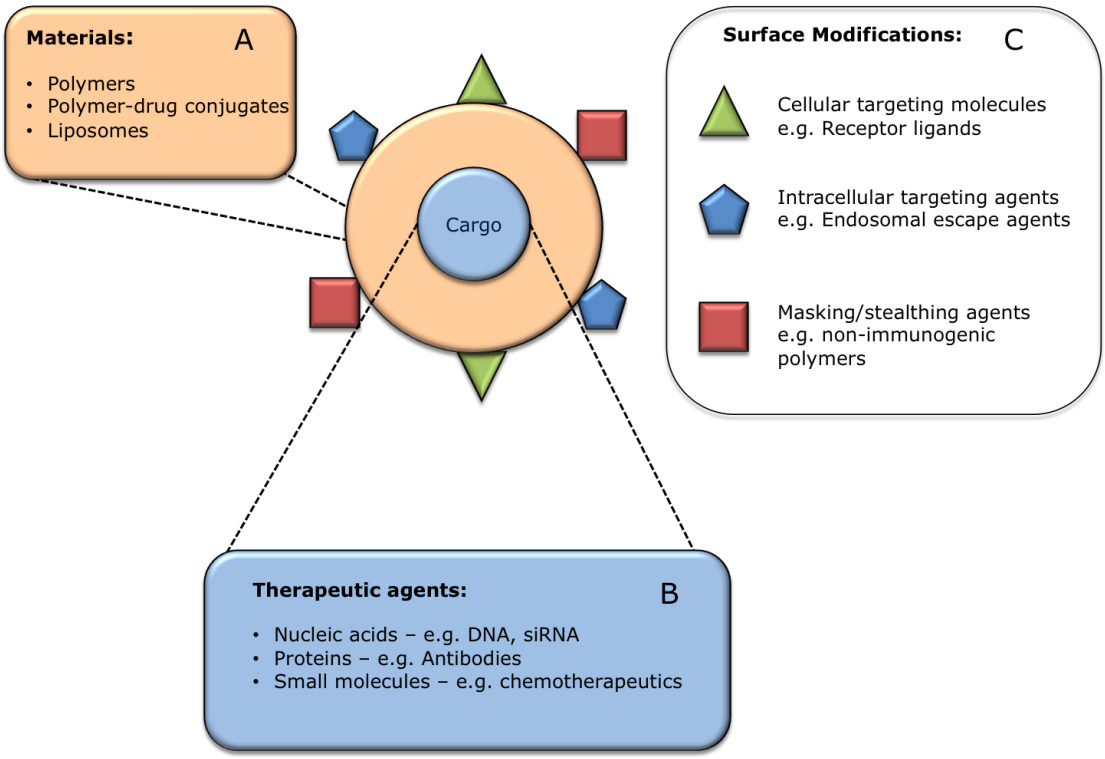

Figure 1.2 *Overview of the design of a multifunctional nanoparticle for intracellular delivery.* (A) Common types of materials used for nanomedicines. Materials within this classification include lipidic devices, block copolymer micelles, nanogels, dendrimers and nanocapsules. (B) Therapeutic agents (C) Surface modifications for optimisation of delivery. See reference[12] for a comprehensive list of nanomedicines currently in clinical trials.

1.1.2 Intracellular delivery of nanomedicines

One of the most significant barriers to intracellular drug delivery and the primary issue addressed in this thesis, is inefficient intracellular trafficking.

1.1.2.1 Cellular entry and endocytosis

The majority of nanoparticles suitable for drug delivery are too large to enter a cell through passive methods, and are taken into cells by a specialised process involving thousands of proteins called endocytosis[13]. Endocytosis is a complex

energy-dependent process which, in addition to its role in the internalisation of foreign material, plays a critical role in cell function in many areas including, cell signalling, regulation of immunological pathways and maintaining cell homoeostasis[14].

There are many different types of endocytosis, which can be employed to internalise a nanoparticle (**Figure 1.3**). These are classified in terms of the proteins which coordinate the endocytic process (reviewed in[11,13,15-17]). Endocytosis is classified into two main types, pinocytosis, commonly know as 'cell drinking' and phagocytosis known as 'cell eating'. Phagocytosis is primarily for the uptake of large material (> 1 μm in diameter), and is mostly associated with a set of specialised professional phagocytic cells such as macrophages, dendritic cells and monocytes. Pinocytosis is a more generalised mechanism found in most cell types, and is primarily for the internalisation of material < 1 μm in diameter. Pinocytosis can be subdivided into groups based on whether or not the protein clathrin is involved in coordinating endocytosis. Clathrin mediated endocytosis is the most well characterized endocytic mechanism (reviewed in Mousavi *et al*[18]). By this mechanism, material to be endocytosed is bound to receptors on the inner leaflet of the plasma membrane. These sites assemble into specialised structures called Clathrin Coated Pits (CCPs), where material is concentrated before internalisation. The main constituents of CCPs are clathrin and adaptor protein-2 (AP-2). Clathrin interacts with a number of accessory proteins including AP-2 in CCPs to form a neck structure connecting the growing vesicle to the plasma membrane. The vesicle then pinches off resulting in the formation clathrin-coated vesicles (CCVs). The neck structure is a site for the recruitment of proteins (dynamin, endophilin and amohiphysin), which facilitate the scission of the CCV from the plasma membrane. The processes for clathrin-independent endocytosis follow a similar structural model for endocytosis to Clathrin-dependent endocytosis (reviewed in Mayor *et al*[19]). However there are major differences in the ancillary proteins, which generate the structural changes required for vesicle formation. These pathways include caveolae-mediated endocytosis and macropinocytosis. Macropinocytosis involves membrane ruffling which permits the internalisation of larger materials than other types of pinocytosis.

Predicting the route of endocytic uptake based on the physicochemical characteristics of a nanoparticle, is a complex issue. This is because nanoparticles can be taken up by more than one pathway at the same time[16]. In addition to this different cell types favour different modes of uptake, for example, caveolae-mediated endocytosis is favoured in vascular endothelial cells[20]. Moreover studies

aiming to investigate the pathway of nanoparticle uptake are usually based on exclusion studies, where a certain pathway is inhibited. In such cases it is likely that down regulation of one pathway will result in up regulation of another pathway to compensate[21].

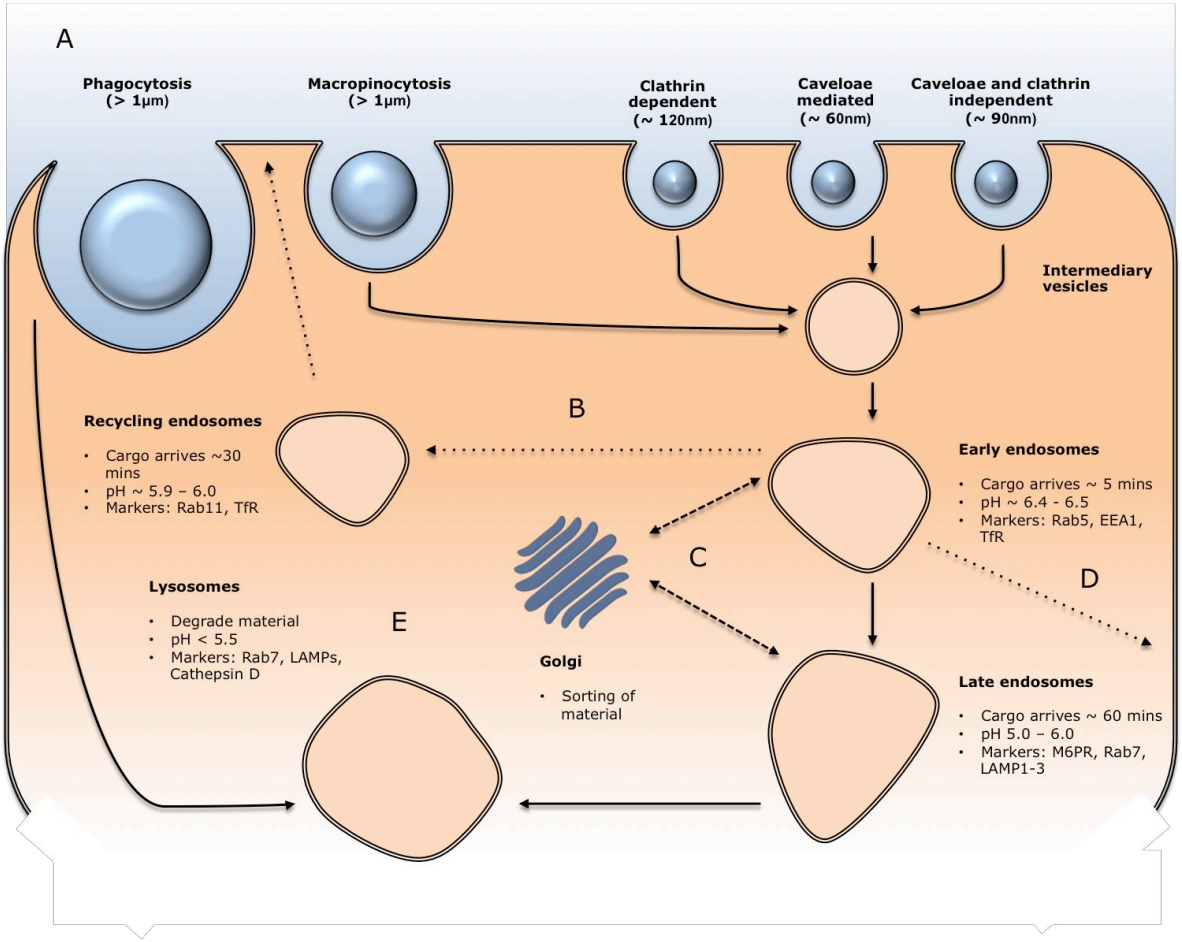

Figure 1.3 *Overview of endocytosis and intracellular trafficking.* (A) Endocytosis. Material is taken up by an endocytic pathway dependent on the physicochemical characteristics of the material and the cell type. (B,C,D,E) Intracellular trafficking. Material is trafficked through intermediary vesicles, early endosomes, late endosomes and lysosomes undergoing progressive acidification. (B) Material may be recycled out of the cell (typically ~ 5-10 minutes), transported to the Golgi for sorting (C), transcytosed out of the cell (D) or deposited in lysosomes for degradation (E).

1.1.2.2 Intracellular trafficking

Following internalisation, the nanoparticle will then be transported through several different sorting stations where its intracellular fate will be determined (**Figure 1.3**). The key organelles involved in this process are early endosomes, late endosomes, recycling endosomes, lysosomes and the Golgi apparatus. Material is translocated between organelles through fusion events involving specialised proteins such as Rab5[22] and SNAREs[23,24]. Of critical importance to the field of nanomedicine is understanding how a cell sorts material following internalisation. This is thought to happen through the complex interplay of a series of molecular signals. The molecular basis of this is yet to be fully elucidated however a group of proteins which form a endosomal-sorting complex required for transport (ESCRT) are known to be involved. ESCRT proteins are found on the surface of early and late endosomes[25]. Sorting is also known to be affected by natural regulatory pathways for example receptor recycling pathways[26]. Currently our understanding of intracellular trafficking is not at a level where trafficking of nanomedicines can be achieved by controlling molecular signalling; rather most nanomedicines use ligands or molecules which have known trafficking pathways to direct delivery[27].

There are several possible final destinations for a nanomedicine after trafficking is completed. The nanomedicine can be delivered to an intracellular compartment[25], recycled to the extracellular space (exocytosis)[26] or transported through the cell (transcytosis)[28]. These are important processes as they may determine the time a drug is resident in the cell. The majority of nanomedicines are thought to be marked for degradation and delivered to highly acidic lysosomes[23].

Consequently, lysosomes are an important organelle when considering the transport of nanoparticles. Lysosomes were first discovered in 1955 somewhat serendipitously by Christian De Duve, during his research into determining the role of insulin in the liver[29]. His group suspected an enzyme; hexose phosphatase may alter the action of insulin. In order to try and identify the enzyme De Duve's group took the approach of utilising the then new technique of centrifugal fractionation to determine the intracellular distribution of different enzymes. They successfully identified the enzyme as glucose-6-phosphatase, however through a series of biochemical analyses they also found the enzyme was contained in sac like compartments, which were different to any of the other organelles found in the cell. Abandoning their work on insulin and carbohydrate metabolism, de

Duve's group identified a further five additional enzymes that were located in these sac-like organelles. All were hydrolases with optimal activity at acidic pH, this was the first indication of the acidic nature of lysosomes. The presence of different acid hydrolases suggested a digestive function for these organelles. Later on the fractions were taken and imaged using electron microscopy, which confirmed the hypothesis. In 1963, 8 years after the initial discovery, the first international symposium on lysosomes was held, and at this point, the role of lysosomes in the digestion of extracellular material was reported across a range of different cell types. Since then > 60 acid hydrolases have been identified to be associated with lysosomes.

1.1.2.3 Endosomal escape

The acidic, hydrolytic environment of endosomes and particularly, lysosomes is a problem for the delivery of drugs because incomplete release from the endo-lysosomal pathway can result in degradation of the drug and/or prevent interaction with targets in other intracellular compartments or in the cytosol[30]. Incomplete release is seen as major bottleneck for the development of several drugs[30-33].

Several strategies have been developed for the optimisation of endosomal release, many of which are inspired by viruses and bacteria, which efficiently release genetic material into the cytoplasm from endosomes[30,33]. These often involve the incorporation of a specialised agent as a component in a drug delivery system. The mechanisms by which these function are summarised in **Table 1.1.** Although progress has been made in this area, incomplete endosomal release remains a key hurdle for drug delivery.

Mechanism of escape	Description	Examples
Pore formation	Involves binding to and insertion of proteins into the membrane leading the remodelling of the cell membrane	Penton base[34], gp41[35,36],Pneumococcal pneumolysin[37]
Membrane fusion	Occurs due to destabilisation of membranes through binding of proteins or lipids	Haemagglutinin[38-40], poly (L-Lysine)[41], diNF-7[42-46]
Proton-sponge	Chemical agents buffer pH in the endosomal lumen resulting in the influx of counterions and water causing eventual swelling and rupture of endosomes	Polyethylenimine (PEI)[47], poly (amidoamines)s[48-50], poly(propylacrylic acid[51]
Photochemical membrane disruption	Photosensitsors are delivered to the endosomal pathway, exposure to light results in the release in formation of reactive oxygen species which destroy the endosomal membrane	$TPPS_4$, $TPPS_{2A}$,$AlPcS_{2a}$[52,53]

Table 1.1 Mechanisms of endosomal escape.

1.1.3 Acidification in the endocytic pathway

The relationship between pH and cellular function is broad and complex[54]. Differences in intracellular proton concentration can affect cell function in a variety of different ways. A major mechanism by which this occurs is through protonation or deprotonating of macromolecules. This can result in a change in conformation, which may activate or deactivate a protein. An example of this are acid hydrolases are only functional at low pH, therefore only function in lysosomes, which prevents cellular autophagy. Controlling intracellular pH is a method by which a cell can regulate its activity; accordingly there is a large degree of heterogeneity in pH throughout different cellular organelles such as the nucleus, endoplasmic reticulum, Golgi network, peroxisomes, secretory granules, mitochondria and the cytosol. The pH in organelles has been measured to be as high as 8 in mitochondria and as low as 4.7 in lysosomes, which is markedly different from cytoplasmic pH of 7.2[55]. Acidification is of critical importance in the

endocytic pathway for regulation of biological processes such as receptor recycling and degradation of foreign material.

Acidification is mediated by proton pumping vacuolar ATPases (V-ATPases) present on the surface of endosomes and lysosomes [56,57]. V-ATPases consist of two units, V1 and V0. V1 comprises is a 500-kDa complex comprising a minimum of 8 different subunits and has the function of generating energy through hydrolysis of ATP. The purpose of the V0 unit, which is a 250-kDa complex comprising a minimum of 5 subunits, is to provide a path for the transport of protons across a membrane. Differences in acidity in different organelles through the endocytic pathway are thought to arise because of an amalgamation of different factors. These include variations in the density of pumps present in certain organelles, changes in the rate of pumping, disassembly of certain pumps by proteins and differences in the rates of proton leak in some intracellular compartments[54].

1.1.3.1 Significance for the delivery of nanomedicines

The pH transitions occurring through intracellular transport are important for designing nanomedicines[58]. Firstly several delivery strategies employ pH-responsive drug delivery systems to promote targeted release[59-61]. Secondly the mechanism of endosomal release in some cases is dependent on pH changes[30,33]. Thirdly pH may give information the intracellular location of a nanoparticle[54].

pH-sensitive drug delivery systems are designed to respond to a drop in pH by changing confirmation to release a drug which permeates through membranes in its free form. This has been exploited for delivery of drugs to the cytosol by tailoring nanomedicines to release drugs at endo-lysosomal pH values[62]. Materials, which respond to pH in this way, have demonstrated a dramatic increase in delivery efficacy[62]. pH-responsive nanomedicines encompass a diverse class of materials, including pH-responsive polymeric nanoparticles, polymer-drug conjugates, liposomes, micellar delivery systems and dendrimers. These systems function as pH brings about a physical change in the particle/construct, which leads to drug release; examples of this are particle-swelling Figure **1.4A**), disruption of the particle structure (**Figure 1.4B**) or acid cleavable linkers (**Figure 1.4C**).

In addition to directing intracellular delivery, pH-sensitive nanomedicines are also useful for the targeting diseased tissues, which are associated with a hypoxic

environment such as cancer. This scenario results in respiration by a pathway which results in the production of lactic acid and a concomitant pH drop in the extracellular environment surrounding the tissue[63,64]. For cancer, pH is lowered in primary and metastasised tumours, from ~ 7.4 to ~ 6.5, consequently designing materials tailored to release drugs in this pH range is an avenue which has been pursued for targeted cancer therapy[60,65].

Due to the significance of pH to nanoparticle delivery, there has been much interest in developing pH-responsive materials. As a result, materials are now available which can be finely tuned to respond to release a drug in a narrow pH range[62].

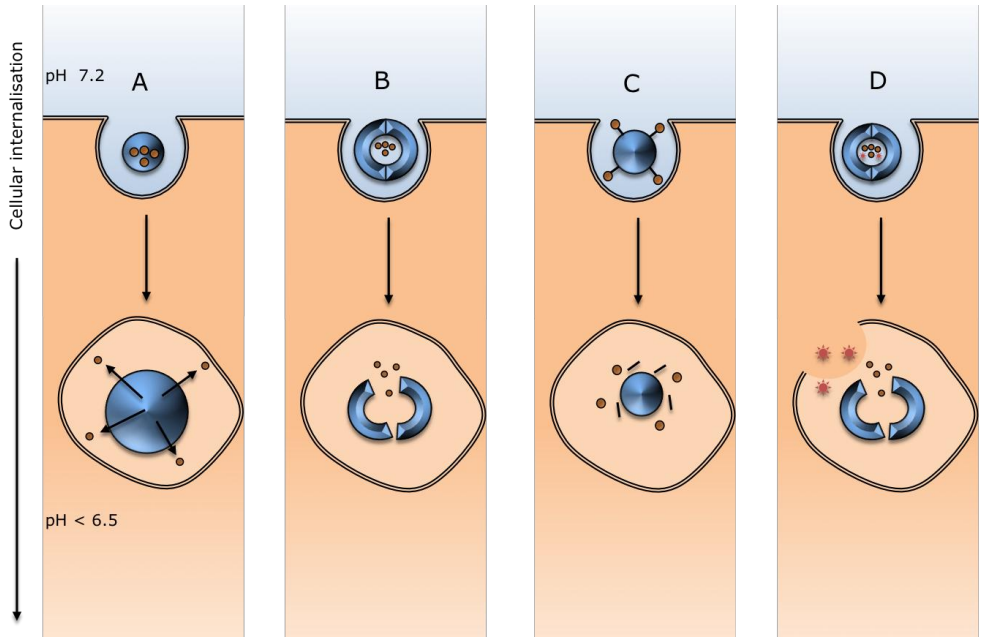

Figure 1.4 *Mechanism of action of pH-sensitive drug delivery systems internalised by endocytosis.* (A) pH dependent swelling[66-72]. (B) pH dependent conformational change[73,74]. (C) pH cleavable linkers[75-81] (D) pH dependent release of an agent promoting endosomal escape e.g. endosomal buffering polymer[82-85], cell penetrating peptide[86-91]. Drug delivery system (blue), drug (orange) and endosomal escape agent (red).

pH is a factor which affects the mechanisms of endosomal escape. For agents that function by the pore formation and fusion mechanisms, low pH is a trigger, which causes a conformational change that induces the initial interaction with the cell membrane. An example of this is the virus-derived endosomal escape agent Heamagglutinin[38-40,92]. This is a protein found on the coat of the influenza virus;

under physiological conditions (pH 7.2) the protein is in a hydrophilic coil formation, a drop in pH results in transition to a hydrophobic state, which induces fusion of the viral membrane with the cellular membrane and causes endosomal rupture. Likewise pH is important in the proton sponge mechanism as the osmotic balance which results in endosomal rupture is dependent caused by the imbalance of H^+ ions in the cellular membrane[93,94].

Due to the heterogeneity of pH in the cell, the pH microenvironment of a nanoparticle is an indicator of intracellular location. This may not always be the case, for example if endosomal release is promoted by the proton sponge mechanism, the local pH in the endosome may be elevated to cytoplasmic pH, however the intracellular location will be unchanged. In combination with complementary techniques such as fluorescence colocalisation microscopy pH measurement can still yield fresh insights into the intracellular location of a nanoparticle. This is significant because accurate methods for determining intracellular location are critical for the rational design of targeted drug delivery systems.

1.1.3.2 Measurement of endocytic acidification

From this discussion, it is apparent that measurement of pH through intracellular trafficking has the potential to yield biological insights, both in terms of improving our fundamental understanding of intracellular transport processes and for the rational design of nanomedicines. Indeed efforts have been made to do this since the discovery of lysosomes.

Christian De Duve's first identification of lysosomes was done by a biochemical determination of cellular enzymes with optimal activity in an acidic environment[29,95]. This subsequently led to the elucidation of the endo-lysosomal pathway and the identification of endosomes as structurally distinct organelles almost 30 years later. Consequently the characterisation of the pH changes occurring in the pathway have been integral to growth in understanding of this pathway. Early knowledge of acidification was found from pH-sensitive fluorophores; these measurements were corroborated by information from functional assays and lipophilic weak bases, which collect in acidic organelles at a specific pH[96].

The earliest reliable quantitative determinations of pH inside lysosomes within living cells were done in macrophages, using pH-responsive fluorophores

conjugated to dextran in a study by Ohkuma and Poole in 1978[97] . At this point there were several studies whereby pH had been measured using biochemical determinations in non-living systems, which indicated pH of lysosomes to be between pH 4.0 and 6.0, however the exact values remained controversial. In this study, dextran, which is known to stably incorporate into endosomes and lysosomes, was conjugated to a pH-sensitive fluorophore, FITC. FITC displays pH dependent changes in fluorescence intensity between pH 4.0 and 7.0. The measurements were made utilising the pH dependence of the excitation spectrum of FITC at an emission of λ519 nm. The spectrum, in alkaline conditions has a large peak at λ495 nm, which is lowered and replaced by peaks at λ480 and λ450 nm. A calibration curve was constructed by taking a ratio between the excitation intensity at λ495 nm and λ450 nm in a range of buffers of known pH. Subsequently FITC dextran molecules were taken into lysosomes in a cell uptake experiment and fluorescence intensity measurements on live cells were made using a customised fluorometer which had a device to hold cells cultured on a coverslip in place whilst measurements were taken. The pH measured using this method, from 38 measurements was determined to be 4.75 ± 0.06. Soon after this a picture was emerging that lysosomes were associated with other organelles and may be part of a pathway with distinct organelles.

This led to the first determination of pH in endosomes, this was done a year before the definitive determination of endosomes as distinct organelles. In a similar approach Tyco and Maxfield utilised a ligand known to internalise by receptor-mediated endocytosis, alpha-2 macroglobulin, conjugated to FITC to measure pH in 3T3 mouse fibroblasts[98]. They demonstrated the rapid acidification of endosomes in pulse-chase experiments. Cells were exposed to FITC-alpha-2-macroglobulin (pulse) and fluorescence intensity was measured using a microscope-fluorometer (chase). Following a 15 minutes pulse, and 5 minutes chase the pH was measured to be 5.0 ± 0.2 considerably higher than the pH measured using FITC-dextran. 4.6 ±0.2. Although measurements at earlier stages in the endo-lysosomal pathway were not reliable, this study revealed the gradual acidification process occurring through the endo-lysosomal pathway.

Assays that utilise the natural function of the pathway to give information about the pathway were essential to the early development of our understanding of acidification. An example of this was in an early determination of pH in endosomes using the Semliki forest virus (SFV) by Ara Helenius' group[99]. SFV is known to enter cells by endocytosis and pass through the endo-lysosomal

pathway from where it is released into the cytoplasm. Several cell-free experiments using liposomes and model membranes demonstrate that glycoproteins on the surface of SFV particles fuse with and disrupt membranes at pH < 6. Using this as a premise, the endosomal release of SFV was followed kinetically, by isolation of acidic vesicles using cell fractionation at different time points. The absence of viral DNA in endosomes after 5-7 minutes implicates the fusion mechanism in endosomal release and suggests the pH of endosomes is less than pH 6. Alternative functional assays can be done utilising substrates for acid hydrolases in lysosomes. In an example of this approach, amino acid methylesterases, which are hydrolysed in lysosomes were exposed to cells. The cells were then fractionated and an assay demonstrated inactivity in the lysosomal fractions indicating the presence of an acidic environment[96].

Fluorescent lipophilic weak bases have been used from since the discovery of lysosomes to stain organelles and estimate pH. These compounds are permeable to cell membranes (lipophilic) and become protonated inside acidic intracellular vesicles, which results in a reduction in membrane permeability leading to accumulation in acidic vesicles. Common examples of such fluorophores are Acridine Dyes. Acridine Orange and 9-amino-6-chloro-2-methoxy- acridine are fluorophores which have been used for staining acidic cell organelles[96]. Acridine Orange is particularly useful because its fluorescence properties change with concentration. At low concentrations in the absence of aggregation, Acridine Orange has an absorbance maximum of λ482 nm and emission maximum of λ530 nm. At high concentrations the absorbance maximum is blue-shifted to λ465 nm and the emission is red shifted to λ655 nm. Therefore the emission ratio between λ530 nm and λ655 nm can be utilised to determine the pH in acidic vesicles. However this approach to pH measurement is limited because the fluorescence properties are significantly affected by the presence of anions and temperature. Acridine Orange has also been demonstrated to increase the pH of endosomes[96]. A more general drawback is that these dyes are not specific for endosomes and lysosomes but specific for all acidic vesicles. A popular alternative to acridine dyes are the commercially available Lysotracker dyes[100]. These are boron-dipyrromethene (BODIPY) derivatives, which accumulate in endosomes and lysosomes. The mechanism for retention in lysosomes is not clear but is presumably due to protonation. Lysotracker dyes do not exhibit pH dependent changes in fluorescence emission therefore are restricted to qualitative analysis. Lysotracker dyes are popular because they are bright due to high molar

absorptivity and are available in a wide variety of colours, which makes them ideal for multicolour applications.

These approaches to intracellular measurements have facilitated the elucidation of the pH environment in organelles through the endocytic pathway. However in the context of nanomedicine, precise dynamic measurements are required to understand the transit of a nanomedicine as it passes through the endocytic pathway. This requires advanced optical sensors.

1.2 Optical nanosensors for intracellular measurement

Ever since cells were discovered as a fundamental building block of human life, science has been progressing towards a more complete understanding of cellular function. In the simplest terms, cells consist of water, ions and molecules, which perform different structural and functional roles within a cell. The cellular environment is maintained in a state of dynamic flux responding to changes in the external environment. Ions (Ca^{2+},H^{+}, K^{+}, $Na^{+,}$ Mg^{2+}) and molecules (PO_4^{3-}, ATP, amino acids, proteins, nucleic acids) perform their various roles as catalysts, substrates or transporters ensuring proper cell function. Consequently the dynamic monitoring of intracellular analytes with high spatial and temporal resolution is an important portal from which we can progress our understanding of cellular activity. This has been the primary motivation, which has driven the development of biological sensors for intracellular measurement.

1.2.1 Introduction

Sensors for intracellular measurement comprise two fundamental components, an analyte detector and signal transducer. The analyte detector specifically recognises the analyte and produces a response. The response is converted into a measureable signal by the transducer. There are several types of sensor, which have been proposed for performing intracellular measurements. These are discussed in the following section.

1.2.1.1 Early approaches

Early approaches to measurement of intracellular analytes were based on fibre-optic based electrodes, developed in the 1990s, (reviewed in Vo-Dinh *et al*[101,102]). These types of sensor consist of an ultra thin fibre with a recognition component at the tip. The fibre is usually connected to a signal transducer, which converts the signal from the analyte into a measurable electrical signal. The fibre is used to probe single cells, by forcibly penetrating the cell membrane. Fibres have been

produced for this purpose with tip sizes ranging from 20 – 100 nm[101]. Although this is several times smaller than the size of the cell, physical perturbation is caused to the cell by puncturing the membrane. Moreover the actual penetration volume is much more significant. If we consider a 100 μm cell, probed by conical fibre with a tip of 200 nm at a penetration depth of 50 μm, the penetration volume will be approximately 20,000 μm^3. Assuming the cell is spherical, the cell volume will be approximately 540,000 μm^3, therefore the penetration volume is almost 4 % of the total cell volume. The majority of mammalian cells are in the region of 10 – 20 μm making this value even more significant. Therein lies the primary limitation of this approach. It is very difficult to probe dynamic environments in intricate sub micron organelles when the probe is so large. In order to progress the field alternative methods have been sought, which are less invasive and offer greater flexibility.

Another early approach to measurement of intracellular analytes was Nuclear Magnetic Resonance (NMR) imaging. Intracellular measurement of pH by NMR is based on the principle that the resonance frequency or chemical shift of ^{31}P is changes with pH. Phosphate is widely distributed throughout the cell, hence pH can be mapped through the cell. However this technique has low sensitivity and low spatial/temporal resolution[103]. Measurements are also restricted to areas in the cell where phosphate is present.

1.2.1.2 Principles of fluorescence

Fluorescence is currently the method of choice for intracellular sensing and has proved to be the most inexpensive, versatile and non-invasive way of detecting intracellular analytes.

Fluorescence is a photophysical phenomenon, which was first noted by Sir George Stokes in the mid 19th Century after he made the observation that the mineral fluorspar glows following exposure to ultraviolet light. The fluorescence he observed is a type of photoluminescence, which occurs through the absorption, and subsequent re-radiation of light. The re-radiated or fluorescent light is usually of a longer wavelength than the absorbed light (known as the Stokes shift). Only certain molecules are capable of fluorescence, usually aromatic hydrocarbons or heterocyclic compounds. These molecules are termed fluorophores, and are usually small molecules (< 1KDa). The fluorescence process can be considered to occur in a series of stages described in **Figure 1.5.**

There are several factors affecting this process, which have significance when utilising fluorophores in biological applications, summarised in **Table 1.2.**

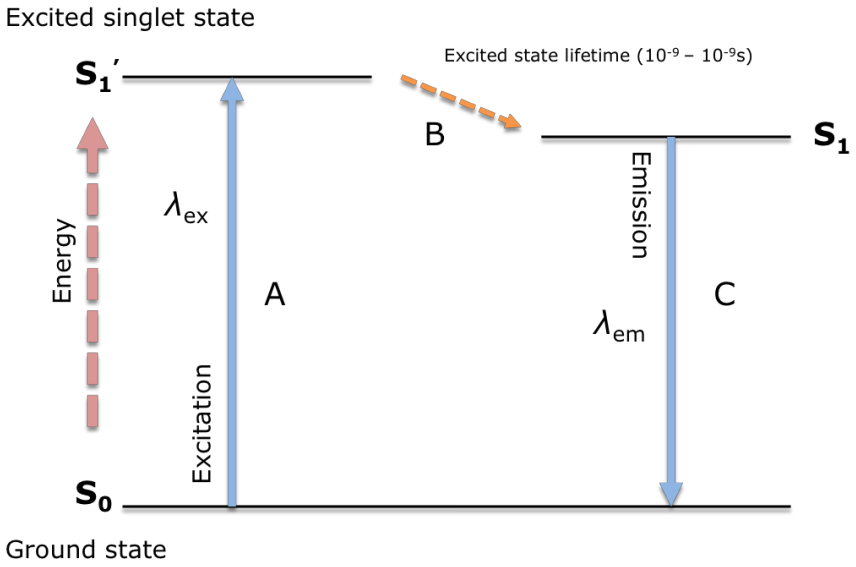

Figure 1.5 *The fluorescence process.* (A) Excitation light of a certain wavelength (λ_{ex}) hits a molecule. The photons in the excitation light are absorbed by electrons in the molecule which are lifted from the ground state (S_0) to a higher energy level (S_1') this process is called excitation. (B) Electrons are maintained in the excited state for a short period of time (10^{-8} – 10^{-9} seconds), some energy is also lost at this time. (C) The electrons then return to the ground state losing energy. The energy, which is lost, is emitted as photons. Due to the loss of energy, the wavelength of this emission (λ_{em}) is longer than that of the excitation light. This emission is called fluorescence.

Fluorophore property	Definition	Significance
Molar extinction coefficient (E)	Amount of light can be absorbed at a given wavelength*	The brightness of the fluorophore is equivalent to the product of the molar extinction coefficient and the quantum yield
Quantum yield	Ratio of emitted photons to absorbed photons	As above
Photobleaching	Disruption of fluorophore structure from photon induced damage **	Results in a loss of fluorescence. This is related to the intensity and exposure time.
Quenching	Loss of fluorescence due to factors unrelated to photobleaching***	Results in a loss of fluorescence

* The molar extinction coefficient is defined by the Beer-Lambert law (A = Ecl) where A = absorbance, E = molar extinction coefficient c = concentration and l = optical path length).
**Resistance to photobleaching is dependent on the structure of the fluorophore.
***Quenching can occur through a variety of sources including Förster resonance energy transfer and side reactions occurring in the excited state.

Table 1.2 Optical properties describing the performance of a fluorophore.

1.2.1.3 Fluorescence-based sensing

Fluorescence-based approaches have found widespread applications in cell biology. For many of the same reasons they also have become the method of choice for performing intracellular measurements. Fluorescence in cell biology is predominantly used for labelling intracellular structures; this is achieved by the synthesis of fluorophores or fluorophore-conjugates which specifically bind a biomolecule. Intracellular fluorescent sensors are based on specialised fluorophores, which change intensity of emission in response to changes in analyte concentration. In this sense the signal recognition component and the

transducer are the same molecule. There are several reasons for the success of this approach.

Purely from a sensing perspective, small quantities of fluorophores generate intense signal relative to background. This is because fluorophores can undergo repeated cycles of the fluorescence process described in **Figure 1.5**, which means fluorophores are capable of absorbing and emitting large quantities of light. Additionally fluorophores show a rapid response to changes in analyte concentration, enabling real-time tracking of dynamic cellular processes. Furthermore it is now possible to synthesise fluorescent probes responsive to a wide array of different analytes and fine-tune their properties for optimal sensitivity. Fluorophores are available which are sensitive to ions (pH, Ca^{2+}, Cu^{1+}, Cu^{2+}, Fe^{3+}, Mg^{2+}, K^{+}, Na^{+} Pb^{2+}, Zn^{2}, Cl^{-}), small molecules (ATP, oxygen, singlet oxygen, H_2O_2), enzymes involved in biological processes (e.g. apoptosis) and physical processes (temperature)[104]. From a biological perspective, the small size of fluorescent probes, means they are physically non-invasive. Coupled with this, signal from fluorophores is easily detected using well-established instrumentation (**Table 1.3**)**.** Such instruments typically comprise 3 common components. 1) A light source to excite the sample 2) light filters to control the excitation wavelength and/or detected emission wavelength 3) A detector, which transduces the signal from the fluorophore into a readable signal. It is important to note advanced fluorescence techniques are now being developed to combine different aspects of these techniques. Considering these factors together fluorescence-based methods represent a practical and versatile approach for intracellular measurement.

Instrument type	Description	Biological application
Fluorometer	Measures average bulk fluorescence properties (µl to ml) includes plate readers	High throughput measurements in biological assays using fluorescent markers
Fluorescent microscope	Measures fluorescence from samples in 2D and 3D with high resolution (< 1 µm)	Detailed studies of cellular function. Imaging through 3D specimens e.g. complex tissues.
Fluorescent scanner	Spatially resolves fluorescence information from micron sized samples or larger in 2D includes microarrays	High throughput measurements in biological assays requiring spatial resolution.
Flow cytometer	Measure fluorescence from a flow stream of particles or cells	High through put analysis and separation of cell populations/particles.

Table 1.3 Overview of instrumentation available for fluorescence detection.

1.2.1.4 Specialised fluorescence techniques

Additionally specialised fluorescence techniques including fluorescence lifetime imaging microscopy (FLIM) and Forster resonance energy transfer (FRET)-based microscopy are available to improve the sensitivity of fluorescence detection methods.

Forster resonance energy transfer (FRET) is a fluorescent phenomenon, which is useful for intracellular sensing and many other biological applications. FRET is the non-radiative transfer of energy between two fluorophores when they are in close proximity. The energy is emitted from a donor in the excited stated to an acceptor in the ground state through long range dipole to dipole interactions. In

order for FRET to occur fluorophore pairs must fulfil 3 main criteria, 1) there must be overlap between the emission spectrum of the donor and the absorption spectrum of acceptor, 2) both fluorophores must have approximately parallel dipole orientations and 3) the donor and acceptor fluorophores must be less than 10 nm apart. The efficiency of FRET is highly dependent on the distance between FRET pairs as the efficiency of energy transfer is inversely proportional to the sixth power of the distance between the donor and the acceptor. Therefore FRET is useful for determining the proximity of biomolecules and has found applications in biology for investigating receptor ligand interactions, understanding protein folding, enzyme activity and detecting hybridisation of nucleic acids[105]. With regards to sensing this is useful because there are many examples of molecules, which change conformation in response to different metabolites. Consequently if the molecule is labelled with a FRET pair the change in confirmation can be detected. An example where this has been exploited is in green fluorescent protein (GFP)-based sensors, which will be discussed in more detail later in this section. Conversely FRET can be problematic for sensing using multiple analyte sensitive and reference fluorophores if multiple fluorophores are incorporated into a particle within close proximity.

Fluorescence lifetime microscopy (FLIM) is a technique, which uses fluorescence lifetime to construct an image. The fluorescence lifetime of a fluorophore is the time the fluorophore is in an excited state after absorption of photons. The amount of time a fluorophore spends in an excited state is dependent on the rate of internal conversion, photobleaching and FRET. The fluorescence lifetime can be dependent on analyte concentrations and thus used to perform intracellular measurements. FLIM imaging has several advantages over intensity-based microscopy for sensing. Measurements are not affected by rates of photobleaching, fluorophore concentration or excitation intensity. Additionally FLIM is not affected as much by fluorophores with closely matched spectral characteristics. Consequently ratiometric probes are not required for FLIM imaging. In general FLIM, permits more reliable quantitative measurements. The drawback of this approach is FLIM requires a highly specialised technical setup, which is difficult to apply for live cell imaging. However FLIM imaging has been exploited in studies to perform pH measurements in living cells[106,107].

1.2.2 Types of fluorescent nanosensors

Fluorophores alone do not address all the design challenges for sensors. Namely, it is difficult to control the location of fluorophores inside cells; they can interfere

with the cellular environment and are not ratiometric. Incorporation of fluorophores into nanoparticles to create fluorescent nanosensors is one way of addressing all these issues. The advantages of this approach are summarised in **Table 1.4.** The first fluorescent nanosensors were first reported in studies by Sasaki *et al*[108] and Clark *et al*[109] in the late 1990s, and were developed under the acronym PEBBLE (photonic explorer for biomedical use with biologically localised embedding). Since then several nanosensor designs have been developed, which will be discussed in the following section.

Nanosensor properties	Advantage	Summary
Size	Non-invasive	A spherical nanoparticle of 200 nm is approximately 1 x10^{-4}% the volume of a mammalian cell. Resulting in minimal physical disruption to the cell. A high surface to volume ratio ensures good accessibility of analytes to the sensing elements
Engineerability	Multiple sensing components	This is advantageous for ratiometric sensing and also detection of multiple analytes simultaneously
	Control of delivery	Nanosensors can be designed to target specific organelles and pathways yielding specific information
Non-toxic matrix	Low toxicity	Nanosensors synthesised from bio-friendly matrix minimise the impact on cell function
	Fluorophore protection	The matrix serves to protect the fluorophore from interaction with biomolecules that can disrupt sensing

Table 1.4 Advantages of particle-based sensors[104].

1.2.2.1 Particle-based fluorescent nanosensors

The first type of particle-based sensor, which will be discussed here, comprises a single sensing/reference component, acting as both the analyte recognition component and the transducer. The sensing/reference components in this type of sensor are usually fluorophores, but can also be a fluorophore conjugates. In the most common design, these components are attached to a homogenous nanoparticle matrix (**Figure 1.6A**). A diverse range of materials have been used for this purpose, the majority of which are polymer and silica-based materials. Examples are 1) polymer-based materials: polyacrylamide[110-124], polydecylmethacrylate[125], poly(styrene-block-vinylpyrrolidone)[126,127], poly(styrene sulfonate)/poly(allylamine hydrochloride)[128,129] and polystyrene[130]. 2) Silica-based materials: Silica/organically modified silica (ormosil)[115,131-140], silica shell over iron oxide[141], silica dextran core-shell[142]. Other materials utilised for nanosensor synthesis include dextran[143], gold[144], carbon nanotubes[145], dendrimers[146], liposomes[147] and micelles[148].

In some cases this design is not ideal as sensing and reference fluorophores can interfere with each other through a FRET interaction. In order to circumvent this sensors have been developed using a core-shell design where the reference fluorophores are held in the core whilst the sensing components are in the shell[117,128,129,131,132,141,149] (**Figure 1.6B**). This has the additional advantage of increasing the surface area for the sensor to interact with the analyte, whilst protecting the reference fluorophore from interference with the biological environment. The matrix used in both these designs is integral to the performance of the sensor.

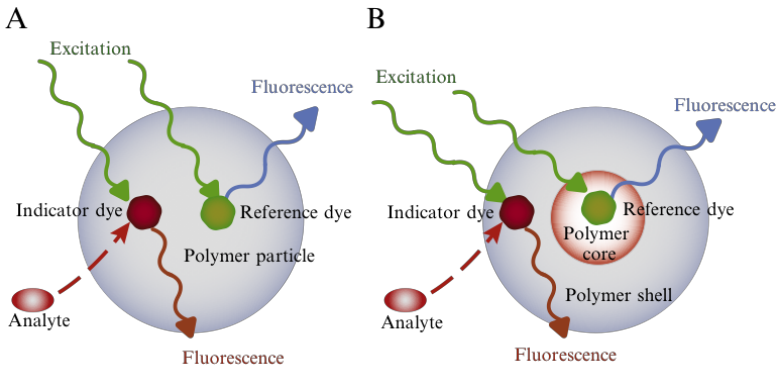

Figure 1.6 *Nanosensor design with fluorophores as the sensing and recognition components.* Nanosensor with a (A) homogenous matrix and (B) core-shell matrix reproduced with permission from[104].

The second type of nanosensor design uses separate component to recognise the analyte with a fluorophore acting purely as a signal transducer or reporter with no direct response to the analyte. This can provide improvements in different ways. Firstly the analyte recognition component provides a way in which to detect analytes for which analyte responsive fluorophores are not available or show poor selectivity. Secondly since reporter fluorophores are not required to be analyte-sensitive, the choice of fluorophores is expanded to fluorophores with optimal optical properties.

The most common sensor of this type is based on the transfer of energy from the analyte recognition component to the fluorophore (**Figure 1.7A-1,A-2**). The analyte recognition component of the sensor can be a fluorophore or non-fluorescent receptor complex, which quenches or enhances signal in the reporter fluorophore. Quantum dots (QDs) have been used as the reporter fluorophore in this sensor design[150-155]. QDs are inorganic semiconductor nanocrystals, which are 10 to 20 nm in size. QDs are fluorescent but absorb and remit photons in a different way to organic fluorophores. They are generally brighter and less susceptible to photobleaching than organic fluorophores and have thus been used to develop more robust sensors for intracellular measurements.

There are several other types of sensors of this type. Specialised ion selective sensors, have been developed for the sensing of K^+, Na^+ and Cl^-[156-158] (**Figure 1.7B**)**.** The primary components of this type of sensor comprise an ionophore and pH-sensitive fluorophore, which are entrapped in a lipophilic matrix. The ionophore is the analyte responsive component. For the sensing cations, the ionophore exchanges cations for H^+, whilst for sensing anions the ionophore absorbs H^+ ions. This transfer is governed by a thermodynamic equilibrium and leads to a local change in pH, which can be detected by a pH-sensitive fluorophore. An additional component is usually added to the particle to maintain a constant ionic strength.

Enzyme-based sensors have been developed for sensing, these take advantage of the high specificity of enzymes to recognise an analyte[116,154,159] (**Figure 1.7C**). In these sensors an enzyme is embedded into the nanosensor matrix with a reference fluorophore. The concentration of the analyte can be monitored if there is conversion of a fluorescent substrate into a non-fluorescent product or vice-versa. This principle has been used to fabricate sensors for hydrogen peroxide in

studies by Poulsen *et al*[116] and Kim *et al*[159]. These sensors incorporate an immobilised horseradish peroxidase (HRP) enzyme which catalyses the oxidation of a substrate in the presence of hydrogen peroxide. The study by Kim *et al* used Amplex red as the substrate, which fluoresces after oxidation whereas the study by Poulsen *et al* used guaiacol, which darkens following oxidation. Alternatively a fluorophore may be incorporated into the sensor, which responds to the concentration of the reactant or products. A key consideration for this type of sensor is to ensure enzymatic activity is maintained following incorporation into the matrix[116].

Sensors have also been developed based on chemiluminescence[160,161] (**Figure 1.7D**). Chemiluminescence is the emission of light derived from a chemical reaction. It is similar to fluorescence in the sense that emission occurs from electrons in an excited state, however the source of the excitation is from a chemical reaction rather than absorption of photons. This has an additional advantage for biological applications, as cells do not require irradiation with potentially harmful excitation light. This was used in a recent study to fabricate a sensor for hydrogen peroxide. Peroxolate, which is an ester that reacts specifically with hydrogen peroxide was incorporated into a nanoparticle matrix with a cyanine dye. Peroxolate reacts to form a high-energy dioxetanedione, which transfers energy to the cyanine resulting chemiluminescence[162].

The final type of sensor to mention are those that cause a fluorescent response based on a physical change which occurs to the particle upon exposure to an analyte[163,164] (**Figure 1.7E**). These types of sensors have been synthesised based on temperature sensitive polymers such as PNIPAM, which are coupled to moisture sensitive fluorophores. PNIPAM is a polymer, which increases in volume with temperature; this results in changes in the water distribution in the nanoparticle causing a response from the fluorophore.

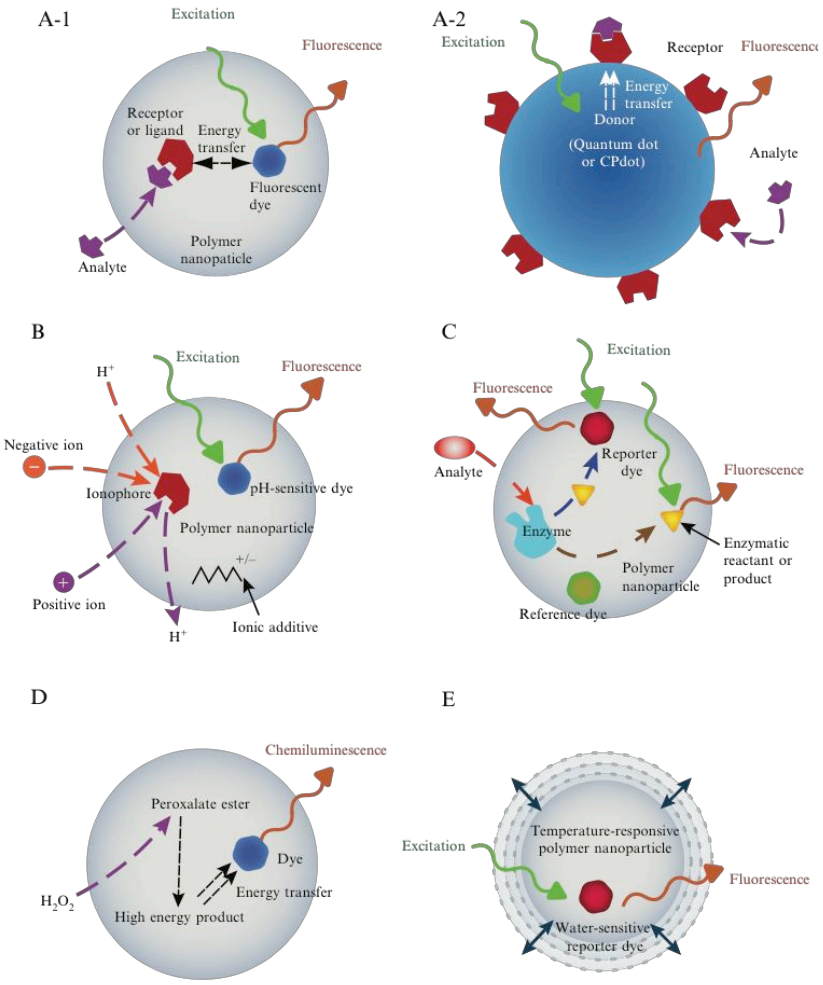

Figure 1.7 *Overview of nanosensor designs based on a separate analyte recognition component.* Recognition component is a receptor or ligand (A-1, A-2). Ionophore (B), Enzyme(C), Peroxoloate (D) or responsive polymer particle (E) reproduced with permission from[104].

1.2.2.2 GFP-based sensors

These sensors are based on derivatives of the green fluorescent protein (GFP) derived from the jellyfish *Aequorea victoria.* GFP was discovered in 1962[165] and successfully cloned 30 years later[166]. GFP has great significance in cell biology because the GFP gene can be fused to the sequence of target proteins and is expressed by most mammalian cells. In this way GFP is routinely used as an intracellular reporter of a broad range of proteins[167]. In addition to this derivatives of this protein have led to a new class of biosensors based on GFP-derived proteins responsive to analytes such as pH, Zn^{2+} and Ca^{2+}[168]. Several designs for this type of sensor have been proposed.

Firstly FRET based sensors[169]. These fall into two categories of sensor: intramolecular-based FRET sensors and intermolecular-based FRET sensors. In the former a donor and acceptor molecule is attached to the same protein. Analyte binding results in a conformational change to the protein resulting in a change in the FRET signal. Intermolecular FRET-based sensors function on a similar principle, except the donor and acceptor are on different molecules, therefore the FRET signal is only generated when the two molecules are bound together. This principle has been utilised for the development of set of sensors for Ca^{2+} called Cameleons[170,171].

Another strategy for synthesis of GFP-based sensors is to attach an exogenous analyte recognition site to the protein. Binding of analytes results in a change in conformation of the protein altering its fluorescent properties. This has been used for the detection of ATP[172], Zn^{2+}[173] and Ca^{2+}[174].

GFP-based sensing has two main advantages, firstly the analyte recognition component can be designed to respond to a more diverse array of metabolites/biological using protein-engineering techniques and secondly, the sensor can be targeted more specifically to specific intracellular compartment with minimal invasiveness. The disadvantage of this type of sensor is that the sensor will be anchored to a specific part of the cell; hence it is not suitable for dynamic measurements of the trafficking of nanomedicines.

1.2.2.3 RNA-based sensors

Recently, Paige and co workers have reported a promising new type of genetically encoded sensor based on RNA[75,175] (**Figure 1.8**). This sensor is based on some of their earlier work where they developed an RNA mimic of GFP called Spinach[176]. Spinach is a 98 nucleotide RNA aptamer that binds to a fluorophore, 3,5- difluoro-4-hydroxybenzylidene imidazolinone (DFHBI), to form a fluorescent complex (**Figure 1.8A**). Both Spinach and DFHBI are non-fluorescent in the unbound state. The fluorophore is a mimic of the chromophore found in GFP. They were able to transform this, into a sensor through insertion of a transducing and analyte recognition module (**Figure 1.8B**). In this configuration, the aptamer is non-fluorescent in the absence of a ligand, i.e. unable to bind DFHBI. However binding of a ligand to the analyte recognition component results in a change in conformation, which permits DFHBI to bind resulting in fluorescence (**Figure 1.8C**). In this way sensors have been fabricated for small molecules (adenosine, ADP, SAM, guanine and GTP) and proteins (thrombin and

streptavidin). Although these sensors are very much in early development, they offer greater versatility than GFP based sensors, primarily because there a powerful techniques for generating aptamers able to bind different analytes, namely, the Systematic Evolution of Ligands by Exponential Enrichment (SELEX) technique.

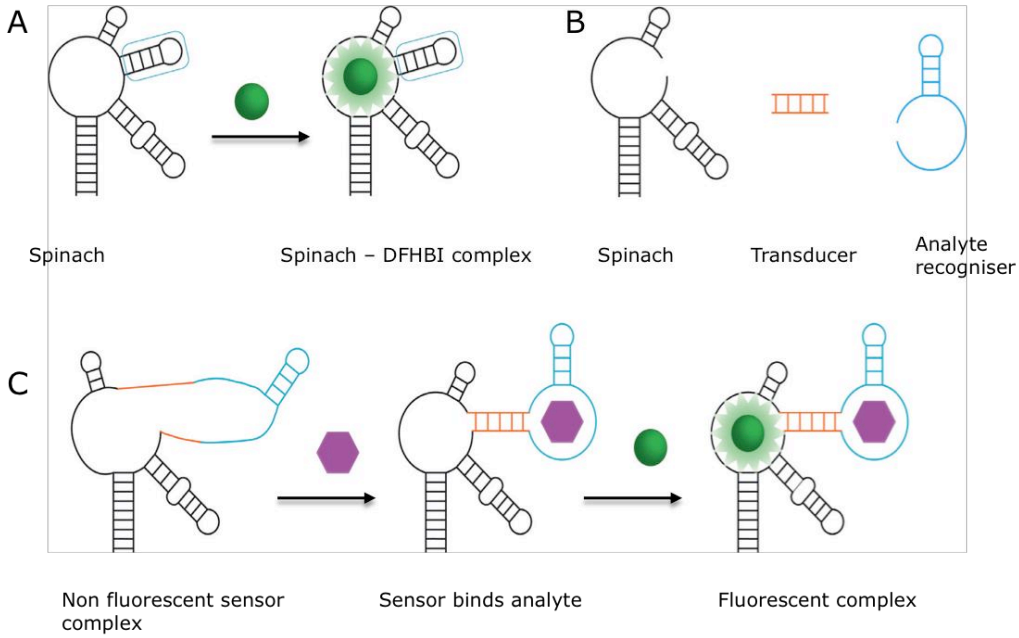

Figure 1.8 *Overview of Spinach-based RNA sensors.* (A) Spinach (aptamer) binds DFHBI. Binding results in a fluorescent complex. (B) Method for creating a sensor. A transducer sequence is incorporated with an analyte recognition component. (C) Mechanism of sensing. The complex is not fluorescent without any bound molecules. Binding of the analyte, results in the transformation of the aptamer into a form in which it can bind DFHBI. Addition of DFHBI results in fluorescence. Reproduced with permission from[175].

1.2.2.4 Surface enhanced Raman scattering (SERS)

Although fluorescence-based approaches are undoubtedly the most widely used approach to intracellular measurement, a promising method for measurement of intracellular pH based on SERS sensors is also under development. SERS imaging of intracellular analytes is based on the principle of Raman scattering. Raman scattering is specialised type of light scattering related to Rayleigh scattering, which arises due to the inelastic scattering of photons, critically the scattering of light is dependent on the molecular constituents of a material. In this way a molecule gives a specific Raman signature, which can be detected by spectroscopic techniques. This signal is often too weak to be used for single molecule detection inside cells, however the signal can be amplified if molecules

are detected in close vicinity to the surface of metal nanostructures, this is the general principle of the SERS technique. SERS has been used for mapping of intracellular 3T3 cells via delivery of SERS sensors into a cell by endocytosis[177]. In theory, the advantage of this method is the high specificity and sensitivity available through the detection of single molecules.

1.3 Aims

The overall aim of this thesis is to develop biological insights into intracellular trafficking using pH nanosensors, with the intention of using these insights to aid the rational design of drug delivery systems. **Chapter 2** describes the fabrication of a nanosensor for this purpose**. Chapters 3 and 4** outline the development and validation of methodology for performing measurements with ratiometric sensors. Applications are explored in **Chapter 5**. The detailed aims of each chapter are outlined here, and are restated at the start of each chapter.

The aim of **Chapter 2** is to fabricate a ratiometric nanoparticle-based pH sensor suitable for performing dynamic measurements throughout the entire intracellular trafficking process for nanomedicines. The minimal and maximum pH, which is expected through this process is ~ 4.5 and ~ 7.4, corresponding to pH in lysosomes and the cytoplasm, respectively[54]. Consequently the sensor should be responsive in this range with adequate sensitivity for performing accurate measurement. In relation to this the sensor must be robust. The sensor should protect fluorophores from potentially interfering with biomolecules, be resistant to fluorophore leaching and show good stability. In the wider context of this thesis, the sensor is intended as a mimic of nanomaterials utilised in drug delivery. Therefore the sensor should be designed to have physicochemical characteristics similar to that of nanoparticles used in drug delivery.

The aim of **Chapter 3** is to develop a reliable methodology for performing intracellular pH measurement. In order to do this factors affecting measurements (nanosensor uptake conditions, instrument settings, calibration and image analysis) are investigated. This is done with the view of developing a generalised guide to optimising experimental methodology for performing ratiometric measurements.

The aims of **Chapter 4** are to deliver nanosensors to the endocytic pathway without interference with natural cell function, perform pH measurements to identify the optimal sensor design and validate measurements. Measurements are validated by determining the intracellular location of the sensors and assessing pH-responsiveness.

The aim of **Chapter 5** is to apply pH nanosensors to gain biological insights into intracellular trafficking. Applications are explored in three different areas. Firstly

pH transitions occurring in different cell types during intracellular trafficking are assessed to provide a basis of the rational design of pH-responsive drug release systems. Secondly the effect of surface charge on the intracellular trafficking of nanosensors is investigated, to explore how the effect of physicochemical characteristics on intracellular trafficking can be investigated using pH nanosensors. Finally fundamental aspects of intracellular trafficking of siRNA formulations are investigated, to explore how pH nanosensors may be used to optimise endosomal escape.

The conclusions of each chapter are summarised in **Chapter 6**.

Chapter 2 Design, synthesis and characterisation of optical pH nanosensors for measurement in the endocytic pathway

2.1 Aim

The general aim of this chapter is to develop an optical pH nanosensor with optimal properties for pH measurement in the endocytic pathway. The minimal and maximum pH, which is expected through the endocytic pathway is between ~ 4.5 and ~ 7.4[54]. This corresponds to values obtained from static measurements of pH in lysosomes and the cytoplasm respectively. Consequently the sensor should be responsive in this range with adequate sensitivity for performing accurate measurement. In relation to this the sensor must be robust. The sensor should protect fluorophores from potentially interfering with biomolecules, be resistant to fluorophore leaching and show good stability. In the wider context of this thesis, the sensor is intended as a mimic of materials used in nanomedicine. Therefore the sensor should be designed to have physicochemical characteristics, which favour cellular uptake by endocytosis. Several nanosensors designs have been proposed in the literature to address this problem however these have limitations primarily in terms of measurement range, the work in this chapter aims to address this gap[104].

2.2 Introduction

There are two major design considerations for fabricating nanosensors. Firstly, the sensor must have suitable physicochemical characteristics to be taken up through the endocytic pathway with minimal impact on natural function. This is mainly determined by the properties of the nanoparticle matrix. Secondly, the sensor must have suitable optical characteristics. In this respect, an ideal sensor would be ratiometric, show rapid response, have high signal to noise and be sensitive to the entire pH range of the endocytic pathway. This is mainly determined by the sensing elements of the sensor, which are the fluorophores. These two critical design considerations are addressed in this chapter.

2.2.1 Synthesis of fluorescent nanosensors

The type of fluorescent nanosensors utilised in this study are fabricated by incorporating fluorophores into a nanoparticle matrix. This offers the possibility of incorporating different combinations of fluorophores into a single particle to create diverse ratiometric sensing systems as summarised in **Table 2.1**. In addition to providing the basis for a ratiometric sensing system, the nanoparticle matrix serves as a platform for delivering and controlling transport of the nanosensor in the endocytic pathway. The matrix also protects fluorophores from interference with natural cell function and vice-versa. This is necessary because some fluorophores are toxic to cells, or show altered optical properties in cells due to binding of biomolecules.[93,104].

2.2.1.1 Polyacrylamide nanosensors

Polyacrylamide is an ideal material for a nanosensor matrix, because it is biologically inert, hydrophilic, porous and optically transparent. Additionally, robust fabrication techniques are available to control the size, charge and shape of polyacrylamide nanoparticles.

Matrix	Indicator	Ref	Size (nm)	Characterisation	Incorporation method	Delivery method	Cells	pH range	Reference
PAA	CNF		20 – 100	SEM				7.0 – 7.7	Clark et al (1999)[110]
	CDMF	SR			Entrapment	Microinjection	Mouse oocytes	6.2 – 7.4	
	BCPCF	SR						6.2 – 7.2	
	FSA	SR						5.8 – 7.0	
	SNAFL							7.2 – 8.0	
	Fluorescein	RhB	50	DLS	Conjugation			5.8 - 7.2	Sun et al (2006)[178]
	OG	RhB	60 – 140	DLS	Conjugation	Endocytosis	HepG2	4.1 – 5.7	Sun et al (2009)[120]
	OG/5(6)-FAM	RhB			Entrapment			3.2 – 7.0	Chauhan et al (2011)[179]
	HPTS		68			Endocytosis	9L glioma	6.0 – 8.0	Ray *et al* (2011)[180]
PAA core-shell	Naphthalamide	SRB	28	DLS	Conjugation			5.0 – 8.2	Schulz et al (2010)[117]
Silica	FITC	RuBPY	42	TEM/DLS	Conjugation	Endocytosis	Murine macrophage/HeLa cells	4.0 – 7.0	Peng et al (2007)[181]
Silica core-shell	FITC	TRITC	70	SEM	Conjugation	Endocytosis,	RBL-2H3	5.0 – 7.4	Burns et al (2006)[132]
SWNTs	Fluorescein		158	AFM	Conjugation	Endocytosis	BT474	5.6 – 8.4	Nakayama-Ratchford et al (2007)[145]
Dextran	FITC	SRB	500	SEM	Conjugation	Endocytosis	Human foreskin fibroblasts	4.9 – 8.2	Horning et al (2008)[143]
PVA-PA with gold core	FITC	RBITC	20-30	TEM	Conjugation	Endocytosis	CHO	5.0 – 8.0	Stanca et al (2010)[144]
PS core-shell	FITC	DPA	18 - 20		Conjugation			4.0 – 6.5	Allard and Larpent (2008)[182]

Acronyms: BCPCF, 20,70-bis-(2-carboxypropyl)-5-(and 6)carboxyfluorescein; CDMF, 5-(and 6-)carboxy-40,50-dimethylfluorescein; CNF; DPA, 1,9-diphenylanthracene; FITC, fluorescein isothiocyanate; FSA, fluorescein-5-(and 6)sulfonic acid; HPTS, 8-hydroxypyrene-1,3,6-trisulfonic acid; PDB, phorbol-12,13-dibutyrate; PEG, polyethylene glycol; PAA, polyacrylamide; PVA, poly(vinyl alcohol); PPE, poly(2,5-di(30,70-dimethyloctyl)phenylene-1,4-ethynylene); RhB, rhodamine B; RuBPY, rhodamine B isothiocyanate; RuBPY, tris(2,20-bipyridyl)dichlororuthenium(II) hexahydrate; SNAFL, 5-(and 6)-carboxy SNAFL-1; SR, sulforhodamine; SRB, sulforhodamine B; TRITC, tetramethylrhodamine isothiocyanate.

Table 2.1 Summary of selected previously reported pH-sensitive nanosensors. *Adapted from[104].*

Polyacrylamide nanoparticles are synthesised via free radical polymerisation of acrylamide and a cross-linker, N,N'methylene-bisacrylamide, in an inverse water-in-oil nanoemulsion. This method was first applied to nanosensor fabrication by Clark *et al* in 1999[110] and has since been modified to produce nanosensors between 50 and 200 nm with a narrow size distribution[117,120,179,180,183]. Briefly, the inverse nanoemulsion consists of a continuous hexane hydrophobic phase (oil) and a hydrophilic aqueous phase (water), the interfaces of the inverse nanoemulsion are stabilised with anionic and non-ionic surfactants, polyoxyethylene(4) lauryl ether (Brij 30) and dioctyl sulfosuccinate sodium (AOT), respectively. Through careful control of the water, oil, and surfactant ratio a narrow distribution of nano-sized water droplets are created. Acrylamide monomers undergo free radical polymerisation in the water droplets resulting in nanoparticles of a narrow size distribution.

Sensing elements, in this case fluorophores can be incorporated into the polyacrylamide matrix before or after synthesis. Fluorophores can either be entrapped in the pores of the matrix or directly conjugated to chemical groups present on the matrix. For entrapment, fluorophores, which are usually too small to be retained in the matrix, are conjugated to a molecule, which is large enough to be trapped in the pores of the matrix (e.g. 10kDa dextran). The fluorophore conjugate is then added to the polymerisation mixture and thus incorporated into the nanoparticle matrix during synthesis. This has been reported as an effective method for fluorophore entrapment[110,179,184]. However there are instances where fluorophores have been seen to leach out of the matrix[110,120,184]. This may be due to variations in the polymeric architecture of nanoparticles synthesised with different monomer to cross-linker ratios. Fluorophore leaching results in an imbalance in the concentration of reference and indicator fluorophores inside nanosensors, distorting ratiometric measurements. An alternative approach is direct conjugation of fluorophores to the nanoparticle matrix. This requires functionalisation with groups such as primary amines[120] or alkynes[185]. Fluorophores with the corresponding reactive group can be attached to the nanoparticle either prior to polymerisation (pre-conjugation) or following synthesis and purification (post-conjugation). Attaching fluorophores in different ways has been observed to alter the brightness of nanosensors presumably due to how much fluorophore is loaded into the particle[120]. This is particularly important in applications where there the sensitivity of detection is low. This is because low sensitivity results in low signal to noise ratios increasing the error from measurements. Signal can be amplified by increasing the intensity of

excitation light or exposure time, however this increases the risk of phototoxicity and photobleaching. Both entrapment and conjugation have previously been used to incorporate fluorophores into nanosensors.

In addition to incorporating fluorophores into the matrix, functionalisation of polyacrylamide nanosensors can be utilised to target the endocytic pathway. Polyacrylamide nanosensors synthesised without any additional functional groups are not taken into a cell without physical methods used to force entry, such as picoinjection and gene gun bombardment[86]. However nanosensors can be delivered to cells via endocytosis by surface functionalisation with agents that actively promote uptake examples of such agents are cell penetrating peptides[186] and hyaluronic acid (ligand for receptor-mediated endocytic uptake by CD44 receptors)[121]. Additionally certain physicochemical characteristics of nanoparticles such as surface charge are known to favour cellular uptake by endocytosis. Accordingly functionalisation of sensors with charged groups has been used as a means of controlling cellular entry[117,120]. The delivery of nanosensors is a complex issue, which is discussed in more detail in **Chapter 4**.

2.2.2 Fluorophores for measurement of intracellular pH

The sensing elements of fluorescent nanosensors are pH-sensitive fluorophores, which must be carefully selected to ensure the sensor has optimal optical properties for the application. Since the first determinations of pH in the endocytic pathway, the majority of live-cell measurements of intracellular pH have been made using pH-sensitive fluorophores. Due to the development chemical techniques for the synthesis of fluorophores, a broad range of fluorophores are now commercially available for measurement of intracellular pH, many of which are sensitive to pH changes occurring in the endocytic pathway (reviewed by Han *et al*[93]).

There are several factors to consider when determining the suitability of a fluorophore for pH measurement in a given application. The factors to consider are summarised in **Table 2.2**.

Fluorophore properties	Summary
Dynamic range	The range of pH between the minimum and maximum response of the nanosensor within the detection limit.
Sensitivity	The change in signal between the maximum and minimum response across the dynamic range.
Resolution	Minimal change in pH, which is required to produce a significant change in response.
Brightness	Overall signal intensity, determined by the molar extinction coefficient and quantum yield
Stability	Changes in fluorescent intensity as a result of factors such as photobleaching and fluorescence lifetime.

[a] The detection limit can be considered to be the intersect between the linear portion of the curve and the intersect between the minimum and maximum asymptote.

Table 2.2 Criteria for assessing the optical properties of a fluorophore.

Purely from a sensing perspective the most important considerations are the dynamic range, sensitivity and resolution of the fluorophore. In order to clearly define these three parameters, it is helpful to consider them in the context of the relationship between pH and signal intensity. Most pH-sensitive fluorophores demonstrate a sigmoidal response to pH (**Figure 2.1**). In this context, the dynamic range is the range between the minimal and maximal response, this equates to the range in which the sensor produces a reliable measurement, required to be between 4.5 and 7.4 for measurements in the endocytic pathway[54]. It is intuitively clear that measurements towards the upper and lower asymptotes are not reliable because sensitivity is low i.e. large changes in pH will result in a small change in the indicator to reference ratio. Therefore a detection limit must be set, there are several ways this can be set. For an objective determination of the detection limit in this work, it is considered to be at the intersect between the linear portion of the curve and the lower and upper asymptote (**Figure 2.1A,B**). Therefore the dynamic range is the pH range between the upper and lower intersects. The sensitivity of pH-sensitive fluorophores is more difficult to precisely define as the sensitivity changes

through the curve. However the sensitivity can be approximated to allow for comparison. An approximation of sensitivity is the change in signal between the minimal and maximal response within the dynamic range. The simplest way of representing this is as a fold change (**Figure 2.1C**). Related to the sensitivity of the fluorophore is the resolution. This is the minimal change in pH required to produce a significant response, this is governed by the error in measurement from the fluorophore. For example if the error in measurement for a given point is within ± 0.5 pH units, then any pH changes within 0.5 pH units will be insignificant. Hence the resolution of the sensor is 0.5 pH units. Greater sensitivity reduces the probability of error, hence is likely to result in better resolution.

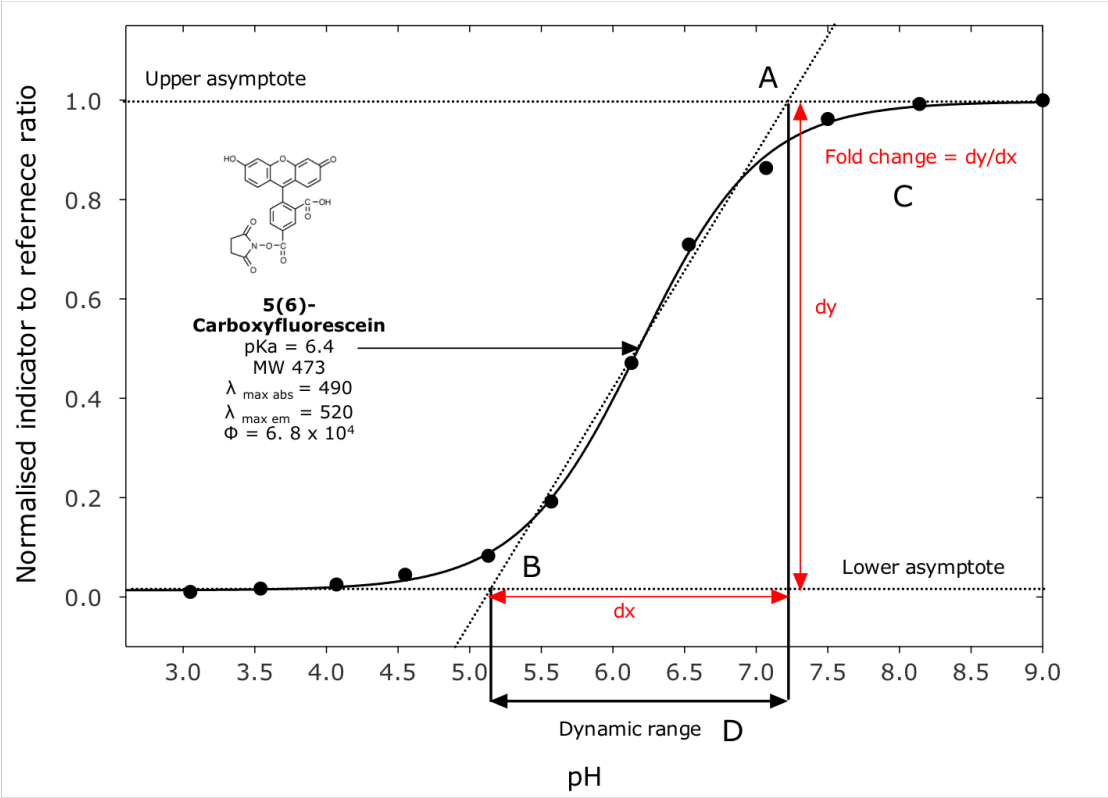

Figure 2.1 *Graphical representation of the sensitivity and dynamic range of 5(6)-Carboxyfluorescein.* (A,B) Detection limits. (C) Fold change, indicates an approximation of sensitivity. (D) Dynamic range.

An approximation of the dynamic range can be made from the acid disassociation constant (pKa) of the fluorophore. The pKa is effectively the value where the fluorophore shows half the maximum response. Based on measurements from previous fluorophores the detection limit can be approximated to be ±1.0 pH

units of the pKa[183]. Consequently pKa is an important parameter in evaluating the dynamic range of fluorophores.

The other properties to be considered in selecting fluorophores are related to the stability and brightness of the fluorophore. Brightness is determined by the molar extinction coefficient and quantum yield, which are inherent properties of the fluorophore. Stability of the fluorophore is dependent on photobleaching and fluorescence lifetime.

2.2.2.1 Commercially available fluorophores

Commercially available fluorophores for pH measurement are summarised in **Table 2.3**. In most applications, pH-sensitive fluorophores are used as free fluorophores. The most common fluorophores used in this way are the fluorescein-derivatives 2',7'-Bis-(2-carboxyethyl)-5-(and-6-)carboxyfluorescein (BCECF) (pKa 7.0)[187] and Carboxy-SNARF-1 (pKa 7.5)[188]. The advantages of utilising these fluorophores relate to their ease of delivery, retention in the cellular environment, resistance to photobleaching and ratiometric nature. Other fluorescein-based fluorophores such as *5(6)*-carboxyfluorescein ((5(6)-FAM))[95], 5(6)-carboxydichlorofluorescein (CDCF)[189] and Oregon Green[190] are not as well retained in cells, but are still widely used presumably because they are more cost-effective with a less complex synthesis route.

Most fluorophores show a decrease in fluorescent intensity with increasing acidity, however there are a few examples of fluorophores, which show the opposite (CypHer5E[191], pHRodo[192] and Lysosensor fluorophores). These fluorophores have an additional advantage of reporting a positive signal in response to endocytic acidification. This is particularly relevant for measurements in the endocytic pathway as the environment in endosomes and lysosomes is highly degraditive and could result in loss of signal. Fluorescein-based fluorophores are also prone to photobleaching, which is another potential source of signal loss.

Fluorophores are continually being developed with enhanced optical properties through structural modifications, which lead to enhanced stability, and spectral properties. Critically modifications have been made to obtain fluorophores with different pKa values. An example of this is the introduction of electron-withdrawing groups on xanthenes of fluorescein resulting in lowering of pKa[190]. This has been used to synthesise Oregon Green (pKa 4.8) and CDCF (pKa 4.7), which are fluorinated and chlorinated derivatives of fluorescein respectively.

However to date there is no ideal fluorophore suitable for measurement in the entire range of the endocytic pathway.

Fluorophore		$\lambda_{max\ abs}$ (nm)	$\lambda_{max\ em}$ (nm)	pKa	ref
Near neutral	5(6)-FAM	492	516	6.5	*95,193*
	BCECF	503	525	7.0	*187*
	BCPCF	505	527	7.0	
	C.SNARF-1[a]	544	575	7.5	*188*
	C.SNARF-1[b]	583	631		
	C.SNARF-4F[a]	529	592	6.4	
	C.SNARF-4F[b]	582	661		
	C.SNARF-5F[a]	560	580	7.2	
	C.SNARF-5F[b]	575	628		
	C.SNAFL-1[a]	510	539	7.8	
	C.SNAFL-1[b]	542	623		
	SNAFL-calcein[a]	492	540	7.0	
	SNAFL-calcein[b]	535	625		
	CypHer 5E	650	665	6.4	
	1,4 DHPN[a]	342	402	8.0	
	1,4 DHPN[b]	453	483		
	HPTS[a]	405	514	7.3	
	HPTS[b]	465	514		
Acidic	Oregon Green 488	490	514	4.8	*190*
	6-carboxyl Oregon Green 488	492	514	4.8	
	Oregon Green 514	506	529	4.8	
	CDCF	503	525	4.7	*189*
	C.SNARF-4F[a]	520	582	6.4	
	C.SNARF-4F[b]	592	661		
	HPTS[a]	405	514	7.3	
	HPTS[b]	465	514		
	Blue- DND-167	373	425	5.1	
	Green DND-189	443	505	5.2	
	Green DND- 153	442	505	7.5	
	Blue DND -192	374	424	7.5	
	Acridine Orange[c]	495	530		
	Acridine Orange[d]	465	655		
	ACMA	419	484	8.6	
	Green-DND-26	504	511		
	pHrodo	560	585	6.5	*192*

[a] Acidic form [b]Basic form [c]Dimer or oligomer [d]Monomer

Acronyms: ACMA, 9-amino-6-chloro-2-methoxy- acridine; BCPCF, 20,70-bis-(2-carboxypropyl)-5-(and 6)carboxyfluorescein; CDCF, 5(6)-carboxydichlorofluorescein; BCECF; 2′,7′-Bis-(2-carboxyethyl)-5-(and-6-)carboxyfluorescein; C.SNARF-X, Carboxy-SNARF-X; C.SNAFL, Carboxy-SNAFL; C.fluorescein, carboxyfluorescein; 1,4 DHPN, 1,4-Dihydroxyphthalonitrile; FITC, fluorescein isothiocyanate; HPTS, 8-hydroxypyrene-1,3,6-trisulfonic acid.

Table 2.3 Commercially available pH-sensitive fluorophores. *Adapted from*[93].

2.2.2.2 Ratiometric fluorophores

Ratiometric methods are desirable for intracellular sensing because fluorophores are often sequestered to organelles after entering a cell. In such cases fluorescence intensity will be affected by fluorophore concentration, in addition to the analyte of interest, thus distorting measurements. There are a few examples of ratiometric fluorophores. Ratiometric fluorophores are differentially responsive to pH at two or more excitation or emission wavelengths for example one wavelength may display an increase in intensity with increasing pH whilst another wavelength shows a decrease or no change. In this scenario a ratio can be taken and related to a value for pH using a calibration. This means measurements are not affected by differences in analyte concentration, sample excitation or the biological environment. However the ratiometric fluorophores suitable for measurements in the endocytic pathway which are currently available, are only sensitive for part of the intracellular pH range e.g. BCECF, C.SNARF-1[188]. Incorporating these fluorophores into polyacrylamide nanosensors has also been seen to lead to a disruption in pH sensitivity[188].

Consequently most sensor designs incorporate a separate reference fluorophore. However it is possible to synthesise sensors with an extended dynamic range by incorporating multiple pH-sensitive fluorophores into a fluorescent nanosensor[179,194]. This sensor design incorporates two fluorophores with identical emission spectra but different pKa values (5(6)-FAM pKa 6.5, Oregon Green, pKa 4.8) and a reference fluorophore TAMRA. Oregon Green is optimally responsive in the acidic range (~3.9-5.7) whilst 5(6)-FAM is optimally responsive in the near neutral range (~5.5-7.3). Consequently at the intracellular acidic extreme, 4.0, the pH the sensor is responsive, due to Oregon Green, whereas 5(6)-FAM is effectively optically silent. As the pH increases towards near-neutral (7.3) the responsiveness of Oregon Green diminishes, and the responsiveness of 5(6)-FAM increases. The net result is the overall response of the nanosensor is maintained. In this way sensors can be generated with a pH measurement range between 4.0 and 7.5.

2.2.3 Nanosensor characterisation

Characterisation of nanosensors involves determining the optical characteristics (dynamic range, sensitivity, resolution, brightness and stability) and physical characteristics (size, shape and surface charge) of nanosensors. Full characterisation is particularly important in a cellular context where small changes in physicochemical properties can alter how a cell interacts with a

material. Several techniques are available for particle characterisation, each with advantages and limitations, for this work a series of complementary techniques were selected. For size characterisation DLS, SEM and AFM were used. For the majority of work, DLS was used because it is a fast and accurate method for measurement of particle size. The limitations of this technique are that DLS measurements are based on a series of assumptions about the particle such as shape and structure, which are incorporated into a model. In addition to this large particles scatter much more light than smaller particles hence a small amount of large particles can obscure the signal from smaller particles. Consequently AFM and SEM were used as complimentary techniques for characterisation. SEM and AFM have the advantage of not relying on such models and permit visualisation of the sample. The limitations of these techniques are that the imaging conditions/sample preparation is not as mild as DLS. In addition to this they provide relatively poor statistical representation of a sample without time-consuming image analysis. For surface charge and optical characterisation light scattering (Zetasizer) were used. Both these techniques were selected as they provide fast and accurate measurements with minimal sample preparation requirements. The principles of these techniques are described in the following section.

2.2.3.1 Dynamic light scattering (DLS)

DLS is a well-established technique for determining the size of nanoparticles as small as 1 nm. DLS measures size by relating the rate of Brownian motion of particles in a liquid to size by the Stokes-Einstein equation[195].

Brownian motion describes the random motion of particles, as they are bombarded by solvent molecules in a suspension. The velocity of Brownian motion is related to particle size where smaller particles have a greater velocity compared to large particles. The velocity of Brownian motion is measured as the translation diffusion coefficient, which is used to calculate the diameter of the particle, with knowledge of the temperature and viscosity of the solvent, by the Stokes-Einstein equation:

$$d(H) = \frac{kT}{3\pi\eta D}$$

Where:

$d(H)$ = hydrodynamic diameter
D = translational diffusion coefficient
k = Boltzmann's constant
T = absolute temperature
η = viscosity

The value measured by DLS describes how a spherical particle diffuses through a liquid at a given temperature with a known viscosity. Therefore the size measured is often described as the hydrodynamic diameter of the particle.

The rate of Brownian motion is actually determined by measurement of the rate at which scattered light fluctuates. In a typical DLS set up the particles are exposed to a laser and the detector measures the fluctuations in scattered light intensity. The rate at which light fluctuates is dependent on the size of the particle. The signal is then transferred to a correlator, which measures the intensity of scattered light at successive time intervals. The rate of fluctuation is then converted into size using the Stokes-Einstein equation. The measurement is then plotted as a distribution of the relative intensity of light scattered by particles of different diameters. The intensity of scattered light is not directly proportional to particle size i.e. larger particles scatter far more, light than smaller particles. Consequently in mixed populations signal from larger particles can often mask the signal from smaller particles. In such cases, it is preferential to present data in terms of number or volume distribution, which corrects for the additional light scattered by the larger particles.

The instrument used in this work was the ZetaSizer Nano ZS (Malvern UK). The Nano ZS has an advantage over older models (Nano S90 and Nano ZS90), which minimises error from light scattered by contaminants. It uses Non-Invasive Backscatter Detection (NIBS) to detect the scattering signal. In backscatter detection, the detector is position to detect scattered light at an angle of 173^{o} as opposed to 90^{o} for older instruments. This is advantageous because large contaminants mainly scatter light in the forward direction (90^{o}). In addition to this light does not have to pass through the entire sample to register on the detector, reducing the effect of multiple scattering caused where light scattered from one particle is further scattered by neighbouring particles.

2.2.3.2 Atomic Force Microscopy

Atomic force microscopy is a scanning probe technique utilised for a number of applications including imaging nanoparticles[196], films[197], proteins, DNA and molecular scale interactions[198]. It was used in this study to image nanoparticles.

The key components of an AFM are a laser, cantilever and detector. The laser shines on the back of the cantilever whilst the cantilever moves across the sample surface. Projections on the sample surface deflect the cantilever, in turn altering the position of the laser. The laser beam is positioned on to a photodiode detector, which is divided into four quadrants. Movements on the cantilever are detected as differences in voltage across different quadrants of the photodiode and used to construct an image of the sample surface. There are different methods for moving the cantilever across the sample. Two common modes are contact mode and tapping mode. In both cases the cantilever is positioned on to the sample by piezoelectric transducers, which are utilised to control the position of the tip with high precision. In contact mode the tip is scanned across the sample, whilst in tapping mode the cantilever is set up to oscillate near the surface of the sample in order to tap the sample. Tapping mode is commonly utilised for soft samples as it minimises damage to the tip and the sample. The ultimate resolution achievable by AFM is dependent on the sharpness of the tip. The tips currently used are made of silicon or silicon nitride have a tip size of a few nanometres but the conical shape prevents the tip from probing surface features positioned between elevated regions of the sample, which are in close proximity. The lateral resolution is typical ~ 30 nm whereas vertical resolutions of ~ 0.1 nm are achievable.

2.2.3.3 Scanning electron microscopy (SEM)

Electron microscopes utilise a beam of electrons to illuminate a sample and produce an image. The wavelength of electrons are many times smaller than that of visible light, producing images with resolutions of less than 1 nm whereas the highest resolution achievable by conventional diffraction-limited light microscopes is ~ 240 nm.

SEM works by scanning a sample with a focused electron beam, as the electron beam interacts with the sample, energy is lost and emitted in different forms such as heat, back-scattered electrons, secondary electrons and X-ray emissions. The variations in these signals are dependent on the topography of the sample surface. Variations in the signals are used to construct an image. A development

of SEM is the environmental SEM[199]. The main advantage of this technique is that it allows a gaseous chamber for imaging whereas other forms electron microscopy requires a vacuum. This means that hydrated samples can be analysed and particles do not require the deposition of a conductive layer on to the surface. This is milder processing method for delicate samples.

2.2.3.4 Zeta potential

The Zeta potential of particle is a property of a nanoparticle in a suspension, which is related to surface charge. This value gives information about the stability of a colloidal system as well as surface characteristics, which are important for cellular interactions[200]. The concept of Zeta Potential originates from a theory developed by Derjaguin, Verwey, Landau and Overbeek (DVLO) in the 1940s, which describes the stability of colloidal systems. This theory states that the stability of a particle in a suspension is described by its total energy potential, V_T. The total energy potential is a balance of the attractive forces from Van de Waals interactions (V_A) and repulsive forces from the electrical double layer (V_R). To a lesser extent the potential energy from the solvent (V_s) contributes to the total energy potential. The relationship is described by the following equations:

$$\mathbf{V_T = V_A + V_R + V_S}$$

$$\mathbf{V_A = -A/(12\,\pi\,D^2)}$$

$$\mathbf{V_R = 2\pi\varepsilon a\zeta^2\,exp(-\kappa D)}$$

Where:

V_T = Total energy potential
V_A = Attractive energy potential
V_R = Repulsive energy potential
A = Hamaker constant
D = Particle separation
κ = Ionic composition
ζ = Zeta potential

The Zeta potential is a factor contributing to the repulsive forces between particles as they interact in a colloidal solution. In general the greater the zeta potential the greater the stability. A Zeta potential of ± 30 is considered to be

stable. Zeta potential is related to surface charge by the electrical double layer, which forms around all charged particles in a colloid. Charged surfaces in a suspension will affect the distribution of ions in the surrounding interfacial region, resulting in the formation of an electrical double layer. A charged surface attracts counter ions which form a layer where ions are tightly bound to the surface (Stern Layer), adjacent to this layer is a more diffuse layer where counter ions are less firmly associated. There is a notional boundary within this diffuse layer, which is the zeta potential. This is illustrated in **Figure 2.2**.

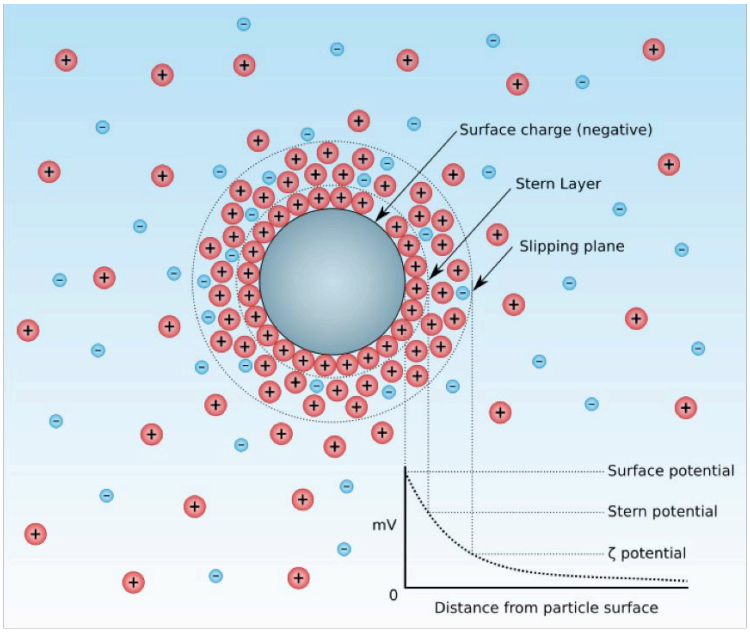

Figure 2.2 *Principle of Zeta Potential. Reproduced with permission.*

The Zeta potential was measured in this study using the ZetaSizer Nano ZS (Malvern UK). This instrument measures electrophoretic mobility, which is converted into Zeta Potential. Electrophoretic mobility is related to Zeta potential by the Henry function:

$$\mathbf{UE = 2\,\varepsilon\,\zeta\,f(\kappa a)/\,3\eta}$$

Where:

UE = electrophoretic mobility
z = zeta potential
ε = dielectric constant
η = viscosity

f(κa) = Henry's function

The particles are placed in a capillary cell with electrodes at different ends. A potential is then applied across the electrodes and particles move towards an electrode. The velocity is measured which corresponds to electrophoretic mobility which is then converted to Zeta Potential. The measurement is made by measuring fluctuations in scattered light caused by particles moving through the medium. Briefly, a laser is used to illuminate the sample, and scattered light is detected. The frequency of fluctuations of scattered light is measured as a potential is applied to the cell, this is then used to calculate zeta potential.

The Zeta potential value is greatly affected by the solution the measurement is taken in, and in particular pH. This is because ionisation is the primary mechanism by which particles acquire a surface charge. Therefore the presence of acidic or alkali conditions will affect the rate of ionisation. For example, if a particle has a positive zeta potential, and an acid is added the particle will acquire a more positive charge due to the presence of H^+ ions. Therefore it is essential to consider the properties of the solution for a Zeta potential measurement.

2.2.3.5 Fluorometry

This is a well-established technique for the measurement of fluorescence from samples. A spectrafluorometer consists of 4 basic components: A light source, monochromator, cuvette holder, a second monochromator and a detector. The light source is the excitation source and is usually a Xenon arc lamp. The light from the lamp passes through a monochromator, which is a type of optical wavelength filter that passes light of a narrow band of user-defined wavelengths. The light passes through the monochromator to the sample placed in a cuvette. Light is then emitted as fluorescence from the sample in different directions; some of this light will pass through a second monochromator positioned at a 90^o angle to the sample cuvette. The light is then focused on to a detector that can be a CCD, photodiode or PMT. The monochromators can be set to measure the emission and excitation spectra of the sample. For the emission spectrum the excitation wavelength is fixed whilst emission intensity is measured across a range of wavelengths. For the excitation spectra, the emission wavelength is fixed and the sample is excited at different wavelengths in a similar manner.

2.3 Materials and Methods

2.3.1 Materials

Reagents: Acrylamide, N, N methylenebisacrylamide (Fluka Analytical), N-(3-Aminopropyl)methacrylamide hydrochloride (APMA) (Polysciences Inc.), polyoxyethylene(4) lauryl ether (Brij30)(Fluka Analytical), dioctyl sulfosuccinate sodium (AOT), Ammonium persulphate (APS), N,N,N,N-tetramethylethylenediamine (TEMED), Hexane (Fisher Scientific), absolute ethanol (Fisher Scientific), deionised water (18.2 Ω), sodium tetraborate, 10,000 MW aminodextran, citric acid, sodium phosphate.

All chemicals were obtained from Sigma Aldrich unless otherwise stated.

Fluorophores: Oregon Green 488 succinimidyl ester (OG), 5(6)-carboxyfluorescein succinimidyl ester (5(6)-FAM), Alexa488 succinimidyl ester, pHrodo succinimidyl ester, CypHer 5E succinimidyl ester (GE healthcare), 5(6)-carboxytetramethylrhodamine succinimidyl ester (TAMRA).

Fluorophores were obtained from Invitrogen unless otherwise stated.

Instruments: pH meter (Jenway model 3510), Centrifuge (Hermle z300), Rotary evaporator (Buchi Rotavapor R-200), flurometer (Cary Varian Eclipse). Argon line at a pressure of 1 bar (14.5 PSI)(BOC gases).

2.3.2 Methods

2.3.2.1 Fabrication of polyacrylamide nanoparticles

200 ml of hexane (oil phase) was purged with Argon for 30 minutes. 40 ml of deoxygenated hexane was then added to a surfactant mixture of 1.59g AOT and 3.08g Brij30 in a 100 ml round bottom flask. The flask was purged with argon for a further 15 minutes prior to addition of hexane. The flask was then sealed under an inert Argon atmosphere using a balloon. An acrylamide monomer mixture of 540 mg of acrylamide and 160 mg of N, N methylenebisacrylamide dissolved in 2 ml deionised water (water phase) was then added to the sealed flask using a syringe. Additional monomers and fluorophores were added at this point, as discussed in the following section. Reagent quantities for the fabrication of blank

and amine-functionalised nanoparticles are shown in (**Table 2.4**). A final volume of 2 ml was maintained. The stirring solution was left for 5 minutes to form the nanoemulsion. 30 µl of a 10% (w/v) solution of APS and 15 µl of TEMED was added to under Argon to initiate the reaction. The emulsion was purged with argon for a further 5 minutes, sealed under Argon and left for 2 hours.

The reaction was terminated by removing the stopper and exposing the reactants to oxygen. Hexane was then removed by rotary evaporation and precipitated in 40ml absolute ethanol. The mixture was then transferred to a 50 ml falcon tube and centrifuged for 7 minutes at 6000 rpm. The supernatant was then removed and the sensors were washed again. The sensors were washed in this way a total of 5 times. Following the final wash, the sensors were suspended in 5 ml of ethanol, which was removed by rotary evaporation. The dried sensors were stored at 4^{o}C.

Functional Group	**Functionalisation reagent**	**Monomers (mg)**		
		Acrylamide	N,N methylene bisacrylamide	Functionalisation reagent
Blank	-	540.0	160.0	-
Amine	APMA	529.5	160.0	27.2

Table 2.4 Reagent quantities used for synthesis of blank and amine-functionalised nanosensors.

2.3.2.2 Incorporation of fluorophores into the nanoparticle matrix

Fluorophores were incorporated into the nanoparticle matrix by two different methods:

I. Entrapment of dextran-fluorophore conjugates into the nanoparticle matrix
II. Covalent attachment directly to the nanoparticle.

I. Entrapment: A stock solution of dextran conjugated to a fluorophore was made. The stock solution was made dissolving 10 mg of 10,000 MW aminodextran in 5 ml of sodium borate buffer (50 mM pH 9). Typically 0.05 mg* of fluorophore was then added and left stirring for 2 h. 250 µl of this solution was added to the acrylamide monomer solution during nanoparticle synthesis.

Any remaining stock solution was stored at 4°C protected from light, and used within a month.

*The amount of fluorophore was varied dependent on the brightness of fluorophore.

II. Covalent attachment: Fluorophores were attached to polyacrylamide nanoparticles either before (pre-conjugation) or after (post-conjugation) synthesis. For pre-conjugation fluorophores were attached to an acrylamide monomer containing a primary amine group (APMA) and then added to the acrylamide monomer solution, whereas for post-conjugation, nanosensors were amine-functionalised by adding APMA to the acrylamide monomer mix during synthesis. The reaction for conjugation of an NHS group with a primary amine group is shown in **Figure 2.3.**

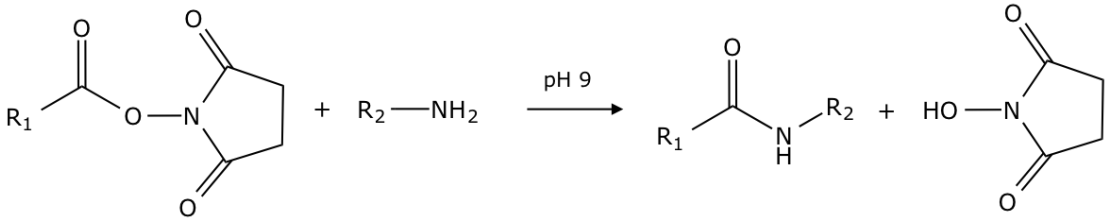

Figure 2.3 *Reaction of primary amine group with an NHS group.*

Pre-conjugation: To synthesise acrylamide monomers conjugated to fluorophores, 5 mg of APMA was dissolved in 2.5 ml of sodium borate buffer (50 mM pH 9). 1.5 mg* of fluorophore was then added to the solution and left stirring for 2 h at room temperature followed by 12 h at 4°C. 250 µl of this solution was then added to the acrylamide monomer solution.

Post-conjugation: For preparation of amine-functionalised polyacrylamide nanoparticles, an acrylamide monomer solution was prepared by dissolving 522.5 mg acrylamide, 160 mg N, N methylenebisacrylamide and 27.2 mg APMA in deionised water. Polyacrylamide nanoparticles were then synthesised as previously described.

50 mg of amine-functionalised nanoparticles were then re-suspended in sodium borate buffer (50 mM pH 9) and 1 mg of succinimidyl ester functionalised

fluorophore was added to the solution and left stirring for 2 h at room temperature followed by 12 h at 4°C (the amount of fluorophore was varied dependent on the brightness of fluorophore). Nanosensors were then precipitated in ethanol and washed by centrifuging at 6000rpm for 7 minutes. This was repeated a total of 3 times. Following the final wash, the sensors were suspended in 5 ml of ethanol, which was subsequently removed by rotary evaporation. The dried sensors were stored at 4°C.

Successful incorporation of amine functionality to the matrix was confirmed by a fluorescamine test for primary amine functionality (**Figure 2.4**). 2 mg of nanosensors were re-suspended in 2 ml of deionised water. 100 µl of 1 mg ml^{-1} fluorescamine was added to the nanosensor solution and was left for 60 minutes. The fluorescence of the sample was then analysed using a fluorometer by measuring emission at λ475 nm.

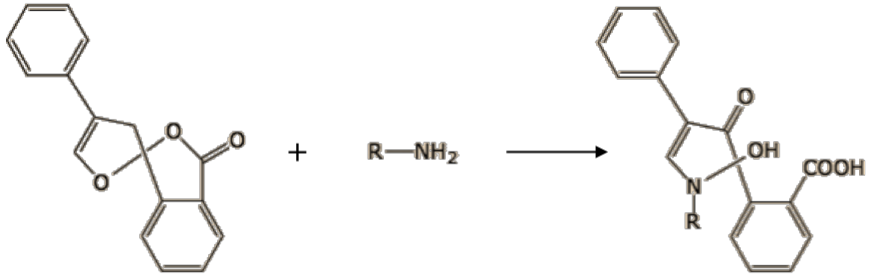

Fluorescamine

Fluorescent product

Figure 2.4 *Fluorescamine reaction with a primary amine.* Fluorescamine reacts with a primary amine to form a fluorescent product.

2.3.2.3 Physical characterisation

Nanosensors were characterised in terms of size and charge by dynamic light scattering (DLS), atomic force microscopy (AFM) and environmental scanning electron microscopy (eSEM). Samples were prepared for characterisation in the following way:

Samples were prepared for characterisation by light scattering (DLS and Zeta potential measurements) by suspending nanosensors to a concentration of 5 mg ml^{-1} in deionised water. Samples were prepared for AFM by re-suspending to a concentration of 0.1 mg ml^{-1} in deionised water, the sample was then spotted

onto a freshly cleaved mica disc and left overnight. Samples were prepared for eSEM by re-suspending to a concentration of 0.1 mg ml^{-1} in deionised water, the sample was then spotted onto a specimen stub and left to dry overnight. The sample was then sputter coated with gold for 30 minutes. All samples were sonicated for approximately 15 minutes prior to preparation for measurement.

Instruments were operated according the manufacturers guidelines.

2.3.2.4 Optical characterisation

Fluorophores were tested for pH sensitivity as free fluorophores and after incorporation into nanosensors, by measurement of fluorescence intensity in universal buffer solutions by fluorometry. The fluorophores tested are summarised in **Figure 2.5**.

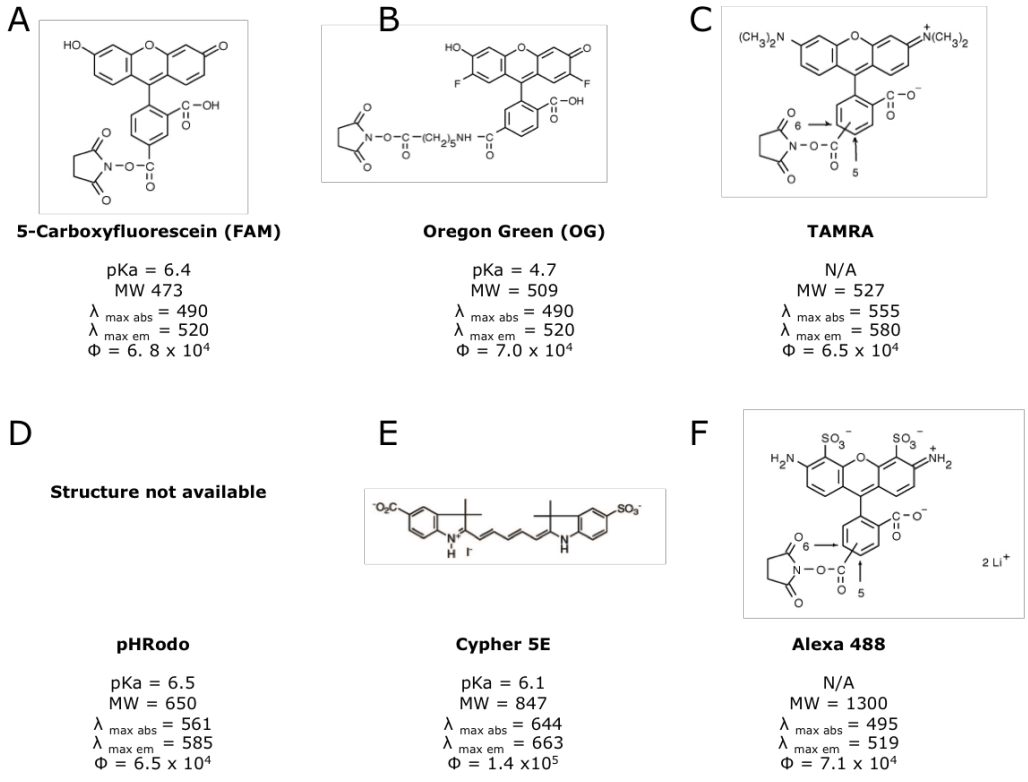

Figure 2.5 *Fluorophores utilised for nanosensor synthesis.* (A,B,D,E) pH-sensitive indicator fluorophores.(C,F) pH-insensitive reference fluorophores.

Universal buffer solutions for pH between 2.5 and 8 were prepared by mixing together solutions of 0.2M dibasic sodium phosphate and 0.1M Citric Acid.

Quantities used are summarised in **Table 2.5.** pH of solutions was measured using a pH meter, which was calibrated prior to use.

pH	Volume (ml)	
	Sodium Phosphate Dibasic (0.2 M)	Citric Acid Monohydrate (0.1 M)
2.5	2.16	17.84
3.0	4.08	15.92
3.5	6.04	13.96
4.0	7.72	12.28
4.5	9.00	11.00
5.0	10.28	9.72
5.5	11.36	8.64
6.0	12.84	7.16
6.5	14.20	5.80
7.0	17.44	2.56
7.5	17.98	2.02
8.0	19.53	0.47

Table 2.5 Quantities used to make universal buffer solutions.

Free fluorophores were reconstituted in DMSO to a concentration of 1 mg ml^{-1}; this stock solution was further diluted to make a stock solution of 1 µg ul^{-1} in deionised water. 1 µl of this solution was then added to 1 ml of the respective buffer solution and vortexed. Fluorophores were excited at the absorbance maximum as stated in the manufacturers recommendations. The emission spectrum was then collected to include the peak emission, which was then plotted against pH. The plots were normalised against the maximum intensity unless otherwise stated.

Nanosensors were suspended to a concentration of 5 mg ml^{-1} in water. Samples were sonicated for approximately 15 minutes prior to use and 50 µl of solution was added to 1 ml of buffer. The emission spectra were then collected as for free fluorophores. In order to construct a calibration curve, the peak emission intensity for the indicator and reference fluorophores were measured and the plotted against pH. The plots were normalised against the maximum intensity unless otherwise stated.

2.4 Results

The aim of this chapter is to develop an optical pH nanosensor with optimal properties for pH measurement in the endocytic pathway. This was done in four stages; firstly, methods for fabrication of polyacrylamide nanoparticles were optimised. Secondly, the optical properties of commercially available fluorophores were tested. Thirdly methods of incorporating into a polyacrylamide nanoparticle were investigated. Finally nanosensor designs based on incorporating different combinations of fluorophores into the nanoparticle were evaluated. A generalised method for nanosensor fabrication is shown in **Figure 2.6.**

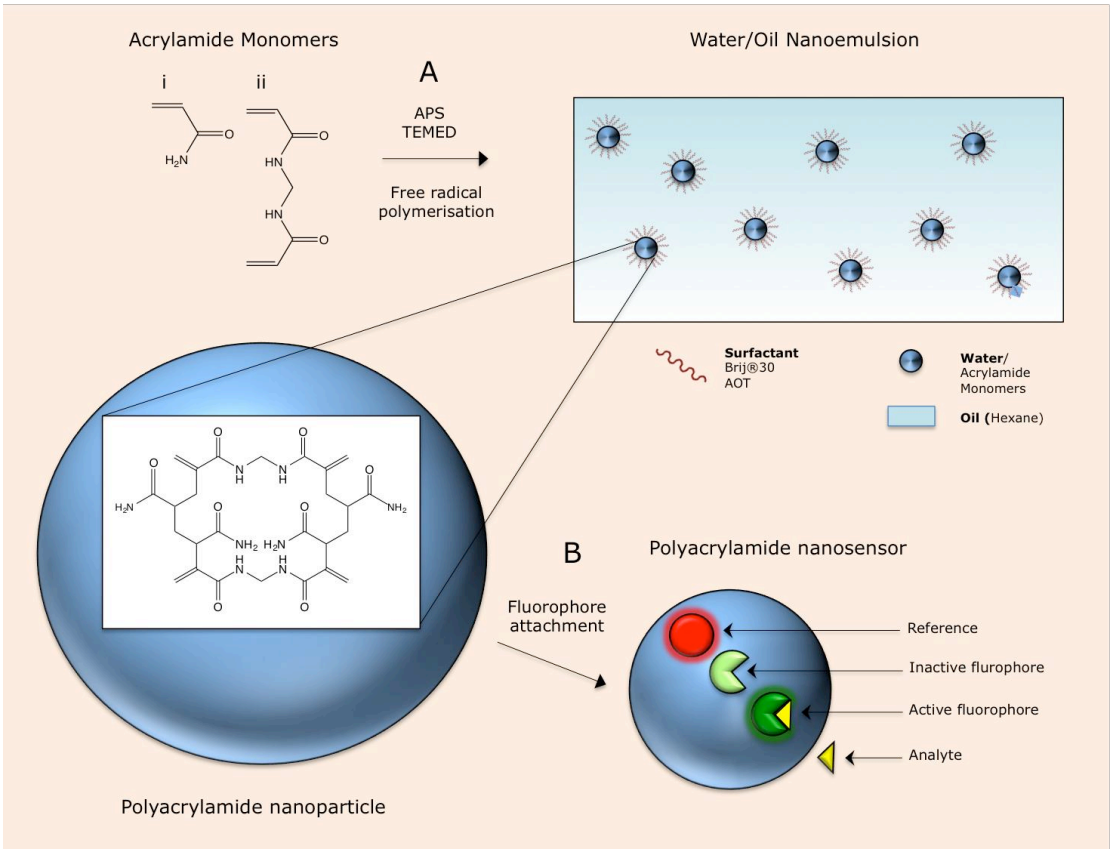

Figure 2.6 *Summary of polyacrylamide nanosensor synthesis*. (A) Free radical polymerisation of (i) acrylamide and (ii) N, N methylenebisacrylamide (cross-linker). (B) Attachment of fluorophores to the polyacrylamide nanoparticle. Fluorophores can be attached before or after nanoparticle synthesis.

2.4.1 Reproducibility of the nanosensor fabrication technique

Polyacrylamide nanoparticles (without the incorporation of fluorophores) were synthesised by emulsion polymerisation, with a hydrodynamic diameter of 48.5 ± 4.9 nm, and a polydispersity index (PDI) of 0.189 as measured by DLS (**Figure 2.7A**). Polydisperse particles are generally considered to have PDI values > 0.7 whereas values obtained for latex standards used to calibrate instruments are ~ 0.05, therefore the polyacrylamide nanoparticles are considered to have a relatively narrow size distribution[195]. A standard deviation (SD) value of 4.88 nm was measured from 10 individual batches of nanosensors demonstrating the reproducibility of the fabrication method.

Type of nanosensor	Size (nm)		PDI	
	Mean	SD	Mean	SD
Unconjugated	48.52	4.88	0.189	0.023
Pre - conjugated	48.13	8.11	0.200	0.062
Post – conjugated	102.7	8.25	0.270	0.029

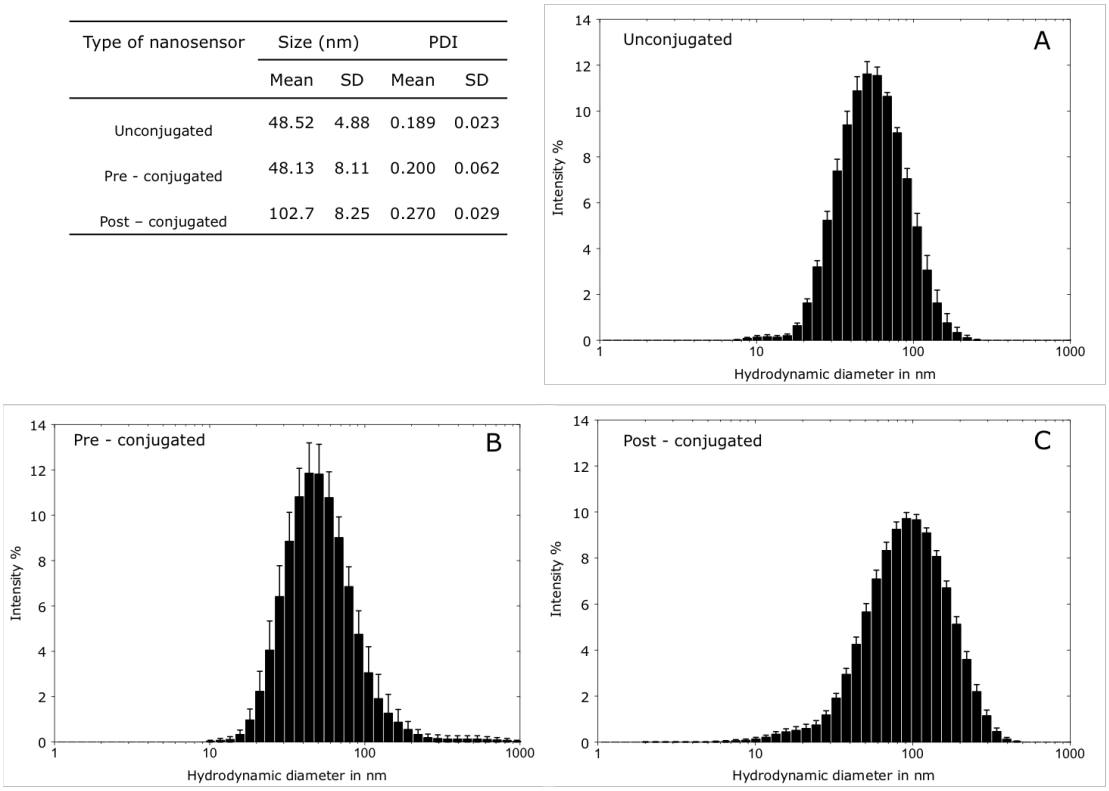

Figure 2.7 *Size characterisation of polyarylamide nanoparticles by DLS.* (A) Polyacrylamide nanoparticles with no functionalisation or incorporated fluorophores. (B) Polyacrylamide nanosensors synthesised by conjugating fluorophores to APMA and subsequent incorporation into a polyacrylamide nanoparticle. (C) Polyacrylamide nanosensors synthesised by conjugation of fluorophores to an amine functionalised polyacrylamide nanoparticle. Table is a summary of results. (n = 10 individual batches).

The model for calculating size by DLS is underpinned by the assumption that particles behave as inert spheres in a liquid; in order to test this assumption

particles were imaged by eSEM and AFM. The sizes correlated reasonably well to DLS, with sizes of ~ 80 nm observed by AFM (**Figure 2.8C,D**). Imaging polyacrylamide nanoparticles by SEM proved to be problematic due to sample preparation and imaging conditions. SEM requires deposition of a conductive layer on the particles and samples are normally imaged in a vacuum. This was observed to destroy the structure of particles giving the appearance of flat sheet where individual features cannot be distinguished. eSEM permits imaging in a gaseous environment. Imaging under these milder conditions was successful, resulting in images of ~ 50 nm spherical particles shown in **Figure 2.8A,B**, which correlates well with the DLS data. However, there appears to be extensive aggregation. This was also apparent in some cases, when particles were imaged by AFM (data not shown). As no evidence was seen for aggregation by DLS, this suggests the source of aggregation is from the sample preparation process. Particles were dried before imaging by AFM and SEM, which could result in aggregation, as the particles are essentially hydrogels. This is also a possible reason why the particles appear to be flat in AFM images. Previously reported polyacrylamide nanoparticles have been synthesised between 20 and 100 nm[110,117,120,179,184], predominately determined by DLS. There are some examples where SEM and AFM have been utilised successfully to image samples however the images, which have been published, show few particles and evidence of aggregation[178]. Nevertheless these images are important for the confirmation of the spherical morphology of the particles and as an approximation of their size.

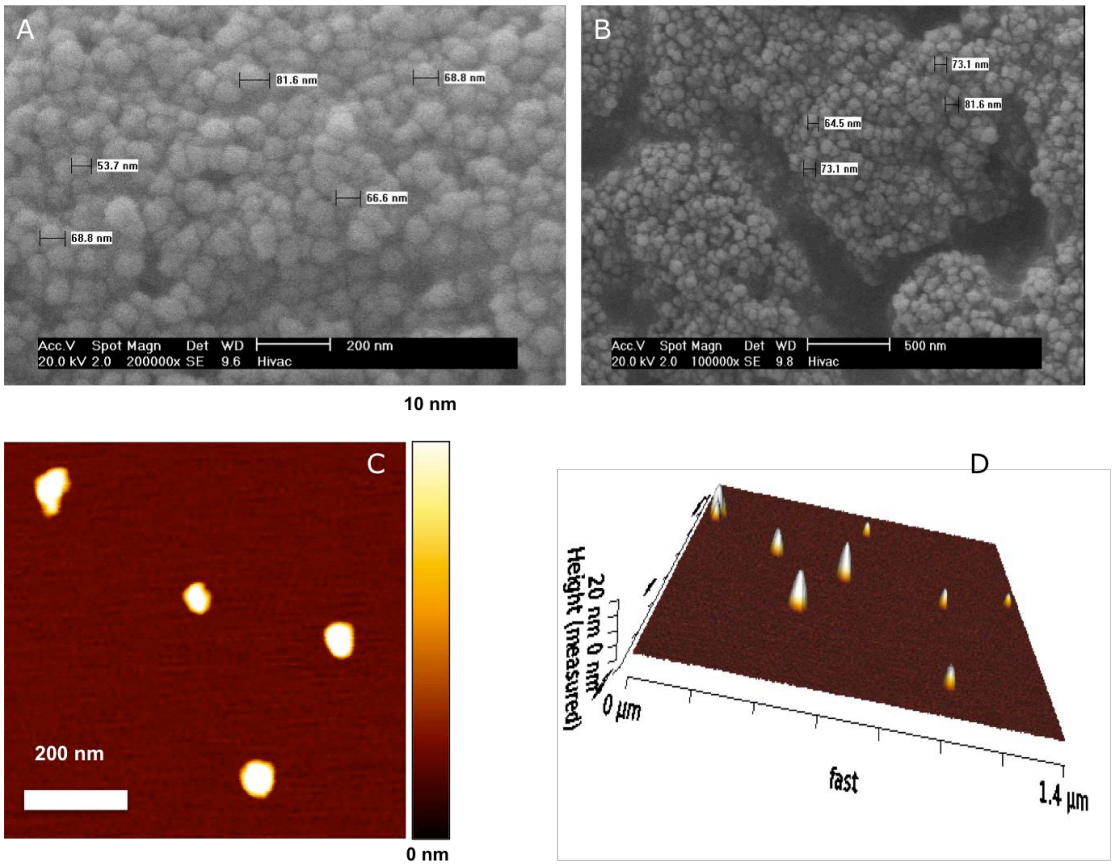

Figure 2.8 *Size characterisation of polyacrylamide nanosensors by SEM and AFM.* Images are of nanosensors with fluorophores incorporated by pre-conjugation. (A,B) eSEM images of polyacrylamide nanosensors at magnification of 200,000x (A) and 100,000x (B). (C,D) AFM images of polyacrylamide nanosensors.

2.4.2 Optical characterisation of commercially available fluorophores

Commercially available fluorophores were used as the sensing elements in the fabrication of nanosensors. Although fluorophores may be supplied as pH-sensitive or insensitive fluorophores, limited information is available about their dynamic range and sensitivity, additionally conditions, which affect fluorophore sensitivity such as concentration and ionic strength, are not always stated. This is because these fluorophores are more commonly used in qualitative studies. Therefore the optical properties of the fluorophores were assessed prior to nanosensor fabrication. In this work, two types of indicator fluorophores were selected for incorporation into nanosensors; firstly fluorophores decreasing in intensity with increasing acidification (5(6)-FAM and OG) and secondly fluorophores increasing in intensity with increasing acidification (pHrodo and CypHer 5E). TAMRA and Alexa 488 were selected as reference fluorophores.

Optical properties of these fluorophores were tested by measuring changes in fluorescence intensity in universal buffers across a pH range of 2.5 to 8.0 by fluorometry (**Figure 2.9**). The fluorophores are assessed in terms of dynamic range and sensitivity (**Table 2.6**). The dynamic range is defined as the range in which, the fluorophore is responsive, and the sensitivity is approximated as the fold change between the maximum and minimal response.

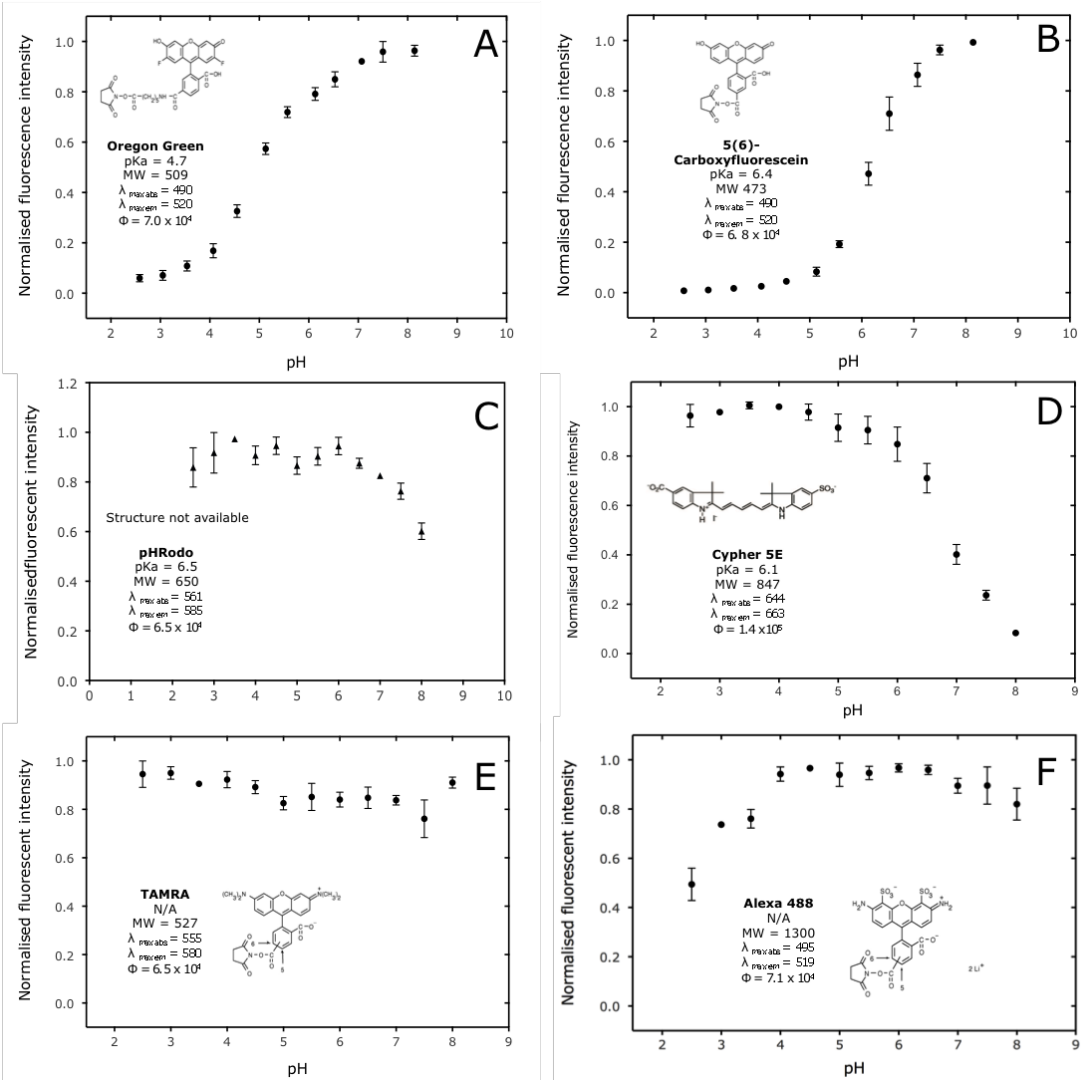

Figure 2.9 *pH sensitivity of free fluorophores.* Fluorescence intensity was measured in phosphate buffers using fluorometry at room temperature (fluorophore concentration = 1 mg ml^{-1}). (A-D) pH-sensitive indicator fluorophores. (E,F) pH-insensitive reference fluorophores. (N = 3 independent experiments, Error bars = S.D).

Fluorophore	Dynamic range	Sensitivity	pKa	pKa $_{lit}$	λ_{maxabs} / $\lambda_{max\ em}$	Brightness Φ[a]
Indicator						
Oregon Green	3.2 - 6.3	9.6	4.7	4.8[190]	490/520	7.0 x 10^4
5(6) - FAM	5.2 - 7.3	10.2	6.4	6.2[95]	490/520	6.8 x 10^4
pHRodo	5.8 - 8.2	2.7	6.6	6.5[192]	561/585	6.5 x 10^4
CypHer 5E	5.2 - 7.8	37.2	6.3	6.4[191]	644/633	1.4 x 10^5
Reference						
TAMRA	N/A		N/A		555/580	6.5 x 10^4
Alexa 488	N/A		N/A		495/519	7.1 x 10^4

[a]brightness is defined as molar extinction coefficient Φ

Table 2.6 Optical properties of free fluorophores. *Values are taken from*[93]*.*

The measured pKa and sigmoidal response for the indicator fluorophores, Oregon Green and 5(6)-FAM correlate with previous measurements from the literature[179], measured pKa values were within ± 0.1 for all fluorophores. Oregon Green (pKa 4.8) is sensitive to latter parts of the endocytic pathway (3.2 – 6.3) (**Figure 2.9A**), whilst 5(6)-FAM (pKa 6.4) is sensitive to the earlier part of the pathway (5.5 – 7.3) (**Figure 2.9B**). Similar fold changes of approximately ~ 10 were recorded for both fluorophores indicating comparable sensitivity. Both Oregon green and 5(6)-FAM are used widely for intracellular sensing, further confirming their suitability for intracellular measurement.

pHrodo (pKa 6.6) and CypHer (pKa 6.3) are relatively less well established fluorophores, having become commercially available relatively recently. They are of particular interest because CypHer 5E and pHrodo are the only commercially available fluorophores, which show an increase in intensity with increasing acidification. As with Oregon Green and 5(6)-FAM the measured responses also correlated well with the literature[201,202]. However pHrodo was measured to have relatively poor sensitivity (~3 fold) compared to other fluorophores (> 9 fold), as well as increased error particularly at low pH (**Figure 2.9C**). Invitrogen does not disclose the exact structure of pHrodo therefore it is difficult to speculate on reasons for reduced sensitivity and error. CypHer 5E, however demonstrates good sensitivity (~ 40 fold). The CypHer 5E fluorophore is a cyanine dye with secondary nitrogen atoms on one or both heterocyclic rings. In the protonated state the chromophore is in the same structure as classic cyanine dyes however

in the basic conditions the chromophore is disrupted and thus non-fluorescent, resulting in an increase in fluorescence with decreasing pH[93]. This is in contrast to most other pH-sensitive fluorophores where protonation results in disruption of the fluorophore.

Two possible reference fluorophores were selected with different absorption and emission wavelengths to prevent spectral overlap with the indicator fluorophores. Both indicator fluorophores show good stability across the range of the endocytic pathway although Alexa 488 becomes unstable below pH 4.

Other considerations were also taken into account in selecting fluorophores including photostability and brightness. In addition to the fluorophores being bright enough for detection, fluorophores should be of comparable brightness to prevent spectral overlap with reference fluorophore. Fluorophores utilised in this study were of comparative brightness (Φ 6.5 x10^4 – 1.4 x 10^5).

2.4.3 Optimisation of methods for fluorophore incorporation

Two methods were explored for incorporation of fluorophores into the nanoparticle; firstly entrapment of fluorophores into the nanoparticle matrix by conjugation to a larger molecule, and secondly directly conjugating fluorophores to the nanoparticle matrix.

The initial strategy for fluorophore incorporation was to conjugate fluorophores to a molecule large enough to be trapped in the pores of the polyacrylamide nanoparticle (entrapment). Dextran was used for this purpose because it is biologically inert and has been used successfully in previous reports[110]. Although this has been seen to be a viable strategy for many fluorophores, conjugation to dextran was found to adversely affect sensitivity of a pHrodo (**Figure 2.10D**). The main effect was increased error from measurements compared to the free fluorophore. This is contrary to reports in the literature where there is little effect of conjugation of pHrodo to biomolecules[192]. These studies utilise pHrodo for a qualitative assessment of acidification rather than measurement. For example a study by Miksa *et* al[192] utilised pHrodo to label apoptotic cells and assess internalisation by macrophages. Any pHrodo signal detected above a threshold was determined to be evidence of phagocytosis. In cases such as this minor changes in fluorescent response are not particularly significant however in the context of performing measurements, this is an important finding. On the contrary, OG dextran conjugates were found to have almost identical pH response

characteristics to the free fluorophore (**Figure 2.10C**). In addition to this other fluorophores selected in this study have been reported to show no change in responsiveness following conjugation to biomolecules. Consequently it is important to assess the effect of conjugation for each fluorophore individually.

Another problem was encountered in the synthesis of nanosensors incorporating CypHer5E. Nanosensors with entrapped CypHer5E-dextran conjugates were observed to have little or no fluorescence. In order to investigate this further, unconjugated nanosensors were mixed with CypHer5E with and without an initiator (TEMED), the mixture containing initiators were observed to have greatly reduced fluorescence (**Figure 2.10B**). This indicates the initiators disrupt the structure of the fluorophore.

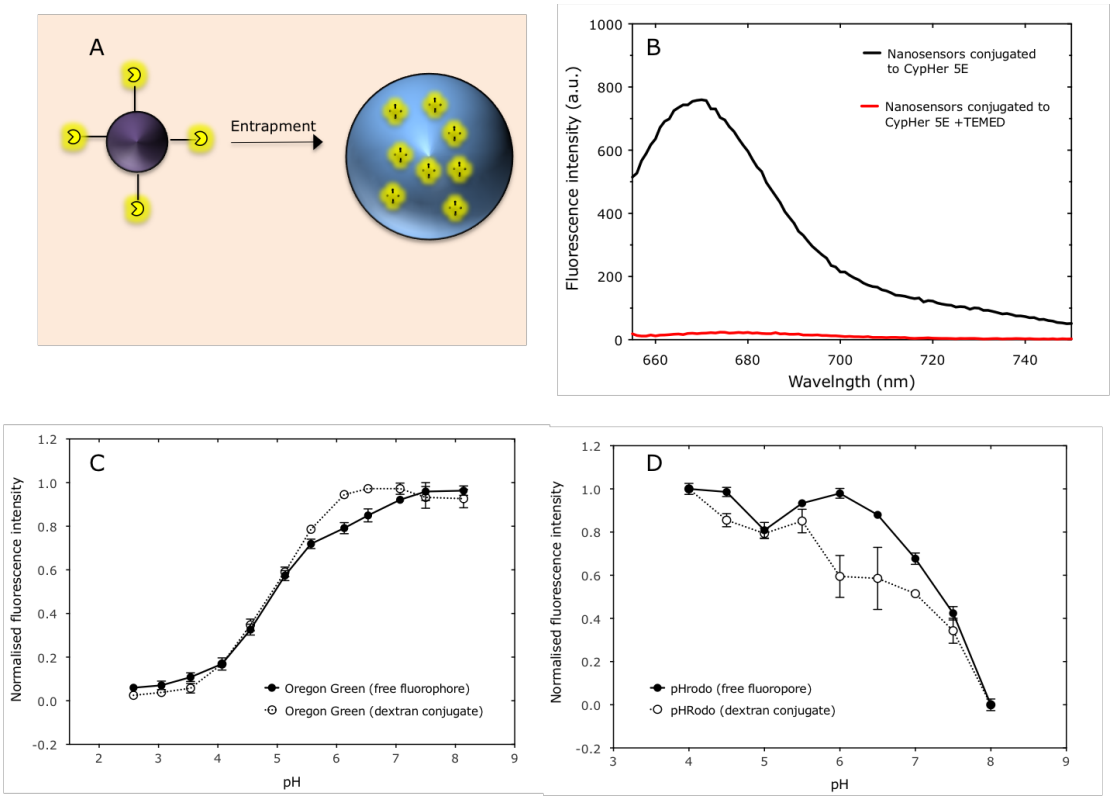

Figure 2.10 *Drawbacks of incorporating fluorophores by entrapment.* (A) Schematic of entrapment. Fluorophores are conjugated to dextran (purple) and trapped in to the pores of the nanoparticle (blue). (B) Loss of fluorescence of CypHer 5E in the presence of TEMED. 10 mg Nanosensors (5 mg/ml) were incubated with 10 µl TEMED for 15 minutes, fluorescence intensity was measured using fluorometry. (C,D) Effect of conjugation of dextran to Oregon Green (C) and pHrodo (D). Fluorescence intensity was measured in phosphate buffers using fluorometry (fluorophore/conjugate concentration = 1 mg ml^{-1}). (N = 3, error bars = S.D).

Moreover a general issue affecting all nanosensors synthesised by entrapment of fluorophore-dextran conjugates is leaching of fluorophores from the matrix. Residual fluorophore in the supernatant was observed for all nanosensors even after as many as 7 wash cycles. This issue has been acknowledged in the literature as a limitation of nanosensors with entrapped dextran bound fluorophore[110].

In light of these findings methods were pursued for covalently attaching fluorophores to the nanoparticle matrix.

Fluorophores were covalently attached to the polyacrylamide nanoparticle by conjugation of a primary amine group with a succinimidyl ester group. This was done in two ways, 1) before nanoparticle synthesis via conjugation of amine-reactive fluorophores to an amine-functionalised acrylamide monomer (pre-conjugation) and 2) after nanoparticle synthesis via synthesis of an amine-functionalised polyacrylamide nanoparticle (post-conjugation) (**Figure 2.11**).

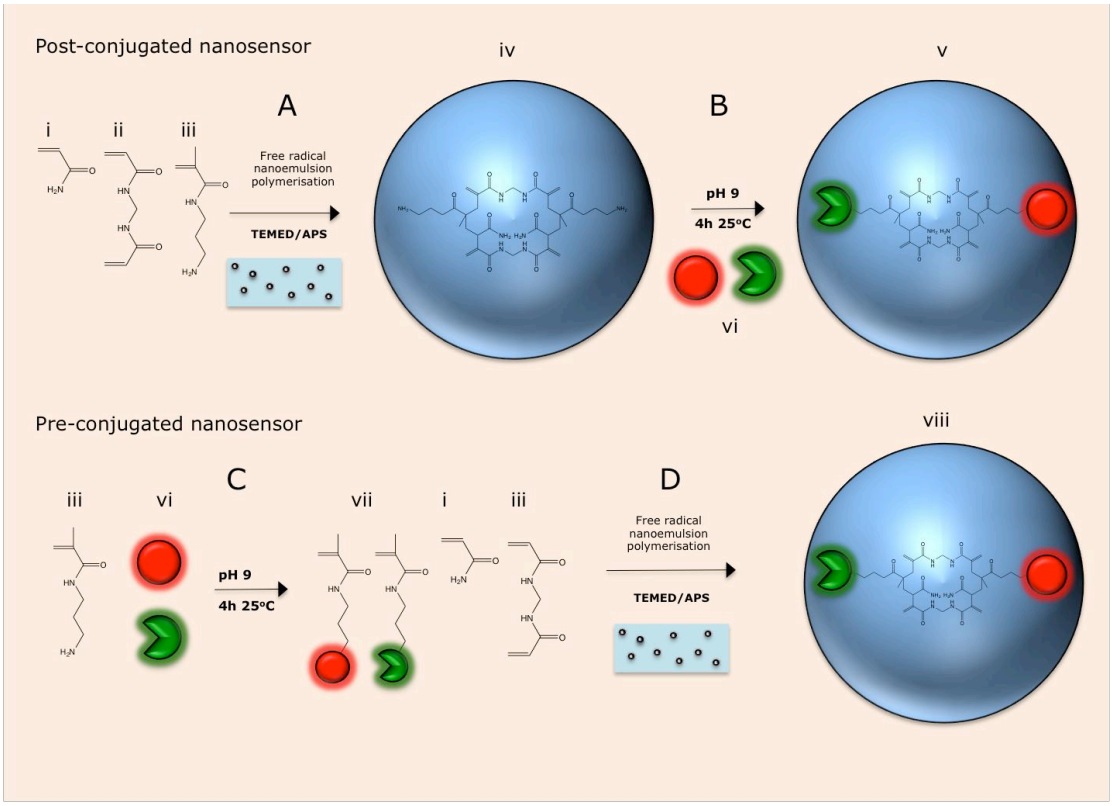

Figure 2.11 *Methods for incorporating fluorophores into polyacrylamide nanoparticles.* (A,B) Post-conjugation. (A) Synthesis of amine-functionalised polyacrylamide nanoparticle through incorporation of acrylamide monomers (i,ii,iii). (B) Conjugation of indicator and reference fluorophores to the nanoparticle to create a nanosensor (v). (C,D) Pre-conjugation. (C) Amine-reactive indicator and reference fluorophores are conjugated to amine-functionalised acrylamide monomer. (D) Emulsion polymerisation of acrylamide monomers (i,ii,iii) to create a nanosensor. (i) acrylamide , (ii) N, N methylenebisacrylamide (iii) N-(3-Aminopropyl)methacrylamide hydrochloride (APMA), (iv) amine-functionalised polyacrylamide nanoparticle, (v) post-conjugated nanosensor, (vi) fluorophores, (vii) APMA-fluorophore conjugates, (vii) pre-conjugated nanosensor.

For post-conjugation, polyacrylamide nanoparticles were functionalised with primary amine groups by replacing 5% wt. acrylamide monomer with a primary

amine containing acrylamide monomer (APMA). The amount of cross linker was kept constant to prevent any effect on the porosity of matrix. Successful incorporation of primary amine groups into the nanoparticles was confirmed by reaction with fluorescamine. Fluorescamine is a fluorescent spiro compound, which only fluoresces following reaction with a primary amine group. An increase in fluorescence following reaction with fluorescamine demonstrates successful incorporation of primary amine functionality (**Figure 2.12B**). Having established this as a successful method for incorporation of primary amine groups in the polyacrylamide nanoparticle, amine reactive reference and indicator fluorophores were conjugated to nanoparticles after synthesis. The sensor was then purified to remove unbound fluorophore.

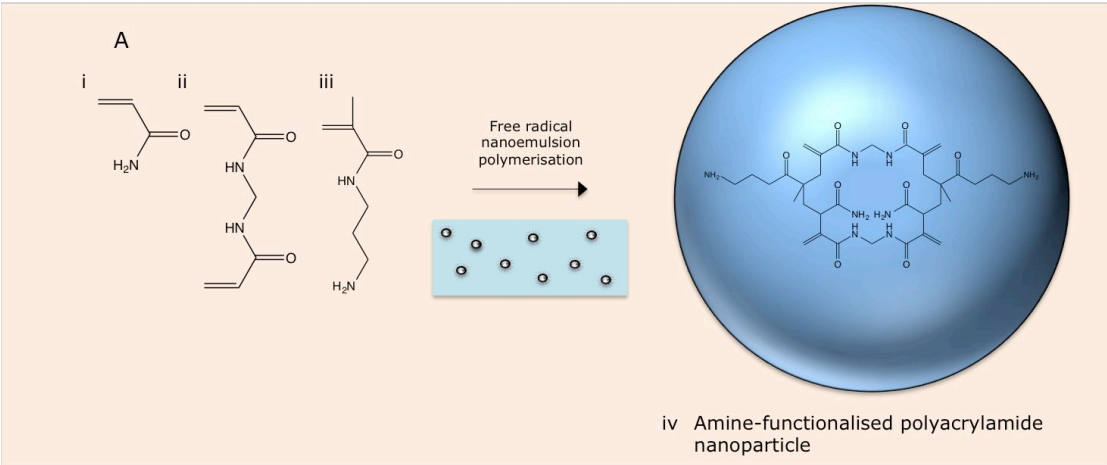

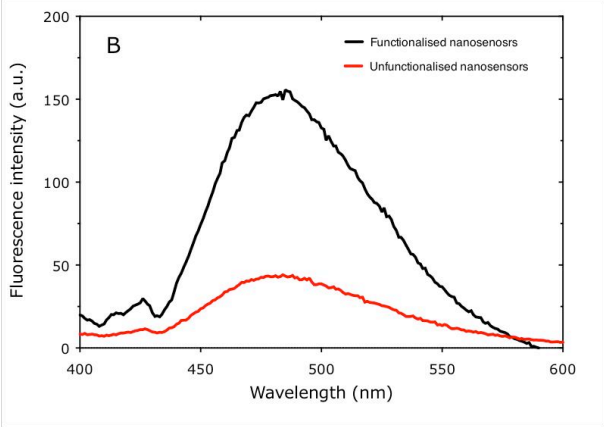

Figure 2.12 *Synthesis of amine-functionalised polyacrylamide nanoparticles*. (A) Synthesis of amine-functionalised polyacrylamide nanoparticle. Amine containing acrylamide monomer is included in the acrylamide monomer mixture, and is incorporated into the matrix during synthesis. (i) Acrylamide, (ii) N, N methylenebisacrylamide, (iii) N-(3-Aminopropyl)methacrylamide hydrochloride (APMA), (iv) amine-functionalised nanoparticle. (B) Fluorescence of amine-functionalised sensors after reaction with fluorescamine, nanosensors (2 mg $ml^{-1)}$ were incubated with fluorescamine (0.05 mg ml^{-1}) for 60 minutes at room temperature. Fluorescence intensity was measured at λ475 nm. Increase in fluorescence indicates the presence of an amine group.

Post-conjugation of fluorophores were found to increase the size of nanosensors from 48.5 ± 4.9 nm for blank polyacrylamide nanoparticles to 102.7 ± 8.3 nm with an increase in polydispersity from 0.189 to 0.270 (**Figure 2.7C**). Notably this increase in size was not seen until after fluorophore attachment. The surface charge was also increased from near neutral to + 17.0 ± 2.62 (**Figure 2.13**), this is likely to be due to presence of free amine groups on the surface of the nanosensor as zeta potential values were measured for unconjugated primary amine containing acrylamide monomers (APMA) (17.0 ± 2.6) and post-conjugated nanosensors (18.4 ± 0.5) (**Figure 2.13**).

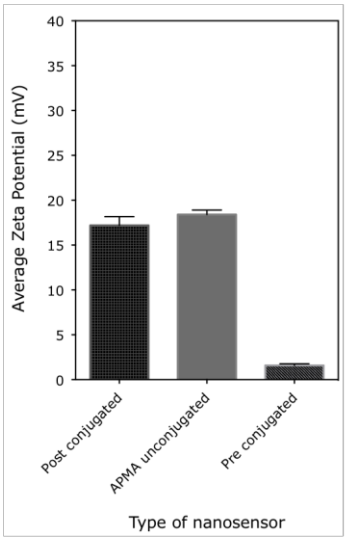

Type of nanosensor	Zeta Potential (mV)	
	Mean	SD
Post-conjugated	17.0	2.62
APMA-unconjugated	18.4	0.5
Pre-conjugated	1.59	0.18

Figure 2.13 *Zeta potential of polyacrylamide nanosensors.* Zeta potential measurements are taken in PBS pH 7.4. APMA unconjugated sensors are amine-functionalised sensors prior to conjugation of fluorophores. (N = 3 measurements, error bars = SD).

Post-conjugated nanosensors were also observed to be prone to aggregation, shown by failure to re-suspend in solution after extensive sonication. In order to reduce aggregation, different storage conditions were explored over a two week period. Aggregation was tested on nanosensors without fluorophores attached. Storage at temperatures below – 20^{o}C was found to significantly reduce aggregation of post-conjugated nanosensors (**Figure 2.14B**).

Previously reported nanosensors synthesised by this method have been reported to be between 50 and 60 nm, with a zeta potential between + 7 and 10 mV[183,203]. The differences in physical characteristics may be due to minor differences in oil to surfactant ratio and different quantities of monomers respectively. However as size is not the variable under investigation in this study the overall size of the nanoparticles is not critical provided the physicochemical characteristics are suitable for cellular uptake into the endocytic pathway. There are numerous studies where nanosensors with a similar size (20 - 100 nm) and charge (+5 - +15 mV) have been delivered to the endocytic pathway[204].

The aggregation occurring under the experimental conditions described increases sizes of nanoparticle agglomerates to over a micron, which could prevent cellular uptake or induce cytotoxicity. One possible reason for aggregation is the presence of free amine groups on the surface of the nanosensor, particularly as there is no

aggregation observed from nanosensors without amine functionalisation (**Figure 2.14A**)**.** Published reports of polyacrylamide nanosensors do not mention aggregation or storage conditions. However this work suggests it may be important to control the storage conditions to reduce aggregation.

A solution to minimise the number of free a primary amine groups and the associated risk of aggregation, is to conjugate fluorophores to primary amine containing acrylamide monomers prior to synthesis of the matrix (pre-conjugation). The fluorophore conjugates were then added to the nanoemulsion. This resulted in nanosensors, which were not prone to aggregation, with little impact on the size (48.13 ± 8.11 nm) and surface charge (1.59 ± 0.18) compared to blank nanosensors, (**Figure 2.7A**) and (**Figure 2.13**). Although this is a method of preventing aggregation of nanosensors, it presents problems for cell uptake studies. Previously reported polyacrylamide nanosensors with near-neutral charge are not taken into a cell by endocytosis and require specialised methods for delivery such as gene-gun bombardment and picoinjection[86]. These nanosensors were also seen show a reduction in brightness compared to post-conjugated nanosensors[120].

Synthesis by post-conjugation does confer some additional advantages. In post-conjugation fluorophores are attached to the same batch of nanosensors, therefore direct comparisons can be made for different nanosensor designs. It also provides the experimenter with greater flexibility in designing the nanosensors because a new batch of nanosensors does not need to be synthesised when optimising fluorophore-sensing ratios. It also may be the only option if fluorophores are degraded by the initiator system required for synthesis of polyacrylamide nanoparticles, as in the case of CypHer5E. As different nanosensor designs were explored in the first part of this work, post-conjugation was used for initial studies.

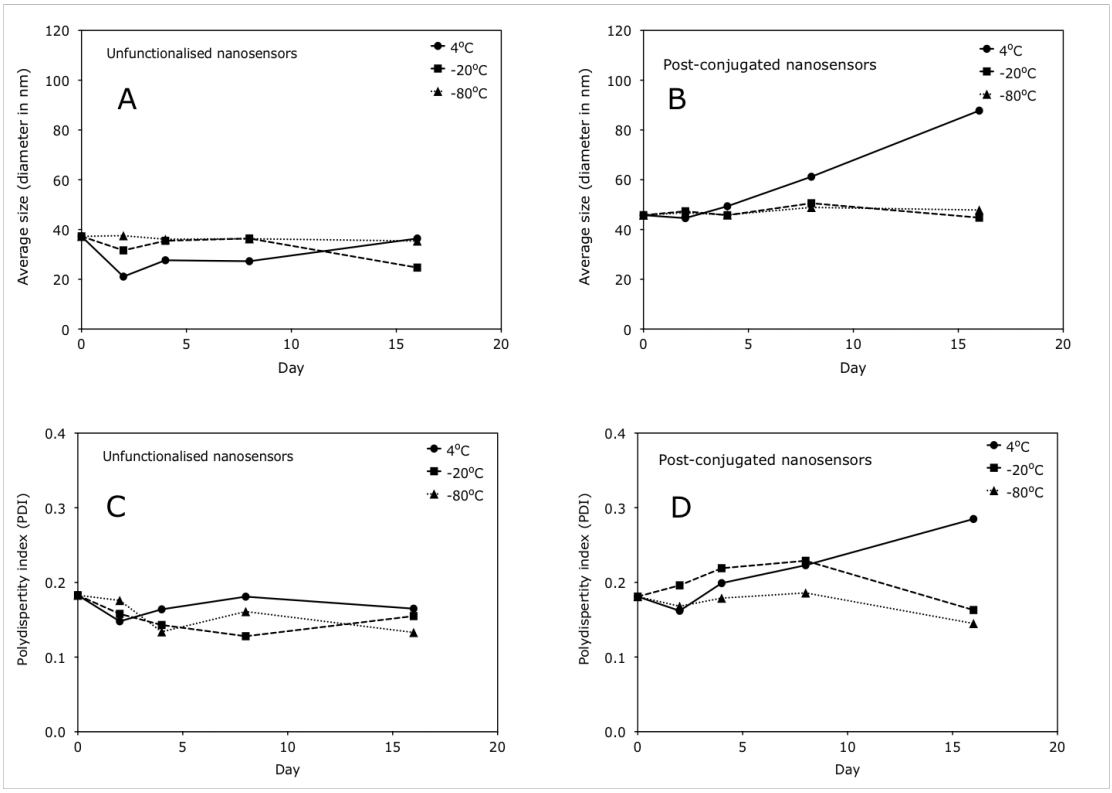

Figure 2.14 *Effect of storage conditions on stability of nanosensors.* The size of sensors was determined by DLS (A,C) Unfuctionalised nanosensors. (B,D) Post-conjugated nanosensors. Sensors were sonicated for 20 minutes before sizing.

2.4.4 Evaluation of nanosensor design for intracellular measurement

Sensor designs were evaluated with the aim of identifying a design with the optimal sensitivity, dynamic range and reliability. Three sensor designs were evaluated; firstly a sensor increasing in intensity with decreasing acidification i.e. in the cytoplasmic environment, if the sensor avoids endo-lysosomal entrapment (NS_{esc}), secondly, a sensor increasing in intensity with increasing acidification i.e. when the sensor is internalised into endosomes and lysosomes (NS_{end}), and thirdly, a dual sensitive sensor responsive to both the acidic and cytoplasmic environment (NS_{ds}). The optical properties of each sensor was assessed using fluorometry. All the sensor designs were observed to have a dynamic range covering the entire intracellular pH range, however there were significant differences in sensitivity, NS_{ds} was the most sensitive showing 48-fold change between maximum and minimum response, followed by the NS_{esc} design (12-fold). The least sensitive was the NS_{end} which only showed a 4-fold change **Figure 2.15**) and **Figure 2.16**).

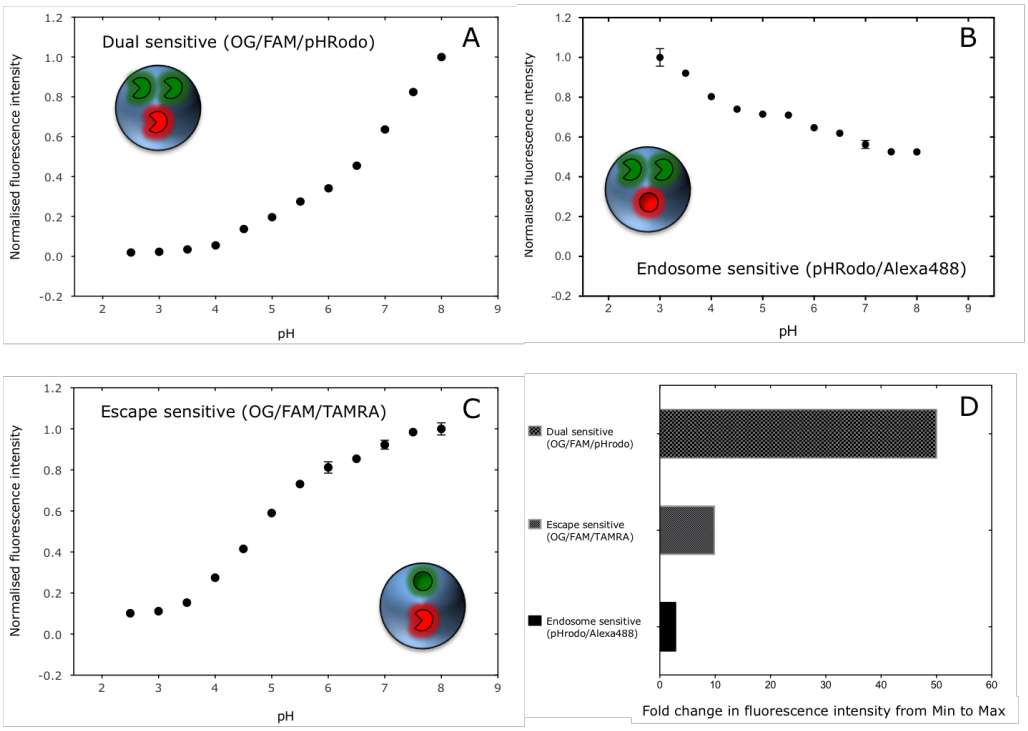

Figure 2.15 *Comparison of optical properties of nanosensor designs.* pH response of (A) NS_{ds} ,(B) NS_{end} ,(C) NS_{esc} sensors. (D) Comparison of the sensitivity of different nanosensor designs. Normalised fluorescence intensity is the ratio between indicator and reference fluorophores. (N = 3 measurements, error bars = SD).

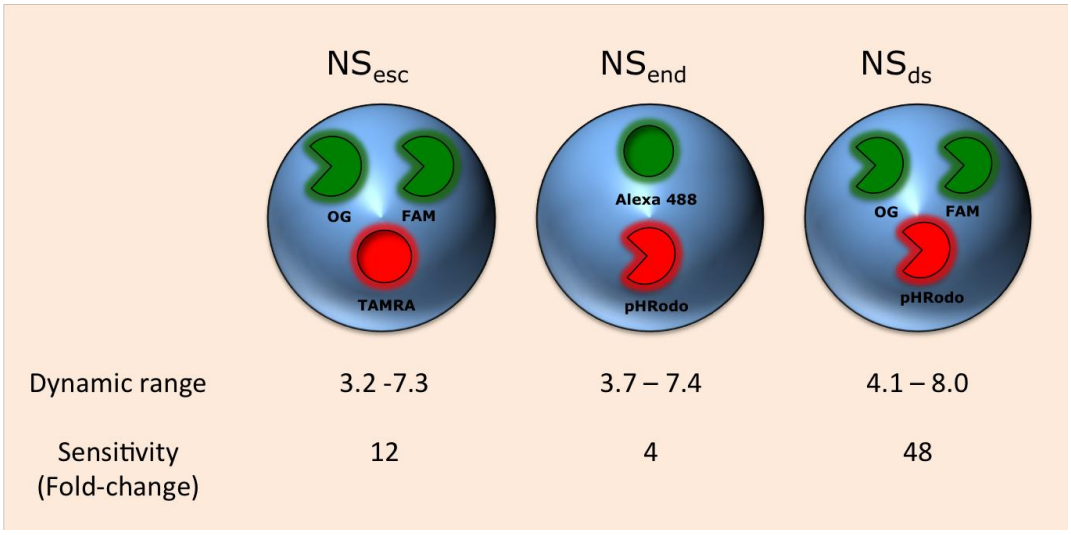

Figure 2.16 *Summary of sensor designs and optical properties*. Dynamic range is the range in which the sensor produces a response, within the detection limits. Sensitivity is expressed as the fold change between the maximum and minimal response of the sensor.

2.4.4.1 Escape sensitive nanosensors (NS_{esc})

This sensor was fabricated based on a design reported by Chauhan *et al*[179] and Sun *et al*[194]. This sensor incorporates two indicator fluorophores: OG and 5(6)-FAM with a reference fluorophore: TAMRA (**Figure 2.17**). OG and FAM fluorophores are responsive to the acidic and near-neutral parts of the endocytic pathway, but they have exactly the same absorption and emission characteristics, so using them together expands the effective dynamic range that can be measured (**Figure 2.17C**). The sensor synthesised using this method, was measured to have a dynamic range between 3.7 and 7.3 with 12 - fold sensitivity. This corresponds to previously reported designs for this type of sensor where fluorophores have been incorporated into the sensor by covalent attachment and dextran entrapment[179,194]. Prior to the development of this sensor, the most common design for polyacrylamide sensors was incorporation of a single fluorescein-based fluorophore into the matrix with a reference fluorophore. Oregon Green, fluorescein, CDCF, and BCECF have all been used for this purpose. But are limited because they are only suitable for performing measurements in one part of the endocytic pathway. These results further confirm the utility of this sensor design for circumventing the limitations of pH-sensitive fluorophores, which are inherently limited in their dynamic range.

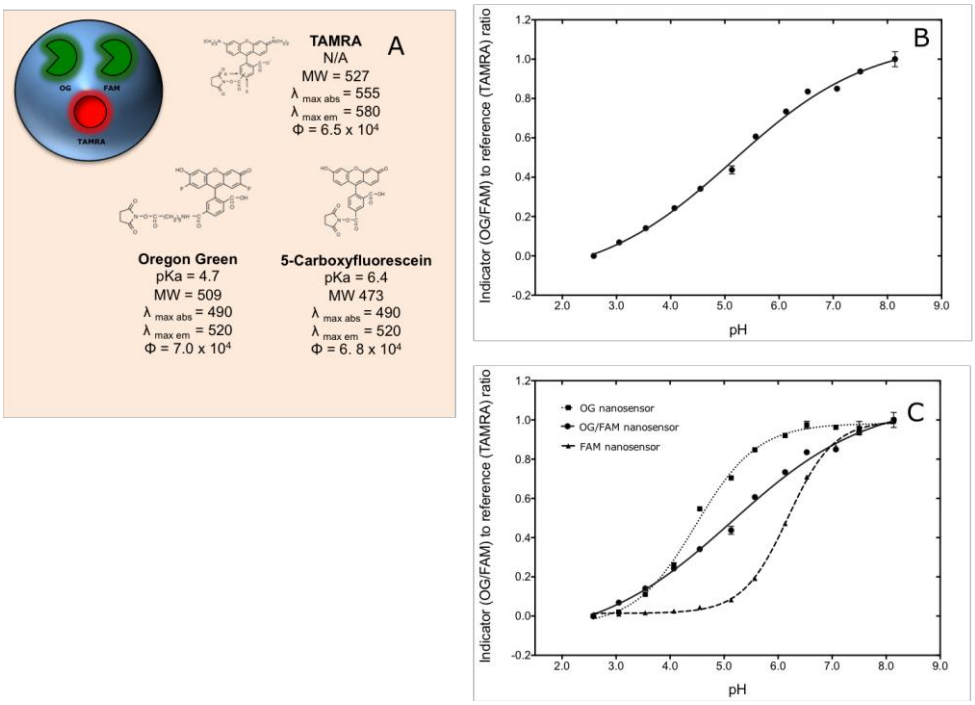

Figure 2.17 *Optical properties of NS_{esc} nanosensors. (*A) Fluorophores. Indicator = OG, 5(6)-FAM, reference = TAMRA. (B) pH sensitivity of the sensor measured by fluorometry. (C) Extended dynamic range of NS_{esc} sensor. (N = 3 measurements, error bars = SD).

2.4.4.2 Endosome sensitive nanosensors (NS_{end})

In an alternative sensing scheme, $NS_{end,}$ sensors were designed to increase in intensity with increasing acidification (**Figure 2.18**). This provides an advantage over NS_{esc} sensors, which decrease in intensity with increasing acidification, for some applications. Considering, a scenario where measurements of acidification are required such as in endosomes and lysosomes, any measurement from NS_{esc} sensors is dependent on a loss of signal from the fluorophore. This is undesirable as the harsh conditions in these vesicles are may cause a loss of signal[104,205]. Consequently it is advantageous to have a sensor with an NS_{end}, which gives a positive signal in response to acidification.

This sensor was fabricated through incorporation of pHrodo and Alexa 488 fluorophores into the sensor. This sensor was observed to have a dynamic range suitable for measurement across the entire endocytic pathway (3.7 – 7.4), albeit with a reduction in sensitivity compared to the NS_{esc} type nanosensors (4-fold) (**Figure 2.18**)**.** There is increased error with respect to the uniformity of the relationship between decreasing pH and increasing intensity. Alexa 488 was also observed to show some pH dependence when conjugated to the nanosensor

matrix. Alexa488 is advertised as a fluorophore, which is stable between pH 4 and 8, however there is little literature to corroborate this. The extended dynamic range is unexpected as free pHrodo fluorophore was observed to have a limited dynamic range (5.8 – 7.2). The extended range is can be attributed to the sensitivity of Alexa 488 at low pH. At low pH Alexa 488 decreases in intensity whilst pHrodo is insensitive, thus maintaining the response of the sensor. This is an unexpected benefit of this type of sensor.

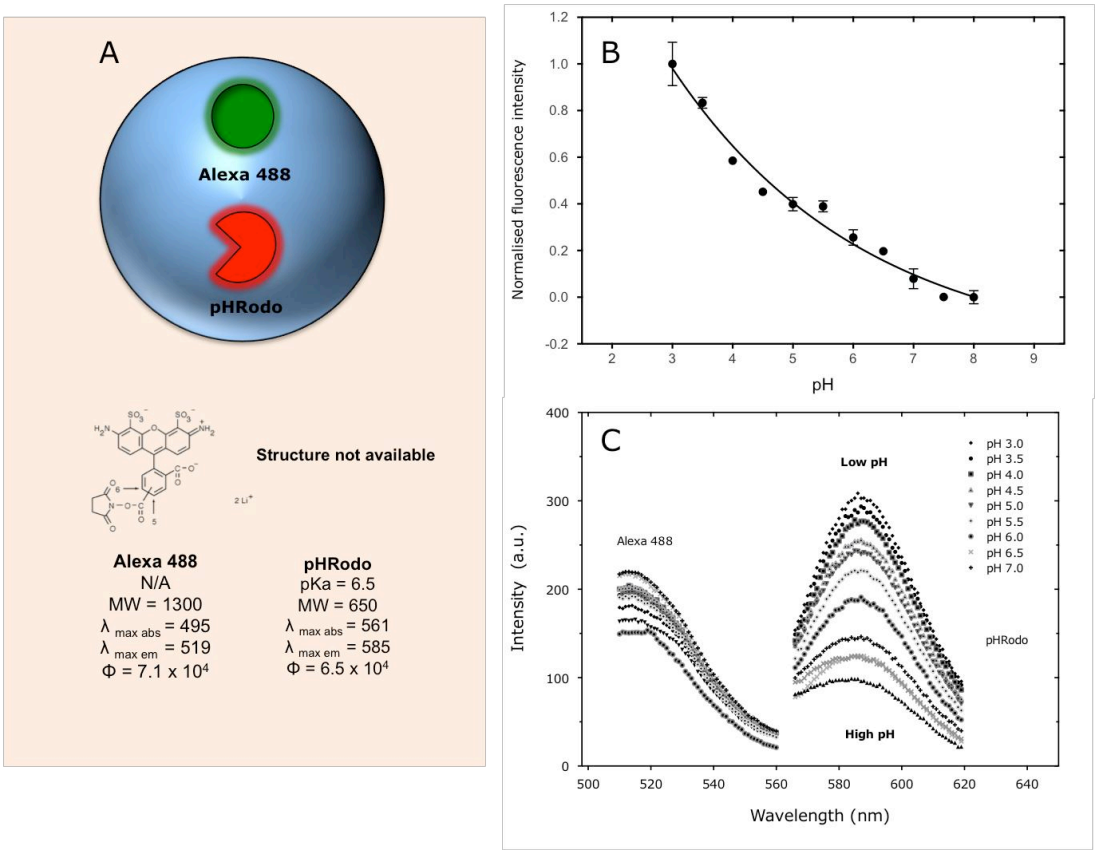

Figure 2.18 *Optical properties of NS_{end} nanosensors.* (A) Fluorophores. Indicator = pHrodo, reference = Alexa 488. (B) pH sensitivity of the sensor measured by fluorometry (N = 3 measurements, error bars = SD). (C) Spectral properties of indicator and reference fluorophores. Normalised fluorescence intensity is the ratio between indicator and reference fluorophores.

Due to the lack of commercially available fluorophores, which increase in intensity with increasing acidification, there are few examples of sensors with this design. One example was reported by Schulz *et al*[117], however this design incorporates a custom synthesised naphthylamide fluorophore (N-allyl-4-(N-methylpiperazinyl)-1,8-naphthalimide) into a core–shell polyacrylamide-PDMPA nanosensor. This sensor was shown to have a pKa of 6.7 with good photostability. The sensitivity

of the fluorophore is modulated on the principle of photoinduced electron transfer (PeT). By this mechanism fluorescence is controlled by a nitrogen containing modulator, which is controlled by protonation and deprotonation of the fluorophore. Although the sensor was delivered to human foreskin fibroblast cells, no measurements have been made. Therefore the relative advantages of this type of sensor in application is yet to be assessed.

2.4.4.3 Dual sensitive nanosensors (NS_{esc})

In an effort to combine the advantages of the sensitivity and low error of the NS_{esc} sensor and the additional reliability provided by the NS_{end} sensor, a third sensing scheme was devised to combine both types of indicator fluorophores into a single nanosensor, to create a dual sensitive sensor NS_{ds} (**Figure 2.19**). In terms of intracellular transport this sensor would result in an increase in one signal as the sensor enters acidic organelles such as lysosomes, this signal would then diminish to be replaced by another signal as the sensor enters a less acidic environment such as the cytoplasm. The advantage of this is that key aspects of the intracellular transport such as endosomal escape is tracked by positive signalling. The NS_{ds} was fabricated by incorporating pHrodo, OG and 5(6)-FAM into a single sensor. This sensor was measured to have a dynamic range across the entire endocytic pathway (4.1 – 8.0) with enhanced sensitivity (48 fold) (**Figure 2.19**)**.** The curve demonstrates low error but increased sensitivity at high pH compared to lower pH as expected. This type of sensor design has not currently been reported. A consideration hampering the utilisation of this sensor design is that there is a lack of pH insensitive reference fluorophore. A reference fluorophore may be useful for determining the proportion of sensors reporting a pH value. To illustrate this point let us consider two compartments in a cell, one reporting pH 5.0 (A) and the other reporting pH 7.0 (B). In this scenario the intensity in the reference channel is utilised to make the pH measurement, but can also be used to determine the concentration of sensors in each compartment, as it is independent of pH. This information is vital for quantitation of processes relevant to the intracellular delivery of nanomedicines such as endosomal release. A possible solution to this problem is to incorporate an additional fluorophore, which is spectrally separated from the sensing fluorophores.

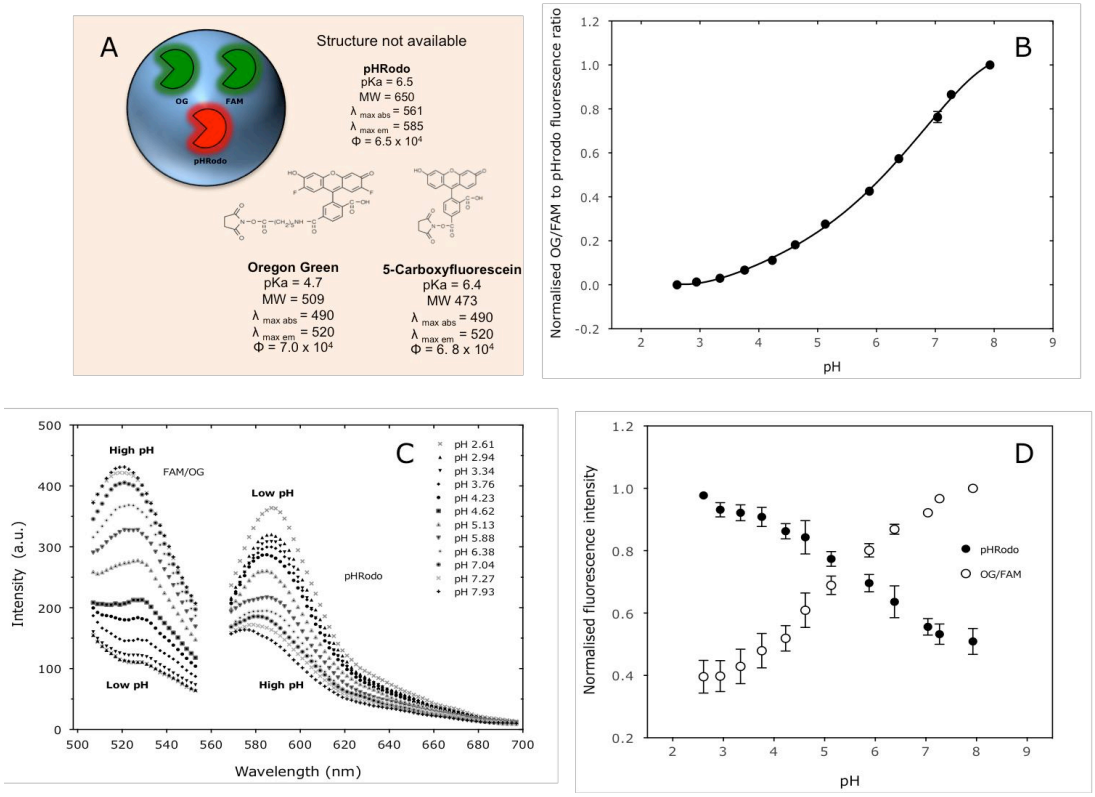

Figure 2.19 *Optical properties of NS_{ds} nanosensor*. (A) Fluorophores. Indicators = OG, 5(6)-FAM, pHrodo (B) pH sensitivity of the sensor measured by fluorometry. (C) Spectral properties. (D) pH response of individual fluorophores. Normalised fluorescence intensity is the ratio between indicator and reference fluorophores. (N = 3 measurements, error bars = SD).

2.5 Conclusions

From the investigations in this study, emulsion polymerisation was found to be a robust technique for the synthesis of polyacrylamide nanosensors. Sensors synthesised by this technique were spherical and sized between 50 and 100 nm in diameter (PDI < 0.3) depending on the method of fluorophore incorporation. The majority of size measurements were done using dynamic light scattering techniques. This was found to be a reliable method for size measurement of polyacrylamide nanosensors indicated by good correlation with eSEM and AFM images.

Conjugation of fluorophores directly to the nanoparticle matrix was found to be the optimal method for fluorophore incorporation. Covalent attachment can be done either before or after nanoparticle synthesis via amine-functionalised acrylamide monomers. In general, attachment before nanoparticle synthesis is preferential because attachment after nanoparticle synthesis results in sensors, which carry an increased risk of aggregation. However in certain cases initiators may degrade fluorophores, in which case post-conjugation is the preferred option. Post-conjugation may also be preferred where flexibility is required in terms of fluorophore selection. In cases where post-conjugation sensors are used aggregation can be minimised by storage at temperatures below – 20^{o}C for up to 2 weeks. In terms of physicochemical characteristics post-conjugated sensors (~ 100 nm) were observed to be larger than pre-conjugated sensors (~ 50 nm). Nanosensors synthesised by post-conjugation also carry a positive surface charge due to the presence of unreacted amine groups, which may facilitate cellular delivery.

All fluorophores utilised for synthesis of nanosensors 5(6)-FAM, OG, pHRodo and CypHer) are suitable for pH measurements showing responsiveness to pH, but significant differences in sensitivity was observed. pHrodo, in particular was found to show comparatively low sensitivity in comparison to other fluorophores. The corresponding reference fluorophores (TAMRA and Alexa 488) were found to show little sensitivity to pH in a free form.

All three sensor designs evaluated in this chapter (NS_{esc}, NS_{end}, NS_{ds}) were responsive in the entire range required for intracellular pH measurement. The optimal nanosensor design depends on the application. Theoretically the most sensitive and reliable sensor is NS_{ds} incorporating three pH-sensitive fluorophores (pHrodo, 5(6)-FAM and OG). However this design does not incorporate a

reference fluorophore, which may be important for quantification of internalisation studies. If a reference fluorophore is required the optimal design is the NS_{esc} nanosensor, incorporating two indicator fluorophores (5(6)-FAM and OG) and a reference. This sensor has adequate sensitivity but does not incorporate a positive indicator for acidification, which means it may be less reliable in a biological context. A key factor in determining the optimal sensor design will be the influence of the biological environment on the performance of the sensors, which will be investigated in **Chapter 4.**

In summary, a method has been optimised for the fabrication of nanosensors suitable for pH measurements in the endocytic pathway. This work shows how different methods for the synthesis of nanosensors can affect physicochemical characteristics and stability. Therefore careful consideration should be given to how sensors are designed. Commercially available fluorophores are often designed for qualitative intracellular pH measurements; consequently sensitivity must be carefully tested to determine their utility for pH measurements. Although the ultimate sensitivity and range of the sensors are governed by the fluorophores available for sensing, the optical properties of the sensor can be tailored for a specific application by incorporating different combinations of fluorophores.

Chapter 3 Development and optimisation of methodology for ratiometric measurements

3.1 Aim

The overall aim of this chapter is to develop a reliable methodology for performing intracellular pH measurements using fluorescence microscopy. In order to do this, the influence of key experimental design parameters on measurements is investigated. These are considered within three areas: conditions for nanosensor uptake, calibration and image analysis. This is done with the view of developing a generalised guide to optimising experimental methodology for performing ratiometric measurements. Although attempts have been made to perform pH measurements using nanoparticle-based sensors in the literature, comparatively little is reported on the technical aspects of experimental design to perform measurements[123]. The work in this chapter aims to address this gap.

3.2 Introduction

In the field of optical nanosensors, there has been a strong focus on the fabrication of pH nanosensors for biological measurements. These efforts have led to the development of creative sensor designs based on a diverse range of materials[104], many of which have been discussed in **Chapter 2**. Although pH nanosensors have been utilised in biological applications (**Table 3.1**), relatively little attention has been given to establishing reliable methodology for performing measurements. Often, studies reporting intracellular measurements do not give detailed information on measurement methodology, as the focus is on the fabrication process of the sensor rather than the application[181,206-208]. As a consequence, methodology for performing measurements remains underdeveloped. This is a problem, because experimental setup for performing ratiometric measurements is technically demanding, requiring consideration of many factors (**Figure 3.1**).

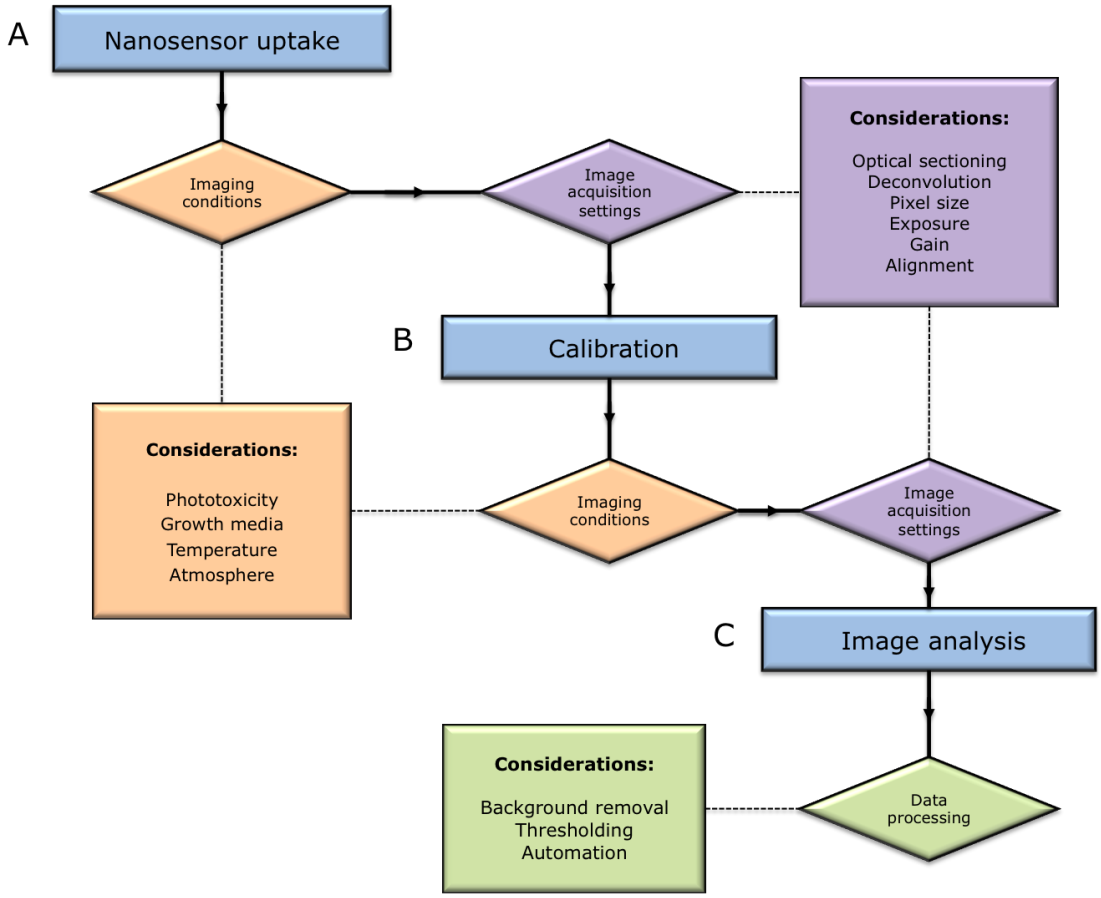

Figure 3.1 *Overview of the process for making ratiometric measurements using fluorescence microscopy.* (A) Nanosensor uptake. Images of the nanosensor inside cells are acquired in the reference and indicator channel. At this stage the conditions in which the cells are imaged and instrument settings are set. (B) Calibration. Nanosensors are calibrated by acquiring images of sensors across the relevant pH range in a controlled environment. Imaging conditions and instrument settings should match those used for nanosensor uptake as closely as possible. (C) Image analysis. Intensity information from images is extracted to produce a calibration curve, which is used to convert intensity data from nanosensor uptake images into pH values.

Reference	Microscope	Calibration conditions	Background removal	Analysis region	Measurement
Burns et al (2006)[132]	Confocal Leica SP2	Universal buffer	Not stated	Pixel by Pixel	RBL-2H3 cells pH 5.1-6.5
Peng et al (2007)[181]	Confocal 40x Leica SP2	Universal buffer	Not stated	Not stated	Hela cell pH 7.2,
Coupland 2009[208]	Confocal Leica SP2 63x	Universal buffer	Not stated	Whole image	Macrophage pH 4.8
Ray et al (2011)[180]	Confocal Leica SP5 10x	Universal buffer (linear between 6-8)	Not stated	Not stated	9L glioma cell pH 6.3
Benjaminsen 2012[183]	Confocal 63x Leica SP2	Universal buffer, nigericin, artificial cytoplasm	Histogram	Pixel by pixel and ROI, custom software	HepG2 cells, pH 4.5 ± 0.4

Table 3.1 Previously reported studies using pH nanosensors in biological applications.

From a general perspective, there are two major challenges, which if not properly addressed, are considered to be major limitations for studies utilising pH nanosensors in biological applications. The first challenge is to calibrate nanosensors in conditions, which faithfully represent the cellular environment. An ideal method for calibration would be to control pH in a cell without any effect on cellular activity. This is problematic because artificially changing pH in live cells leads to a loss in cell viability. Consequently alternative methods have been proposed for calibration, but how well these conditions represent the cellular environment remains controversial[183]. The second challenge is to establish reliable methods for extracting data from images. Various methods for image analysis have been proposed[123], invariably involving setting parameters such as background removal and thresholding. However the subjectivity of such values and their potential to influence measurements is a concern. An additional consideration is that resolving subcellular structures requires operating close to the maximum resolution limit of conventional optical microscopes, therefore small variations in setup have the potential to severely influence measurements.

Although it is intuitively clear that many factors affect the process for performing ratiometric measurements, an important question is to what extent do these

factors affect the final measurement? Answering this question is required to develop more reliable methodology, which will ultimately increase the value of biological insights gained from applications using pH nanosensors.

3.2.1 Fluorescence microscopy for ratiometric measurements

Fluorescence microscopy is commonly used in studies employing optical pH nanosensors for intracellular measurements. This is primarily because there is a wealth of information to be gained from imaging cells at the sub micron scale. Additionally techniques in fluorescence microscopy are well developed for live-cell imaging.

Several types of microscopy techniques are available which are suitable for live-cell imaging. The following section is a discussion of the relative advantages and limitations of instrumentation used in fluorescence microscopy within the context of performing measurements with nanosensors.

In the simplest terms, the function of a fluorescent microscope is to excite a sample with light of a specific band of wavelengths; if the sample is fluorescent it will then emit light at a longer wavelength than the excitation light, the function of the microscope is then to isolate the emitted light from the much more intense excitation light. Ideally, this will result in a high contrast image which can be detected by eye or using a camera.

Oskar Heimstädt[209] invented the first fluorescent microscope in 1911, since then there has been a continual development of sophisticated microscopes designed to push the boundaries of conventional optics. Notable milestones include the design of the confocal microscope by Marvin Minsky in 1957[210] and the development of commercial super-resolution techniques in the 1990's[211]. These techniques were evolved from conventional widefield fluorescent microscopes, which will be discussed first.

3.2.1.1 Widefield fluorescence microscopy

A cross-section of a typical configuration for a conventional inverted widefield fluorescent microscope is shown in **Figure 3.2A**. A sample is illuminated by a light source contained within the epifluorescence lamphouse. Epifluorescence refers to fluorescence, which arises through illumination by light, which is reflected on to the sample, rather than transmitted through to the specimen. The light source is a high power lamp emitting a broad range of wavelengths,

commonly a xenon arc or mercury vapour lamp. Light from the lamp passes through an excitation filter and is reflected off a dichromatic mirror at a 90^{o} angle towards the sample. The dichromatic mirror is a selective wavelength filter, which passes and reflects light of specific wavelengths. This light is then passed through an objective, which focuses an intense beam of light onto the sample. Any emitted fluorescence, which will be of a longer wavelength than the excitation light, is passed back upwards through the objective towards the dichromatic mirror, which now passes the light through an emission filter and finally to the detector or eyepiece. The excitation filter, dichromatic mirror and emission filter are usually contained in a filter block as shown in **Figure 3.2B**. The arrangement of the lenses and filters, which direct fluorescence emission light to the detector, is referred to as the optical train of the microscope. The performance the microscope is often determined by alignment of components in the optical train.

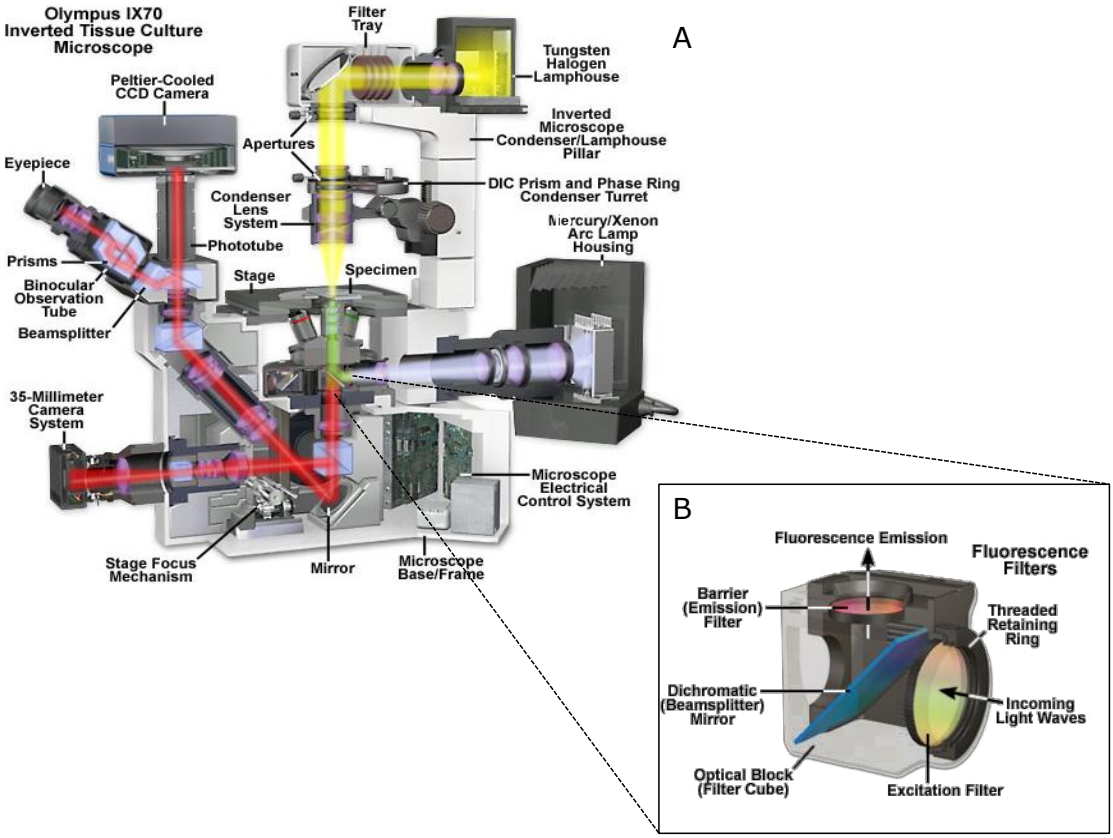

Figure 3.2 *Cross-section view of a conventional inverted widefield fluorescent microscope.* (A) Microscope[212]. Green represents light focused on to the specimen, red represents passage of fluorescent light emitted from the sample, and yellow represents transmitted light. (B) Filter block[14]. The filter block is placed in an inverted configuration within the microscope (so that fluorescent emission light is directed downwards). Reproduced with permission.

Other configurations are available for widefield microscopes, notably upright microscopes where the objective is positioned above the sample. The main difference is that for upright microscopes light passes through the top of the sample, whereas for inverted microscopes, light passes through the bottom of the imaging vessel. This is significant because the refractive index of the medium between the objective and the sample must be matched to allow adequate focusing. In general higher magnification objectives require a medium with a higher refractive index, in such cases oil or water is used. In the case of an upright configuration the objective either has to be immersed in the imaging medium or a cover slip must be placed on the cells so a medium with the correct refractive index can be placed between the sample and the objective. This is more invasive than using an inverted microscope.

3.2.1.2 Confocal Laser Scanning Microscopy

A limitation of conventional widefield microscopes is that there is often large amounts of out of focus light or blur in an image from adjacent optical planes, this is because the entire sample is illuminated by the light source. This problem results in a hazy appearance when imaging fluorescent structures inside cells; this is exacerbated further when imaging highly fluorescent thick samples such as tissues.

Confocal microscopy circumvents this problem by incorporating an additional pinhole in a conjugate focal plane to the objective through which light must pass through to reach the detector. This to a degree eliminates out of focus light from adjacent focal planes. A further development of this technique is confocal laser scanning microscopy where the sample is excited by scanning a focused laser beam across a sample. Emitted fluorescence is detected by photomultiplier tubes (PMTs), which are positioned on motors and can be tuned by the operator to detect light of a defined wavelength[213].

Confocal microscopy is the overwhelming method of choice for conducting intracellular measurement because it provides a higher resolution than conventional widefield systems and less background due to the elimination of out of focus light. However widefield microscopy techniques maintain some advantages of confocal microscopy for biological applications. In general widefield systems are less inclined to cause phototoxicity and photobleaching, this is because illumination light is less intense than the laser light used in confocal microscopy. Also widefield techniques are more sensitive. This is because confocal microscopy removes large amounts of light to achieve higher resolution. As a result very bright specimens are required.

3.2.1.3 Deconvolution

Deconvolution is a post-image acquisition image processing technique for improving the contrast and resolution of an image by removing or reassigning out of focus light or blur[214]. Blur arises from the spreading of light (diffraction), which occurs as light passes through the optical train of the microscope before reaching the detector. The way in which the light is diffracted is a function of the components of the microscope, principally the objective. Therefore it is possible to mathematically model the blur and remove or reassign it from an image. As all optical systems produce blur, it is possible to use deconvolution on different types

of microscopy techniques including confocal microscopy. However it is a particularly powerful technique for addressing the limitations of widefield systems producing dramatic improvements in image quality.

Deconvolution algorithms are based on based on the concept of considering each pixel of an image as a 3D point-spread function (PSF)[215]. The PSF is a 3D diffraction pattern, which is generated by a point of light in a sample as shown in **Figure 3.3C.** The most intense point of light is at the centre of the sample, which is then spread out. In a 2D sense this will have the appearance of a series of concentric rings around a single point, termed an Airy disk (**Figure 3.3A**). By this theory a convoluted image is formed of multiple points of lights each with an individual PSF. The PSF can be modelled mathematically or measured experimentally.

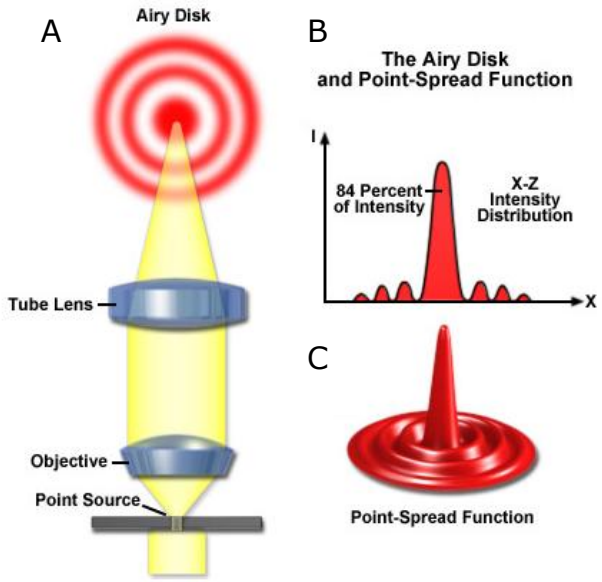

Figure 3.3 *Illustration of an airy disk and point spread function*[214]*.* (A) Airy disk. Formation of an airy disk through a microscope. (B,C) Point spread function. (B) Intensity distribution though a point spread function. (C) 3D representation of a point spread function. Reproduced with permission.

During the process of image acquisition each point in an image is convoluted as a function of the corresponding PSF. Each object of the PSF can be represented in terms of position, intensity and frequency by Fourier transformation. The advantage of this is that a series of objects can be summarised in one function called the Fourier space. Once converted into Fourier space, the image can be

reconstructed by multiplying the Fourier transform of the PSF and image. This operation is equivalent to the convolution process of an image, reversing this process is basis for most deconvolution algorithms.

The first algorithms developed for deconvolution were inverse filters in the 1960's. These types of filters are called Wiener deconvolution, regularised least squares, linear least squares or Thikhonov-Miller regularisation[214]. They function by dividing the Fourier transform of the image by the Fourier transform of the PSF, which reverses the convolution process. The drawback of this method is that variations in the Fourier transform result in increased noise. Modelling the noise in a process called regularisation can reduce this.

Constrained iterative algorithms were developed to reduce noise from inverse filters. These algorithms function by developing an approximation of the deconvolved or restored image, this image is then convoluted utilising the PSF, to reconstruct the raw image. This image is then compared with the raw image, differences in the image are assigned as error. A new deconvolved image is then estimated and the process is repeated, until the error is reduced to a certain threshold. These algorithms also apply certain constraints to the allowable estimate of the image, such as smoothing or regularisation to help minimise error.

In an ideal system the PSF would have perfect axial and radial symmetry, however chromatic aberrations result in a deviation from the theoretical PSF. This can be from misaligned components in the optical train but the most common source is from a mismatch between the refractive indices of the objective and the imaging medium. This is a factor, which can affect the image restoration process by deconvolution.

3.2.2 Experimental considerations for ratiometric measurements

Regardless of the type of microscopy technique used for detection image acquisition settings and imaging conditions need to be optimised for performing measurements. The factors affecting measurements (see **3**) should be kept consistent throughout the measurement experiment. In the context of performing ratiometric measurements, this requires settings to be maintained for both nanosensor uptake and calibration. The following section is a description of the factors required to address the primary experimental considerations when performing ratiometric measurements.

The factors, which will be discussed in the following section, are:

I. Exposure, laser power and gain
II. Pixel size and magnification
III. Alignment
IV. Bleed through
V. Optical sectioning and 3D imaging
VI. Imaging conditions

I. Exposure, laser power and gain:

Exposure of a microscope refers to the length of time the sample is exposed to excitation light, and the laser power refers to the intensity of light used to excite a sample. Both these factors determine the amount of light used to excite a sample. There is a trade-off when determining exposure settings because high exposure or laser power will result in increased signal to noise (S/N) ratios but also an increased risk of phototoxicity[216]. Where possible phototoxicity should be assessed to determine the highest possible exposure settings without causing toxicity. Gain is a setting related to the sensitivity of the detector, this could be increased to the maximum possible without saturation. However this will result in increased background. The saturation point of the camera is a threshold above which intensity can no longer be detected. Saturated pixels in an image will skew intensity measurements therefore this should be avoided. Points of saturation can be removed during image analysis, however this is not ideal as this means the data is lost.

II. Pixel size and magnification:

The pixel size refers to the area covered by a single pixel in an image. This size will be determined by the total number of pixels selected for an image, the pixel bin and the magnification properties of the objective. Pixel binning is when adjacent pixels are combined to represent one pixel, for example if the pixel bin is set to 2 x 2, 4 pixels will be combined into one increasing the size of each pixel in an image. In order to take advantage of the maximum resolving power of the microscope, it is desirable to use a pixel size below the theoretical resolution limit of the microscope (~ 250 nm)[211]. This should also be set to satisfy the Nyquist sampling theorem, which is required for adequate signal processing in digital microscopy. The Nyquist sampling theorem requires the sampling frequency to be at least double the bandwidth of the detected signal[217]. Practically this means the

pixel size should be at least half the size of the object to be resolved. The theoretical resolution limit of the microscope is determined by the Rayleigh criterion[213], which is the smallest resolvable distance between two points in an image. This is defined by the formula, where the smaller the value for d, the greater the resolving power:

$$\mathbf{d = 0.61\lambda/NA}$$

Where:

d = Rayleigh criterion
λ = Wavelength
NA = numerical aperture

Consequently the maximum resolution of images is obtained by selecting objectives with the highest numerical aperture, which in general increases with the magnification of the objective. A disadvantage of using high-resolution images is that this limits the field of view. Mammalian cells are typically 10 - 20 μm in size, using a 60x objective to produce a 512 x 512 image will result in an image of approximately 150 μm. This is enough to cover approximately 5 - 10 cells in each image. It is reasonable to allow imaging of ~ 50-100 cells per experiment before cell viability is compromised. As a consequence, using higher power objectives will result in less representative data. The number of cells from which data is obtained by fluorescence microscopy is very low compared to techniques such as flow cytometry where typically thousands of cells are considered per experiment. This is a general limitation of using fluorescence microscopy as a detection technique. However microscopy techniques offer detailed information about the intracellular distribution of analytes, which is not currently available from higher throughput techniques.

III. Microscope alignment:
Microscope alignment; in this context refers to the alignment of images acquired at different wavelengths or channels. In a perfectly aligned microscope a point will register in the exact same point in different channels. For example if an image is taken with a multicolour fluorescent bead, the fluorescence signal will be perfectly colocalised in all the channels corresponding to the different filter sets. In practice improper alignment can result in inaccurate registration between different channels when images are merged. Ratiometric measurement involves

taking intensity ratios between corresponding channels hence it is imperative there is proper alignment. In the cases where there is not adequate alignment, software is available to perform registration correction.

IV. Bleed through:

Fluorescence bleed through is when emitted fluorescence from one channel is detected in another channel. This may occur when utilising fluorophores, which are not adequately spectrally separated, a fluorophore emits a much stronger signal than another fluorophore or when using filters which pass a broad range of wavelengths. High levels of bleed through will mask signal preventing adequate calibration.

Bleed through can be minimised by selecting clearly spectrally separated fluorophores and optimising concentrations to balance intensity in each channel. In terms of the instrumental set up, the filter block must be selected to match the spectral characteristics of the fluorophores contained in the sample i.e. the filter block should reflect light of wavelengths close to the excitation maximum of the fluorophore and pass light of wavelengths close to the emission maximum. In general the closer the match the more intense the signal will be from the sample. Poor matches may result in an image with increased bleed through and/or low S/N. Commercially available filter blocks are usually designed to pass a range of wavelengths to permit compatibility with different fluorophores; this is suitable, providing the sample is bright enough. Bleed through is less of a concern for confocal techniques as the detection wavelengths can be set more precisely[213].

V. Optical sectioning and 3D imaging:

Deconvolution widefield microscopy and confocal microscopy offer the possibility for taking optical sections through a sample; these sections can be reconstructed to form a 3D image. 3D images are made up of pixels, which represent volumetric space in the image, and are termed voxels. As with determining pixel size, it is important to determine the size of voxels, applying the same principles, this should be set to be below the axial resolution of the microscope[218]. 3D imaging is most useful for determining the spatial location of particles within a cell, due to the relatively low axial resolution in 3D images, predominately 2D images are used for ratiometric imaging using nanosensors.

VI. Imaging conditions:

In addition to determining the optimal instrument settings it is just as important for the correct imaging conditions to be applied. Generally in fluorescence microscopy, cells can be imaged fixed or live. Fixation involves using a chemical agent such as formaldehyde to preserve the cell. Aside from the obvious advantages of imaging fixed samples, samples are also fixed to permit fluorescent staining using antibodies or toxins. These require cellular interactions, which would not be tolerated by a cell in live conditions. However cellular fixation can produce artefacts[219], which should be considered in sensitive studies such as in the investigation of the intracellular distribution of nanomedicines.

In the context of intracellular pH measurements it is essential cells are maintained under live conditions. Consequently imaging conditions should be controlled to be as non-invasive as possible. In order to ensure cell viability during imaging, cells must be maintained in a suitable environment during imaging. The factors to be controlled are temperature, humidity and CO_2. This is particularly important when imaging over long periods. Most microscopes set up for live-cell imaging are supplied with a chamber where atmospheric conditions can be controlled. Another consideration is the growth media used for imaging, which should not result in any background fluorescence.

3.2.3 Calibration

In general terms, reliable calibration of all nanosensors regardless of the analyte is a requirement for accurate measurements. The more closely the calibration conditions match the nanosensor uptake conditions, the more reliable the result. This is particularly important in the context of intracellular measurements where nanosensors will be exposed to a complex environment where many different factors may affect nanosensor performance. Inadequate calibration has been demonstrated to be the primary limitation in many applications of nanosensors[183].

Setting calibration conditions is an aspect of experimental set up specific to the analyte the sensor is used to detect. The following section is a discussion of approaches to calibration of nanosensors specifically for detecting pH. It is relatively straightforward to maintain consistent instrument settings, although practically it is preferential to determine the instrument settings during nanosensor uptake prior to calibration, as it is easier to optimise calibration conditions than nanosensor uptake conditions.

It is less straightforward to match the experimental conditions used for calibration to those for nanosensor uptake. In an ideal method for calibration, it would be possible to precisely control intracellular pH without affecting the cells natural function, however it very difficult to achieve precise control of pH inside a cell in this way. The simplest method for calibration is to suspend nanosensors in a buffer solution of pre-determined pH, where the pH of the solution is measured using a pH meter[181,183,208,220]. The suspension is then imaged in the same way as images are acquired for experimental acquisition. The drawback of this approach is that a number of experimental conditions are not controlled to match those for nanosensor uptake; most significantly these are nanosensor concentration, ionic strength and presence of biomolecules. Although the nanosensor matrix is designed to mitigate these variances, it is not ideal.

Methods for *in situ* calibration have been reported in previous studies, the first of which was by Thomas *et al* in 1979[221]. These methods are based on using molecules that transfer ions across cell membranes (ionophores) to modulate intracellular pH. An example is Nigericin, which exchanges K^+ for H^+ ions. In the study by Thomas *et al,* cells containing a pH-sensitive fluorophore (fluorescein diacetate) were incubated in a series of K^+ rich buffers in the presence of nigericin, resulting in the influx of H^+ to a point of equilibrium. In this way the intracellular pH is assumed to match the pH of the surrounding medium. However there are a number of reasons why this may be problematic for nanosensors taken into a cell by endocytosis. If nanosensors are predominantly taken into endosomes and lysosomes, this introduces another membrane through which ions have to pass. Consequently there is an assumption that there are enough ionophores present in membrane bound organelles to maintain equilibrium in the cell. However most of them are likely to be situated in the cell membrane. Another consideration is that interfering with an already complex system of ion transport could result in up or down regulation of alternative ion transport pathways, which disrupt the equilibrium. These issues have shown that this mode of calibration is not suitable for calibration of BCECF fluorophores[222]. However there are studies where this method has been used to produce a calibration curve from nanosensors. In an approach avoiding the complexity of altering the cellular ion transport system sensors have been mixed with a mixture of lysed cells and universal buffer solutions to produce a calibration curve. This preserves the impact of biomolecules on fluorophore performance but is not reflective of intracellular fluorophore concentrations. In a comparison of all three methods for calibration using nanosensors by Benjaminsen *et al*[183], although the curves do not

appear to be radically different, there are significant differences which are important for precise measurements (**Figure 3.4**).

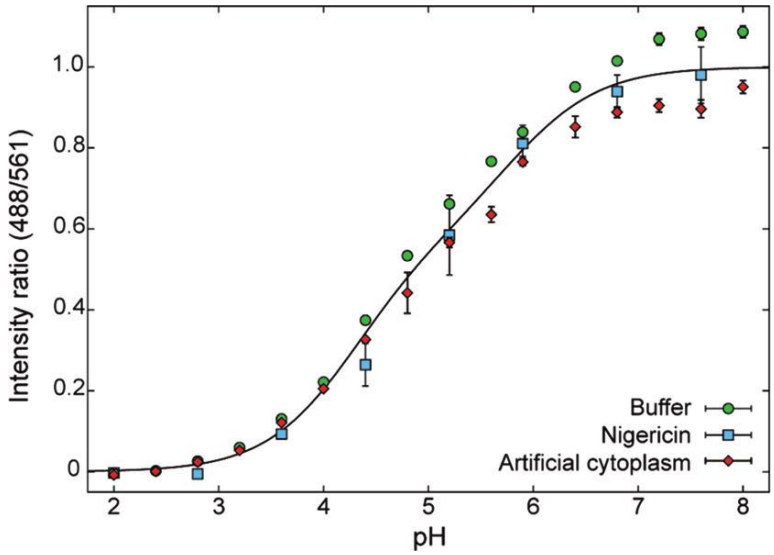

Figure 3.4 *Comparison of calibration of pH nanosensors under different conditions in a study by Benjaminsen et al*[183]*.* Nanosensors are calibrated in a series of buffer solutions (buffer), using an ionophore to modulate pH in HepG2 cells (nigericin) and by mixing sensors in buffers supplement with sonicated cells (artificial cytoplasm). Fluorescence was detected using confocal microscopy.

The relationship between the intensity and pH in the calibration curve is modelled by fitting an equation. This equation is subsequently rearranged to represent intensity as function of pH values. In most cases there is a sigmoidal relationship between intensity and pH. In such cases it is most appropriate to fit the following equation:

$$R_i = R_{min} + \frac{R_{max} - R_{min}}{1 + 10^{(pKa - pH).hillslope}}$$

R_i = Indicator to reference ratio

R_{min} = Minimum detectable nanosensors response (lower asymptote)

R_{max}= Maximum detectable nanosensors response (upper asymptote)

p*K*a = Point at half maximum response

Hillslope = Slope of the curve

This is rearranged as:

$$\mathrm{pH} = -\frac{\log_{10}\left(\frac{R_{max} - R_{min}}{R_i - R_{min}} - 1\right)}{hillslope} + pKa$$

This is a common fitting equation used for calibration of many different types of sensors[158,179,183]. This was established in early work by WolfBeis and co workers on ionophore-based electrochemical sensors[223]. In other studies measured intensity ratios have been modelled by a linear equation, particularly in instances where few points have been taken to generate the calibration[180]. Accordingly this is a source of an error in measurements, which is not often taken into account for measurements.

3.2.4 Image analysis

One of the least explored areas for performing ratiometric measurements is image analysis. Often the method for image analysis is not stated in detail or not described at all[132,180,181,208]. The key considerations for image analysis are outlined here, these include:

I. Determination of the measurement region (thresholding)
II. Background removal
III. Automation of image analysis
IV. Data presentation

I. Determination of the measurement region (thresholding):

Following image acquisition, the area of the image, which will be considered for measurement, must be determined. This is particularly important in the context of intracellular measurements where sensors are often concentrated in different compartments. Previously reported approaches are to take the overall ratio of an entire image, consider each pixel separately or consider discreet regions of interest (ROIs) in an image[183,220,224,225]. The advantage of taking the entire image is that it is possible to generate large amounts of data quickly, however the disadvantage is that it gives no information about the distribution of intracellular pH. Conversely taking a pixel-by-pixel approach allows for a more detailed analysis however the computational time to process images is much larger and it is also more susceptible to errors in the instrument settings, for example microscope alignment. A ROI approach where the cell is considered as discrete regions is a compromise between the two approaches. The differences between the methods for image analysis were discussed in a study by Benjaminsen *et al*[183]. For the ROI-based processing method, regions greater than 0.15 μm^2 above a threshold were determined to be nanosensor-containing ROIs. This produced identical results to the images processed by a pixel-by pixel method[183]. However it is reasonable to expect differences where there is a broader distribution of pH in the sample of interest. It is also difficult to assess the impact of the measurement region on measurements, as other variables in the image analysis process such as thresholding will affect the measurement.

Independent of the approach used, the image must be thresholded to distinguish the regions of the cell that produces signal. Considering an image of a single cell, most of the image will have little or no signal (dark regions). This region does not contain any sensors but may still return a ratio, if there are small amounts of background fluorescence. Consequently the image either has to be thresholded or the background fluorescence removed in some other way.

II. Background removal:

Images acquired by microscopy and other fluorescence-based methods invariably contain background. The source of this background could be from cell autofluorescence, media fluorescence or noise from the detector. Various methods for background subtraction have been proposed for conducting intracellular measurements. The most popular approach is to take an image of the cell without any sensors, and approximate this to a mean value, which is

subtracted from an image[226]. In a similar method this value has been obtained from identifying an ROI outside the cell[225]. Other studies have approximated the background by analysing the frequency histogram of an image[183]. In a typical image, there will be a high proportion of pixels, which only contain background; this results in a low intensity peak that can be approximated to be the background. Different methods of background removal will inevitably lead to different values for subtraction, however the impact of this on final measurements has not been studied in detail. Moreover most studies do not include a detailed explanation of how background is removed from the images[132,180,181,208].

III. Automation of image analysis:

Analysis of multiple images is required to extract representative data from images, however this can be time consuming when working with large data sets. As performing ratiometric measurements with nanosensors is not routinely done, there are few examples of commercially available software with facilities for performing this type of analysis, therefore custom software solutions have been used in most studies. FIJI (open source) and MATLAB are widely available software solutions that can be tailored to perform ratiometric measurements.

IV. Data presentation:

It is important to consider how pH measurements from intracellular sensors are presented. Measurements have been reported as an average figure for an entire image or set of experiments[208], a histogram representing the distribution of pH values in an image or a colour map showing discrete regions in a cell at a specific pH[183,220]. The latter two are better as they represent the distribution of pH in an image and also the location of pH. Additionally in an image there are always likely to be measurements, which are outside the range of the calibration curve. It is important that these pixels are represented.

3.3 Materials and Methods

The materials and methods in this section are described for performing ratiometric measurements after nanosensor uptake. Experimental procedures for cell culture are described in **Chapter 4.**

3.3.1 Nanosensor uptake

Cells were imaged live following nanosensor uptake. Cells were imaged in 35 mm glass-bottomed dishes (Intracel, UK) or 8-well Nunc Lab-Tek II Chamber Slides (Sigma, UK). Prior to imaging cell culture media was replaced with serum free phenol red free growth media. Samples were protected from light and transferred to the microscope. The conditions within the imaging chamber of the microscope were maintained at 37^{o}C, with a steady flow of CO_2. A vial containing damp cotton wool was added to humidify the imaging chamber. Cells were imaged for a maximum of 2 h in any one imaging session.

3.3.2 Calibration

3.3.2.1 Buffer calibration

50 µl of universal buffer solution was mixed with a 5 µl of a stock solution of nanosensors at a concentration 10 mg ml^{-1} to result in a final concentration of 1 mg ml^{-1}. 25 µl of this solution was then dropped onto a microscope slide and the sample was imaged. The edge of the droplet was used to focus the microscope, and images were taken in 5 different regions around the centre of the spot.

3.3.2.2 Cell lysate calibration

HeLa cells were resuspended in deionised water to a concentration of approximately 1 x 10^5 cells per ml and vortexed to break up the cells. Nanosensors were then added to this solution to a final concentration of 10 mg ml^{-1}. 1 µl of this solution was added to 50 µl of universal buffer solution and imaged as described above.

3.3.2.3 Fixed cell calibration

Following uptake of nanosensors, cells were fixed in 4% v/v paraformaldehyde (Sigma, UK) in PBS solution for 15 minutes. The samples were then permeabilised by incubated with Triton X-100 (Sigma, UK) for 10 minutes at

room temperature. Universal buffer solutions were then added to the permeabilised fixed cells and imaged in the vessel used for uptake.

3.3.3 Image acquisition

1) Leica DMIRE2 time-lapse inverted fluorescence microscope (University of Nottingham).

Images were taken with a 63x HCX PLAPO, NA 1.3, glycerol objective (Leica). Images were detected on a Hamamatsu OrcaER monochrome camera (6.45 µm x 6.45 µm, 28Mhz) acquired with Leica software. The image size used to acquire images was 1024 x 1024 pixels with a 2 x 2 bin. This resulted in pixel dimensions of 0.233 µm x 0.233 µm x 0.285 µm. The light source was a Mercury lamp used to excite samples via the corresponding filter blocks, in the green channel λ470/40 nm and red channel λ575/50 nm whilst emission intensity was registered at λ525/50 and λ640/50 nm respectively. Typically, transmission intensity, exposure and gain were set to 50%, 10 ms, and 1.00 respectively for both green and red channels (in some cases exposure, gain and transmission intensity were varied dependent on the brightness of the sample). Images were acquired in both red and green channels using an optical sectioning thickness width of > 200 nm.

Deconvolution was performed with Volocity imaging software using a proprietary constrained iterative deconvolution algorithm with a confidence limit of 95% and an iteration limit of 99.

2) Deltavision Elite (Applied Precision) inverted widefield fluorescent microscope with Olympus IX71 stand (University of Nottingham/University of Melbourne).

Images were taken using a 60x, 0.90 NA immersion oil (refractive index 1.415) objective (Olympus UPlan FL). Images were detected on a CoolSNAP HQ^2 CCD camera (6.45 µm x 6.45 µm, 1Mhz). Acquire software (version 5.5.0) was used to acquire images. The image size used to acquire images was 512 x 512 pixels with a 2 x 2 bin. This resulted in pixel dimensions of 0.240 µm x 0.240 µm x 0.200 µm. The light source was an Insight SSI solid state illuminator, which was used to excite samples via the corresponding filter blocks in the green channel λ475/28

nm and red channel λ542/27 nm whilst emission intensity was registered at λ523/36 and λ594/45 nm respectively. Transmission intensity, exposure and gain were set to 10%, 10 ms, and 1.00 respectively for both green and red channels (in some cases exposure, gain and transmission intensity were varied dependent on the brightness of the sample). Images were acquired in both red and green channels with an optical sectioning thickness of > 200 nm.

Images were deconvolved using a proprietary algorithm supplied by Deltavision based on constrained iterative deconvolution.

In order to assess the power of the deconvolution imaging technique to improve resolution of widefield imaging, cells were fixed and labelled using fluorophores stains for actin the nucleus. The following procedure was used for staining:

Cells were fixed prior to staining by immersing cells in a 4% solution of paraformaldehyde in PBS for 10 minutes. The samples were then washed with PBS a minimum of three times. F-actin and the cell nucleus were stained using phalloidin (Invitrogen) and Hoechst 3342 (Invitrogen) respectively. Cells were stained following fixation. For phalloidin staining a stock solution in methanol was added to the cells to a final concentration of 0.6 μM, a stock solution of Hoechst 3342 stain in PBS was added simultaneously to a final concentration of 1 mg ml^{-1}. Samples were periodically checked until adequate staining was achieved (~ 20 minutes).

3.4 Image analysis

In order to extract the maximum information about the distribution of intracellular pH, a pixel-by-pixel a high throughput automated batch processing method for image analysis was developed. The process was implemented using MATLAB and FIJI open source software. The final measurements were presented either as a histogram where each pixel is represented as a pH value or a colour map where pH is represented by colour on a linear scale.

3.4.1 Nanosensor uptake

The process of for analysing images from nanosensor uptake is summarised in **Figure 3.5**. In general terms, a ratiometric image is generated (**Figure 3.5A-E**) which is then converted into a pH value via the calibration curve and presented either as a colour mapped image or a histogram (**Figure 3.5F-I**). Any pixels within the masked region which are outside the range of the calibration are nominally presented as pH > 10. These pixels are presented in the colour-mapped image as black pixels.

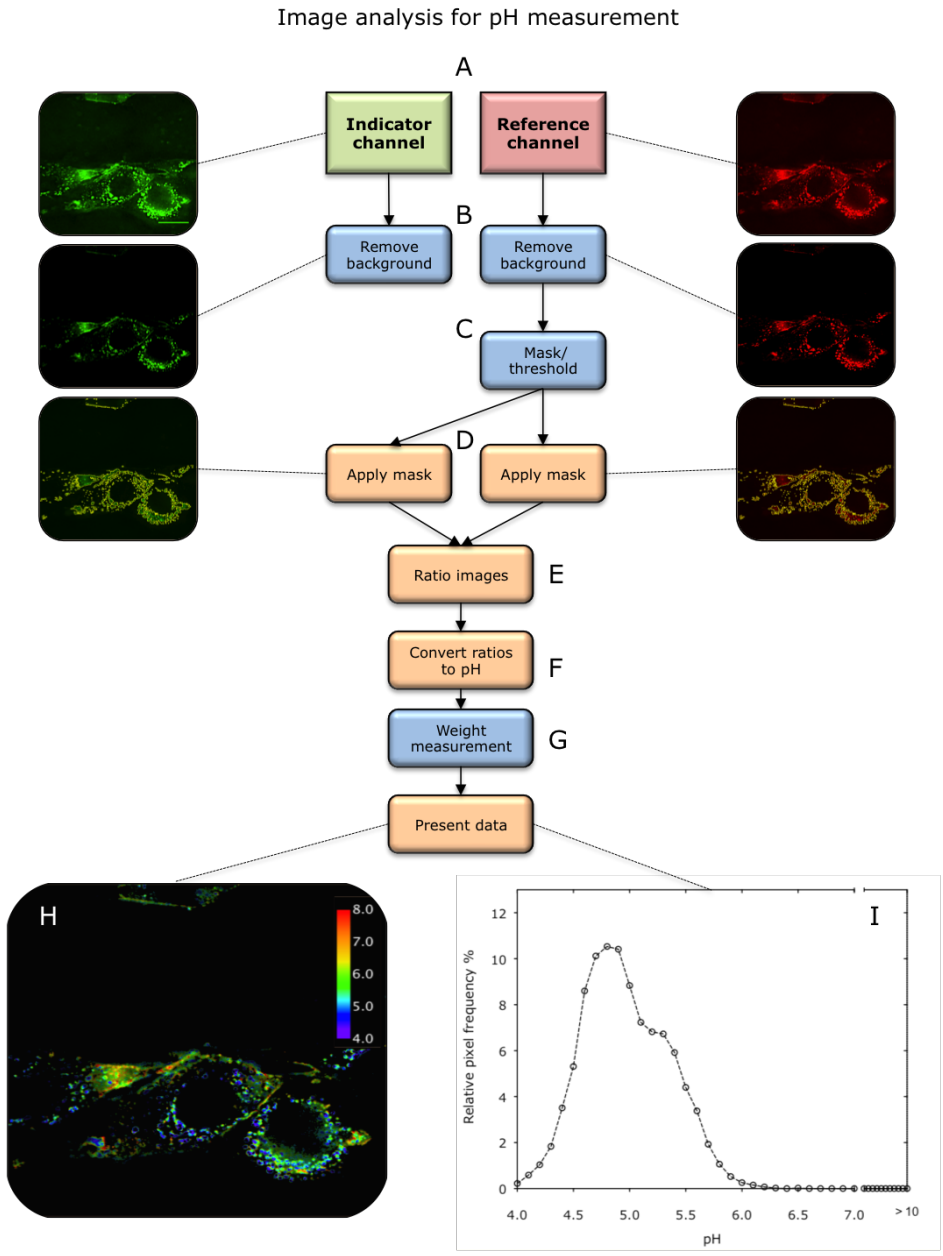

Figure 3.5 *Overview of image analysis for nanosensor uptake.* (A) Images are acquired in the indicator (green) and reference (red) channels after nanosensor uptake. The central most in-focus slice selected for analysis. (B) Background is removed in both channels. (C) Pixels containing nanosensor signal are isolated from the image. This is achieved by applying a threshold to the reference image, above which pixels are considered to contain nanosensors. This effectively creates a mask. (D) The mask is subsequently applied to the corresponding image in the indicator channel. (E) A ratio of indicator to reference intensity is taken for each pixel within the masked region. (F) This then converted to pH via the calibration curve. (G) The ratios are then weighted according to the intensity in the reference channel. (H,I) The image is then presented as a colour map or a histogram.

3.4.2 Calibration

The process for analysing images is different dependent, on the experimental conditions used for calibration i.e. free nanosensors in universal buffer or nanosensors in fixed permeabilised cells. An overview of the process for the latter is represented in **Figure 3.6**. The same process, excluding the thresholding step, is used to acquire calibration images acquired from free nanosensors in universal buffer. This is because all pixels in the image contain nanosensors removing the need to isolate nanosensor-containing pixels.

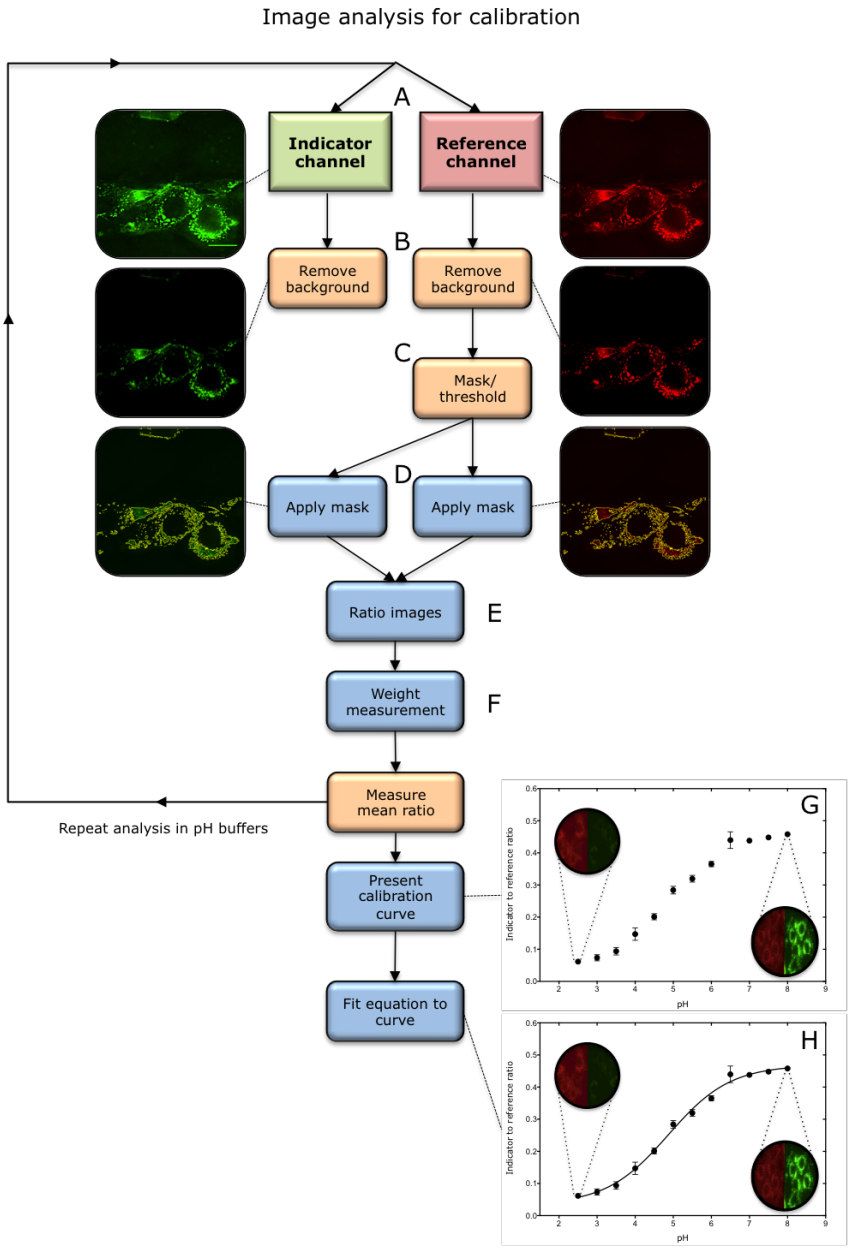

Figure 3.6 *Overview of image analysis process for calibration.* (A) Images are acquired in the indicator (green) and reference (red) channels in a universal buffer solution of known pH. The central most in-focus slice selected for analysis. (B) Background is removed in both channels. (C) Pixels containing nanosensor signal are isolated from the image. This is achieved by applying a threshold to the reference image, above which pixels are considered to contain nanosensors. This effectively creates a mask. (D) The mask is subsequently applied to the corresponding image in the indicator channel. (E) A ratio of indicator to reference intensity is taken for each pixel within the masked region. (F) The ratios are then weighted according to the intensity in the reference channel. (G) The process is repeated over a pH range from 2.5 to 8.0, and the mean intensity is utilised to construct a calibration. (H) An equation is then fitted to the plot.

The significance of background removal and thresholding for nanosensors calibrated in fixed permeabilised cells can be intuitively understood from the effect of these processing steps on the calibration plot**,** represented in **Figure 3.7.** In the unprocessed image, every pixel reports a ratio, including pixels, which clearly do not contain sensors (dark regions). The majority of pixels do not contain sensors; therefore all pH values report similar mean intensities (**Figure 3.7A**). However once pixels are isolated by creating a mask via thresholding a trend can be seen (**Figure 3.7B**). The masked or thresholded region is indicated by the red region in the images shown in **Figure 3.7D-F.** Removal of background from the image further isolates signal from the nanosensors resulting in the final calibration curve (**Figure 3.7C**).

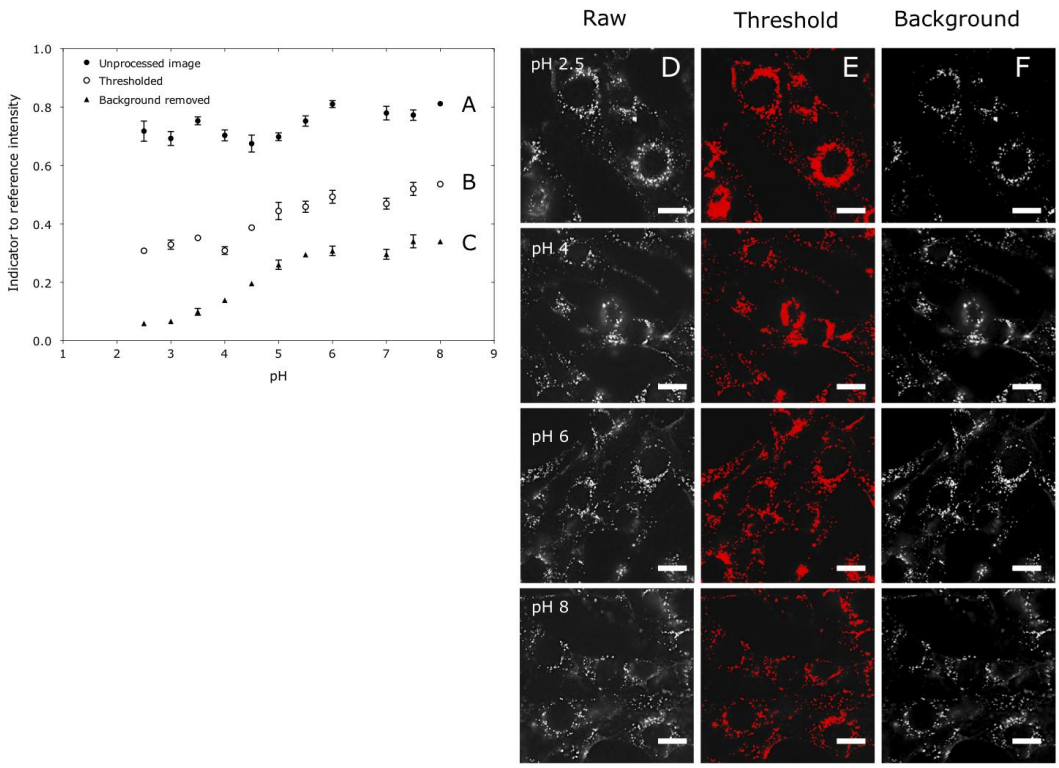

Figure 3.7 *Effect of background removal and thresholding on calibration. Images are of nanosensors internalised in 3T3 cells.* (A-C) Effect of different image processing parameters on calibration. (n = ~ 20 cells, error bars = SD). (D-F) Images of cells after application of imaging processing parameters. Images are in grayscale to improve visualisation. Red region indicates thresholded region. Scale bar = 6 µm.

3.4.3 Weighting measurements

This is an additional processing step incorporated to increase reliability of measurements. In the case of an unweighted image, each pixel is assigned a pH value, which is represented in the histogram. The problem with this is that a pixel is represented as one unit on the histogram whether it has a very intense or very weak signal. However it is apparent from the images that nanosensors are concentrated within discrete areas of the cell. This is expected, as the nanosensors will localise in discrete vesicles through the endocytic pathway. This may be misleading as exemplified in **Figure 3.8**. In the colour map of the unweighted image (**Figure 3.8D**), it appears most of the pixels are pH > 5.0 (green), however from observing the raw images, intuitively, most of the sensors are in the regions which are pH < 5.0 (blue/purple). The image and histogram of the unweighted image are a representation of the distribution of pH inside the cell, however there is no information on the proportion of nanosensors at different pH. In order to correct for this, pixels are weighted using the intensity of the reference image. A difference in the mean of 0.12 pH units is observed (**Figure 3.8A**). This is accompanied by a change in the distribution of pH. The effect of weighting is further illustrated by apply mask to weight the colour mapped image (**Figure 3.8C**). This mask uses an overlay of the reference image to block the signal from the colour map based on intensity from the reference. Weighting measurements has little effect on analysis of calibration images because all the nanosensors are reporting close to the same ratio (**Figure 3.8B**). The weighting aspect is essential to determine the proportion of sensors which are reporting a pH, this is important as without this measurement of pH would merely be an indicator of the spatial distribution of pH inside a cell.

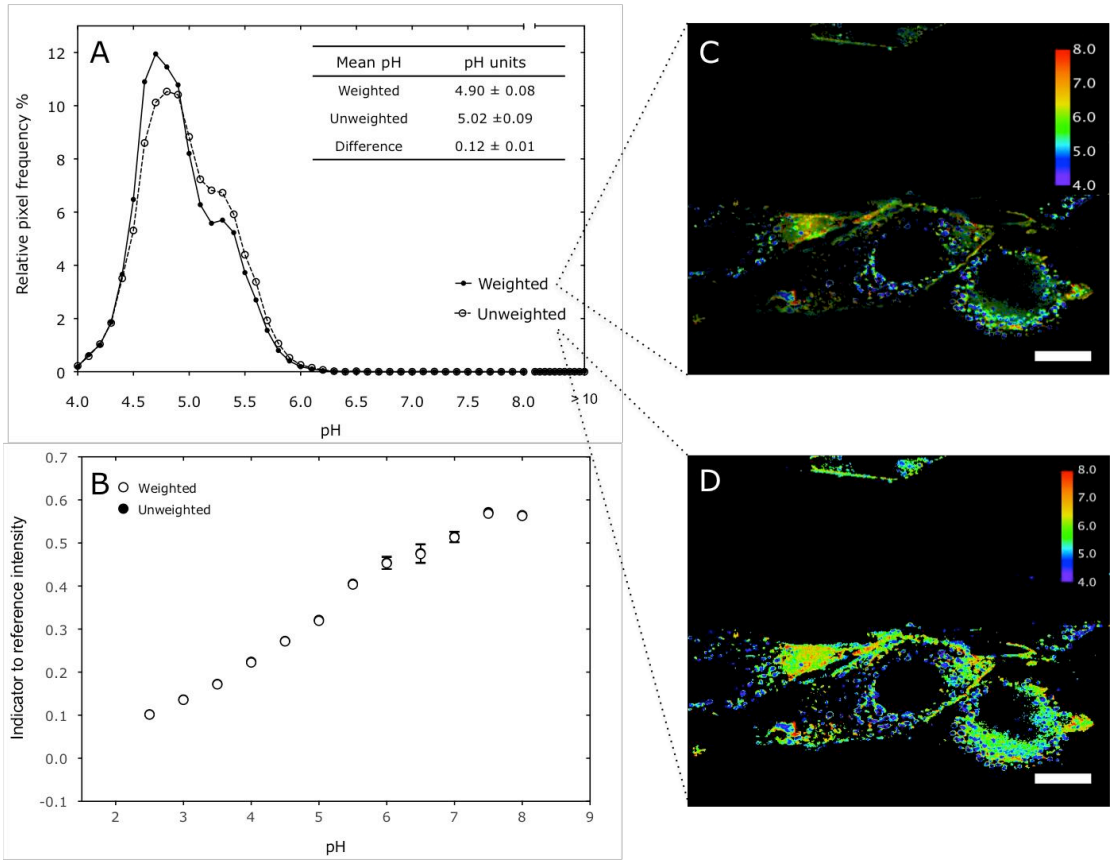

Figure 3.8 *Effect of weighting on nanosensor uptake measurements and calibration plot.* Images are of nanosensors in 3T3 cells. (A) Effect of weighting on the pH distribution of a single image. (B) Effect of weighting on a calibration plot. (n = ~ 20 cells, error bars = SD). (C,D) Weighted and unweighted false colour pH maps. Colour scale on the top right indicates pH. Scale bar = 15 µm.

3.4.4 Background removal

Background was removed by acquiring images of cells without sensors for each experiment, if this was not possible, the mean intensity from a region of interest outside the cell was taken as the background. There was found to be little variation in background between experiments. The mean value of intensity was then subtracted from the entire image. Background was removed from the calibration in images in the same way as for nanosensor uptake images. Background was subtracted using FIJI software.

3.4.5 Thresholding

The threshold value was selected at the lowest value where < 10% pixels reported a pH outside the measurement range of the nanosensor. This is discussed in more detail in the next section.

3.4.6 Data presentation

Data was presented as a histogram (generated in MATLAB) or a colour map (generated in FIJI). 100 bins were used in the histogram for nanosensor uptake images and 1000 bins for calibration images. The colour maps were generated using a custom made macro in FIJI, where images were processed in the same way as for MATLAB.

3.4.7 Automation of image analysis

Histograms representing multiple images were generated using a script in MATLAB. This script has a facility for input of values for threshold, background and calibration equation. The script was also written to convert images into a 16-bit image format.

3.5 Results and Discussion

The overall aim of this chapter is to develop a reliable methodology for performing ratiometric measurements using fluorescence microscopy. In order to do this, factors affecting the three main stages in the process of performing ratiometric measurements (nanosensor uptake, calibration and image analysis) were investigated.

A fundamental consideration before performing ratiometric measurements is the mode of fluorescence detection. Confocal microscopy is the method of choice in previous studies using optical nanosensors for intracellular measurements, however during preliminary experiments, low signal to noise (S/N) and high phototoxicity was observed using these techniques. Low S/N was observed almost universally in all sensor designs. Laser power was increased to attain satisfactory S/N ratios however this resulted in cells detaching rapidly. As an alternative, widefield microscopy coupled with deconvolution was explored to image cells. Widefield microscopy is not used routinely for intracellular measurement using nanosensors because of the high S/N generated by widefield illumination, however deconvolution delivered a significant improvement in S/N ratios, moreover images were of a comparable resolution to those obtained using confocal microscopy. By qualitative assessment, deconvolution of images delivers a sharp image without blur from adjacent planes (**Figure 3.9**) (Deltavision Elite imaging system). This was seen across all the imaging systems utilised in this work. Therefore widefield deconvolution microscopy was deemed to be the optimal technique for performing measurements. Examples of studies using widefield microscopy with deconvolution for nanosensor measurements are rare. This is because deconvolution requires a meticulous technical setup and laborious post processing techniques. However systems such as the Deltavision Elite microscope are specialised for deconvolution. This has led to more reliable results and faster data processing times. The main advantage of these systems is that they are less invasive and do not require very bright samples. There are other methods to increase the brightness of sensors, for example increasing fluorophore loading, however for some fluorophores, it is not cost effective to use such high amounts of fluorophores. In this work, we found approximately 10 times less fluorophore was required to register adequate S/N ratios (3:1) from a deconvolution imaging system relative to confocal.

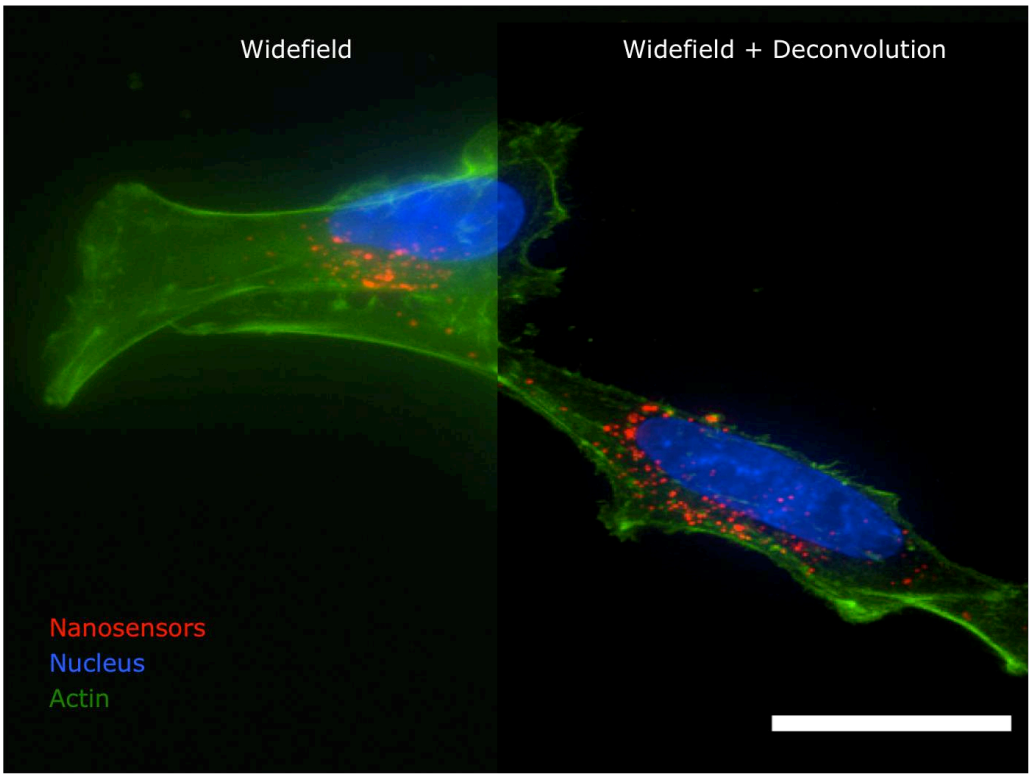

Figure 3.9 *Image enhancement by deconvolution.* Fixed HeLa cells after 24 h exposure to nanosensors labelled with TAMRA (red). F-Actin is stained with phalloidin conjugated to Alexa 488 (green), nuclei are stained with Hoescht 3342 (blue). Image was acquired using a Deltavision Elite microscope. Scale bar = 20µm.

3.5.1 Impact of image acquisition settings on ratiometric measurements

From a microscopy perspective, performing intracellular measurements using nanosensors is technically demanding because most intracellular structures are < 300 nm whereas the theoretical resolution limit of conventional optical microscopes is ~ 250 nm[211]. Operating close to the resolution limit means measurements are susceptible to small variations in instrument settings. These settings are not often discussed in the literature, but are essential for evaluating the reliability of measurements. In addition to this there are currently no studies where deconvolution has been used to perform intracellular measurements with nanosensors. Therefore aspects of instrumental setup affecting measurement (alignment, bleed through, fluctuations in lamp power and optical sectioning) were investigated experimentally. Additionally is it is critical that the imaging conditions are optimised to be as non-invasive as possible.

Some of these factors are dependent on the design of nanosensor used to make the measurement. The following discussion is in the context of the NS_{esc} sensor incorporating Oregon Green, 5(6)-FAM and TAMRA fluorophores.

3.5.1.1 Alignment

The alignment of the microscope was tested by assessment of colocalisation in signal from nanosensors in the indicator and reference channel following uptake in 3T3 fibroblast cells. As indicator and reference fluorophores are incorporated into the same particle signal should be colocalised. A measured Pearson's correlation coefficient (PCC) of 0.937 (statistical measure of colocalisation, where 1 indicates perfect colocalisation) from uptake images indicates adequate alignment (**Figure 3.10Cii**). In addition to this the colocalised channel shows most of the pixels are colocalised (**Figure 3.10Ciii**). Additionally alignment of the microscope was tested by imaging multicolour Tetraspek beads ~ 200 nm, without cells as shown in **Figure 3.10A**, by qualitative assessment there is no observable incorrect registration between channels for the beads. The risk of misalignment is greater in widefield microscopy as mechanical shifting of filter blocks is required during image acquisition. However as is the case for all microscopy techniques, misalignment also occurs as a result of sample movement during image acquisition, the source of which can come about as a result of the stage expanding and contracting, and also if the sample moves during image acquisition. This is particularly important, as intracellular trafficking is a dynamic process; indeed methods for image analysis have been developed to account for 'pixel-drift' during acquisition[183]. Consequently alignment should be checked frequently when performing ratiometric measurements in widefield systems. In the case of misalignment it is possible to apply registration corrections to mitigate the error.

3.5.1.2 Bleed through

Fluorescence bleed through was assessed by labelling nanosensors exclusively with reference or indicator fluorophores and measuring intensity in the corresponding channels minimal fluorescence bleed through was detected as indicated in **Figure 3.10B.** Bleed through is a particular concern for widefield microscopes because filter sets are often designed to excite and emit a range of wavelengths to increase fluorophore compatibility. Although not a concern in this work, this should be considered when selecting fluorophores for nanosensor measurements.

3.5.1.3 Fluctuations in lamp power

The influence of fluctuations in lamp power on fluorophore emission intensity was tested by continuously monitoring the indicator to reference ratio over an hour. No significant changes, which could be attributed to fluctuations in lamp power, were observed. Measurements performed using widefield microscopy are less susceptible to errors due to fluctuations in the intensity of excitation light compared to CLSM. This is because there is a single illumination source in widefield systems i.e. the lamp. Therefore any fluctuations are likely to affect both channels hence a constant ratio will be maintained. Whereas separate lasers are used to excite the sample in confocal microscopy hence variations in one laser will distort the ratio.

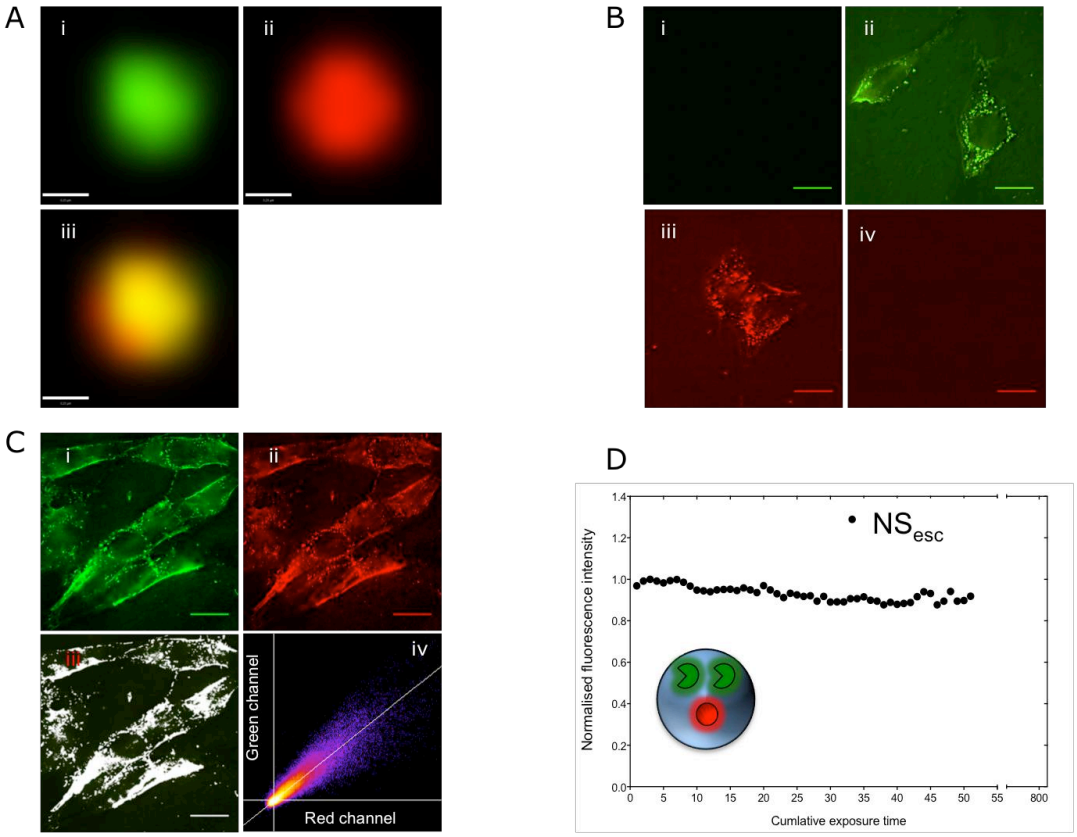

Figure 3.10 *Alignment, bleed through and fluctuations in lamp power during image acquisition.* (A) Test for microscope alignment. (i,ii) Tetraspek bead labelled with a red and green fluorophore, (iii) merged image. Scale bar = 200 nm. (B) Test for bleed through. Nanosensors labelled exclusively with OG/5(6) FAM (i,ii) and exclusively with TAMRA (iii,iv). An image is taken in both the red and green channels for each nanosensor. Scale bar = 15 µm. (C) Test for microscope alignment. Images of nanosensors after 24 h uptake in 3T3 fibroblast cells. (i) indicator channel, (ii) reference channel, (iii) Colocalised channel (colocalised pixels are coloured white). (iv) Colocalisation plot of red and green channels (PCC = 0.937). Scale bar = 15 µm. (D) Test for fluctuations in lamp power. Continual measurement of indicator to reference ratio in nanosensors in a pH 6.0 buffer solution.

3.5.1.4 Optical sectioning

Multiple optical sections were acquired for all images as is required for accurate deconvolution of images. The step size of each z-plane was taken to be within the vertical resolution limit of the microscope, typically 200 nm, and the images were acquired so that the most focused plane was in the centre of the stack. By qualitative assessment, planes above and below the central planes appeared to be blurry even after deconvolution as shown in **Figure 3.11**. The explanation for this is that most of the sensors are in the most focused plane. These sensors

interfere with planes above and below resulting in a blurry image. Deconvolution of the images does not eliminate the blur because the out of focus light is very intense. The significance of this finding is that only the central planes should be considered for measurements.

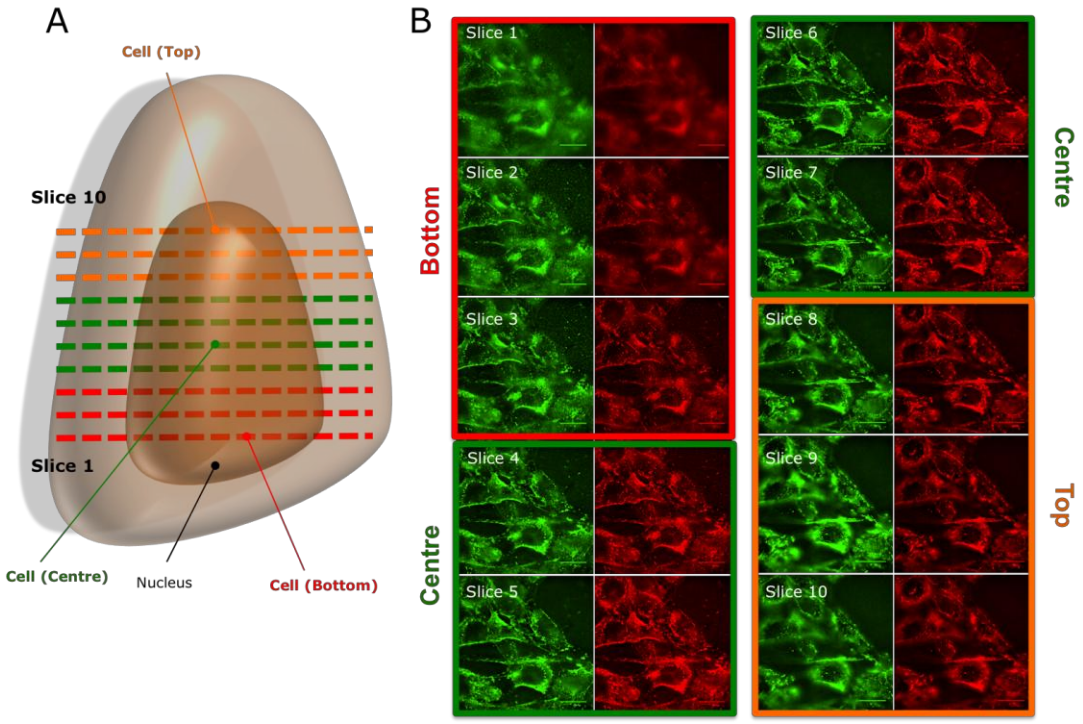

Figure 3.11 *Inadequate reconstruction of optical sections in an image produced by deconvolution microscopy.* Images are of 3T3 fibroblast cells following 24h exposure to nanosensors labelled with Oregon Green and TAMRA. Images are taken using a Delatvision Elite deconvolution microscope (Applied Precision). (A) Diagram showing the optical sectioning of a cell. (B) Optical sections taken through a 3T3 fibroblast cell. The central planes (Slices 4 -7) are in focus; other planes are out of focus. Optical sections were taken through the sample at intervals of 240 nm. Scale bar = 12 μm.

3.5.1.5 Imaging conditions

The impact of imaging conditions on cell viability during image acquisition was assessed by observing cells over time during repeated exposure to excitation light. A cell was repeatedly exposed to fluorescent light at the same exposures as typically used for uptake experiments every 10 minutes for 6 hours. Brightfield images of cells are shown in **Figure 3.12**. Significant changes in cell morphology are observed after 2 hours, with signs of cells detaching after 3 hours. The impact on cell viability could be due to phototoxicity and/or sub optimal conditions on the

stage. The amount of light exposed to cells by deconvolution microscopy is far below the laser power used routinely in CLSM for live cell applications. Therefore it is likely the loss in viability is due to sub optimal conditions on the microscope stage. Additionally for temporal studies undertaken in this work, cells were imaged and subsequently placed in a cell incubator. No changes in cell morphology were observed when imaging in this way, suggesting excitation light is not the primary factor leading to loss of cell viability. As with most standard microscope stages used for live-cell imaging, the incubator had a facility for precise control of temperature but no facility for controlling humidity or CO_2 atmosphere. The ideal atmosphere in cell incubators is 5% CO_2, whereas the incubator used in this study only had a facility for controlling flow of CO_2. A humidified atmosphere was created by placing vials with damp cotton wool in the cell chamber, which marginally improved viability. This type of technical consideration, which is not usually discussed in the literature, presents difficulties when comparing experimental procedures as often only representative images of viable cells are presented making it difficult to assess the true impact of imaging conditions on the experiment.

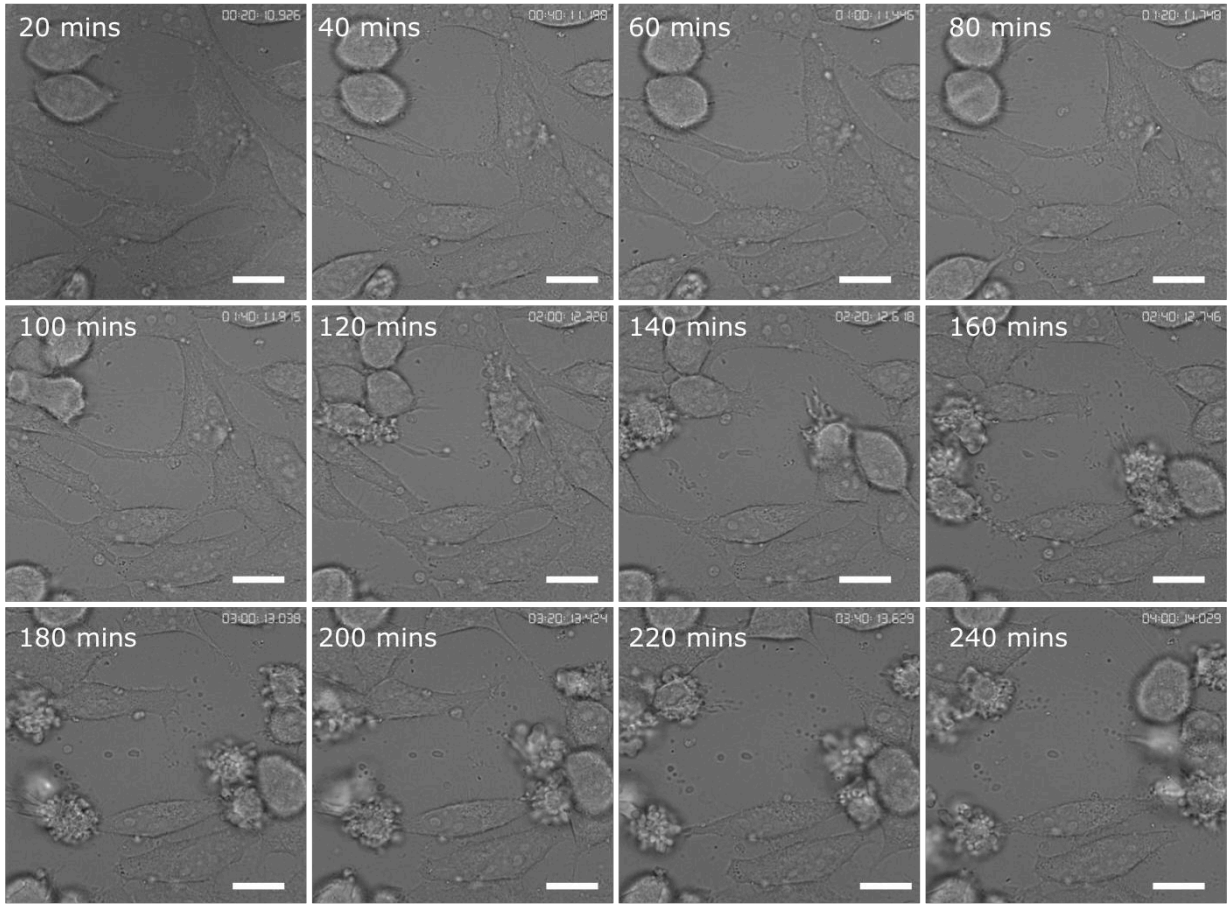

Figure 3.12 *Cell viability time course. Images are of HeLa cells following exposure to fluorescence excitation light at 6-minute intervals for 3 hours.* Scale bar = 15 μm. Images are taken using a Delatvision Elite deconvolution microscope (Applied Precision).

3.5.2 Evaluation of calibration conditions for pH measurement

The aim of calibration is to measure the response of fluorescent nanosensors in an environment, which most faithfully represents the intracellular environment in which the final biological measurement will be made. To understand how different calibration methods affect measurements, calibration was performed under three different conditions.

In the perhaps least intuitively representative condition, universal buffer solutions were mixed with nanosensors to a final concentration of 100 μg ml^{-1}. As indicated in **Figure 3.13** images appear as a fluorescence haze, with few dark spots. This is because the concentration of nanosensors is sufficiently high to cover the entire surface area of the imaging vessel. Proteins binding to nanosensors have been hypothesised to interfere with fluorophore sensitivity[110]. To create a condition more faithfully representing the cellular environment sensors were calibrated in the presence of biomolecules found in the intracellular environment. This was done by mixing sensors with freshly lysed cells and universal buffer. The images from this mode of calibration appear similar to those with the universal buffers alone. However the images from both these calibration methods appear different to cell images therefore a method was sought to conduct an *in situ* calibration of sensors. A method was developed involving fixing the sensors in the cells after cell uptake and subsequently permeabilising the cell. This permits buffer solution to permeate through the cell, interact with the nanosensor and elicit a response.

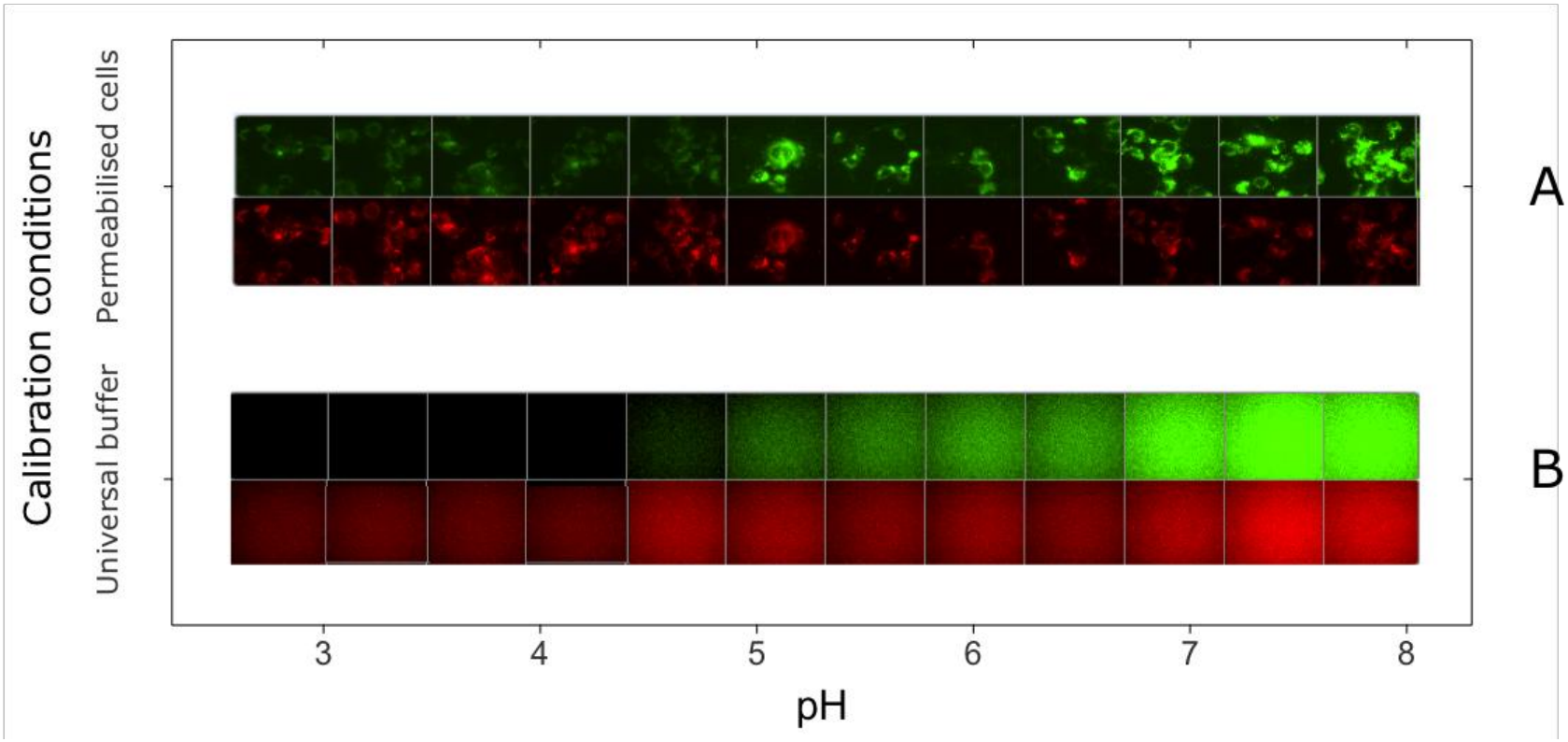

Figure 3.13 *Images of sensors under different calibration conditions.* (A) Calibration in permeabilised cells. Images are of cells, which have been fixed, permeabilised and then immersed, in universal phosphate buffer solutions. (B) Universal buffer. Calibration of sensors immersed in buffer.

All the measurements from the different conditions follow broadly the same shape as shown in **Figure 3.14**. Although there is a subtle difference between the calibrations conducted in universal buffer compared to calibrations conducted in cell lysate and fixed cells (**Figure 3.14D**)**.** The similarity in the calibration curves under different conditions shows fluorophores response is unaffected by factors in the biological environment such as binding of molecules, concentration and ionic strength. All of these are factors, which have been shown to affect the sensitivity of free fluorophores. Consequently this provides direct evidence for the protective effect of the polyacrylamide matrix, validating much of the early premises for the development of polyacrylamide nanosensors[109].

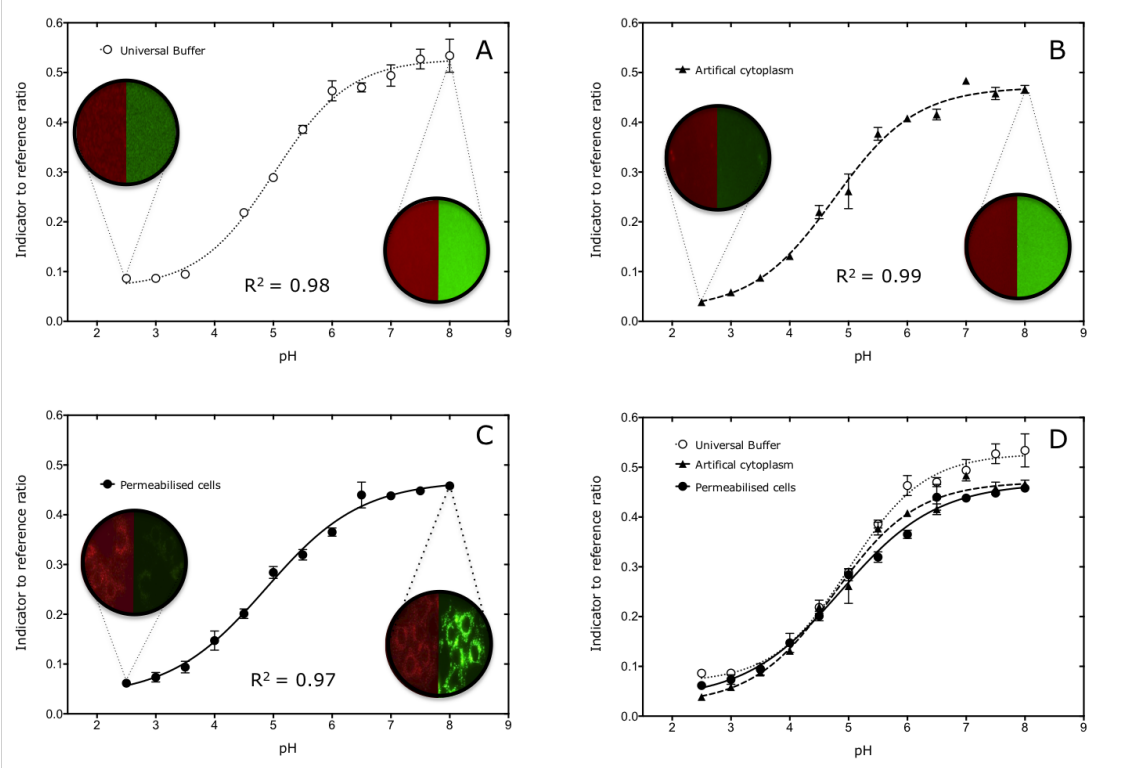

Figure 3.14 *Calibration of nanosensors under different conditions.* (A) Universal buffer. Calibration of sensors in buffer alone. (B) Cell lysate calibration. Calibration of sensors in universal buffer mixed with cell lysate. (C) Permeabilised cells. Cells were fixed, permeabilised and then calibrated in a range of universal buffer solutions. (N = 3, error bars = S.D).

3.5.3 Impact of image analysis variables on ratiometric measurements

The key variables affecting image analysis are how much background is removed and where the threshold is set. An understanding of how these variables affect final measurements is required to determine what values should be used as well as for evaluating the validity of the final measurement. In general the values for thresholding and background removal from calibration images should be kept consistent with that of nanosensor uptake images.

3.5.3.1 Thresholding

The influence of the thresholding variable on calibration and measurement from nanosensor uptake images was investigated by removing background from an image and setting the threshold to an intensity between 0 and 400. The corresponding calibration curves and representative thresholded images are shown in **Figure 3.15**. Minimal variation is seen when the threshold is taken at any value between 0 and 400 (**Figure 3.15A**)**.** The threshold essentially determines which sensors are considered for measurement as is indicated in **Figure 3.15B-F**, where the thresholded region is coloured red. Minimal variation at different threshold values is expected for calibration images because pH is controlled so all the sensors report approximately the same intensity ratio.

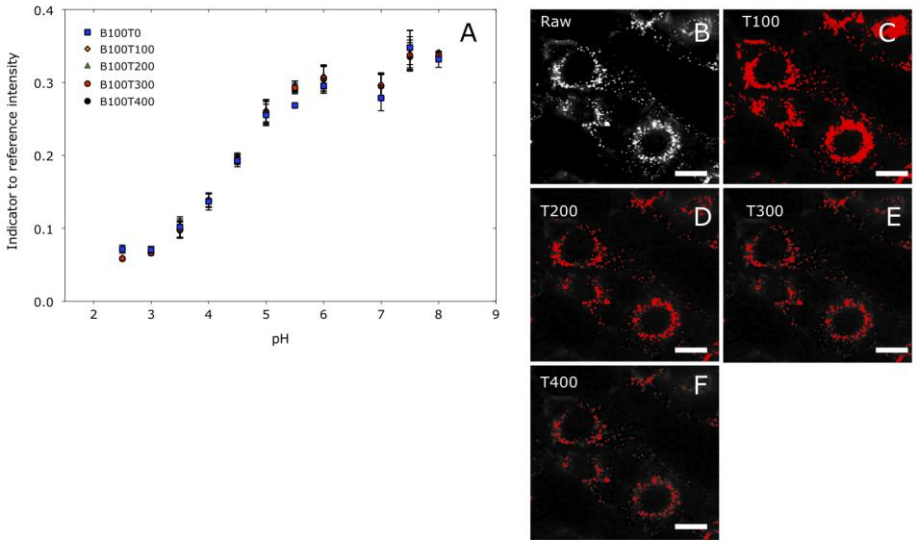

Figure 3.15 *Influence of different threshold values on calibration.* (A) Calibration curves for threshold intensities between 0 and 400, after background removal. B = Background, T = Threshold. (B-F) Thresholded images of sensors in fixed cells at pH 5.0. Thresholded pixels are shown in red. Scale bar = 15 µm. (N = ~ 10000 pixels, error bars = S.D).

Conversely setting different threshold values when analysing nanosensor uptake images affects the final measurement as shown in **Figure 3.16**. A decrease in the mean pH of 0.64 units from 5.20 to 4.56 is determined when thresholding is progressively increased from 0 to 400. The greatest drop in average pH is seen at low threshold values, whereas once the threshold is raised above 100 there is progressively less deviation in the measurement (**Figure 3.16A**). At low threshold values there are also a large proportion of pixels outside the calibration range compared to at higher threshold values (> 100) this indicates there are a greater proportion of pixels are being considered which do not contain nanosensors (**Figure 3.16B**). Although these pixels are not considered in the final measurement, this increases the amount of low intensity pixels, which are considered. This is shown in the corresponding images in **Figure 3.16C-G** where increasing thresholding eliminates low intensity pixels. There is an increased error from low intensity pixels as these measurements are affected by small variations in signal intensity. This data shows that more reliable measurements are obtained by setting a higher threshold. However it is still important to standardise where the threshold set to eliminate subjectivity. For this work it is proposed to set the threshold to the lowest level where at least 90% of the pixels are within the range of the calibration curve, in this example the value is ~ 200.

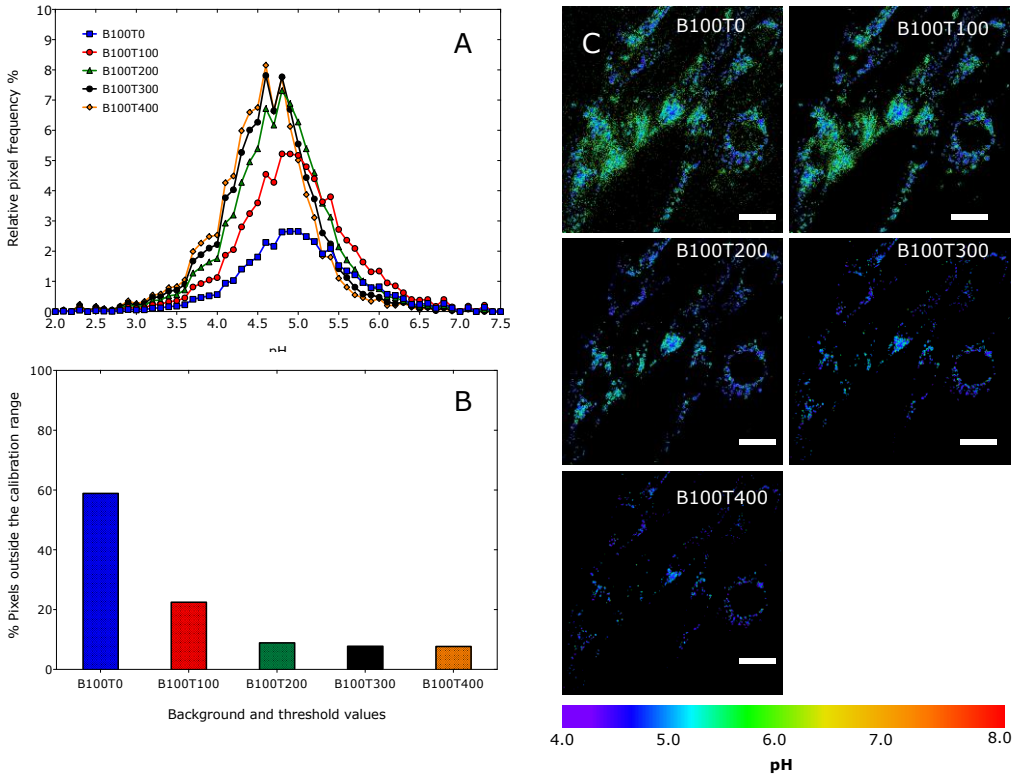

Figure 3.16 *Influence of different threshold values on pH measurements.* (A) Distribution of intracellular pH taking threshold values between 0 and 400. (B) Proportion of pixels reporting pH outside the range of the calibration curve at threshold values between 0 and 400. (C) False colour pH maps of a single image thresholded at values between 0 and 400. (B = Background, T = Threshold). Scale bar = 12 μm.

3.5.3.2 Background removal

The influence of background removal on pH measurements was investigated by performing image analysis on a test image, setting values for background to be between 100 and 200 (taking threshold to be 200). Values between 100 and 200 were used as background values because measurements from region of interests (ROIs) outside the cell in this example were found to be within this range. The reconstructed calibration curves, and corresponding histograms are shown in **Figure 3.17**. **Figure 3.17B** shows pH measurements when different amounts of background are removed from both the calibration and nanosensor uptake images. There appears to be no significant variation for background values between 100 and 160, however above this there is much greater variation when a value greater than 160 is subtracted. This indicates there is a range of background values where there is unlikely to be major effects on the final measurement. The amount of background in images of cellular uptake is

dependent on the experimental conditions. If the sensors are removed and washed off, the same amount of background should be removed as for the calibration images.

However in certain scenarios it may be necessary to remove different amounts of background from the uptake images compared to the calibration. For example in highly temporally resolved measurements where sensors cannot be removed and washed fast enough. In such cases background can be removed by selecting a region of interest (ROI) outside of the cell and this value can be taken as background. In **Figure 3.17C**, the background removal for the calibration was set as 100 whilst background values in the uptake images were removed from 100 to 200. The result is decreasing values for the final measurement. This highlights the importance of selecting the correct value for background removal.

For this study, background was determined by measurement of cells without nanosensors, observed to be ~ 100 au. The amount of background was observed to be consistent in both image acquisition channels. Therefore the same value was removed from all images.

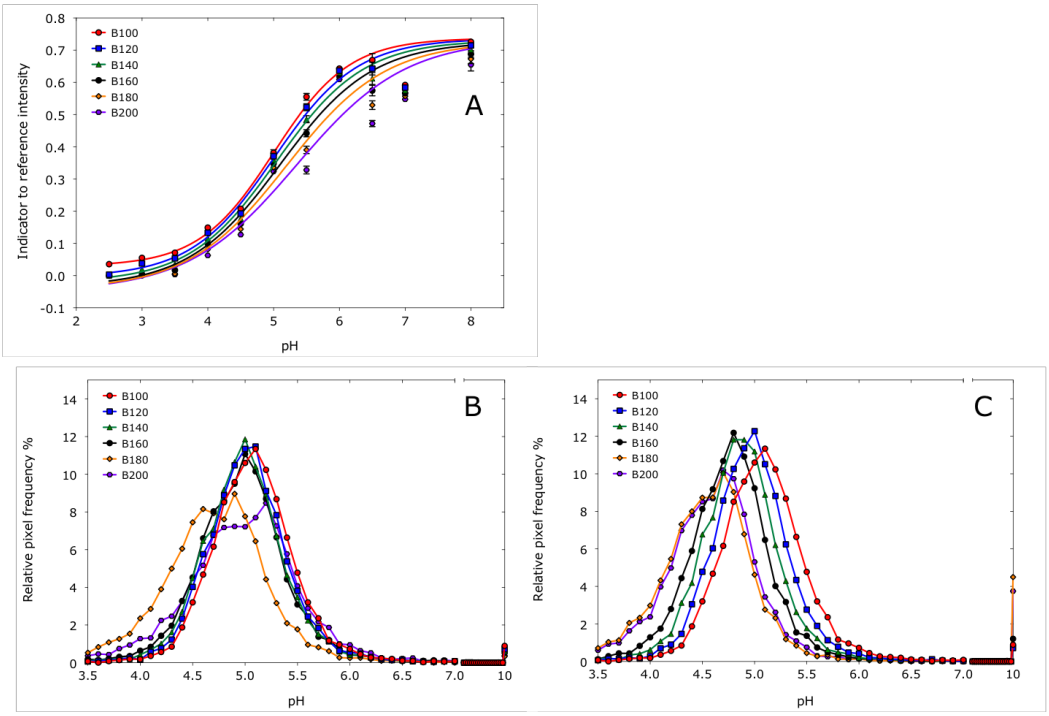

Figure 3.17 *Influence of background subtraction on nanosensor uptake measurements.* (A) Calibration curves after background removal. (B) pH measurements altering the amount of background removed in the uptake image and the calibration (C) pH measurements when keeping background removal in calibration images constant (B100) and varying the background removed in the uptake image. (B = Background, T = Threshold).

3.5.3.3 Selection of optical section for measurement

The images utilised for image analysis were the most focused plane, which was determined subjectively during image acquisition. It was observed that it is very difficult to determine when a sample is precisely in focus, therefore the effect of taking measurements from different optical sections in the calibration and after nanosensor uptake was investigated. For calibration significant variations in mean intensity were observed particularly at higher pH values (**Figure 3.18A**) however the central planes demonstrate little variation. The same is observed for pH measurements (**Figure 3.18B,C**). The variation can also be seen in the corresponding colour mapped images (**Figure 3.19**), excluding the central planes (slice 5,6 and 7). The reason for the variation is that out of focus images are inadequately reconstructed by deconvolution hence a blurry appearance. From the point of view of image acquisition, this demonstrates there is a range of approximately 0.6 µm where an image must be focused.

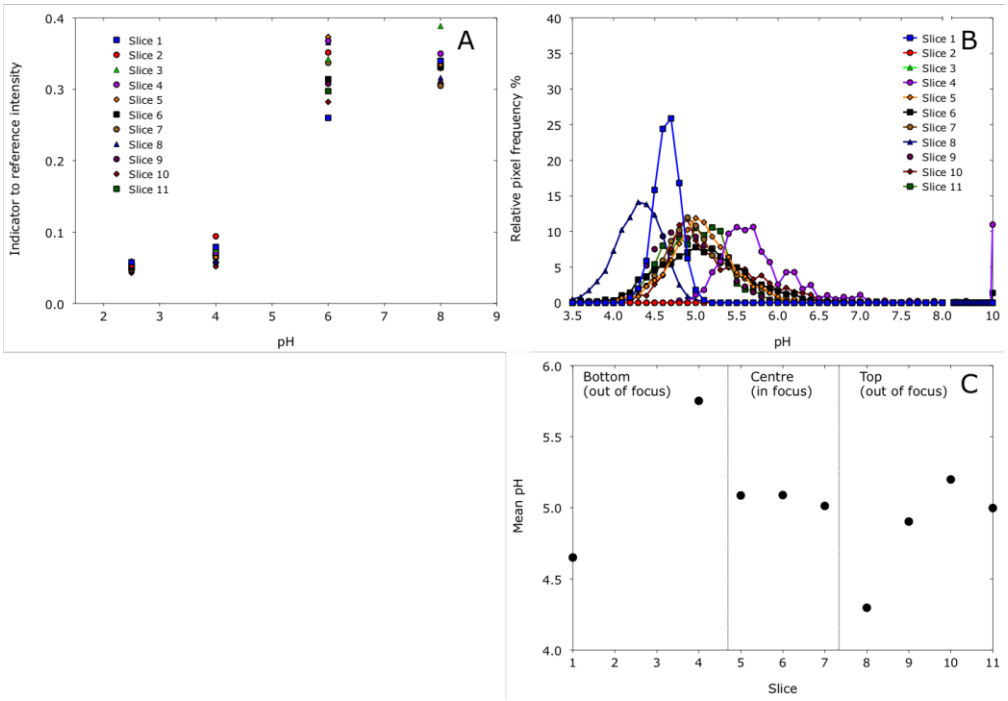

Figure 3.18 *Influence of optical sectioning on pH measurement and calibration.* (A) Calibration plot representing the indicator to reference intensity measurement across all the optical sections of one image at pH 2.5, 4, 6 and 8. (B) Histogram of pH distribution in different optical sections. (C) Mean pH in each optical section.

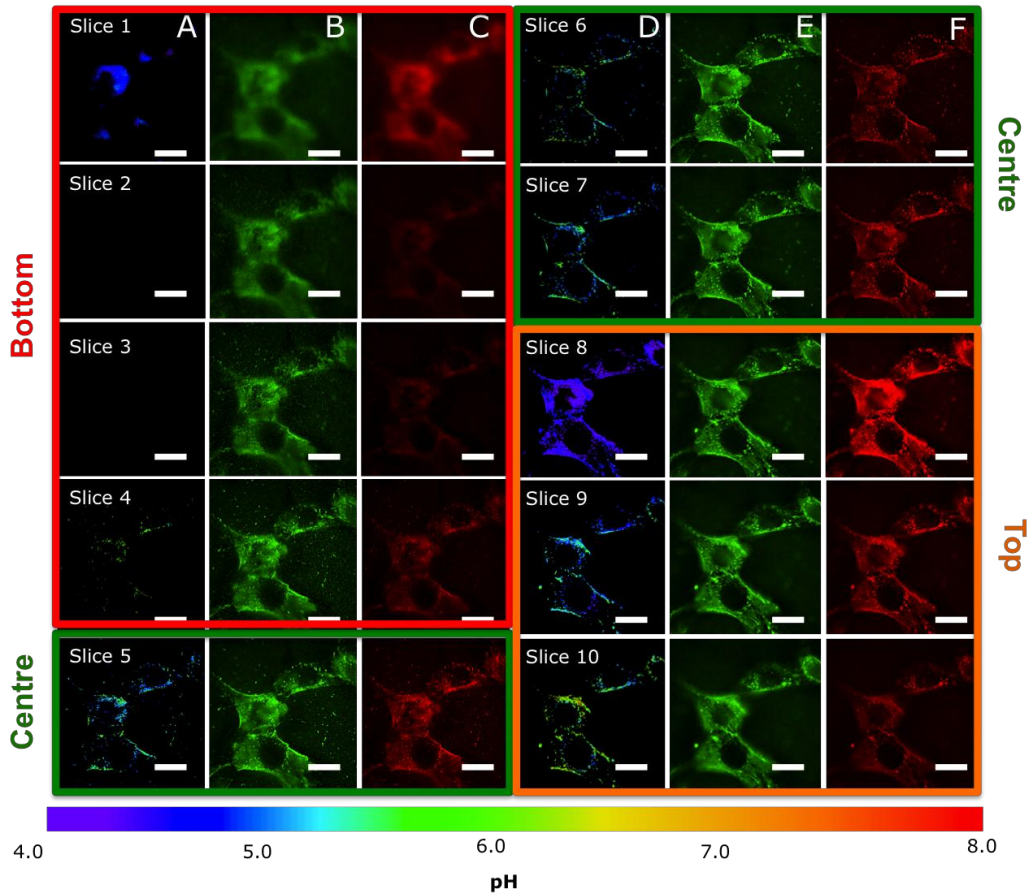

Figure 3.19 *Influence of optical sectioning on pH measurement.* Images show 3T3 fibroblast cells following 24h exposure to nanosensors. (A,D) False colour pH maps. (B,E) Indicator channel. (C,F) Reference channel. Optical sections are taken through the cell at intervals of 240 nm. Scale bar = 8 μm.

3.6 Conclusions

A procedure for performing ratiometric measurements using fluorescent nanosensors detected by deconvolution microscopy has been established. Several factors affecting nanosensor uptake, calibration and image analysis have been investigated in the context overall pH measurement. The general considerations to be taken into account when designing methodology for measurement are summarised in **Table 3.2**, with steps incorporated into the methodology for controlling these factors.

Process stage		Settings	Consideration	Design parameter
Nanosensor uptake	Image acquisition settings	Exposure and Gain	Minimise to avoid phototoxicity and photobleaching (<50 ms).	Maximum exposure used 10 ms
		Pixel size	Set below the resolution required with consideration to the Nyquist sampling theorem	Max pixel size used = 0.240 µm x 0.240 µm
		Deconvolution	Measure PSF experimentally, avoid algorithms which remove light	PSFs were measured and checked regularly, restorative algorithm was used
		Optical sectioning	Acquire multiple optical sections, for maximum information, set Z step size to within the axial resolution of the microscope. Take care to focus image	Optical sections of < 200 nm were used
		Alignment	Ensure adequate registration in channels used for the experiment	Alignment was check regularly using fluorescent beads
		Light source power	Ensure no fluctuations in the intensity of the light source during image acquisition	Fluctuations in lamp power checked by measuring intensity following repeated sample exposure
		Bleed through	Ensure no detectable bleed through is present. This can be minimised by using narrow band pass filters.	Checked experimentally
	Imaging conditions	Cell imaging chamber	Temperature, humidity and CO_2 need to be controlled.	Imaging chamber was modified to allow control atmospheric conditions
		Imaging time	Minimise imaging time to prevent affect on cell viability	Cells were imaged for a maximum of 2 hours at one time
Calibration	Image acquisition settings	As above	Should be kept identical to acquisition settings. Practically easier to determine image acquisition settings prior to calibration	Settings were kept identical
	Imaging conditions	Calibration conditions	Calibration conditions should match nanosensor uptake conditions as closely as possible	Cells were calibrated in permeabilised cells
		Fitting calibration	Sigmoidal fit, R^2 should be more than 0.95	$R^2 > 0.95$ used for experiments
Image analysis	Variables	Background removal	Should be kept the same for calibration and nanosensor uptake if possible.	Measured using ROI based method and measurement of control cells
		Thresholding	Should be set to a level where there is minimal error	Set to where < 10% of pixels are outside the calibration range
	Other considerations	Optical sectioning	Consider central planes, take care to focus images	Only central planes considered for measurement
		Automation	Use software such as MATLAB or FIJI to automate image analysis. Should consider computational time as well.	Scripts for batch processing were developed
		Weighting	Weighting gives information about the proportion of sensors reporting a pH as well as intracellular distribution.	All images were weighted

Table 3.2 Summary of considerations for performing ratiometric intracellular measurement.

The findings from this chapter demonstrate that performing ratiometric measurements requires a meticulous experimental setup in terms of instrument settings. Additionally the results show methodology for image analysis can greatly influence results, which is not taken into account in the majority of literature describing intracellular measurements [132,181,208]. Variations in background removal and thresholding were found to be key factors affecting overall measurements. Accordingly we propose a method of standardising where a threshold is set by ensuring < 10 % of pixels are outside the calibration range of the sensors. Conversely different calibration conditions were not found to greatly affect measurements. This demonstrates protective effect of the polyacrylamide matrix.

The experimental design considerations presented can be applied when performing ratiometric measurements in different settings with nano and micro sized sensors and/or different microscopes techniques. Key considerations when translating this methodology is i) the type of image acquired in terms of sensor distribution and background. Images with evenly distributed signal do not require thresholding but every application requires careful consideration of how background is removed. ii) It is important the calibration methodology reflects the experimental conditions as faithfully as possible.

Chapter 4 Optical pH nanosensors for measurement in the endocytic pathway: Delivery, validation and measurement

4.1 Aim

The first aim of this chapter is to deliver nanosensors to the endocytic pathway without interference with natural cell function. The second aim is to perform pH measurements inside cells utilising the sensors and methodologies developed in **Chapter 2** and **Chapter 3**. This is with the view of establishing the optimal sensor design for intracellular measurements. The final aim of this chapter is to validate pH measurements performed using nanosensors by correlating measurements to intracellular location. In the context of the wider literature this chapter aims to build a greater understanding of the performance of nanosensors following delivery to cells.

4.2 Introduction

4.2.1 Cellular delivery of polyacrylamide nanosensors

For the purposes of this study, polyacrylamide nanosensors are required to enter the endocytic pathway, however polyacrylamide nanosensors do not have physicochemical characteristics which favour uptake by endocytosis. From extensive research into how materials interact with cells, it is clear that there is a link between the physicochemical properties (size, shape, charge etc.) of a material and how it is uptaken into a cell[13,15]. Therefore altering the physicochemical characteristics of a material to favour uptake is a means of targeting nanosensors to the endocytic pathway. The following section is review of some of the key parameters (size, charge, shape, rigidity and targeting ligands) known to affect the uptake and intracellular trafficking of materials.

It is important to note that, in an ideal situation these properties would be tuned to control how a material enters a cell, and to some extent this is possible. However establishing reliable generalisations about how these factors influence uptake is problematic because there are often a number of interrelated factors at play. Moreover, there are such a diverse array of materials under investigation in a range of different cell types, that comparisons between different studies is not straightforward[9].

4.2.1.1 Size

The link between particle size and cellular uptake has been extensively studied. The effect of size on uptake is very much dependent on the cell type, and more specifically on the mechanism of uptake (**Figure 4.1**). Broadly speaking endocytosis can be split in two main mechanisms, phagocytosis (uptake of large particles up to 20 μm)[13] and pinocytosis (uptake of fluids). Only uptake by pinocytosis is considered here because it is a universal uptake mechanism whereas phagocytosis is only relevant to relatively few highly specialized cells such as macrophages and dendritic cells. Although materials up to around 5 μm have been seen to be uptaken by pinocytosis[13], it is generally accepted that uptake is greatly enhanced for particles < 200 nm, this is both in terms of overall uptake and speed of uptake[13,204,227,228]. However assessment of the impact of size on uptake is particularly unclear because many materials have a high polydispersity. Therefore the most insightful studies in this area are when other

factors are tightly controlled. This has been aided by techniques for the design of monodisperse nanoparticles such as the particle replication in non-wetting templates (PRINT) process (**Figure 4.2**).

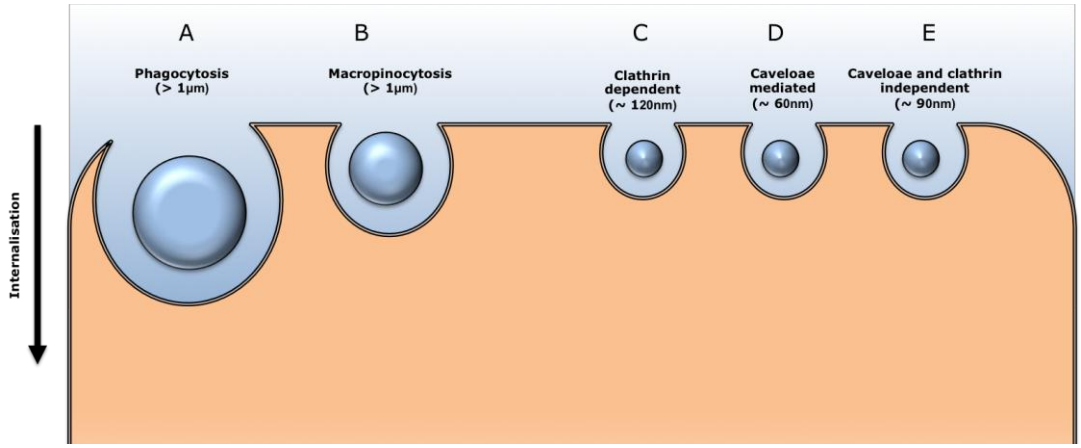

Figure 4.1 *Size dependence of endocytic mechanisms.* (A) Phagocytosis. Internalisation of large particles by specialised cells such as macrophages and dendritic cells. (B) Macropinocytosis. Generalised mechanism for internalisation of large particles. (C) Clathrin-dependent endocytosis. (D) Caveolae-mediated. (E) Caveolae and clathrin independent (F). Size limits vary between cell types. Blue spheres represent nanoparticles.

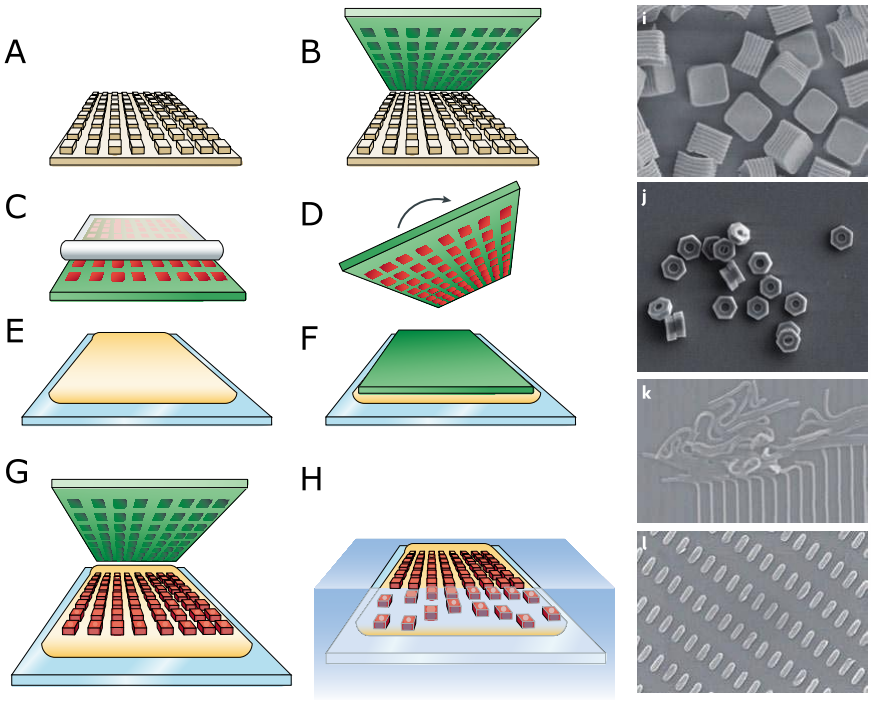

Figure 4.2 *PRINT process for the synthesis of monodisperse nanoparticles.* (A) A silicon master template is prepared. (B) Fluorocarbon moulds of the template are generated. (C) The mould is filled with liquid precursors, which react to form a nanoparticle. (D) The mould containing the particles is placed onto a harvesting layer. (E) The mould is the run through a roller pattern side down. (F) This is then placed on a liquid harvesting film. (G) The film is then dried and the mould is peeled away. (H) The individual particles are produced by dissolving the harvesting film. (I-L) SEM images of PRINT nanoparticles and microparticles. Reproduced with permission from[6].

In a notable study using this technique by Gratton *et al,* the internalisation cube-shaped nanoparticles of diameter between 150 nm and 5 μm were investigated in HeLa cells by flow cytometry[229]. The results showed that smaller particles (< 500 nm in diameter) were internalized much faster than larger micron sized particles. Although it is difficult to precisely define what is the optimal size for uptake, it appears that nanometre sized particles give the maximum rate of uptake. In terms of size polyacrylamide nanosensors synthesized in this study, which are less than 100 nm in diameter are suitable for uptake, however size alone does not result in uptake.

4.2.1.2 Surface charge

Another key factor influencing uptake is surface charge. The surface charge on particles strongly influences a key stage in the internalisation of nanoparticles, namely cellular attachment. Attachment occurs at the first point of contact between the material and the cell. The efficiency of adhesion is primarily governed by non-specific electrostatic interactions between the exterior of the cell membrane and the nanoparticle surface. The outer leaflet of the cell membrane is negatively charged due to the presence of phosphate groups, but there are also cell surface proteoglycans called glycosaminoglycan's (GAGs), which are highly anionic[230]. GAGs are thought to play a key role in promoting cellular attachment and internalisation of cationic nanoparticles[230]. It has also been hypothesised that charged groups transiently pierce the cell membrane facilitating transport into the cell[231]. There are a diverse range of nanomaterials uptaken into cells which are cationic in character (e.g. PLGA[232], chitosan[233], PEI[234], DOTAP[31]), additionally attachment of positively charged groups on to material has been seen to result in enhanced uptake[117,120].

Importantly for this work, increasing positive charge on polyacrylamide nanosensors has been utilised as a strategy for delivering sensors into cells by endocytosis in a range of cell types. This has been achieved through introduction of a positively charged group on the surface of the nanoparticle (e.g. PDMPA[117], APMA[120], TAT peptide[208]). However the extent to which surface charge influences uptake and the process of intracellular trafficking is unclear.

Interestingly there are also a few studies where negatively charged particles have been uptaken into cells, and in one study by Zhang *et al* on the internalisation of Quantum Dots (QDs), negatively charged particles were seen to internalise more rapidly than oppositely charged particles of the same composition[235]. The reasons for this are unclear, but it is likely to occur by a mechanism specific to QDs, due to the weight of evidence suggesting cationic particles promote uptake. On the contrary nanoparticles with neutral charge without any further modification to promote uptake almost always show poor uptake[6].

When considering the impact of surface charge it is important to consider the biological conditions. Serum proteins in cell culture media have been shown to bind nanoparticles and result in the formation of a protein corona around the nanoparticle, this changes the charge of the surface presented to the cell. How the corona forms depends on the material composition as well as the surface

charge of the nanoparticle[236]. This could be a possible explanation of the uptake variations seen in similarly charged nanoparticles.

4.2.1.3 Shape and rigidity

The impact of shape and rigidity of a nanoparticle on cellular uptake has been studied in less detail than size and charge due to the technical challenges associated with producing particles with different geometries on the nanoscale. However recent studies have shown this could play a significant role in cellular uptake[227,237]. It is important to note, the majority of these studies have been undertaken in the context of phagocytosis with few examples for pinocytosis. The general findings from these studies are that increased aspect ratios result in increased uptake, however caution must be taken in interpreting such results as altering the shape of a particle will change a series of interrelated factors such as surface area, volume and size which also affect cellular uptake. The softness of materials may also affect cellular uptake but this has not been studied in detail.

4.2.1.4 Active targeting

Nanomaterials can be actively targeted by attaching a group such as a peptide, antibody or ligands, to the surface of the particle to promote cellular internalisation. The mechanism of entry will vary dependent on the targeting group. The most common approach is to attach a ligand or antibody, which binds to a corresponding receptor on the cell surface. This initiates a signalling cascade which triggers endocytosis by promoting cellular attachment or in more specialised systems, receptors can be targeted which constitutively internalise ligands or antibodies by endocytosis. In such cases the nanomaterial is internalised with the targeting group. Examples of this are transferrin, folate, epidermal growth factors (EGF) and monoclonal antibody meditated targeting[238]. Most of these examples have been developed because the corresponding receptors are highly expressed in target cells. In addition to this attaching cell penetrating peptides to a particle has been shown to promote uptake by endocytosis, however the mechanism for this remains unclear and is the cause of much debate[239].

4.2.2 Fluorescence-based methods for studying cellular internalisation of nanomedicines

Uptake and intracellular location of nanomaterials can be determined by different fluorescence-based methods. The key challenge for such techniques is to resolve small differences in location. For uptake, material, which is outside or bound to

the surface of a cell, must be distinguished from material, which has been internalised, whilst for intracellular location it is important to distinguish between sub-micron sized subcellular compartments. Another challenge is in producing representative data. Flow cytometry is a high throughput, low-resolution technique, which is commonly used to determine cellular uptake, whilst quantitative fluorescence microscopy is lower throughput but can reach the resolutions required to distinguish between intracellular compartments. The following section is an overview of fluorescence-based instrumentation and approaches for studying the internalisation of nanomaterials.

4.2.2.1 Flow cytometry

Flow cytometry is a technique in which material is continuously characterised as it flows through an instrument, usually by fluorescence and/or light scattering methods.

In the first stage of the process, the sample is suspended in a liquid and passed through the fluidic system to a point where the sample is interrogated by a laser. At this stage, cells are focused in a single cell stream by a process called hydrodynamic focusing. Most flow cytometers achieve this by injecting the sample into a sheath fluid or saline solution. Each cell in the sample will then scatter light and/or fluoresce; this light is directed by the optics to the detectors and that generates a signal that is processed by a computer into a readable digital signal. Although a cell will scatter light in all directions, detectors are positioned to detect scattered light either in the forward or side direction, in the latter; the detector is positioned at a 90^{o} angle to the sample. The magnitude of forward scatter is approximately proportional to the size of the cell, whilst magnitude of side scatter is proportional to the internal complexity or granularity of the cell. Plotting forward and side scatter together as a 2D plot can be used to distinguish between different cell populations in a sample. Another common parameter used in flow cytometry in fluorescence. Once a cell is fluorescently labelled, the fluorescent light is detected in a similar way to side scatter. Fluorescent emission is passed through a series of wavelength filters, which direct the light with a specified range of wavelengths to the corresponding detector. The magnitude of fluorescence gives information about the amount fluorophore associated with a cell. The advantage of flow cytometry is the multi parametric analysis which permits analysis of heterogeneous cell populations and also the high throughput continuous flow process which enables analysis of large populations of cells, typically 50,000 events are recorded per experiment.

Flow cytometry is now established as a standard technique for analysis of nanoparticle uptake[240]. The advantage is that large numbers of cells can be analysed quickly however flow cytometry is not a high-resolution technique. As a result of this, it is not possible to distinguish between material bound to the surface of the cell and internalised material. Consequently stringent techniques are often required to wash off unbound material. This can be achieved by agents, which interfere with electrostatic interactions between proteoglycans on the cell surface, such as heparin[183]. Alternatively trypan blue exclusion staining can be used to quench fluorescence[240]. In this method cells are mixed with trypan blue, which quenches fluorescence on the surface of the cell. In another approach, materials, which are taken up exclusively by endocytosis, can be prepared under conditions that inhibit endocytic uptake such as low temperatures and used as a negative control[21]. Although flow cytometry is useful for studying the internalisation of nanoparticles the resolution is currently too low to determine the intracellular location of a nanoparticle with accuracy.

4.2.2.2 Fluorescence widefield colocalisation microscopy

Widefield fluorescence microscopy offers the prospect of higher resolution imaging than flow cytometry, and is the method of choice for assessment of intracellular location. The technique can also be used to assess cellular uptake, but is lower throughput than flow cytometry, typically imaging tens of cells compared rather than thousands.

The best established approach for determining intracellular location is fluorescence colocalisation microscopy studies where subcellular structures and the material of interest are labelled with different fluorophores[241] and colocalisation between the two signals is observed by microscopy. Colocalisation is quantified from images by determining the pixel-by-pixel or object overlap in two different colour channels. Statistical measures such as Pearson Correlations[242] and Manders[243] coefficient have been developed to quantitatively describe colocalisation.

Organelles in the endocytic pathway have traditionally been marked by proteins known to traffic by certain pathways such as transferrin or cholera toxin B (CTB) or small molecular mass probes which accumulate in acidic organelles such as Lysotracker or Acridine Orange[13]. However these methods often suffer from poor selectivity and show variations between cell types[17]. Recent developments have

made it possible to genetically label proteins on the surface of organelles within the endocytic pathway examples, include Rab[244] and LAMP[245] proteins found on endosomes and lysosomes, respectively. This technology uses a proprietary BacMam viral transduction method to incorporate a sequence encoding these markers attached to a fluorescent protein into the host cell[246].

4.2.2.3 Super-resolution fluorescence colocalisation microscopy

The utility of conventional optical microscopy techniques for fluorescence colocalisation studies is limited by resolution. The maximum resolution of widefield microscopes is not sufficient to resolve sub-micron subcellular structures such as endosomes and lysosomes. Practically this means objects may appear to be colocalised but are merely in close proximity. A series of pioneering techniques first reported and demonstrated in the 1990's are now being developed, capable of overcoming the diffraction limit that has previously restricted resolution of optical microscopy techniques. There has been a rapid growth in these techniques, a general overview is given here, however more detailed information can be found in a series of comprehensive reviews available in this area[247-250].

The resolution of conventional light microscopes is restricted to a theoretical limit imposed by the properties of diffraction, as proposed by Ernest Abbe in 1873[251]. By this theory each object in an image consists of a series of spots, the shape of which in 3D, is described by the point-spread function (PSF) and in 2D is represented as an Airy disk. Due to the elongated shape of the PSF, the axial resolution will always be greater than the lateral resolution. Abbe states that two objects are fully resolved if the distance between them is equal to or greater than the width of the Airy disk or PSF. However for practical purposes the generally acceptable minimal resolvable distance for lateral and axial resolution is given by the Rayleigh criterion[252] based on the quantitation of intensities in the Airy disk this distance is approximately equivalent to the full width at half the maximum intensity (FWHM) of the Airy disk, as described by the formula:

$$\textbf{Lateral resolution} = 0.61\lambda/NA$$

$$\textbf{Axial resolution} = n\lambda/NA^2$$

$$NA = n.\sin\theta$$

Where:

λ = excitation wavelength

NA = Numerical Aperture
n = refractive index of the imaging medium
θ = half the angular aperture of the objective

Consequently the overall resolution is dependent on the wavelength of light and the NA. The NA is feature of the objective, which for modern microscopes can be up to ~ 1.49. This is very close to theoretical maximum based on physical restraints. It is also not possible to use shorter wavelengths than 400 nm due the optical properties of glass and incompatibility with live-cell imaging. Therefore the maximum achievable resolution of conventional microscopes is laterally between 200 and 250 nm and axially between 500 and 700 nm, this limit is referred to as the diffraction barrier. Fluorescent microscopy techniques, for imaging at resolutions below this limit, are termed super-resolution techniques.

One of the first approaches to imaging below this resolution limit was demonstrated using near-field optical microscopy[247]. The main source of the loss of resolution in an optical system is from propagation of light as it passes through a distance smaller than the wavelength of excitation light, the extent of this increases with distance from the aperture. Near-field techniques collect information close to the fluorophore, typically < 100 nm, preventing loss of resolution. Examples of these techniques are near-field scanning optical microscopy (NSOM) and total internal reflectance microscopy (TIRF) (reviewed in[253]). Although classed as super-resolution, these techniques are not suitable for imaging inside cells. The following discussion of super-resolution techniques will focus on far-field imaging techniques summarised in **Table 4.1**.

	Near-field		Far-field					
Principle	Small aperture scanning (no lens)	Evanescent wave illumination	Wide-field + deconvolution	Confocal laser scanning	Moiré effect with structured illumination		PSF shaping with saturated emission depletion	Photoswitching and localization of single molecules (pointillism)
Acronym	**SNOM/NSOM**	**TIRFM**		**CLSM**	**SIM** (HELM, PEM) **3D-SIM**	**SSIM** (SPEM)	**STED/CW-STED**	**PALM/FPALM/STORM/ dSTORM/PALMIRA**
Illumination-emission dependence	Linear	Linear	Linear	Linear	Linear	Non-linear	Non-linear	Linear
Detector	Scanning PMT/APD	Wide-field CCD/ CMOS	Wide-field CCD/ CMOS	Scanning PMT/ APD	Wide-field CCD/ CMOS	Wide-field CCD/ CMOS	Scanning PMT/APD	Wide-field CCD/CMOS
XY-resolution	20–120 nm	200–300 nm	180–250 nm	180–250 nm	100–130 nm	50 nm	20–100 nm	20–50 nm
Z-resolution	10 nm (near-field range)	100 nm (near-field range)	500–700 nm	500–700 nm	250–350 nm	N.D.	560 nm (CW-STED) to 700 nm (100 nm with z-phase mask)	100 nm (TIRF) 20–30 nm (3D-STORM, TIRF) 75 nm (BP-FPALM, in plane)
Serial z-sectioning	No	No	Yes	Yes	Yes	Yes	Yes	Yes
Z stack range	N.A.	N.A.	100 µm	100 µm	10–20 µm	N.A.	>20 µm	100 nm – few µm (BP-FPALM)
Dyes	Any	Any	Any	Any	Most conventional dyes (photostable)	Dyes require special characteristics	Dyes require special characteristics (CW-STED works with many conventional dyes)	Dyes require special characteristics
Simultaneous colors	2	3	>3	>3	3	1	2	2
Temporal resolution for 512 × 512 image	s-min	ms	ms	ms-s	ms-s	s-min	ms-min	s-min
Energy load/ intensity	Low	Low	Low	Medium	Medium	High	Medium-high	Medium-high
Live-cell imaging	Yes	Yes	Yes	Yes	Restricted (2D-TIRF)	No	Restricted	Restricted
Postprocessing required	No	No	Yes	No	Yes 9–25 raw images per slice	Yes ~100 raw images per slice	No	Yes >1,000 raw images per slice
Notes	No intracellular imaging	Restricted to region near the coverslip	Risk of artifacts; better for sparse samples		Reconstruction bears risk of artefacts	High excitation required; reconstruction bears risk of artefacts	Complex instrumentation; photobleaching	May require TIRF setup for best performance; labeling density is critical; performs better on particles and filaments as on volume stains
Dual lens implementation			**I^{5}M**	**4Pi**	**I^{5}S**		**4 Pi-STED/iso-STED**	**iPALM**
Z-resolution			70 nm	80 nm	100 nm		20–100 nm	10 nm (depth ~200 nm)

N.A., not applicable; N.D., not described.

Table 4.1 Overview of super-resolution microscopy techniques taken from[247]

There are many possible ways in which far-field super-resolution techniques can be classified. Classification is made more complex because many of the techniques can be combined. For this discussion super-resolution techniques will be placed in two categories, firstly techniques involving single molecule imaging. Included in this category are stochastic optical reconstruction microscopy (STORM) and fluorescence photoactivation localisation microscopy (PALM). Secondly those involving spatially patterned light. Included in this category are structured illumination microscopy (SIM), saturated structured illumination microscopy (SSIM) and stimulated emission depletion microscopy (STED). Additionally purely optical techniques for extending the resolution of a microscope (4Pi and I^5M) are discussed. SIM was used in this study to identify the location of nanosensors; consequently the focus of this discussion is techniques using spatially patterned excitation.

4.2.2.4 Super-resolution techniques using single molecule imaging (STORM/PALM)

Imaging a single fluorophore molecule with high resolution is not difficult; this is because there are no overlapping fluorophores, which obscure the spatial location of the molecule. However Fluorescently labelled biological samples are typically labelled with thousands, possibly millions of fluorophores at high density, which makes them difficult to resolve. This problem can be overcome by separating otherwise overlapping fluorophores by sequentially switching fluorophores on and off. This is the principle by which STORM and PALM (also referred to as pointillism microscopy) achieve super-resolution imaging. In order to further understand how this principle works, it is helpful to consider a number of objects, which are less than 200 nm apart. It would be possible to resolve them if every object was labelled with a different fluorophore, this is because the resolution of objects with different spectral characteristics is not limited by diffraction. However if you are for example labelling proteins on the surface of an endosome, it is not possible to label each protein individually. In single molecule super-resolution microscopy, each fluorophore is switched on stochastically in a way that it can be individually imaged, localised and switched off. This process is then repeated so that the coordinates of each molecule can be identified. The information is then used to reconstruct the image.

Super-resolution techniques developed using this principle are STORM and PALM[254]. Spatial resolutions of between 20 and 50 nm are possible by this technique. These techniques require specialised photoswitchable fluorophores,

which can be activated and deactivated, within a diffraction-limited region. Consequently they are not suitable for sensing applications using the fluorophores discussed in this work. An additional consideration is that approximately 1,000 raw images are required to construct an image. The time and light exposure this requires means that these techniques are currently severely restricted in their applications for live-cell imaging.

4.2.2.5 Super-resolution techniques using spatially patterned light (SIM/STED)

These are super-resolution techniques, which utilise interactions between a sample and sub-micron diffraction features in excitation light to generate an image. Two methods are discussed here SIM (used in this work) and STED.

SIM is a super-resolution technique, which functions by this method and can be used to reach resolutions of approximately half of that of conventional diffraction limited microscopes. It is one of the most flexible super-resolution techniques commercially available having been first reported by Gustafasson an co workers in 2000[255].

In SIM, the sample is excited by a fine sinusoidal pattern of light, which has the appearance of a series of parallel stripes. During excitation, this patterned illumination light is superimposed onto light emitted from the sample. Critically there is interference between the two, resulting in a third characteristic form of light called Moiré fringes. Moiré fringes have a lower spatial frequency than the structures in the sample; this means that the light can be transmitted by the objective. Variations in all the different patterns can be used to extract high spatial frequency information using computer algorithms, which estimate experimental parameters, resulting in an overall increase in resolution. As no signal variation is observed for samples parallel to the illumination light, stripes are moved across the sample in different orientations. Typically 3 different orientations with the stripes moved across the sample at 3 - 5 different positions are required. This means, in order to construct an image of an 8 μm cross-section in a mammalian cell, typically 1,000 raw images are acquired. The resolution is determined by how fine the illumination light projected on to the sample is, which is limited by diffraction. Using light as close to the diffraction limit as possible, it is possible to achieve a two-fold increase in lateral resolution. 3D-SIM achieves a two-fold increase in axial resolution, when an interference pattern is introduced to the sample along the z-axis in a similar way. Therefore the overall resolution achievable by 3-D SIM is ~ 100 nm laterally and ~ 250 nm axially.

The advantages of 3D-SIM are that it is does not require any specialised methods for labelling fluorophores and is suitable for multicolour applications. Live cell imaging is also favourable with 3D-SIM compared to other techniques as it requires less overall excitation laser power and has been used in studies combining this technique with TIRF[256]. It also currently offers the highest frame rates out of all the super-techniques making it the most suitable super-resolution technique for temporal imaging.

One of the first examples of the application of 3D-SIM imaging in biology was in a study by Schermelleh *et al*[257] where structures in the nucleus, chromatin, nuclear lamina and nuclear pore complexes were labelled simultaneously in fixed C2C12 myoblast cells. This work showed it is possible to see invaginations from the nucleus during mitotic prophase, these take the form of tubular extensions, which have previously only been seen by electron microscopy. This pioneering work was done on one of the first custom 3D-SIM microscopes developed at the University of Munich in 2008 and led to the development of the commercial Deltavision OMX Blaze system used to acquire the images in this study. The commercial availability of these systems offers the prospect of probing new mechanisms for intracellular transport.

Stimulated emission deletion (STED) microscopy is another super-resolution technique based on spatially patterned excitation light. STED works by using a combination of two lasers, one laser to excite the sample and another (STED laser) to supress fluorescence emission from around the point of fluorophore excitation[258]. In this process photons in the excited state are returned to the ground state by a process called stimulated emission. The STED laser is a doughnut shape which supresses fluorescence emission around a PSF. In this way spatially patterned light is used for suppression emission rather than excitation as the case for SIM. Spatial resolutions of between 20 and 100 nm are achievable by this method. Fluorophores with high photostability are required for STED imaging.

4.2.2.6 Optical super-resolution techniques (4Pi/I^{5}M)

4Pi and I^{5}M are purely optical techniques in the sense that they do not involve specialised fluorophores or photophysics to enhance resolution. For this reason they can be combined with conventional widefield and confocal techniques. In conventional microscopes light is lost because the microscope objective only registers light from one side of the sample. The 4Pi and I^{5}M techniques use

additional objectives to collect light from a wider angle to effectively increase the aperture of the objective. 4Pi microscopy was developed by Stefan Hell and co workers in the 1990s[259]. This technique uses a combination of two objectives for focusing excitation light as one wave on to the sample; emitted light is then combined for detection. In effect the power of the objectives is combined in way that the NA is doubled resulting in resolutions of ~ 100 nm. I^5M developed by Gustafasson and co workers is capable of achieving similar resolution and works on a similar principle to but in a widefield configuration as opposed to a confocal configuration[260].

4.2.2.7 Subcellular fractionation

Another method for determination of the intracellular location of a particle is subcellular fractionation; this involves lysing a cell followed by isolating fractions containing the organelles of interest and assaying the contents[261-263]. This technique is based on separation by density gradient fractionation. The fraction containing specific organelles can be assayed by detecting proteins associated with endocytic organelles using fluorescence or western blots. In addition to this, markers, which accumulate in specific organelles, can be used for example Transferrin for early endosomes. The limitations with this approach aside from being time consuming, is that obtaining fractions with high purity requires meticulous preparation methods and stringent controls. It also not possible to observe the dynamic events of trafficking by this method and requires sample destruction/sacrifice.

4.2.3 Functional assays for modulating intracellular pH

These methods involve modulating an aspect of cellular function utilising a pharmacological inhibitor to generate a measurable response. In the case of nanosensors designed to be delivered into the endocytic pathway modulating the pH in endosomes and lysosomes is one way in which the intracellular location of the sensor can be determined, and a also a way of testing the response of sensors in live-cell environment.

Previously reported pharmacological inhibitors for modulating pH inside a cell are summarised in **Table 4.2.**

Type	Pharmacological Agent	Conditions	Cell types	Reference
Lysomotropic agents	Chloroquinine	100 µM, 0 min 200 µM, 20 min 500 µM, 30 min	K562 HUVEC COS-7	*264-267*
		100 µM	293T	
		20 µM	HeLa	
	Ammonium chloride	50 mM, 30 min	A459	*268*
	Amantadine	1 mM	HeLa	*267*
Carboxylic ionophores	Monesin	50 µM, 30 min 4°C 25 µM	HepG2 293T	*269*
	Nigericin	10 µM 15-20 min 10 µg/ml	CHO HepG2	*183*
V-ATPase Inhibitors	Bafilomycin A1	125nM, 30 min 175nM 200 nM 1 h 200 nM, 1 h	Hela HepG2 HUVEC COS-7	*265,270,271*
	Concanamycin A	100 µM	HepG2	*224*

Table 4.2 Pharmacological methods for modulation of intracellular pH in the endocytic pathway. *Adapted from*[30]*.*

Pharmacological modulators of the endocytic pathway can be placed in three classes based on the mechanism of action. All of these methods result in a raising of pH within endocytic vesicles. Firstly, lysomotropic agents, which are weak bases that selectively, accumulate in endosomes and lysosomes. These agents become protonated in the acidic environment, effectively buffering the pH in endocytic vesicles. The second class are carboxylic ionophores, which facilitate the exchange of protons across the cell membrane in exchange of ions such as K^+ and Na^+. The third and newest class are vacuolar (V-ATPase) inhibitors. The regulation of pH in the endocytic pathway is primarily governed by V-ATPases on the surface of endocytic vesicles; these are enzymes, which are molecular motors that translocate protons against a concentration gradient into the lumen of the endocytic vesicle. The most common type of inhibitors in this area is the bafilomycins and concanamycins, which bind the c subunit of V_o part of the V-ATPase[272]. These inhibitors have been particularly well studied as V-ATPases have

been targets for antibiotics and implicated in diseases including osteoporosis, distal renal tubular acidosis and sensorinueral deafness[272].

In most studies utilising these inhibitors, cells are pre-treated for a period of time. The time of incubation is dependent on cell type and the experimental context. Shorter periods of time are likely to result in a transient change in intracellular pH whereas longer incubation times are likely to result in a longer-term effect. It should also be considered that raising the pH for extended time periods will result in a loss of cell viability, this may be effected by altering signalling pathways or by destabilising endocytic vesicles through creation of an osmotic imbalance.

4.3 Materials and Methods

4.3.1 Materials

Regents: Phenol red-free Dulbecco's modified Eagle's medium (DMEM) media. Eagle's minimum essential medium (MEM), (Sigma, UK). Fetal bovine serum (FBS). L-glutamine. Trypsin (0.25 % w/v) - ethylenediaminetatraacetic acid (EDTA) (0.02 % w/v) (1X) supplemented with inorganic salts, phenol red and D-Glucose. Phenol red-free alpha minimum essential medium with ribonucleosides, deoxyribonucleosides, 4 mM L-glutamine and 1 mM sodium pyruvate. Murine granular monocyte colony stimulating factor (GM-CSF). (3-acrylamidopropyl) trimethylammonium (ACTA) (Sigma, UK). Phosphate buffered saline (PBS). Paraformaldehyde. Penicillin-Streptomycin 100x (10,000 units penicillin and 10 mg streptomycin/ml) (Sigma, UK). Bafilomycin A1. CellLights Early Endosomes-GFP, BacMam 2.0. CellLights Lysosomes-GFP, BacMam 2.0. Lysotracker Blue DND-22. Anhydrous DMSO (Sigma, UK). SlowFade gold anti-fade reagent. Hoechst 3342. Alexa Fluor 488 Phalloidin. Trypan Blue.

All reagents were supplied by Invitrogen, UK unless otherwise stated.

Aliquots of solutions of FBS and L-Glutamine were stored at – 20^{o}C. Aliquots were thawed at room temperature prior to use. Complete cell culture media and Trypsin-EDTA solutions were kept at 4^{o}C and used within 3 months. No antibiotics were used for cell culture.

4.3.2 Methods

4.3.2.1 Delivery of polyacrylamide nanosensors

4.3.2.1.1 General cell culture

Sensors were delivered to four cell lines (MRC-5, HeLa, NIH/3T3 and JAWS II). All cell lines were obtained from American type culture colony (ATCC).

HeLa, MRC-5 and NIH/3T3 cells were cultured by the same method. HeLa and NIH/3T3 cells were maintained and cultured in DMEM media supplemented with 10% FBS and 2 mM glutamine in a cell culture incubator at 37^{o}C in a 5% CO_2 with a humidified atmosphere. MRC-5 cells were maintained under the same

conditions in MEM media supplemented with 10% FBS, 1% non-essential amino acids (NEA), 1% penicillin-streptomycin and 2 mM L-glutamine. Cells were passaged before confluence (2-3 days) by trypsin. Briefly for T-75 flasks, media was removed and replaced by 3 ml of trypsin (0.25 % w/v) - EDTA (0.02 % w/v) and left at 37°C / 5% CO_2 until cells detached (~ 5 – 10 minutes). 5 ml of culture media was then added to deactivate trypsin and cells were transferred to a 20 ml vial and centrifuged at 300 g for 5 minutes (acc/dec = 3). The supernatant was removed and cells were resuspended in cell culture media. Cells were passaged to the desired cultivation ratio (typically 1: 3) and transferred to a T-75 flask to a final volume of 15 ml.

JAWS II cells were maintained and cultured in Alpha minimum essential medium with ribonucleosides, deoxyribonucleosides, 4 mM L-glutamine, 1 mM sodium pyruvate and 5 ng/ml murine GM-CSF supplemented with 20% v/v FBS in a cell culture incubator at 37°C in a 5% CO_2 with a humidified atmosphere. Cells were passaged before confluence (3-5 days) by trypsinisation. Briefly for T-75 flasks, media was removed and replaced by 3 ml of trypsin (0.25 % w/v) - EDTA (0.02 % w/v) and left at 37°C / 5% CO_2 until cells detached (~ 5 – 10 minutes). 5 ml of culture media was then added to deactivate trypsin and cells were transferred to a 20 ml vial and centrifuged at 300 g for 5 minutes (acc/dec = 3). The supernatant was removed and cells were resuspended in cell culture media. Cells were passaged to the desired cultivation ratio (typically 1: 2) and transferred to a T-75 flask to a final volume of 15 ml.

All cells were tested for viability by trypan blue staining between passages.
Trypan blue staining was done by mixing equal volumes of a cell solution with a 0.4% Trypan Blue solution in PBS and observing cells under a microscope. Cells were discarded if viability was observed to be less than 80%.

All cells were cultured through a minimum of 2 passages following reanimation before use in experiments. Cells were discarded after a maximum of 25 total passages.

All cells were frozen for long-term storage at -80°C in 1 ml of 10% DMSO at a concentration of ~ 1 x 10^6 cells/ml. Cells were reanimated prior by transferring frozen aliquots into a T-75 flask containing cell culture media.

4.3.2.1.2 Nanosensor uptake

Cells were seeded into Lab-Tek 1 chambered cover glass sides (Thermo Fisher Scientific, UK) or 35 mm glass bottomed dishes (Intracel, UK). Cells were seeded at a concentration of 2.5 x 10^4 (200 µl media) for Lab-Tek chambered cover glass and 5 x 10^4 (500 µl media) for 35 mm dishes. Cell viability was tested prior to seeding by trypan blue staining, cells were seeded if > 95% viability was observed. Cells were left overnight in preparation for nanosensor uptake the following day.

Dried nanosensors were resuspended in cell culture media or PBS to obtain a stock solution of nanosensors at a concentration of 10 mg ml^{-1}. Nanosensors were sonicated until a clear solution was seen (~ 15 – 60 minutes). The stock solution was added to cells grown in a suitable vessel for imaging to a final concentration of 100 µg ml^{-1}. For LabTek 1 chambered cover slides, 2 µl of nanosensor stock was added to 200 µl of cell growth media whereas for 35 mm glass bottomed dishes, 5 µl of nanosensors were added to 500 µl of media. Nanosensors were left to incubate with cells for 24 h. Cells were then washed 5 times with PBS to remove surface bound nanosensors and cell culture media was replaced with phenol-red free media of the same composition prior to imaging.

pH measurements were then performed according to the methods described in **Chapter 3.**

4.3.2.1.3 Fabrication of positively charged nanosensors

Positively charged nanosensors were synthesised by post-conjugation utilising the generalised procedure described in **Chapter 2 Section 2.3.2.1** and incorporating positively charged monomers with (3-acrylamidopropyl) trimethylammonium (ACTA) into the acrylamide monomer solution. 5% wt. of acrylamide was replaced with ACTA. The quantities used are summarised in **Table 4.3.**

Functional Group	Functionalisation reagent	Monomers (mg)		
		Acrylamide	N, N methylene bisacrylamide	Functionalisation reagent
Blank	-	540.0	160.0	-
Amine	APMA	529.5	160.0	27.2
Amine/Ammonium	APMA/ACTA	630.0	160.0	35.0/35.0

Table 4.3 Reagent quantities used for fabrication of positively charged nanosensors.

4.3.2.2 MTS Assay for cell viability

Cell viability following uptake was assessed by MTS assay for cell proliferation using Cell Titer 96 AQ_{ueous} Once Solution Cell Proliferation Assay System (Promega). This is a colorimetric assay for determining the number of viable cells. The solution comprises a tetrazolium compound [3-(4,5-dimethyl-2-yl)-5-(3-carboxymethoxyphenyl)-2-(4-sulfophenyl)-2H-tetrazolium, inner salt; MTS] and an electron-coupling reagent (phenazine ethosulfate; PES), which is reduced to a coloured product (formazan) in the presence of dehydrogenases produced in metabolically viable cells (**Figure 4.3**). The colour change in formazan is measured by absorbance[273].

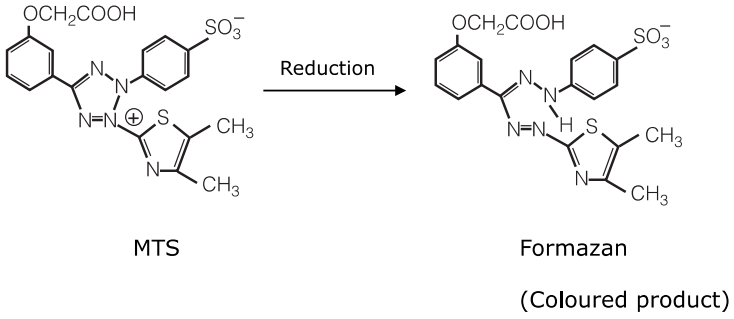

Figure 4.3 *Chemical basis for the MTS assay.* MTS is reduced to formazan by dehydrogenase enzymes (NADPH or NADH) found in metabolically active cells.

For viability assays, cells were cultured in 96 well plates in 100 µl of media until 70% confluent. Nanosensors were then added to the cells at the required concentration for a specified time period maintaining the same overall volume. 20 µl of MTS solution was subsequently added directly to the cells for 2 h. Absorbance was measured at λ490 nm using a plate reader (FLUOstar OMEGA

BMG LABTECH). Background was removed by measurement of media containing wells without cells. Measurements were normalized against cells without any nanosensor treatment. All measurements were done in quintuplet.

4.3.3 Assessment of cellular internalisation and intracellular location

4.3.3.1 Flow cytometry

Flow cytometry analysis was done in MRC-5 cells. MRC-5 Cells were grown in 6 well plates until 70% confluency. The uptake experiment was then performed under identical conditions to those used for imaging. The nanosensors used for uptake analysis were labelled with TAMRA fluorophores alone.

After 24 h, uptake sensor containing media was removed and cells were washed a minimum of 5 times with PBS. Following the final wash, 3 ml of trypsin (0.25 % w/v) - EDTA (0.02 % w/v) solution was added and left at 37°C / 5% CO_2 until cells detached (~ 5 – 10 minutes). The cell suspensions were transferred into FACS tubes containing ~ 2 ml of media. The tubes were then centrifuged at 300 g for 5 minutes acc/dec = 3. The supernatant was removed; cells were resuspended by vortexing in PBS and centrifuged again. The supernatant was removed and cells were fixed in 400 µl fixing solution (0.5% formaldehyde in PBS). Samples were protected from light and left at 4°C for a maximum of 7 days prior to analysis.

Samples were analysed using a flow cytometer (Altra: Beckman Coulter, High Wycombe, UK). Samples were interrogated with a λ568 nm laser. A minimum of 50,000 cells were recorded for each experiment and background was removed by measuring cells without any nanosensors. Data was analysed using Walter and Eliza Analysis Software: Electrical and Lucid (WEASEL) version 2.4 (http://www.wehi.edu.au/cytometry/WEASEL. html).

4.3.3.2 Fluorescence colocalisation microscopy

Fluorescence colocalisation microscopy was done in HeLa cells using widefield and super-resolution colocalisation microscopy. Two methods were used for labelling endosomes/lysosomes, Lysotracker and CellLights.

For labelling with Lysotracker, cells were incubated with medium containing Lysotracker Blue DND-22 (373/422 $\lambda_{Ex}/\lambda_{Em}$). The stain was supplied in DMSO at a concentration of 1 mM and diluted to an optimised working concentration of 100

nM in growth media. Cells were incubated for 30 – 60 minutes and visualised using microscopy.

For labelling with CellLights, Early endosomes (Rab5a) and lysosomes (LAMP1) were labelled with Early Endosome-GFP and Lysosome-GFP constructs respectively. Cells were cultured until 50% confluent. CellLights reagent was supplied at a concentration of 1 $x10^8$ viral particles per ml. Solution was added to cells to an optimised viral particle to cell ratio of 40 and left overnight. Viral particles were the removed and the cells were imaged live.

4.3.4 Testing pH-responsiveness of nanosensors

Bafilomycin A1 (inhibitor of endosomal acidification) was added directly to cells following uptake of nanosensors. Cells were treated for 30 minutes at an optimised final concentration of 200 nM, and imaged immediately.

4.3.5 Imaging acquisition

4.3.5.1 Widefield fluorescence microscopy

Cells were imaged using a Deltavision Elite microscope (University of Melbourne) using the same settings as described in **Chapter 3 Section 3.3.3**. Cells were imaged live unless otherwise stated. Colocalisation analysis was done using Volocity software version 6.1.1 and FIJI open source software.

4.3.5.2 Confocal microscopy

The microscope used was a Leica TCS SP2 SE confocal microscope equipped with Argon and Krypton laser lines at λ488 and λ568 nm respectively as well as a UV lamp for excitation at shorter wavelengths. Samples were imaged using 63x oil immersion objective. Samples were fixed before imaging.

4.3.5.3 Super-resolution microscopy

Super-resolution images were acquired using a three-dimensional structured illumination microscope (3D-SIM) OMX blaze imaging system (Applied Precision, GE Healthcare).

Samples were imaged using a Plan Apo N 60x NA 1.42 oil immersion objective with a working distance of 0.15 mm. Samples were excited with a 6 colour InsightSSI illuminator with laser lines of λ405, λ488 and λ658 nm and detected with the corresponding single-band pass filters of λ435/31, λ528/48 and λ609/37

nm. The system was equipped with 4 sCMOS cameras with an effective pixel size of 512 x 512, maximum frame rate of 400/s. Images collected were set to a pixel size of 8 nm. Images were reconstructed and analysed using Deltavision OMX SoftWorx software. Fixed specimens were used for imaging. SlowFade was added to the samples to supress photobleaching.

In order to assess the power of the imaging techniques, cells were fixed and labelled using fluorophores stains for actin the nucleus. The following procedure was used for staining:

Cells were fixed prior to staining by immersing cells in a 4% solution of paraformaldehyde in PBS for 10 minutes. The samples were then washed with PBS a minimum of three times. F-actin and the cell nucleus were stained using phalloidin and Hoechst 3342 respectively. Cells were stained following fixation. For phalloidin staining a stock solution in methanol was added to the cells to a final concentration of 0.6 μM, a stock solution of Hoechst 3342 stain in PBS was added simultaneously to a final concentration of 1 mg ml^{-1}. Samples were periodically checked until adequate staining was achieved (~ 20 minutes).

4.4 Results and Discussion

4.4.1 Enhancement of nanosensor uptake

Positively charged Post-conjugated sensors were used for uptake studies. These sensors were synthesised as shown in **Figure 4.4** and characterised by the light scattering techniques described in **Chapter 2** to have a hydrodynamic diameter of 102.7 nm and Zeta potential of 16.7 mV.

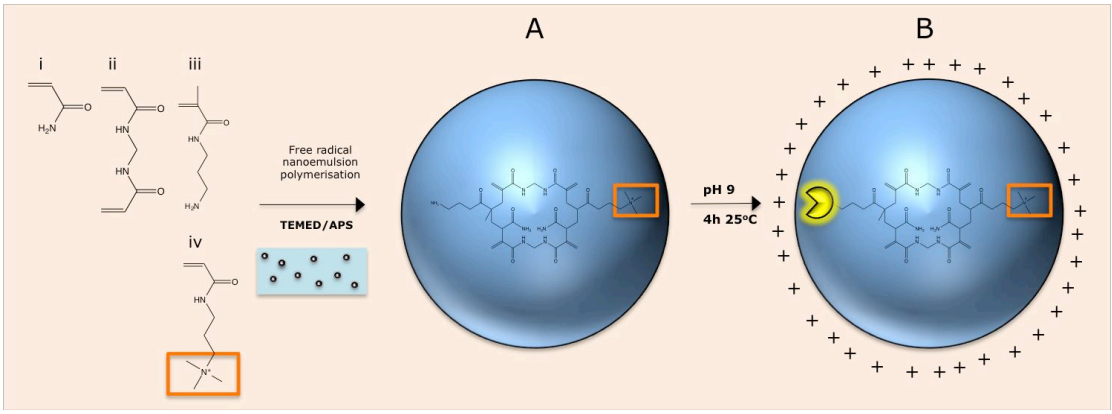

Figure 4.4 *Diagram of synthesis of positively charged nanosensors.* (i) acrylamide (ii) N, N methylenebisacrylamide, (iii) N-(3-Aminopropyl)methacrylamide hydrochloride (APMA), (iv) (3-acrylamidopropyl) trimethylammonium (ACTA). (A) Synthesis of amine-functionalised polyacrylamide nanoparticle. (B) Conjugation of fluorophores to create a nanosensor.

To test if these sensors would be internalised by endocytosis, MRC-5 cells used as a model cell line, were exposed to sensors at a concentration of 100 µg ml^{-1} and imaged by widefield fluorescence microscopy. Although some uptake was observed, this was limited **Figure 4.5Bi,ii**). Moreover the signal was very weak and likely to result in unreliable measurements from image analysis. This was unexpected because cationic polyacrylamide sensors with a zeta potential of between +10 and +20 mV have been previously reported to be adequately taken up into a variety of cell types including HepG2[183], primary human foreskin fibroblasts[117] and 9L glioma cells[180]. This suggests poor uptake may be due to a factor related to the cell type. In an effort to promote uptake in MRC-5 cells, the surface charge of the sensors was increased. This was achieved through incorporation of positively charged acrylamide monomers (ACTA) into the sensor. By this method the zeta potential of the sensors was approximately doubled to + 36.3 mV without any effect on the overall size of the sensor. This resulted in increased uptake in MRC-5 cells as seen by widefield microscopy (**Figure 4.5Biii,iv**)**.** To confirm this finding in a more representative way, cell association was quantified by flow cytometry. Strongly cationic sensors were measured to have 85.4% cell association compared to weakly cationic sensors, which only had an association of 0.62% (**Figure 4.5A**). Although this is convincing evidence that there is increased uptake for strongly cationic sensors, some caution must be taken when considering the absolute values. This is because flow cytometry is limited in the sense it does not distinguish between sensors, which are internalized, and those that are merely bound to the surface (hence the term 'cell

association'). Several wash steps were incorporated to remove surface bound sensors, however this is unlikely to remove all the sensors. As a result the cell association value of 85.4% does not indicate 85.4% of sensors are internalized. However considering this result in conjunction microscopy images, there is convincing evidence to suggest there is increased internalisation due to surface charge. To test if this finding translates to other cell types of interest in this study, uptake in HeLa, 3T3 and JAWS II cells was assessed by widefield fluorescence microscopy. Adequate uptake in all these cell types was observed as indicated in **Figure 4.6A-D.** For the purposes of this study the most critical factor is not the extent of uptake but that there is adequate signal to produce a reliable measurement. This is because measurements performed on images with low signal are prone to errors. Consequently flow cytometric analysis was not performed for all cell types, but through qualitative assessment, delivery was deemed to be satisfactory for performing measurements.

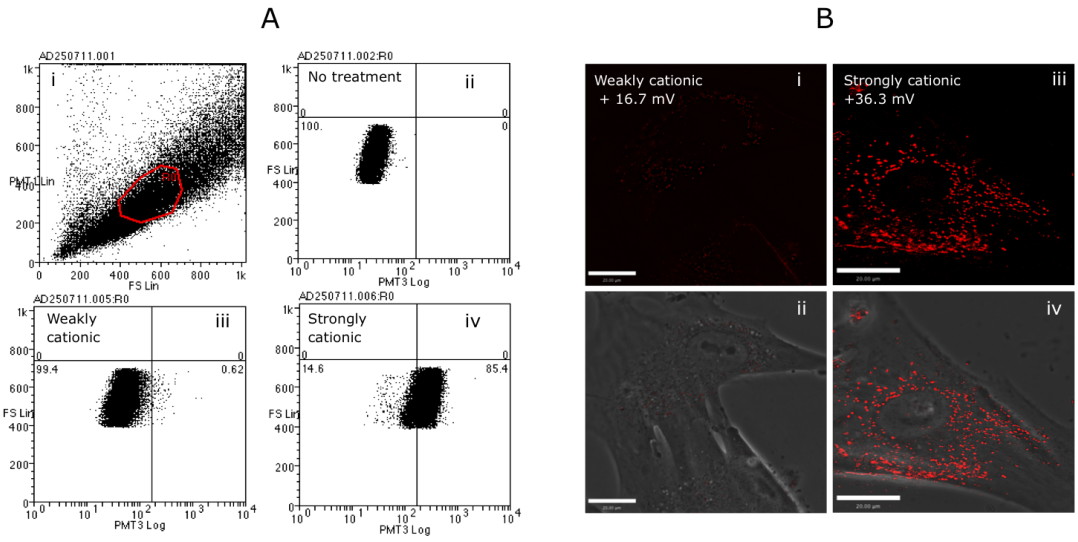

Type of Nanosensor	Zeta Potential (mV)	% Cell association
Weakly cationic	+ 16.7	0.62
Strongly cationic	+ 36.3	85.4

Figure 4.5 *Effect of surface charge on nanosensor uptake in MRC-5 cells after 24 h exposure.* (A) Cell association measured by flow cytometry. (i) Forward (x-axis) and side scatter (y-axis) graph of cells. Red region represents gated region taken forward for measurement. (ii) Cells with no sensors (control). iii) Cells with weakly cationic sensors. iv) Cells with strongly cationic sensors. (ii, iii,iv) x-axis represents fluorescence measured from sensors (λ565 ± 10), y axis is forward scatter. (B) Qualitative assessment of cell uptake by widefield fluorescence microscopy. Representative images MRC-5 fibroblast cells of following 24h exposure to (i,ii) weakly cationic sensors and (iii,iv) cationic sensors. (ii, iv) Show a brightfield overlay. Scale bar = 20 μm.

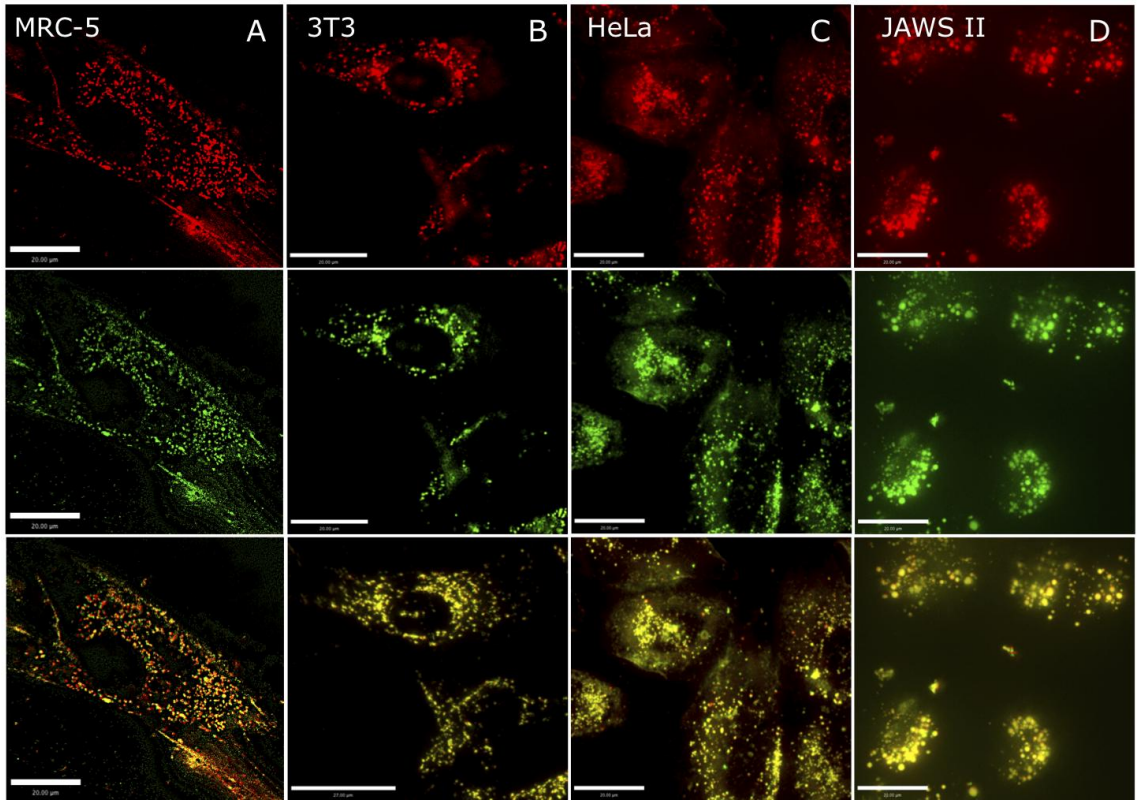

Figure 4.6 *Uptake of strongly cationic nanosensors in different cell types after 24 h. Representative images, taken using widefield deconvolution microscopy.* (A) MRC-5, (B) 3T3, (C) HeLa, (D) JAWS II cells. Reference channel (red), indicator channel (green), merged channel (yellow). Scale bar = 20 µm (unless otherwise stated).

In the wider context, ACTA incorporation into polyacrylamide nanosensors has been observed to promote uptake in HepG2 cells by Sun *et al*[120]. In this study nanosensors of + 25.8 mV and diameter of 100 nm (measured by DLS) were seen to be uptaken after 5 hours, whereas no detectable fluorescence was observed from weakly charged sensors (-9.5 mV, 50 nm). Interestingly approximately double the amount of ACTA in terms of wt.% was used to synthesise nanosensors used in this study but this resulted in sensors with a weaker Zeta potential than the sensors fabricated in this work. This could be because of differences in the polymeric architecture of the particles, which would determine the number of exposed charged groups on the surface of particle. Possible reasons for this could be differences in the overall ratio of ACTA, acrylamide and cross-linker ratios used for synthesis. In this context, it would be interesting to determine whether or not this has an effect on the endocytic route employed to gain entry to the cell.

4.4.2 Impact of nanosensors on cell viability

The intended application for pH nanosensors developed in this study requires sensors to mirror the transport of nanomedicines through the intracellular trafficking pathway. In most cases, nanocarriers are required to pass through the trafficking pathway without unduly affecting any aspect of natural cell function (aside from the drug target). Consequently it is important that the sensors also act in this way. Another important consideration is that viability is likely to be linked to the amount of particles uptaken, which will be determined by the concentration of nanosensors exposed to cells. This is a trade-off because using low concentrations is likely to minimise toxicity whilst high concentrations will maximise uptake and S/N. In order to address both these points, cell viability after treatment with strongly cationic nanosensors at different concentrations was assessed by an MTS assay for cell proliferation (indicator of viability) using MRC-5 cells as a model cell line (**Figure 4.7A**).

The effect of nanosensors on cell viability was tested over 2 h, 4 h and 24 h at concentrations up to 5 mg ml^{-1}. Considering strongly cationic nanosensors, there is clearly a proportionate decrease in cell viability with increasing concentration after 2 h (**Figure 4.7A**), however after 4 h there is an improvement in cell viability with a viability of less than 80% observed only for concentrations above 3 mg ml^{-1} (**Figure 4.7B**)**,** this appears to continue, and after 24 h there is an even further improvement with all concentrations up to 5 mg ml^{-1} showing

viability of greater than 80% (**Figure 4.7C**). This suggests there is an improvement in cell viability over time.

A possible explanation for this is that the introduction of large amounts of foreign material into the cell results in displacement of the cells natural trafficking pathways causing an initial loss in cell viability, whilst at later time points material may have been transported to the final intracellular destination causing less disruption. It is generally thought material is transported to lysosomes after 2 h at the earliest[11,26]. Therefore if most sensors are delivered to lysosomes this may be the reason for increasing cell viability. This theory implies the trend is due to a factor dependent on internalisation of sensors. To test whether or not this is the case, viability was assessed following treatment with uncharged sensors, which show a lesser extent of internalisation. An increase in cell viability over time was observed at 2 h (**Figure 4.7A**) and 24 h (**Figure 4.7C**), suggesting an interaction of the sensors outside the cell is in fact, causing the increase in viability. However this was not seen after 4 h (**Figure 4.7B**), hence the results are inconclusive with regards to an explanation for the change in viability with time. An additional consideration is that the MTS assay is an indicator of activity of cellular reductase enzymes, but this may not always an indicator of cell viability as cells can respond to stress by transiently increasing reductase[274].

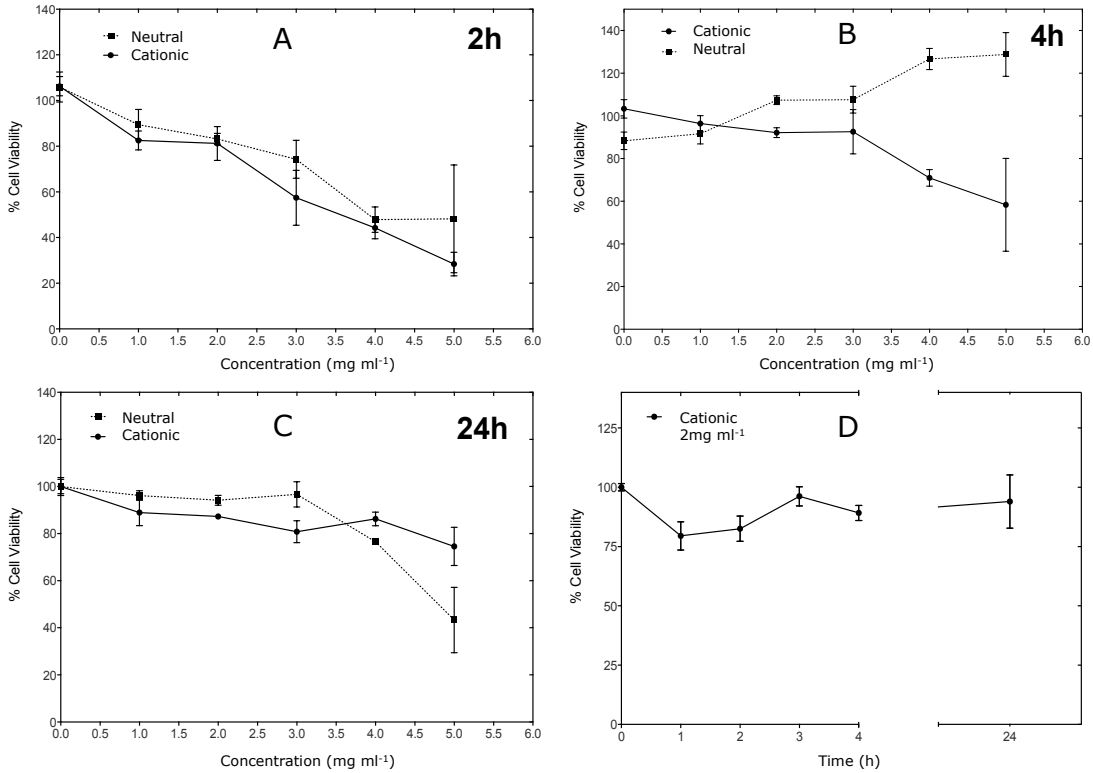

Figure 4.7 *Effect of nanosensors on viability of MRC-5 cells assessed by an MTS assay.* Viability is normalised against untreated cells. Cell viability is indicated by the activity of cellular reductase enzymes. A-C Effect of concentration on cell viability after (A) 2 h, (B) 4 h and (C) 24 h. (D) Cell viability over 24 h at a concentration of 2 mg ml-1.

To confirm the MTS results are valid, a rudimentary assessment of cell viability was made by qualitatively assessing the morphology of cells after nanosensor treatment at a concentration of 2 mg ml^{-1} by flow cytometry and microscopy (**Figure 4.8A,B**). For flow cytometry, side scatter and forward scatter plots (measures of the size and granularity) of cells with and without nanosensor treatment were compared. This shows there is no effect on the cell (**Figure 4.8A**). Additionally no obvious changes in the shape or morphology of cells were observed when cells treated with sensors were visualised by microscopy (**Figure 4.8B**).

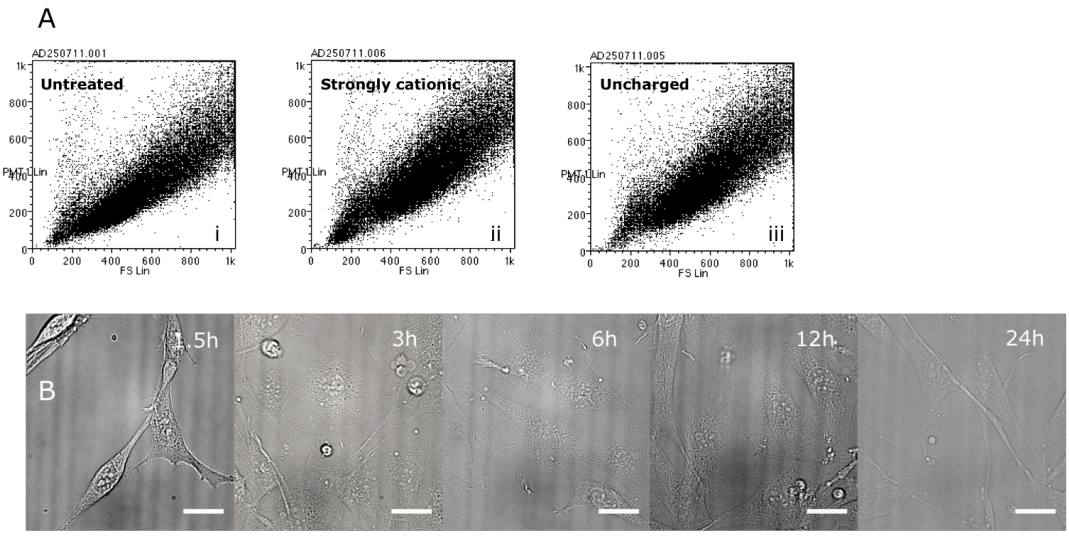

Figure 4.8 *Effect of nanosensors on viability of MRC-5 cells assessed by microscopy and flow cytometry.* (A) Cell viability assessed by flow cytometry. (i) Untreated cells, (ii) cells treated with strongly cationic sensors (2 mg ml^{-1}) for 24 h, (iii) cells treated with neutral sensors. X-axis is forward scatter, y-axis is side scatter. (B) Brightfield images of cells treated with strongly cationic nanosensors (2 mg ml^{-1}) for 24 h. Scale bar = 12 μm.

For the purposes of the study, the most important finding from these results is that treatment of MRC-5 cells of less than 2 mg ml^{-1} resulted no significant loss of cell viability after 24 h **Figure 4.7D**). However it is important to note that this is an approximate assessment of viability, as like with all assays for cell viability, the MTS assay only measures one indicator of cell function. For detailed assessment other methods should be used such as a lactate dehydrogenase (LDH) assay or propidium iodide staining (test for membrane integrity).

Additionally it is also not clear how these findings translate to other cell types of interest in this study (3T3, HeLa and JAWS II cells). In order to mitigate the risk of sensors having an impact on natural cell function, in most cases concentrations of 0.1 mg ml^{-1} were used. This was found to result in adequate S/N ratios for measurement.

4.4.3 Intracellular pH measurement

Having established a method for delivering sensors to cells by endocytosis without any effect on cell function, measurements were performed to evaluate the most suitable nanosensor design for biological measurements.

4.4.3.1 Evaluation of nanosensor design

In order to determine the most appropriate nanosensor design, HeLa cells were imaged following 24 h uptake of three different sensor designs (NS_{ds}, NS_{esc}, NS_{end}) (**Figure 4.9**) under the same conditions**.** Although a calibration of NS_{end} sensors was obtained by fluorometry in **Chapter 2**, signal intensity was too weak to perform an adequate calibration by widefield microscopy. However reliable calibration and measurements were made with NS_{ds} and NS_{esc} sensor designs utilising the methodology optimised in **Chapter 3**. Typically more than 90% of pixels returned pH values within the calibration range in most images for both sensors. NS_{ds} and NS_{esc} returned average pH values of 4.7 and 5.6 respectively (**Figure 4.10A,B**). Interestingly, NS_{ds} sensors report higher pH values than NS_{esc} sensors. A possible explanation for this is that NS_{ds} sensors cannot be weighted due to the absence of a reference fluorophore. Hence the increase in pH may be attributed to a few sensors reporting high pH. Considering the methodology in **Chapter 3**, which demonstrates the importance of weighting pH it is likely the NS_{esc} delivers the more useful result. The key advantage of weighting that it is a means of quantifying the proportion of sensors, which report a pH value. This is significant in the context of using sensors for developing biological insights, because it yields information regarding the proportion of sensors in an intracellular location. Based on this rationale, the NS_{esc} sensor design was determined to be the optimal sensor design for intracellular measurement. Measurements in multiple cell types using the NS_{esc} design are shown in **Figure 4.11.** These values suggest the majority of sensors are located in acidic parts of the cell. The punctate distribution in the corresponding colour maps suggests sensors are likely to be in vesicles. These are likely to be lysosomes based on previously reported values for lysosomal pH reported in the literature[54], however further work is required to confirm this.

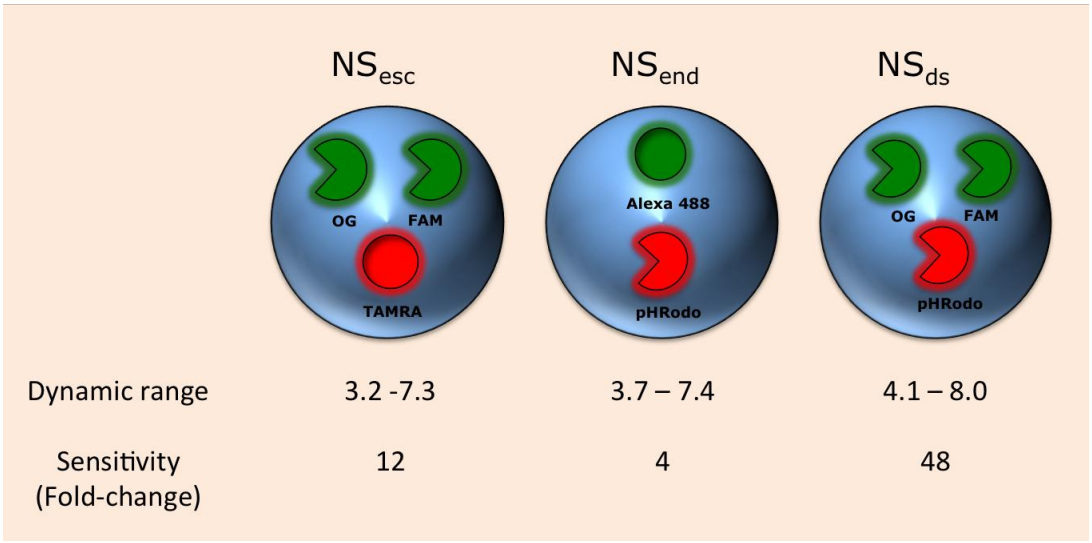

Figure 4.9 *Overview of pH nanosensor designs in this study.*

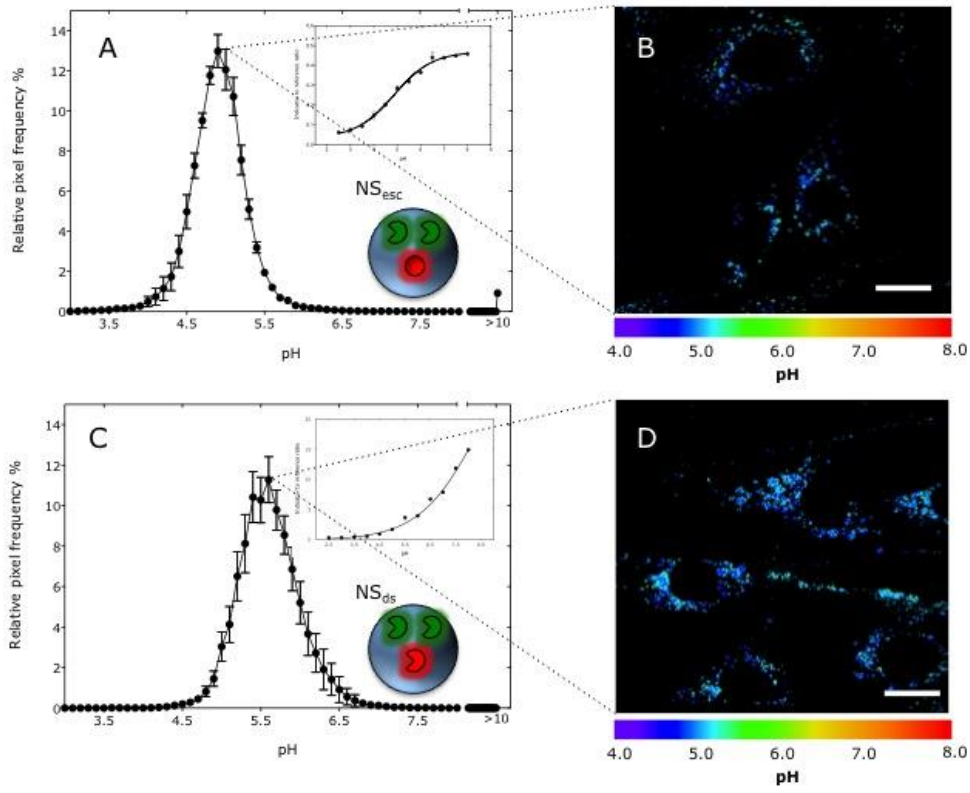

Figure 4.10 *pH measurements from NS_{esc} and NS_{end} sensor designs.* Images are taken in 3T3 fibroblast cells. (A) pH measurement using the NS_{esc} design. Inset is calibration, x axis = pH, y axis = intensity ratio. (C) pH measurement using the NS_{ds} design. Inset is calibration. For pH measurement n = ~ 50 cells, for calibration n = ~ 20 cells, error bars = S.D. (B,D) Corresponding false colour pH maps. Scale bar = 15 µm.

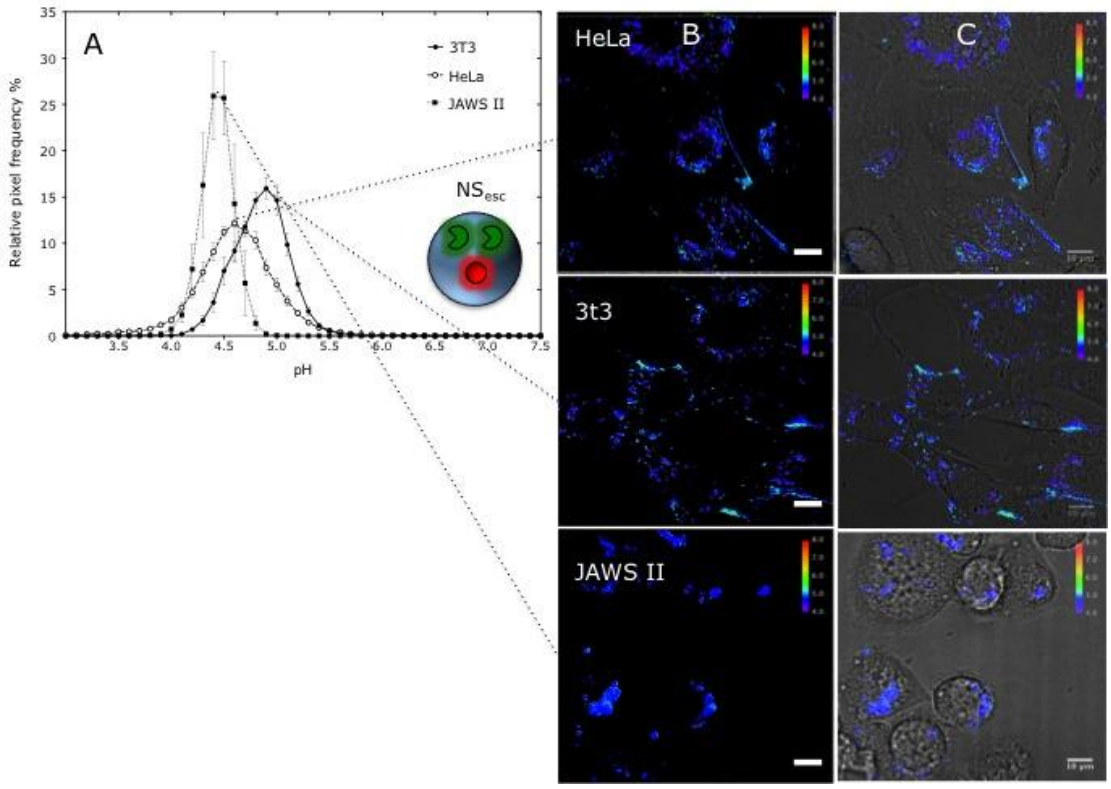

Figure 4.11 *pH measurements from NS_{esc} nanosensor design in different cell types.* (A) Histogram of pH distribution, n =~ 50 cells, error bars = SD. Corresponding false colour pH maps are shown on the right (B) with brightfield overlays (C). Scale bar = 10 μm.

4.4.3.2 Statistical error in measurements

In order to determine what are significant differences in pH values in biological investigations, it is necessary to determine the inherent error from the sensor. This was done using a method reported by Chauhan *et al*[220]. The factors contributing to measurement error include, error in the measurement of pH of buffers using a pH meter, error in the fitting equation for the calibration curve and error from reproducing measurements. To measure the error, firstly, a calibration is generated by measuring indicator to reference (I/R) ratios of calibration images using the image analysis process discussed previously and fitted to the calibration fitting equation as shown in **Figure 4.12A.** The I/R ratio for each individual calibration image is then taken and converted into pH by applying the calibration fitting equation. These values are plotted against pH measured from the pH meter in **Figure 4.12B.** Comparing the difference between the pH measured by image analysis and the pH measured from the pH meter shows the error from the image analysis procedure. This is represented by the Bland-Altman mean difference plot shown in **Figure 4.12C**. This shows, there

is an error of ±0.18 in measurements with a 95% confidence interval. From this we can conclude differences in mean pH values of greater tan 0.18 are significant.

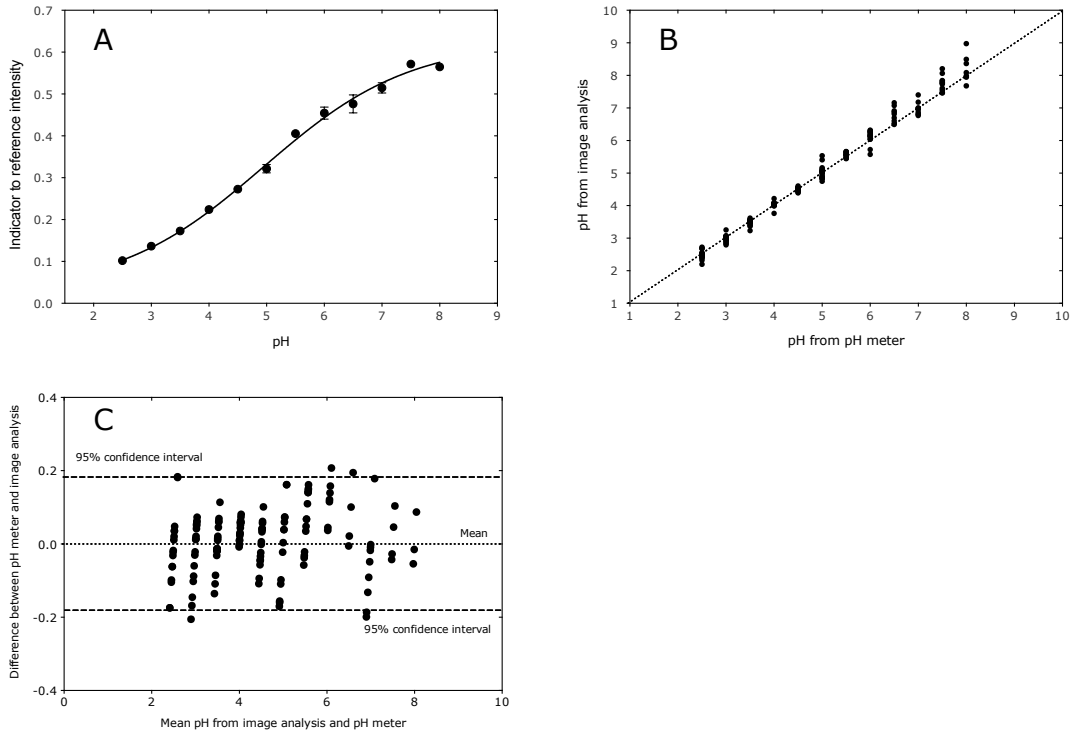

Figure 4.12 *Error calculation from pH measurements.* (A) Calibration of nanosensors. (B) pH measurement from calibration compared against pH measurements taken from a pH meter. (C) Bland-Altman plot showing the difference between mean pH measurements.

4.4.4 Validation of pH measurements

Up to this point the results in this chapter suggest sensors are delivered to cells by endocytosis and are trafficked to acidic vesicles presumably lysosomes. However we cannot be sure that the pH values measured are actually lysosomal pH values or due to a factor to relating to the methodology used to make the measurements. We have already seen performing ratiometric measurements requires a meticulous setup, which has shown there are many reasons why the measured values may not be reliable. In order to validate measurements, the intracellular location of nanosensors was investigated using fluorescence colocalisation microscopy. Additionally, pH inside cells was modulated using a pharmacological inhibitor of intracellular acidification.

4.4.4.1 Assessment of intracellular location by widefield microscopy

Fluorescence colocalisation was used to investigate the intracellular location of sensors in HeLa cells. In this approach, early endosomes and lysosomes were genetically labelled using fluorescent protein constructs (CellLights). Sensors exclusively labelled with a reference fluorophore (to prevent spectral overlap with markers), were then exposed to cells for 24 h and imaged under the same conditions in which pH measurements were made. Following uptake, sensors showed strong colocalisation with lysosomes in the perinuclear region (PCC = 0.735) (**Figure 4.13A**), whereas partial colocalisation is seen for early endosomes (PCC = 0.4432) (**Figure 4.13B**).

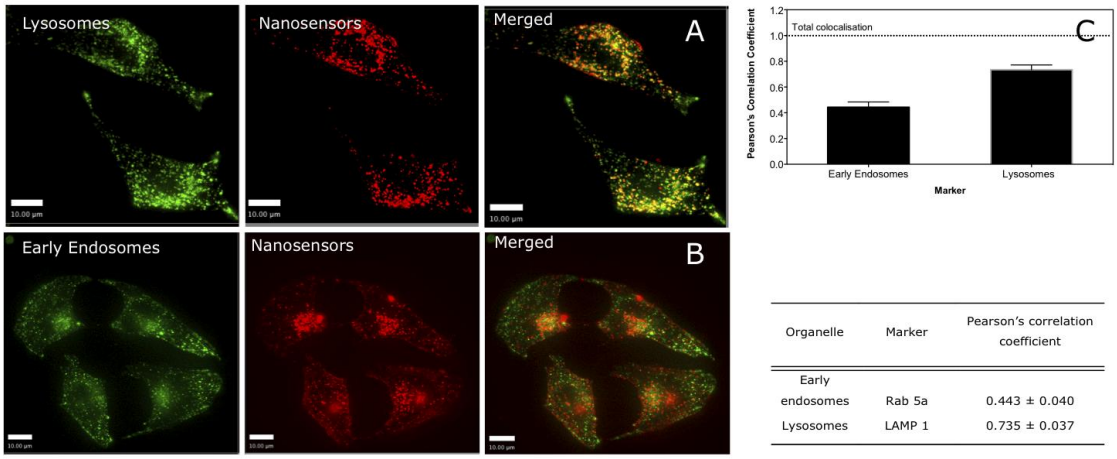

Organelle	Marker	Pearson's correlation coefficient
Early endosomes	Rab 5a	0.443 ± 0.040
Lysosomes	LAMP 1	0.735 ± 0.037

Figure 4.13 *Intracellular location of nanosensors in HeLa cells determined by widefield colocalisation microscopy.* Early endosomes and lysosomes were labelled with CellLights markers for Rab5a and LAMP1 respectively. Nanosensors (labelled with TAMRA only) were exposed to cells for 24 h. (A) Colocalisation with lysosomes. LAMP1 marker (green), nanosensors (red), merged. (B) Colocalisation with early endosomes. Rab 5a marker (green), nanosensors (red), merged. Scale bar = 10 μm. (C) Pearson's correlation coefficient (PCC) of colocalisation for early endosomes and lysosomes. N = 20 cells.

The results from (**Figure 4.13**) also suggest sensors are located in lysosomes, which correlates to the measured pH values mean pH 4.6 (**Figure 4.10A**), but they also suggests there are a significant number of sensors located in early endosomes (pH ~ 6.5)[54], which is not reflected in the pH measurements.

The relationship between intracellular location and measured pH was explored further in a temporal study (HeLa cells). In this experiment, colocalisation of nanosensors with lysosomal CellLights was monitored continuously for 4 hours (**Figure 4.14**). In a parallel experiment, pH was measurements were taken over

the same time period, under the same conditions (**Figure 4.15**). In the colocalisation experiment, nanosensors appear to be deposited into lysosomes rapidly between 1 and 2 hours. However, the pH measurements show there is a continuation of acidification after the 2-hour point where nanosensors are fully colocalised with lysosomes. If we assume that colocalisation is a perfect indicator of intracellular location, this suggests the pH measurements are not totally linked to intracellular location. The most obvious explanation is that nanosensors are deposited in lysosomes after 2 hours and then undergo acidification without a change in the intracellular location. In the context of the design of pH-sensitive nanomedicines this is a significant insight. The goal of many drug delivery systems is to release a drug before the drug reaches the lysosome to prevent degradation. Consequently this result gives information about where the pH trigger should be set and the time frame in which the drug should be released.

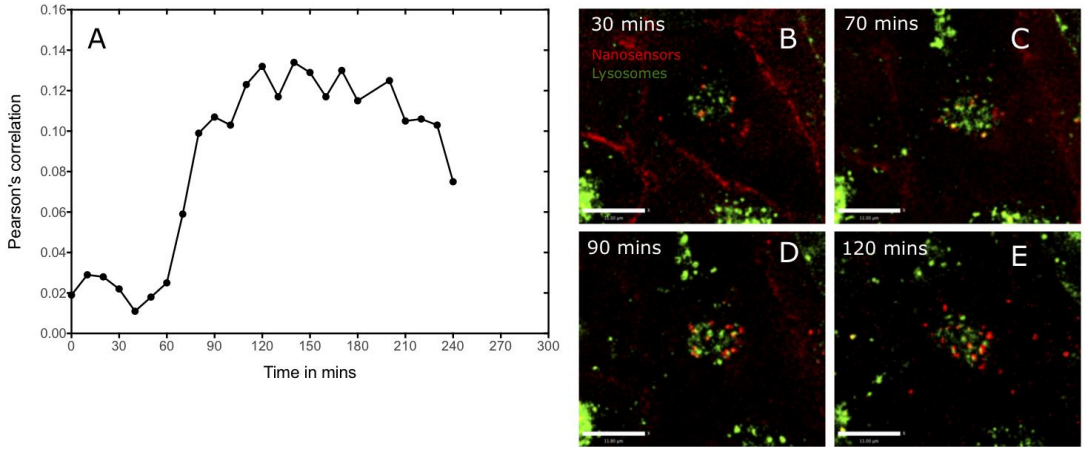

Figure 4.14 *Single cell time resolved time course colocalisation in HeLa cells.* (A) Measured PCC over a 4-hour period. (B-E) Corresponding images showing colocalisation of nanosensors (red) with lysosomes (green), labelled with CellLights. Scale bar =11 μm.

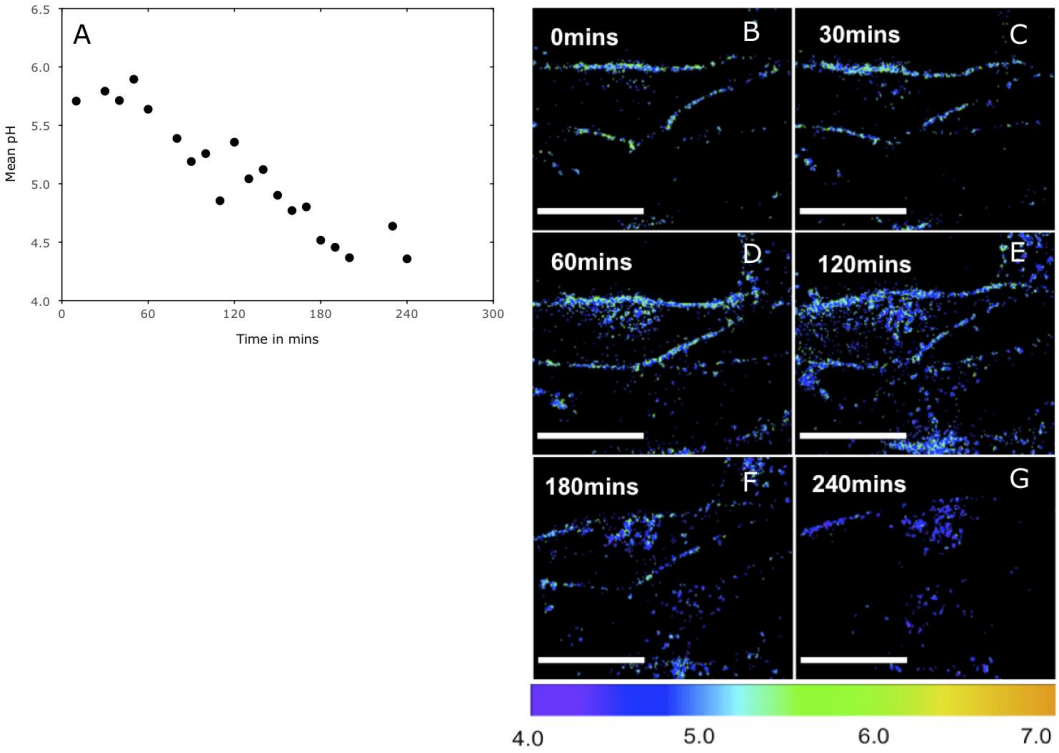

Figure 4.15 *Single cell time resolved pH measurements in HeLa cells*. Cells were exposed to nanosensors (1 mg ml^{-1}) and pH measurements were taken periodically. (A) Mean pH over 4 hours. (B-G) Corresponding false colour pH colour maps. Scale bar =20 μm.

However some caution should be taken when interpreting these results. Firstly, during the course of these experiments some toxicity was observed to be associated with CellLights markers, indicated by a reduction in uptake of nanosensors in cells showing strong expression of the markers (**Figure 4.16**). In order to mitigate this risk the CellLights were titrated to identify the lowest possible concentration of reagent which would generate a detectable signal from the marker but isolated cases of toxicity were still observed. Of greater concern is whether or not this affects the intracellular trafficking process of nanosensors. If this is the case, the temporal measurements of colocalisation and pH measurements are not comparable.

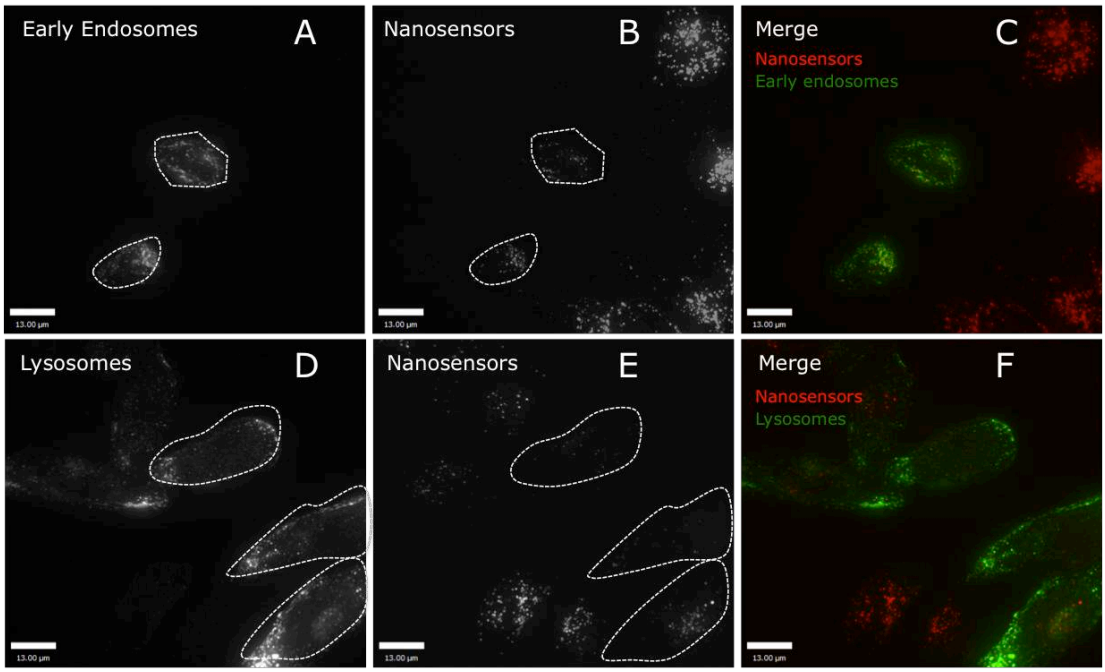

Figure 4.16 *Reduction in cell uptake in HeLa cells expressing CellLights.* (A) Early endosome cell lights. Dotted white line indicates cells showing reduction in uptake of nanosensors. (B) Nanosensors (labelled with TAMRA only). (C) Merge. Nanosensors (red), early endosomes cell lights (green). (D) Lysosome cell lights. (E) Nanosensors (labelled with TAMRA only). (F) Merge. Nanosensors (red), lysosome cell lights (green). Scale bar =13 µm.

In light of this, a method was sought to measure intracellular pH at the same time as monitoring colocalisation. This was done using an alternative marker for lysosomes, Lysotracker Blue. Lysotracker Blue is a weakly basic probe, which accumulates, in acidic organelles. As it is spectrally separated from the fluorophores used for the sensor, it is possible to make measurements and assess colocalisation in the same experiment. In **Figure 4.17**, a colour-mapped image is generated using the sensors with any pixels reporting a pH < 5.0 coloured yellow (**Figure 4.17D**). This has been super imposed onto an image of Lysotracker Blue (**Figure 4.17E**). A high degree of colocalised signal indicates sensors are faithfully reporting pH in lysosomes.

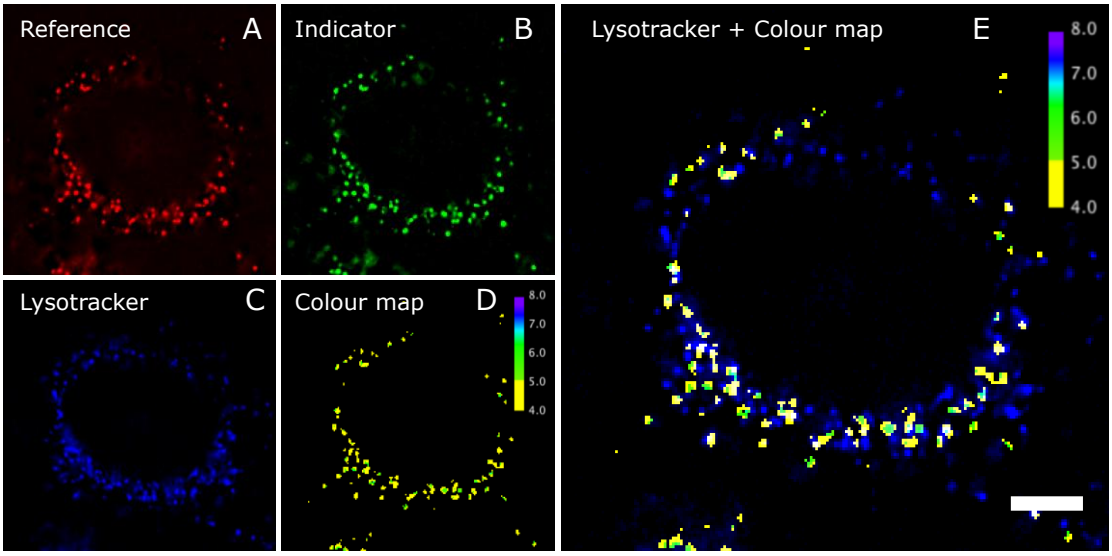

Figure 4.17 *Simultaneous pH measurement and colocalisation of nanosensors in 3T3 cells.* Cells were exposed to nanosensors for 24 h and Lysotracker blue for 1 h (A) Reference channel, (B) indicator channel, (C) Lysotracker Blue, (D) false colour pH map. (E) Merge of pH colour map and Lysotracker Blue. Scale bar = 2 μm.

Considering these results together provides some evidence that sensors are predominately located in lysosomes after 24 h. This validates pH measurements to some extent. However points of contention remain as some of the colocalisation data suggests a large proportion of sensors are located in early endosomes (**Figure 4.13**), which is not reflected in pH measurements. In addition to this temporal pH measurements do not show the same trend as in the colocalisation data, although there may be alternative explanations for this as discussed previously.

In reality it is likely that colocalisation is not a perfect indicator of intracellular location due to limitations of widefield microscopy. The limitation with this technique, as is the case for all conventional microscopy techniques including confocal is that the highest possible resolution is a perfect scenario is ~ 250 nm, whereas intracellular structures including early endosomes and lysosomes can be much smaller than this. Practically this means that it is not always possible to observe from widefield images whether nanosensors are residing inside early endosomes/lysosomes or are merely in close proximity.

4.4.4.2 Assessment of intracellular location by super-resolution microscopy

3D structured illumination microscopy (3D-SIM) was employed to overcome the shortcomings of widefield microscopy and definitively define the intracellular

location of nanosensors. 3D-SIM is capable of producing images with lateral and axial resolutions of 100-130 nm and 250-350 nm respectively ideal for precise determination of intracellular location. The images in the following section were taken using a 3D SIM OMX Blaze (Applied Precision) imaging system at the University of Melbourne.

Preliminary experiments were conducted to identify the insights 3D-SIM offers over confocal and widefield imaging. Fixed HeLa cells were imaged following uptake of sensors (nucleus and actin were also stained) (**Figure 4.18**). 3D-SIM offers several insights. Firstly it is possible resolve subtle differences in the chromatin structure inside the nucleus, represented by intense wire like structures (**Figure 4.18Ci**). Secondly precise filamentous actin structures are visible from phalloidin staining (**Figure 4.18Cii**). The power of the 3D-SIM techniques over the widefield technique is represented in **Figure 4.19.** This shows an image before and after an image is reconstructed demonstrating the capability of 3D-SIM to image structures, which evade capture by conventional microscopy techniques.

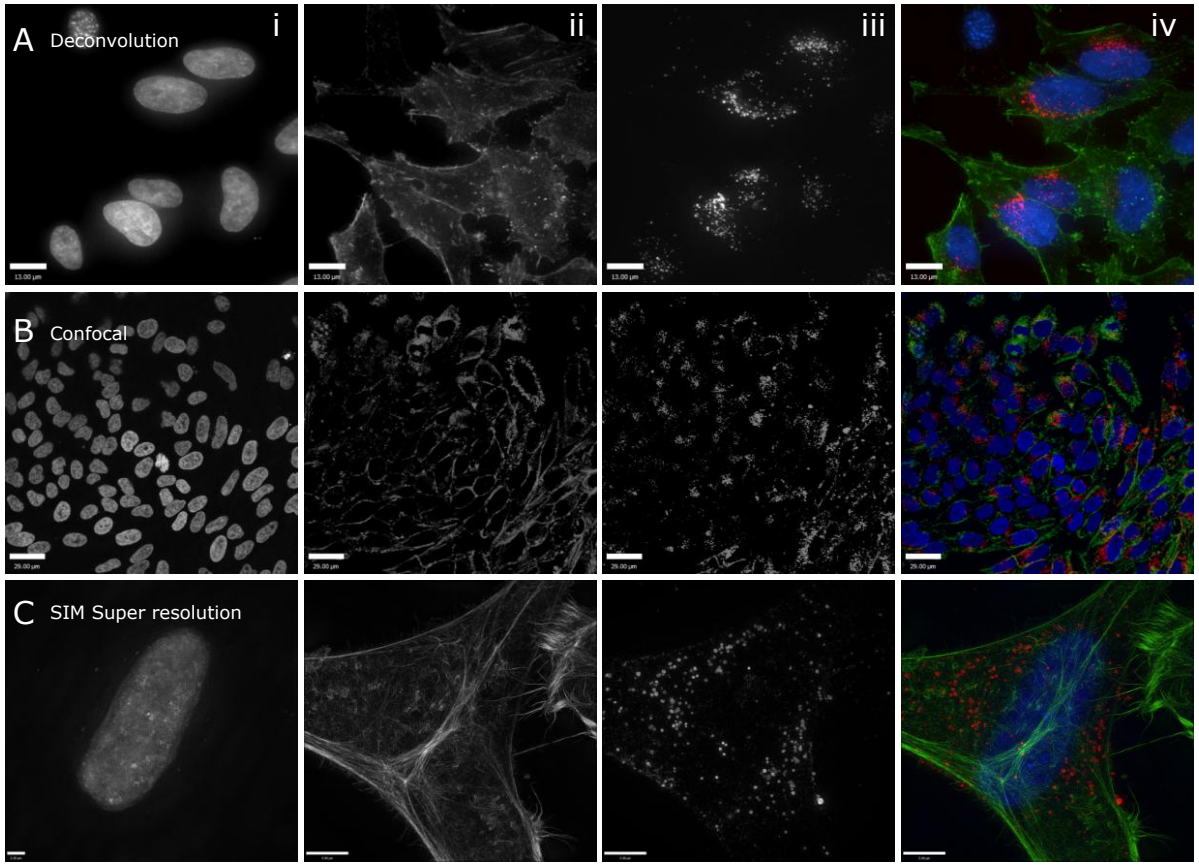

Figure 4.18 *Imaging of nanosensors by different microscopy techniques.* Images are of fixed HeLa cells after 24 h exposure to nanosensors labelled with TAMRA (red). F-Actin is stained with phalloidin conjugated to Alexa 488 (green) and nuclei are stained with Hoescht 3342 (blue). (A) Widefield deconvolution microscopy (Deltavision Elite). Scale bar = 13 μm. (B) Confocal microscopy (Leica SP2). Scale bar = 29 μm. (C) 3D-SIM (OMX BLAZE). Scale bar = 5.9 μm (unless otherwise stated). (i) Nucleus, (ii) actin, (iii) nanosensors, (iv) colour merge.

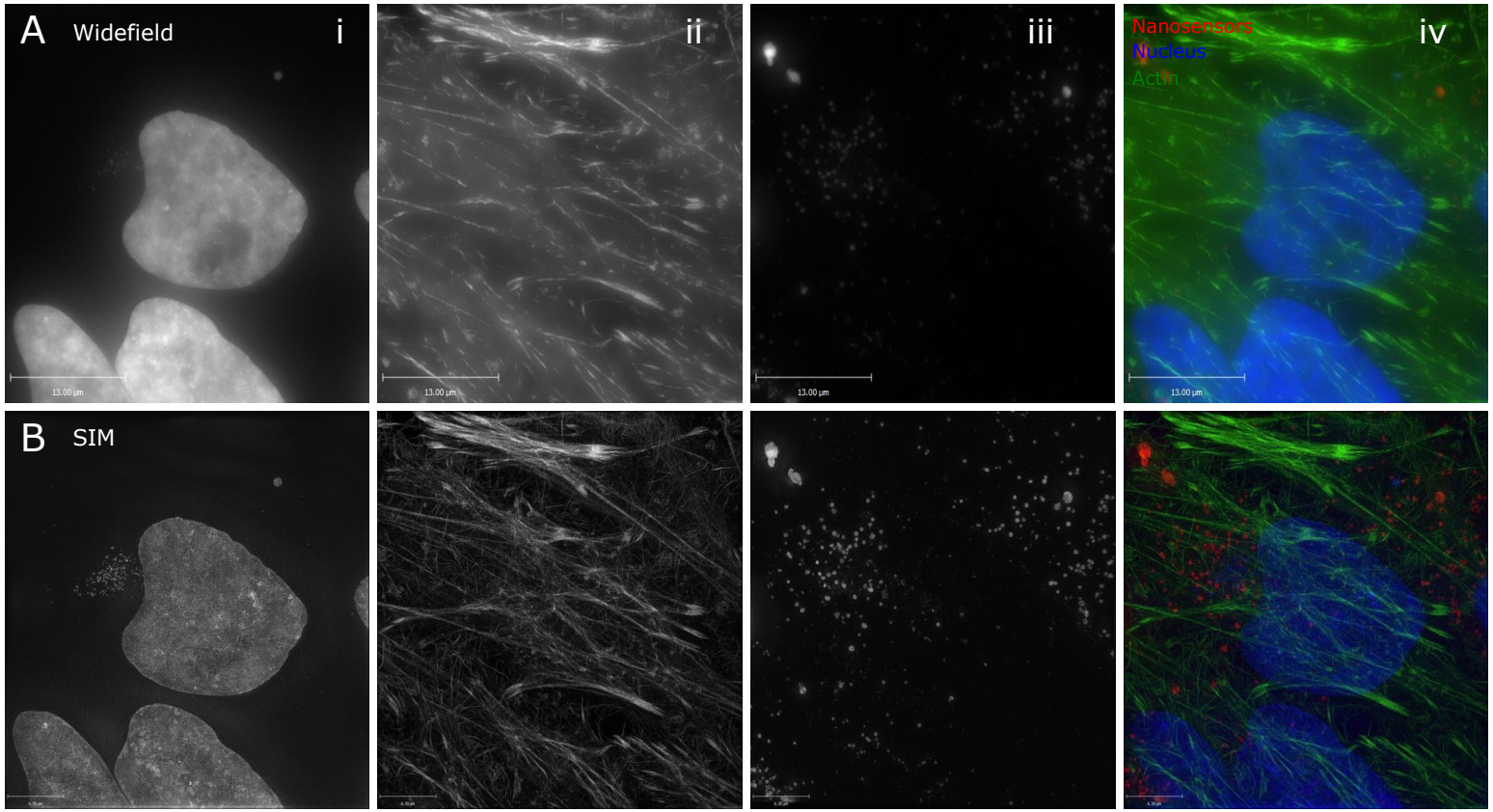

Figure 4.19 *Reconstruction of images by super-resolution microscopy.* Images are of fixed HeLa cells after 24 h exposure to nanosensors labelled with TAMRA (red). F-Actin is stained with phalloidin conjugated to Alexa 488 (green) and nuclei are stained with Hoescht 3342 (blue). Images are taken with 3D-SIM (OMX BLAZE). Scale bar = 13μm. (i) Nucleus, (ii) actin, (iii) nanosensors, (iv) colour merge. (A) Widefield image. (B) 3D-SIM image.

3D-SIM has the added advantage of generating high-resolution 3-D images. This capability was utilised to identify the spatial location of nanosensors. Nanosensors are localised to the periphery of the nucleus in punctate spherical vesicles as shown in the 3D reconstruction of SIM images in **Figure 4.20.** Previous reports using electron microscopy have shown that lysosomes are predominantly localised to the nuclear periphery while early endocytic vesicles are more evenly distributed throughout the cytoplasm[245]. Hence the observation of sensors in nuclear periphery is the first indication nanosensors are situated in lysosomes.

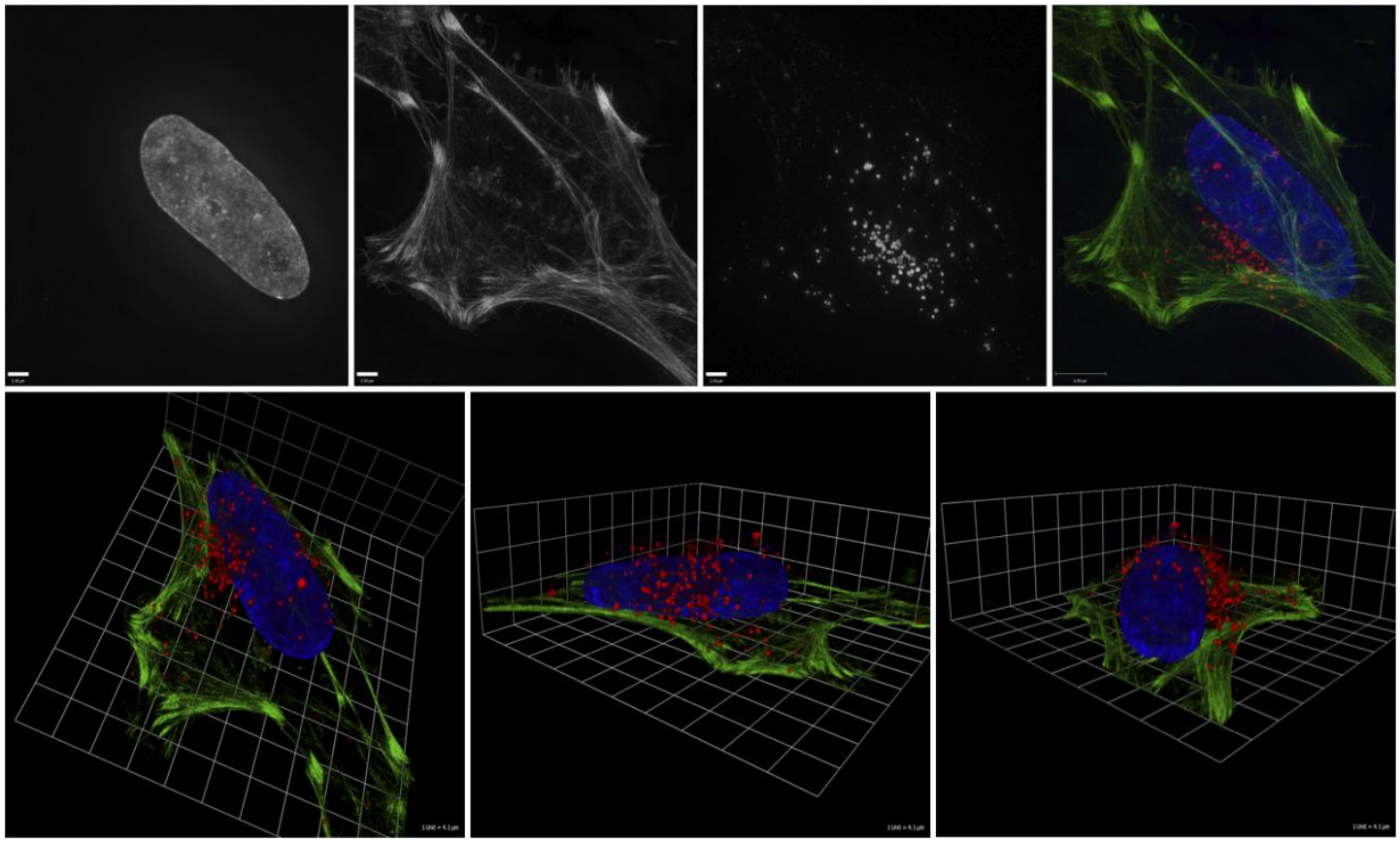

Figure 4.20 *3D imaging of nanosensors by SIM.* Images are of fixed HeLa cells after 24 h exposure to nanosensors labelled with TAMRA (red). F-Actin is stained with phalloidin conjugated to Alexa 488 (green) and nuclei are stained with Hoescht 3342 (blue). Images are taken with 3D-SIM (OMX BLAZE). Scale bar (i-iii) = 2.5 μm (iv) = 6 μm (A-C) 1 unit= 4.1 μm. (i) Nucleus, (ii) actin, (iii) nanosensors, (iv) colour merge. (A-C) 3D reconstruction of images.

In further analysis, objects in the images were identified by recognising regions of greater than 120 μm^2 above a background threshold (set using a ROI outside of the cell) as nanosensor containing vesicles as shown in **Figure 4.21**. The mean surface area of the vesicles is ~ 620 nm^2, which assuming the vesicles perfectly spherical corresponds to a diameter of 28 nm, which is surprising considering the nanosensors have been measured to have a hydrodynamic diameter of 100 nm (see **Chapter 2**). Nanosensors synthesised in this study are relatively monodisperse, however there is still a mixed population of sizes. It is possible that uptake is favoured by smaller particles in the population. In order to confirm this the study should be repeated on monodisperse particles. If this is the case, this further emphasis the necessity to utilise monodisperse particles when determining the effect of size on cell uptake.

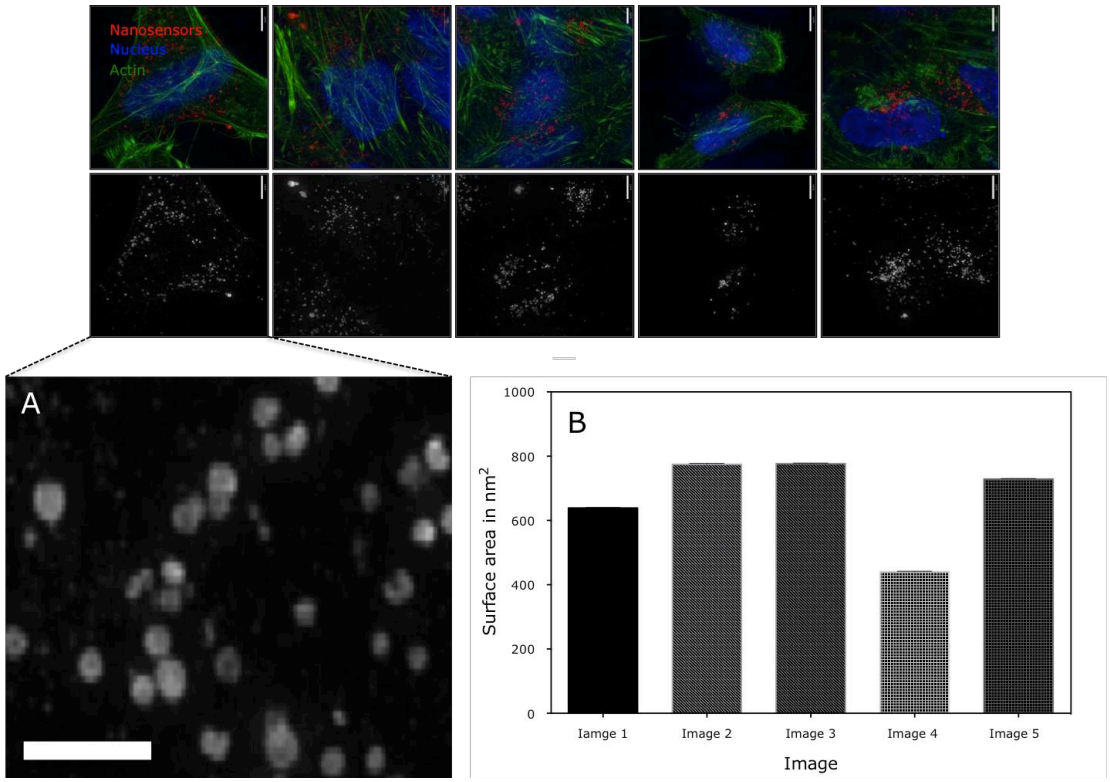

Figure 4.21 *Size measurement of nanosensor containing vesicles by 3D-SIM. Images are of fixed HeLa cells after 24 h exposure to nanosensors labelled with TAMRA (red).* F-Actin is stained by phalloidin conjugated to Alexa 488 (green) and nuclei are stained with Hoescht 3342 (blue). Images are taken with 3D-SIM (OMX BLAZE). (A) Nanosensors. Scale bar = 200 nm. (B) Measurements are of the average surface area of nanosensors in each image. For small images scale bar = 6.3 μm.

Although spatial analysis of images yields important information about the location of nanosensors, more reliable information is obtained from detailed colocalisation analysis. In this context 3D-SIM reveals information about the structure and location of endosomes and lysosomes, as indicated in **Figure 4.22B,** which shows a ring structure represents LAMP proteins on the surface of lysosomes (labelled using CellLights). Colocalisation experiments were performed using 3D-SIM in the same way as for widefield studies using CellLights, except cells were fixed in preparation for imaging. The images are shown in **Figure 4.23, Figure 4.24 and Figure 4.25.**

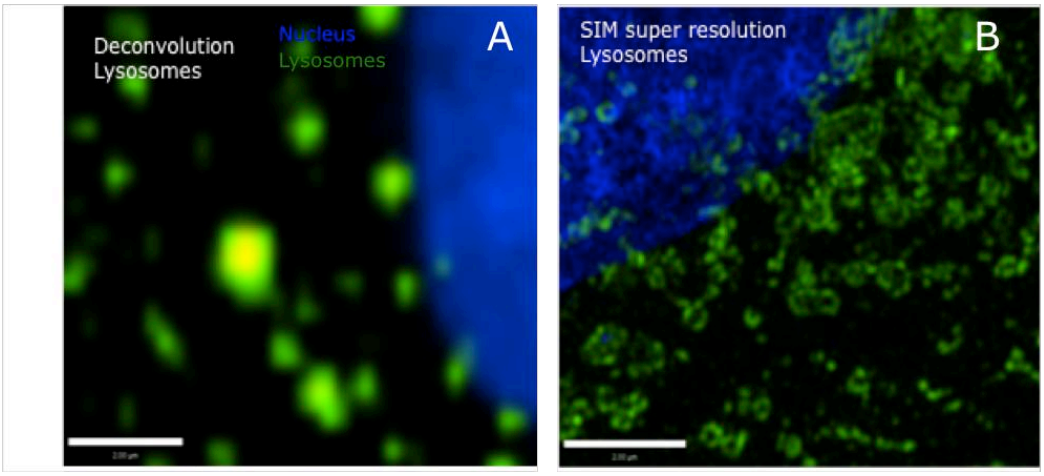

Figure 4.22 *Improvement by SIM microscopy.* Lysosomes are labelled with CellLights markers for LAMP1 (green) nucleus is labelled with Hoescht (blue). (A) Widefield deconvolution microscopy (Deltavision elite microscope, Applied Precision). (B) SIM microscopy (OMX Blaze 3D-SIM microscope, Applied Precision. Scale bar = 2 μm.

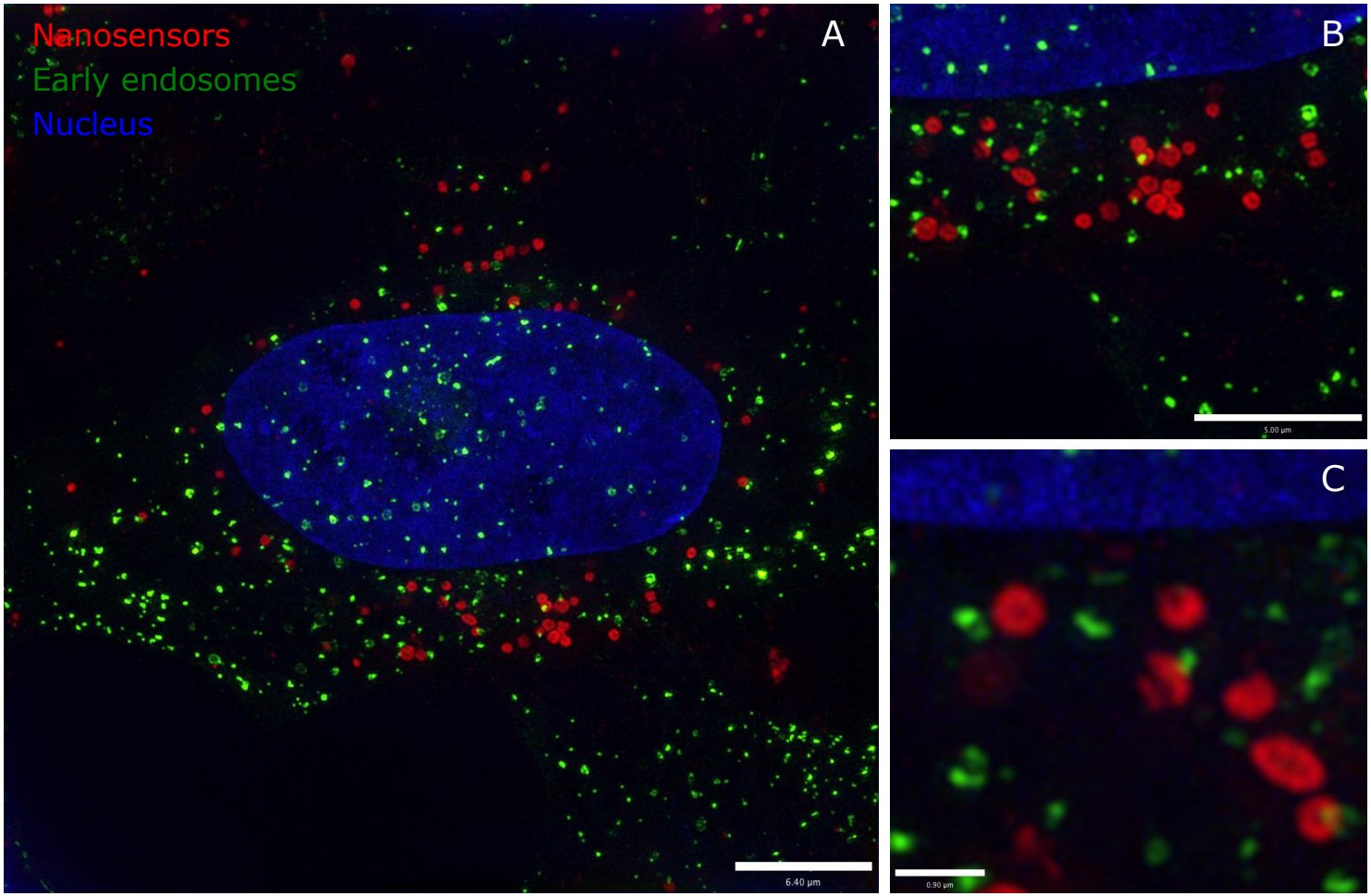

Figure 4.23 *Images of nanosensors with early endosomes in HeLa cells determined by 3D-SIM.* Images show lack of colocalisation of nanosensors with early endosomes. Early endosomes were labelled with CellLights markers for Rab5a (green). Nanosensors (labelled with TAMRA only) (red) were exposed to cells for 24 h. (A) Scale bar = 6.4 µm. (B) Scale bar = 5 µm. (C) Scale bar =0.90 µm.

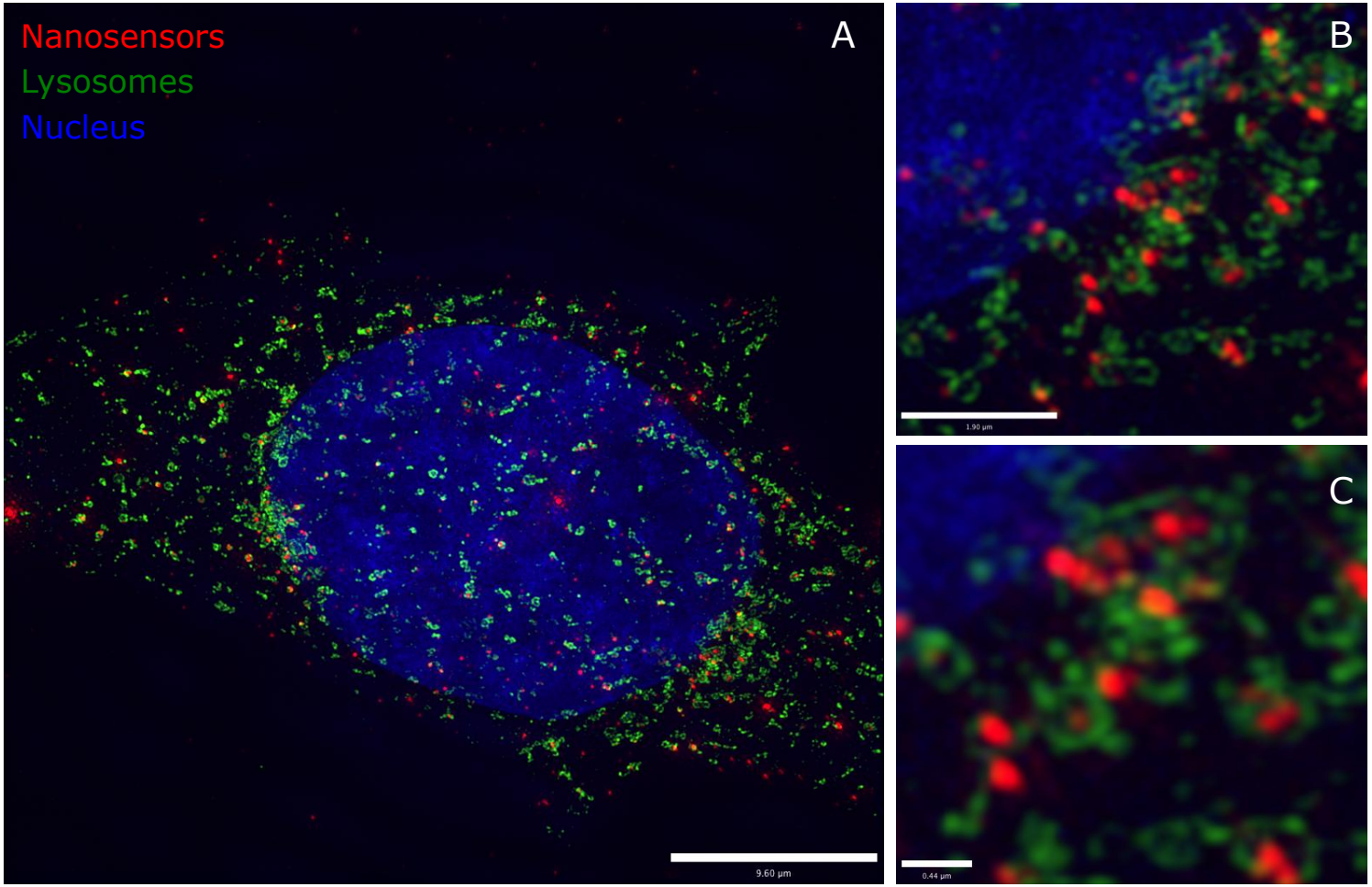

Figure 4.24 *Colocalisation of nanosensors with lysosomes in HeLa cells determined by 3D-SIM.* Images show tight colocalisation of nanosensors with lysosomes. Lysosomes were labelled with CellLights markers for LAMP1 (green). Nanosensors (labelled with TAMRA only) (red) were exposed to cells for 24 h. (A) Scale bar = 9.6 µm. (B) Scale bar = 1.9 µm. (C) Scale bar = 0.44 µm.

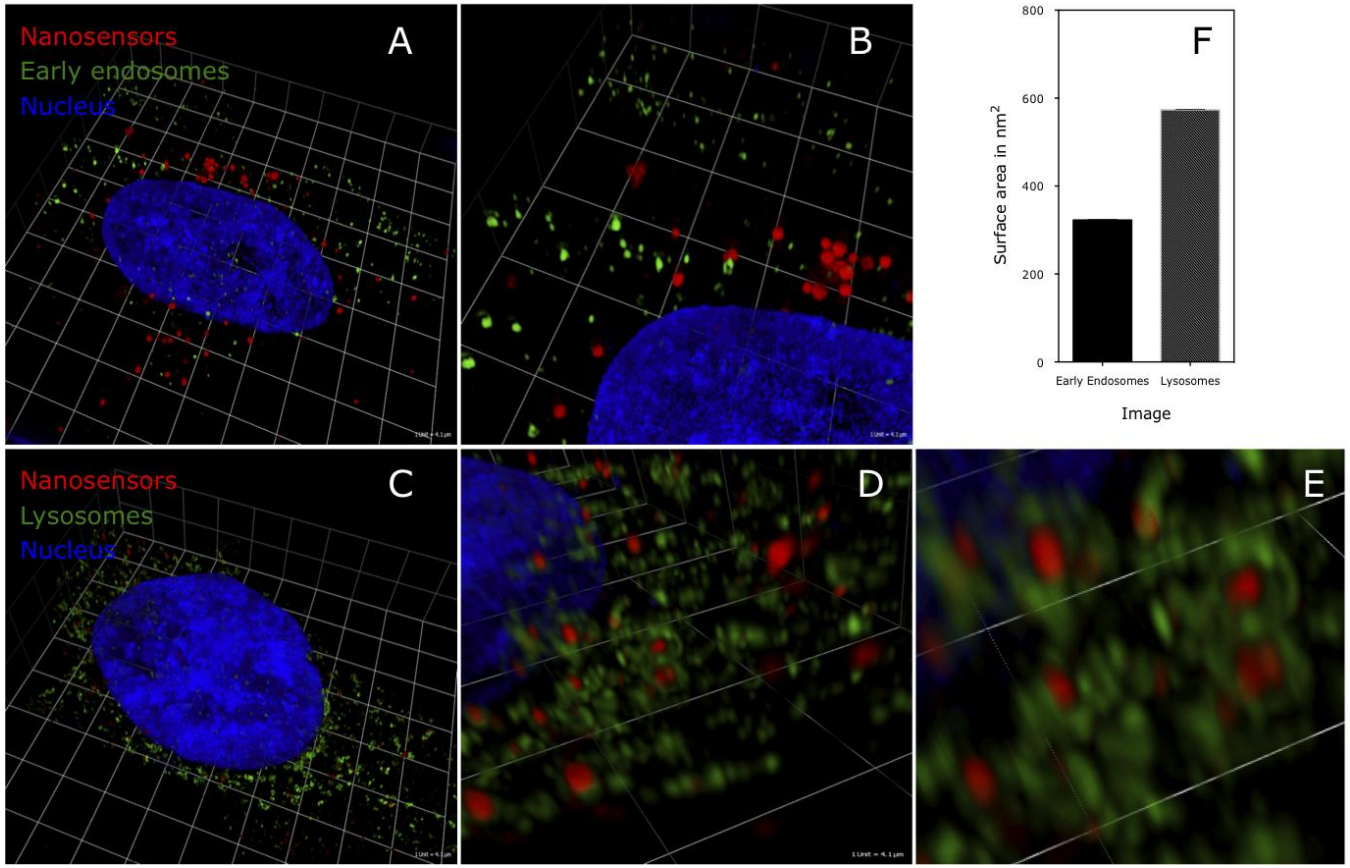

Figure 4.25 *3D reconstruction of SIM images of nanosensor colocalisation with endosomes and lysosomes in HeLa cells*. Images show a lack of colocalisation of nanosensors with early endosomes and tight colocalisation of nanosensors with lysosomes. Early endosomes/lysosomes were labelled with CellLights markers for Rab5a/LAMP1 (green). Nanosensors (labelled with TAMRA only) (red) were exposed to cells for 24 h. (A, B) Early endosomes. (C-E) Lysosomes. (F) Measurements of the surface area of endosomes and lysosomes. Scale: 1 unit = 4.1 µm.

The images provide further evidence to support that sensors are inside lysosomes (**Figure 4.24**), (**Figure 4.25C,D,E**). Sensors can clearly be seen to be located within the ring structure of the lysosomes. Conversely it is also apparent that there is almost no observable colocalisation with early endosomes, which appear to be several times smaller than the sensors, this is in contrast to the same experiment using widefield microscopy where partial colocalisation was seen (**Figure 4.13**). There also appears to be sensors in close proximity to the lysosomes but not located inside. This could be due to incomplete labelling of lysosomes by CellLights.

As an additional point there also appears to a ring like appearance to the nanosensors (**Figure 4.23C**), this suggests that the fluorophore is concentrated on the surface of the nanosensors. In an ideal situation the fluorophores would be evenly distributed throughout the sensors to maximise the impact of the protective matrix. Consequently it may be preferential to synthesise nanosensors by the pre-conjugation as oppose to the post –conjugation method used here, as it is more likely to result in a even distribution of fluorophore in the sensor.

In summary these images show definitively that sensors are predominately located in lysosomes, providing strong evidence that the measurement methodology is reliable. Additionally the images were acquired using identical sample preparation procedures to those used in conventional microscopy demonstrating the versatility of this technique. Further insights into the intracellular location of sensor would be gained by imaging using SIM under live conditions. The imaging system utilised in this study was not equipped to do this, moreover additional methods, which are not compatible with live cell imaging were required (addition of SlowFade) to prevent photobleaching of fluorophores. If this issue can be overcome SIM imaging also provides the possibility of high-resolution pH measurements. As a wider point the comparison of colocalisation experiments using SIM and widefield techniques demonstrate how widefield colocalisation microscopy can be misleading as method for determining intracellular location. In light of this measurement of pH may a more reliable indicator of intracellular location. However it is important to consider that pH may be influenced by other factors, which are not linked to intracellular location or methodology for example inherent buffering effects of the material.

4.4.4.3 Test for nanosensor response

In order to test the responsiveness of nanosensors inside endocytic vesicles as a means of further sensor validation, cells were treated with Bafilomycin A1, an

inhibitor of endosomal acidification. Cells were treated 30 minutes 24 h after nanosensor uptake, the resulting pH measurements and corresponding colour maps are shown in **Figure 4.26.** All the cell types under investigation showed a response to the inhibitor but to differing extents. HeLa cells showed the largest response with a mean increase in pH of 0.45 pH units which is similar to previous reports in HepG2 cells[183], whereas 3T3 and Jaws showed an increase of < 0.3 pH units. The inhibitor functions by binding V-ATPase proton pumps on the surface of endocytic vesicles, which are found in different concentrations in different cell types. Therefore low expression of the V-ATPase pumps in JAWS II and 3T3 cells could be an explanation for the weak response. There is also a marked difference in the distribution of signal shown in the images, with treated cells showing a less punctate pH distribution. This may be expected, as inhibition of endosomal acidification will result in an osmotic swelling and eventual rupture of the endosomes and lysosomes. The differences could be attributed to partially ruptured endocytic vesicles. This shows sensors are responsive inside endocytic vesicles.

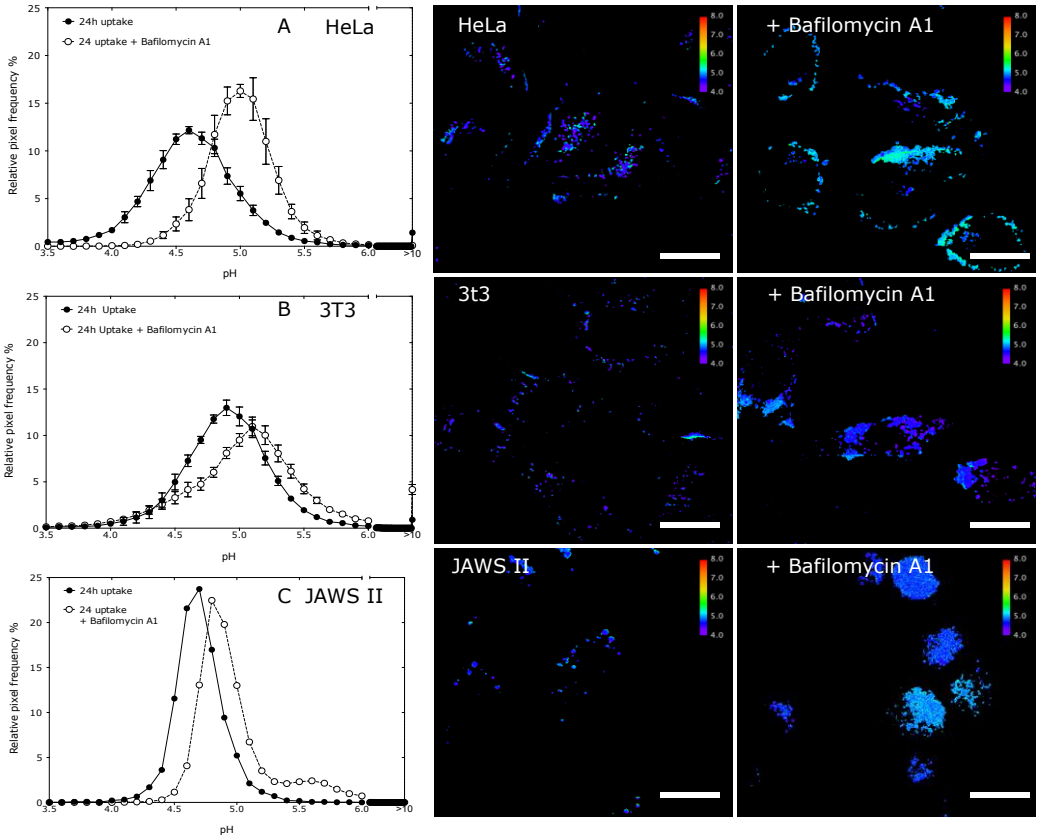

Figure 4.26 *Nanosensor response to inhibition of endosomal acidification.* Cells were treated with NSesc nanosensors for 24 h and treated with Bafilomycin A1 (inhibitor of endosomal acidification) for 30 minutes. (A–C) Histograms of pH distribution (n = ~ 20 cells) error bars represent SD. Corresponding false colour pH maps are shown next to the histograms. Scale bar = 15 μm.

4.5 Conclusions

In summary, nanosensors have been delivered the endocytic pathway in a range of different cell types and shown to be likely to have minimal effect on cell viability. pH measurements have been shown to correspond to the intracellular location of the nanosensors. Finally, nanosensors have been shown to be responsive to changes in pH inside cells.

Nanosensors were delivered into cells by increasing the positive charge on the surface of a nanosensor. Incorporating charged ammonium groups on to the sensor resulted in increased charge from + 16.7 mV to 36.3 mV without any impact on size. This resulted in 85.4% cellular association with MRC-5 cells, these nanosensors were observed to be uptaken into four cell types, HeLa, MRC-5, 3T3 and JAWS II, after 24 h exposure without any further methods to facilitate delivery. This provides further evidence of that surface charge promotes cellular internalisation.

Intracellular measurements were attempted using three different nanosensor designs, i) NS_{esc} (OG_{ind}/5(6)-FAM_{ind}, $TAMRA_{ref}$), NS_{end} ($pHrodo_{ind,}$ Alexa 488_{ref}) and NS_{ds} ($pHrodo_{ind,}$ OG_{ind}/5(6)-FAM_{ind}). Sensors with weak signal and high background resulted in a large proportion of pixels outside the calibration range of the nanosensor. This was a particular problem with $pHrodo_{ind}$. Therefore a sensor design incorporating the pHrodo fluorophore, as the only indicator was deemed to be sub optimal for intracellular measurements. Measurements from NS_{ds} and NS_{esc} were achieved with < 10% of pixels outside the range of the calibration curve. pH was measured as 4.6 ± 0.2 and 5.5 ± 0.2 respectively following 24 h uptake in HeLa cells under the same conditions. However NS_{ds} were not weighted due to the absence of a reference fluorophore. Weighting was found to have a significant affect on measurements, critically giving information about the proportion of nanosensors as well as the distribution of nanosensors reporting a given pH value. The proportion of nanosensors is important for gaining biological insights into the mechanism of intracellular trafficking as discussed in **Chapter 3**. Therefore the NS_{esc} sensor design was utilised in biological applications. The overall error from measurements in HeLa cells utilising a Deltavision microscope setup was found to be 0.18 within a 95% confidence interval. Demonstrating the accuracy of measurements.

Spatial assessment and colocalisation microscopy showed the majority of nanosensors are delivered to lysosomes in HeLa cells. Nanosensors were also seen to respond to changes in intracellular pH over time and also respond to artificial modulation of intracellular pH. This demonstrates nanosensors are robust enough to function in the cellular environment.

Assessment of colocalisation using widefield microscopy showed that sensors were partially colocalised to early endosomes. However analysis by 3D SIM super-resolution showed there is no colocalisation with early endosomes. This corresponds to pH measurements, which report lysosomal pH values of < 5.0. This shows is that widefield colocalisation microscopy can result in misleading results when assessing intracellular location. Although widefield microscopy gives an approximate indication of intracellular location care should be taken when making conclusions about the proportion of sensors in a given location. This is particularly important in designing delivery systems for intracellular targeting. The development of super-resolution techniques should address this issue in the future.

Chapter 5 Application of pH nanosensors for biological insights into the intracellular trafficking of nanomedicines

5.1 Aim

The aim of this chapter is to evaluate potential applications of pH nanosensors for gaining biological insights into the intracellular trafficking of nanomedicines. This is done with the view of using these insights to aid the rational design of nanomedicines. Applications are explored in three areas. In the first application, pH nanosensors are utilised to characterise pH transitions occurring through the intracellular trafficking process in different cell types. Secondly the effect of altering the nanoparticle surface charge on the intracellular trafficking process is investigated via the use of pH nanosensors. In the final application pH nanosensors are utilised to investigate the intracellular trafficking process of siRNA delivered to a cell in different formulations. Currently the majority of reports in the literature have focused on optimising sensor design for pH measurements with few examples of applications, particularly in the area of intracellular trafficking[104]. This chapter aims to develop the field by investigating different applications for nanosensors in this area.

5.2 Introduction

5.2.1 Significance of intracellular pH for the design of nanomedicines

The progressive acidification, which occurs through the endo-lysosomal pathway, has been the exploited in nanomedicine to achieve targeted release of a drug[62]. This is typically achieved through pH-responsive materials, which change their physicochemical properties in response to endo-lysosomal acidification in a way that results in the release of a drug. Mechanisms by which this occurs include pH dependent swelling, dissociation and charge shifting. These are useful materials in nanomedicine, because finely tuning the response of the material is a way of targeting a drug for intracellular release, and also as a method for controlling where in the endo-lysosomal pathway the drug is released, which is important for avoiding lysosomal degradation.

The pH values currently used to determine the pH range in which these materials should respond are guided predominately by static measurements of pH at discrete stages of the endocytic pathway. A major drawback for using these measurements is that they do not offer temporal information about local pH changes as a nanoparticle is transported through the endocytic pathway. Temporal measurements are required to tailor the intracellular release profile of a pH-sensitive nanomedicine. The significance of this is best illustrated by considering the delivery of a drug sensitive to lysosomal degradation by a pH-sensitive nanocarrier internalised by endocytosis. In this case the drug is required to be released in the early stages of the endocytic pathway in order to avoid lysosomal degradation. In most cases the nanocarrier will only be held in early endosomes for a limited period of time before it is trafficked for degradation in lysosomes. Consequently knowledge of the temporal aspects of pH transitions occurring during intracellular trafficking is required to design a nanocarrier capable of targeted release.

In addition to the lack of temporal information on pH transitions occurring during the intracellular trafficking of nanosensors, it is relatively unknown how pathways for acidification differ between different cell types. A wide range of different pH values are reported for different organelles in the endocytic pathway[54]. Typically early endosomes are quoted as having a pH > 6.0, late endosomes between pH 5.0 and 6.0 and lysosomes < 5.0[27]. These are nominally used as a guide when

designing materials for drug delivery, however the field would benefit from a more precise characterisation of pH in different cell types.

Nanosensors acting as mimics of nanomedicines have the potential to be utilised for temporal measurements in the endocytic pathway across different cell types. It is important to note that the utility of these measurements is based on the assumption that nanosensors are trafficked in the same way as the nanomedicine under investigation. The validity of this assumption is dependent on how well the physicochemical characteristics of the delivery system match that of the nanomedicine. Due to the diverse array of materials available to synthesise nanosensors it is feasible to construct a sensor with similar properties to a wide range of nanomedicines to ensure this assumption is valid[104]. There are few examples where nanosensors have been used to make temporal measurements, and even fewer comparing different cell types. Comparisons between cell types used in different studies are further complicated by deficiencies in methodology, which could be the source of differences in measurements.

Previously reported pH measurements using nanoparticle-based sensors are presented in **Table 5.1** and **Figure 5.1.** It is important to note that some of these studies have weaknesses in measurement methodology, which have been discussed in **Chapter 3**. On the assumption measurements are broadly accurate, with the exception of the study by Peng *et al*[136], pH is measured between 4.0 and 6.6. This is based on measurements performed using different materials (Pdots[275], silica[132,276] and polyacrylamide[180,183,208]) across different cell types, indicating sensors are universally trafficked to late endocytic compartments. The study by Peng *et al* reports a pH of 7.2 in HeLa cells using silica-based sensors. This appears to be an anomaly compared to the rest of the literature.

Comparing the literature, it is unclear how long it takes for sensors to be transported to late endocytic compartments. Some studies show this to occur in less than 1 h, whereas others studies have been conducted over a longer period making it difficult to assess at what point sensors actually reach late endocytic compartments. In addition to this a range of cell types have been utilised with different materials, making direct comparisons very difficult.

To further elucidate intracellular pH transitions, polyacrylamide pH nanosensors fabricated in this study were utilised to perform temporal pH measurements in three different cell types (HeLa, 3T3 and JAWS II).

Reference	Sensor material	Cell type	Uptake Time	pH measurement
Burns et al 2006[132]	**Silica core/shell**	**RBL-2H3**	**1 h**	**5.1-6.6**
Peng et al 2007[181]	Silica	Macrophage HeLa	0.5 h 4 h	4.8 7.2
Coupland 2009[208]	Tat conjugated polyacrylamide	CHO-K1	2 – 3 h	4.88 – 5.10
Ray 2011[180]	F3 peptide conjugated polyacrylamide	9L Rat Glioma	20 h	7.1±0.2 (targeted) 6.3± 0.2 (untargeted)
Benjaminsen 2012[183]	**Positively charged polyacrylamide**	**HepG2**	**1.5 h** **2.0 h** **24 h**	**5.1 ± 0.6** **4.9 ± 0.6** **4.5 ± 0.4**
Chan 2011[275]	Pdots	HeLa	Not stated	4.8 – 5.0 ± 0.9
Chen 2012[276]	Mesoporus silica	HeLa	4 h	6.0 – 6.3 (positively charged) < 5.0 (negatively charged)

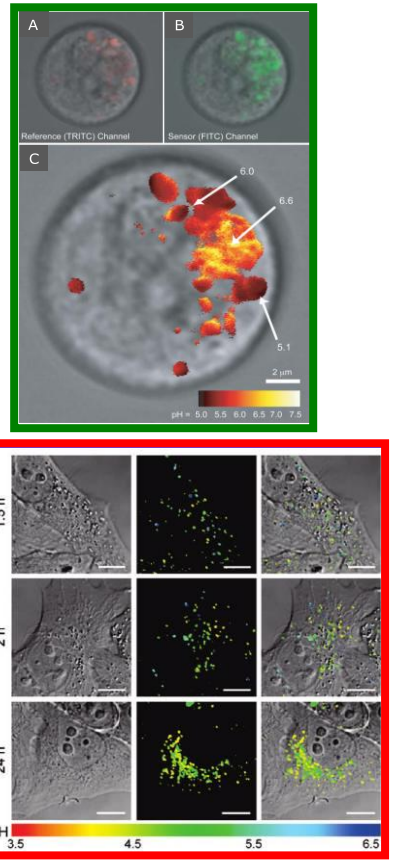

Table 5.1 Overview of previously reported intracellular pH measurements performed using ratiometric nanosensors.

Figure 5.1 *Images of previously reported pH measurements using nanosensors.* (A,B,C) pH measurements taken from Burns et al[132]. Measurement were performed using silica/core shell nanoparticles in RBL-2H3 cells following uptake after 1 h. (A), reference channel (TRITC), (B), indicator channel (FITC), (C), colour mapped image overlaid on brightfield image. (D) pH measurements taken form Benjaminsen et al[183]. Measurements were performed using polyacrylamide nanosensors in HepG2 cells after 1.5 h, 2 h, and 24 h. All measurements were acquired by confocal microscopy.

5.2.2 Effect of surface charge on intracellular trafficking of nanomedicines

Surface charge has been highlighted in many studies and reviews as a key physicochemical characteristic which affects the cellular uptake and intracellular trafficking of a nanoparticle[229,276-278].

5.2.2.1 Cellular uptake

The surface charge of a particle has been suggested as a factor determining the mechanism of endocytic uptake of nanoparticles, which indicates charge also influences intracellular trafficking pathway[229,235,279]. Although, there is a strong body of evidence indicating the majority of polymeric materials designed for drug delivery entering a cell by endocytosis are eventually deposited in lysosomes, the material will pass through a series of different intermediary endocytic vesicles depending on the mechanism for uptake. For example material entering by macropinocytosis will pass through macropinosomes whilst material internalised by dynamin and flotillin dependent mechanisms pass through clathrin-independent carriers and GPI-enriched early endosomal compartments (CLICs and GEECs). These vesicles are recognised to be distinct by their structural features, however less is known about the environment inside the vesicle and the time required for material to pass through them. However it is clear that the mechanism of uptake is an indication that differentially charged nanomedicines will have different intracellular itineraries. Consequently the uptake route is important when considering how surface charge affects intracellular trafficking.

One example where this has been considered is a study by Dausend *et al*[235], where the uptake mechanism of oppositely charged ~ 100 nm polystyrene particles was investigated in HeLa cells using pharmacological inhibition of endocytic pathways. The findings showed that the uptake of positively and negatively charged nanosensors were dependent on dynamin and F-actin, whilst positively charged nanoparticles favoured uptake by macropinocytosis. In another study by Harush-Frenkel *et al*[279], differentially charged poly(ethylene glycol)-D,L-polylactide (PEG- PLA) nanoparticles of a similar size to those used in the study by Dausend *et al*, were exposed to MDCK epithelial cells. Clathrin mediated uptake was found to be favoured for both positively and negative charged nanoparticles but little uptake was seen by macropinocytosis. Interestingly cationic nanoparticles were found to be transcytosed through the cell whilst anionic particles were deposited into lysosomes. These somewhat contradictory findings exemplify the difficultly in making generalisations about the effect of charge on uptake. The differences could be attributed to the cell type, material

composition or even cell viability. Furthermore the uptake pathways for these studies were determined by exclusion studies using pharmacological inhibitors, which may not be reliable. Inhibitors are rarely specific, and down regulating one pathway can result in up regulation of other pathways to compensate as was shown in a study by Vercauteren *et al*[21]. Although the literature may be contradictory there is evidence to suggest differentially charged sensors are processed differently.

5.2.2.2 Endosomal escape

Surface charge has been hypothesised to play a central role in two key mechanisms of endosomal escape, namely the proton-sponge method and through membrane disruption by pH-sensitive endosomal escape agents. These are important mechanisms routinely incorporated into multifunctional nanocarriers to promote delivery to the cytoplasm[30].

The proton sponge hypothesis is a theory first proposed by Behr in 1997[94] stipulating that cationic buffering polymers absorb protons in the endosome, resulting in a charge imbalance, which causes the influx of counterions, most notably Cl^- into the endosome. The ensuing osmotic imbalance leads to an influx of water into the endosome resulting in swelling, rupture and release of the contents. Sonawane *et al*[226] conducted an important study supporting this hypothesis, where the chloride concentration, pH and endosomal volume was measured over time using ratiometric probes in cells exposed to strongly buffering cationic polymers. The results show an increase in chloride concentration in endosomes exposed to strongly buffering cationic polymers polyethylenimine (PEI) or polyamidoamine (PAM), was accompanied by elevated pH compared to control cells (5.9 to 5.3). In addition to this, endosomal rupture was observed after 45 minutes following a 20% increase in the relative volume of endosomes. However the mechanism remains controversial because many cationic polymers with strong buffering capacity have shown poor endosomal release properties. In addition to this Benjaminsen *et al*[203] recently conducted a study using ratiometric sensors to measure lysosomal pH finding that endosomal buffering polymers such as PEI do not alter lysosomal pH. In this study, polymeric pH nanosensors were incorporated into lysosomes of HepG2 cells. The cells were then exposed to polyethylenimine-DNA polyplexes (PEI-DNA). Transfection was not correlated to a change in lysosomal pH. This may be expected if the buffering of pH by PEI is counteracted by the action of V-ATPase proton pumps, which maintain the acidity of the lysosome, however there are other factors to consider. The authors used a theoretical model of a lysosome to

approximate the critical size a lysosome can expand to before it bursts due to osmotic pressure, which is dictated by the concentration of PEI in lysosomes. By measuring the concentration of PEI in lysosomes, they found that lysosomes would typically have to be > 1 μm before they burst in a cell, as a conservative estimate. This is clearly not possible suggesting the proton sponge effect is not the major route of endosomal release. It may be that the proton-sponge effect may be a less potent effector of endosomal release than originally thought.

Surface charge is also linked to membrane disruption, which could result in enhanced endosomal escape. Experimental and theoretical studies of cell free membrane particle interactions, suggest cationic particles disrupt cellular membranes. In a notable study by Leroueil *et al*[280] several cationic materials used for drug delivery including PMAM dendrimers, TAT peptides and polyethylenimine were tested for the disruptive effect on a model supported lipid bilayer using AFM. All these materials were found to result in either pore formation or a thinning of the membrane. This has also been seen in studies by Mecke *et al*[281] and *Verma et al* [282]. It has long been hypothesized that this facilitates endosomal escape however there is no direct evidence in cells to support this.

Endosomal escape remains a major bottleneck for the intracellular delivery of nanomedicines. Increasing understanding of the mechanisms of this process is important for the development of more potent endosomal escape agents and therefore more efficacious nanomedicines.

5.2.2.3 Influence of serum proteins

Most studies on the internalisation of charged nanoparticles are conducted in serum free conditions because proteins bind to cationic nanoparticles altering their physicochemical properties[11]. This effect is substantial to the extent that particles are considered to have a biological identity distinct to their synthetic identity once placed in biological environment[283]. Studies aiming to isolate the effect of physicochemical characteristics on intracellular trafficking are often conducted in serum free conditions, so that these characteristics are not changed radically in the biological environment. However consideration of how a particle interacts with serum proteins are required to move towards more clinically relevant investigations of fundamental particle trafficking.

When nanoparticles are exposed to biological conditions proteins are immediately adsorbed to the surface of the particle resulting the formation of a 'corona'. This corona has been proposed to be the main factor determining the biological

identity of a particle to a cell. This is a theory first put forward as a concept by Cedervall *et al*[284] in 2007. Since then, corona formation has been reported on silica[285], gold[286] and polystyrene nanoparticles[287]. Corona formation occurs through the initial deposition of a monolayer of proteins on to the surface ('hard layer'), this is a tightly bound layer on the particle. On top of this layer, is a transient layer of proteins, which is continuously exchanged as the nanoparticle moves through different biological environments ('soft layer'). An important question is how the formation of this corona affects cellular uptake. This is not easy to answer, because the binding of proteins is in a constant state of flux inside the cell. However it is clear that corona plays a key role in nanoparticle-cell interactions.

5.2.3 Challenges for the delivery of siRNA therapeutics

RNA interference (RNAi) is a naturally occurring pathway found in many eukaryotic cells whereby gene expression is inhibited by post translational gene silencing mediated by small RNA molecules termed microRNAs (miRNA)[288] and short interfering RNAs (siRNA)[289-291]. miRNAs are endogenously produced in mammalian cells and have an important role in modulating natural function, in contrast siRNAs are not produced endogenously. Both miRNAs and siRNAs have been utilised in therapeutic applications, this work focuses on therapeutic applications of siRNAs. Delivery is a major challenge for siRNA-based therapeutics because their physicochemical characteristics mean they do not readily cross cell membranes. Therefore delivery systems have been developed to facilitate transport. These systems primarily enter the cell by endocytosis and subsequently localise to endosomes and lysosomes. siRNA must be released from endosomes into the cytoplasm to avoid degradation in lysosomes and enter the RNAi pathway. The low-efficiency of this process is a bottleneck for the effective application of siRNA therapeutics. Intracellular pH measurements from nanosensors have potential to increase understanding of escape from the endosome, aiding the rational design of delivery systems for siRNA formulations optimised for endosomal escape.

5.2.3.1 Mechanism of RNAi by siRNA

RNAi by siRNA is initiated by the cleavage of long sequences of exogenously produced double stranded RNA (dsRNA) in the cytoplasm by the enzyme Dicer dsRNA is cleaved into short 21-23 nucleotide long fragments called siRNA[292,293]. siRNA released by Dicer associates with the RNA-induced silencing complex (RISC) where a multifunctional protein, Argonaute 2 unwinds the siRNA and removes the sense strand[293,294]. The RISC complex in its activated state carrying

antisense siRNA, binds to complementary mRNA. The target mRNA is then cleaved preventing translation[294]. The activated RISC complex can seek out other complementary mRNAs to cleave, propagating the gene silencing effect[295]. RNAi mediated knockdown can be maintained for 3-7 days in rapidly dividing cells and for several weeks in non-dividing cells[295]. A common approach in RNAi therapeutics is to introduce synthetic siRNA in order to reduce expression of a disease associated gene. This eliminates the need for Dicer and also reduces the chance of an innate immune response and any aberrant alteration in gene expression that can occur due to the interaction of long strands of dsRNA with intracellular RNA receptors[296]. siRNA based therapeutics have great potential because effective application would present a broader spectrum of targets than conventional small molecule drugs.

5.2.3.2 Barriers to siRNA delivery

Although siRNA based therapies have progressed quickly into early stage clinical trials, many issues with the delivery of siRNA to their intracellular targets still remain unresolved[3]. The barriers to siRNA delivery depend on the mode of administration. Generally regional delivery has fewer obstacles compared to systemic delivery. Considering systemic delivery via intravenous injection, siRNA enters the bloodstream and is distributed through the blood circulation; in this model siRNA also undergoes elimination. Once in the organism RNA must leave the intravascular space within a blood vessel to enter the intestitum, siRNA is then transported across the interstitial space to the target cells. siRNA must then cross the cell membrane and enter the cytoplasm.

In order to enter the RNAi pathway, siRNA must be delivered into the cytoplasm in a form where it can associate with the RISC complex. However siRNAs do not readily cross cell membranes due to their physicochemical characteristics. These include sensitivity to degradation, negative charge and large size (13kDa). In some therapeutic applications, chemically modified siRNA has been introduced to cells without a delivery system. These studies have shown some potential but this is limited to more accessible physiological environments such as the eye and lung. In most other tissues, a delivery system is required to facilitate transfection into the cytoplasm. Consequently delivery systems for siRNA have been the subject of intense research (reviewed Gallas et al[297]).

In addition to crossing cell membranes, these systems also address other more general obstacles to delivering siRNA to the cytoplasm, such as low retention time in the body and non-specific cell targeting. But crossing the plasma membrane

and subsequent intracellular trafficking is a barrier that must be overcome by all siRNA-based therapies regardless of the delivery strategy.

5.2.3.2.1 Endosomal escape

As with many other nanomedicines, low efficiency of endosomal escape is seen as bottleneck in siRNA delivery and also, gene delivery[5,219,298]. Optimisation of endosomal escape will increase knockdown efficiency, making drugs more potent and also reduce therapeutic concentrations of siRNA required for a therapeutic effect. This is particularly important because over saturation of cells with exogenously introduced siRNA can interfere with cellular components involved in the endogenous RNAi pathway, resulting in off-target effects and/or trigger an innate immune response[299,300]. Toxicity is seen by many as the single greatest obstacle to the development of siRNA therapeutics[3].

Researchers aiming to develop effective drug delivery strategies for siRNA have developed different strategies to optimise endosomal escape (reviewed in Dominska et al[32]) these delivery systems incorporate fusogenic lipids, endosomal buffering polymers, fusogenic peptides, pore-forming peptides and agents for photochemical internalisation. Fusogenic lipids are specialised lipids that merge with endosomal membranes in a way that results in a structural change to the membrane. In an aqueous environment most lipids form into thin bilayer sheets (lamellar phase), however fusogenic lipids form into cylindrical like structures (hexagonal phase). In a study by Koltover *et al*[301] lipids adopting hexagonal phase structures were shown to fuse with model endosomes (G-vesicles), promoting transport across the endosomal membrane. Fusogenic lipids such as dioleoylphosphatidylethanolamine (DOPE) incorporated in lipoplexes have successfully been used to increase knockdown efficiency in vitro[302]. Endosomal buffering polymers prevent acidification inside endosomes by acting as 'proton-sponges' (discussed in section 5.1.3.2). Fusogenic peptides are specific peptide sequences found on viral envelopes, which destabilise endosomal membranes. These were derived from the study of how viruses deliver DNA to the cytoplasm. The most commonly used sequences are derived from a fusogenic N-terminal domain found on the HA2 subunit of a heamagglutinin protein from the influenza virus[303]. diINF-7 is an example of a fusogenic peptide derived from this protein. It has been shown to result in a 2-fold increase in the knockdown of EGFR gene expression in human epidermoid cancer cells in comparison to a commercially available transfection agent, Lipofectamine[42]. Pore forming peptides are derived from viruses (viroporins)[304] and function by creating channels in the cell

membrane. Recently an envelope glycoprotein found in the HIV virus (gp41) was complexed with PEI and was shown to enhance delivery of nucleic acids in HeLa cells[305]. Photochemical internalisation is another technique that has been used to enhance endosomal escape. By this technique, a photosensitisor is co-transfected with siRNA[306]. A reactive oxygen species is generated when the photosensitisor is exposed to light resulting in the destabilisation of the endosomal vesicle and release of siRNA into the cytoplasm. The short half-life of the photosensitisor means that the membrane of the endocytic vesicle is damaged without affecting any other organelles within the cell. This method has been shown to enhance knockdown efficiency of EGFR by siRNA in human epidermoid cells[53].

Strategies for targeting siRNA to a specific cell type are well developed compared to strategies specifically designed for intracellular targeting. This is because there are several challenges for researchers when studying intracellular trafficking. With around 64,000 papers on endocytosis describing a diverse array of proteins and mechanisms, the first challenge is to understand the sheer complexity of transport mechanisms[14]. Transport mechanisms are also dynamic meaning time course experiments must be considered. In addition to this most organelles involved in intracellular trafficking are less than 500 nm in size so any imaging must be done at nano- scale resolutions. The most widely used approach for determining the amount of endosomal escape from a delivery system is to deliver fluorescently labelled siRNA into cells with fluorescently labelled organelles and observe any co-localization using fluorescence microscopy (see **section 4.2.2.2**). The disadvantage is that this approach is always limited by the selectivity of the marker being used. In addition, reliably quantitating co-localization from images is not straightforward. A different more quantitative approach for studying endosomal escape is subcellular fractionation[307], where specific organelles are isolated from a cell and the contents are analysed using an assay. Although this method can yield interesting results, membrane purity is an obstacle, it is time consuming and unsuitable for high throughput analysis. Membrane models[301] have also yielded information on how delivery systems interact with endosomes but again this is limited by incomplete knowledge of the structure of endosomes.

pH nanosensors offer a novel approach to understanding the intracellular trafficking of siRNA. In this work we have utilised pH nanosensors to measure pH changes as siRNA is trafficked through the cell. Yielding information on the location and the mechanisms of trafficking.

5.3 Materials and Methods

NS_{esc} sensors were used for all experiments in this section. Nanosensors were synthesised by post-conjugation or pre-conjugation as stated. Methods for nanosensor fabrication are stated in **Chapter 2 section 2.3.2**. All images were obtained using widefield deconvolution microscopy; the parameters for experimental set up and image analysis were identical to those used in **Chapter 3 section 3.3.3** and **3.4** unless otherwise stated. Materials are stated if not mentioned previously.

5.3.1 Temporal pH measurements in different cell types

Measurements were performed in HeLa, 3T3 and JAWS II cells. Cells were cultured and maintained as described in **section 4.3.2**. Nanosensors synthesised by post-conjugation were exposed to cells for a total period 24 hours at a concentration of 100 µg ml^{-1}. Time course measurements were performed throughout the experiment. For time course imaging, cells were imaged and then placed back into a cell incubator at 37°C, 5% CO_2 until the next timepoint. pH measurements were performed as described previously. Approximately ~ 50 cells were imaged per timepoint.

5.3.2 Measurement of differentially charged nanosensors

Investigation of charge was conducted in 3T3 fibroblasts. Cells were cultured and maintained as described previously **section 4.3.2**.

5.3.2.1 Reagents

N-acryloxysuccinimide (NAS) (Sigma, UK).

5.3.2.2 Methods

5.3.2.2.1 Fabrication of differentially charged nanosensors

Nanosensors were synthesised by pre-conjugation utilising the generalised method described in **section 2.3.2.2.** Briefly fluorophores were conjugated to amine containing acrylamide monomers (APMA). The sensor was then synthesised by emulsion polymerisation, part exchanging acrylamide monomer with fluorophore-conjugated monomer. Positive charge was incorporated into the nanosensor through substitution of different amounts of acrylamide with (3-acrylamidopropyl) trimethylammonium (ACTA). A negative charge was

incorporated by addition of N-acryloxysuccinimide (NAS). The quantities used are summarised in **Table 5.2**.

Functional Group	Functionalisation reagent	Monomers (mg)		
		Acrylamide	N, N methylene bisacrylamide	Functionalisation reagent
Blank	-	540.0	160.0	-
Positive 2.5%	ACTA	522.5	160.0	23.3
Positive 5%	ACTA	505.0	160.0	46.7
Positive 20%	ACTA	400.0	160.0	186.7
Negative 5%	NAS	505.0	160.0	35.0

Acronyms: (3-acrylamidopropyl) trimethylammonium (ACTA), N-acryloxysuccinimide (NAS).

Table 5.2 Reagent quantities for synthesis of differentially charged nanosensors.

5.3.2.2.2 Nanosensor characterisation

The size and charge of nanosensors were characterised by DLS and Zeta sizing respectively. Particles were sized at a concentration of 5 mg ml^{-1}. For measurements in serum, samples were resuspended in serum containing media by sonication for ~ 20 minutes. Samples were then suspended in water to a final concentration of 5 mg ml^{-1} and sized immediately.

5.3.2.2.3 Assessment of cell viability

The toxicity of differentially charged sensors was investigated by an MTS assay for cell viability (see **section 4.3.2.2**). Differentially charged sensors were incubated with sensors for 24 h at a concentration of 0.1 mg ml^{-1}. The cells were then incubated with the MTS reagent for a further 4 h and absorbance was then measured at λ490 nm using a plate reader. The viability was normalised against untreated control cells following subtraction of media background from all samples.

5.3.2.2.4 Serum based measurements

For serum containing experiments, cells were grown and imaged in identical media with serum.

5.3.3 Investigation of intracellular trafficking of siRNA formulations

5.3.3.1 Reagents

Cell culture: Phenol red free RPMI, L-glutamine 200 mM, Fetal Bovine Serum (FBS). Trypsin (0.25 % w/v) - ethylenediaminetatraacetic acid (EDTA) (0.02 % w/v) (1X) supplemented with inorganic salts, phenol red and D-Glucose. Puromycin (Sigma, UK).

Aliquots of solutions of FBS and L-Glutamine were stored at – 20^{o}C. Aliquots were thawed at room temperature prior to use. Complete cell culture media and Trypsin-EDTA solutions were kept at 4^{o}C and used within 3 months. No antibiotics were used for cell culture.

siRNA transfection: Positive and negative control siRNA suspended in RNAase free H_2O (Eurogentec, UK). Opti-MEM I Reduced Serum Medium (1X, liquid) with L-Glutamine, 2400 mg/L sodium bicarbonate, HEPES, sodium pyruvate, hypoxanthine, thymidine, trace elements and growth factors. Lipofectamine2000 (lipid-based transfection reagent)*, siPORTAmine (polyamine-based transfection reagent), HiPerFect (lipid-based transfection reagent)* (QIAGEN GmbH). D – Luciferin (Caliper, USA).

siRNA was reconstituted to a concentration of 25 μM in RNAase-free H_2O supplied by the manufacturer and stored as 50 μl aliquots at -80^{o}C. Aliquots were thawed at room temperature prior to use, and returned to at -80^{o}C immediately. Care was taken to minimise freeze-thaw cycles. Transfection reagents were stored at 4^{o}C. A stock solution of D-Luciferin was stored at 15 mg ml^{-1} in PBS at -20^{o}C. The solution was thawed and diluted to a concentration of 0.15 mg ml^{-1}in PBS prior to use. This solution was protected from light at all times, stored at 4^{o}C and used within 1 week.

All reagents were supplied by Invitrogen, UK unless otherwise stated.

5.3.3.2 Methods

5.3.3.2.1 Cell culture

MCF-7 cells were obtained from the American type culture collection (ATCC). The cells were transduced to incorporate a luciferase expressing sequence and a sequence to confer resistance to puromycin.

Cells were cultured in phenol red free RPMI supplemented with 2 mM L-glutamine and 10% v/v FBS. Cells were passaged when 80% confluent in a cell culture

incubator at 37°C in a 5% CO_2 humidified atmosphere. Cells were passaged before confluence (3-5 days) by trypsinisation. Briefly for T-75 flasks, media was removed and replaced by 3 ml of trypsin-EDTA and left at 37°C / 5% CO_2 until cells detached (~ 5 – 10 minutes). 5 ml of culture media was then added to deactivate trypsin and cells were transferred to a 20 ml vial and centrifuged at 300 g for 5 minutes (acc/dec = 3). The supernatant was removed and cells were resuspended in cell culture media. Cells were passaged to the desired cultivation ratio (typically 1: 2) and transferred to a T-75 flask to a final volume of 15 ml.

In order to enrich the culture for adequately transduced cell lines, cells were subjected to puromycin selection once a week. By this method cells were incubated overnight in media containing 4µg ml^{-1} puromycin.

MCF-7-Fluc cells were frozen for long-term storage at -80°C in 1 ml of 10% DMSO at a concentration of ~ 1 x 10^6 cells/ml. Cells were reanimated prior by transferring frozen aliquots into a T-75 flask containing cell culture media. Cells were cultured through a minimum of 2 passages following reanimation before use in experiments. Cells were discarded after a maximum of 25 total passages.

5.3.3.2.2 siRNA transfection

Three reagents were used for siRNA transfection: siPORTAmine, Lipofectamine and HiPerFect.

On the day prior to transfection, cells were seeded into 96 well plates with 100 µl of growth media. Cells were seeded to result in a final confluency on the day of transfection of 50 – 60%. Accordingly approximately 4 x 10^4 cells were seeded per well.

The following transfection procedures are for one well of a 96 well plate. The quantities are summarised in **Table 5.3.**

Transfection Reagent	Amount of siRNA per well of 96 well plate				Volume of reagent µl	Volume of media µl
	Volume of 25 µM stock	Final Concentration nM	Mass ng	Moles picomoles		
Lipofectamine	0.25	62.4	83.3	6.3	1	100
siPORTAmine	0.25	101.6	83.3	6.3	0.75	61.5
HiPerFect	0.25	62.4	83.3	6.3	0.75	100

Table 5.3 Quantities of reagents used for siRNA transfection.

The quantities used were optimised based on the manufacturers recommendations for each transfection reagent.

Lipofectamine mediated transfection: Two solutions were prepared. In tube A 1 µl of Lipofectamine was mixed with 50 µl of Opti-MEM. In Tube B 0.25 µl of 25 µM siRNA was mixed with 50 µl Opti-MEM. Both solutions were then mixed together and left on a plate rocker for 20 minutes to allow complexes to form. Growth media was then removed from the cells and the siRNA containing solution was added.

siPORTAmine mediated transfection: 0.75 µl of siPORTAmine was mixed with 11.5 µl of Opti-MEM and incubated at room temperature for 20 minutes. 0.25 µl of siRNA was then added to the siPORTAmine solution and left for a further 20 minutes. This was then added to 50 µl of Opti-MEM. The growth media was then removed from the cells and replaced with siRNA containing media (62.5 µl total).

HiPerFect mediated transfection: 0.75 µl of HiPerFect, 25 µl OptiMEM, 0.25 µl siRNA and 65 µl growth media were mixed together and incubated for 5 – 10 minutes to allow complexes to form. Growth media was removed and replaced with siRNA containing media.

In order to minimise toxicity, sample plates were placed on a cell rocker for 5 – 10 minutes immediately following the addition of transfection reagents. Cells were left to incubate with the transfection reagents containing media for 5 -6 hours. This media was then removed and replaced with 100 µl fresh growth media, and left for a further 12 hours.

5.3.3.3 Assay for knockdown

Knockdown was measured by assaying for luciferase activity. The principle of this assay is that luciferase converts the D - Luciferin into a luminescent substrate, the amount of luminescence is proportional to the amount of luciferase activity. Consequently a reduction in luminescence reflects the amount of knockdown. Therefore to investigate the efficacy of transfection reagents in mediating knockdown, siRNA was designed to target the luciferase gene transduced into the cell line (target sequence: UCAGAGUGGUGCUGAUGUA). This was done in parallel with siRNA containing a non-targeted sequence as the negative control.

Following transfection, 1:100 solution of D - Luciferin in growth media (final concentration 0.15 mg ml^{-1}) was added to the cells and left for 10 minutes. Luminescence was then measured using a plate reader (FLUOstar Optima, BMG Labtech). In order to assay at different time points, D – Luciferin-containing media was replaced with fresh media until the desired time point.

5.4 Results and Discussion

5.4.1 Characterisation of pH transitions in different cell types

Initially HeLa cells were selected for temporal measurements. HeLa cells were selected because they are one of the most widely used cell lines in cell biology having been used as a model cell line for the development of many nanomedicines. Furthermore, nanosensor based measurements have been performed in this cell line, allowing for comparison[136,276]. Average pH was measured in HeLa cells to be 5.46 ± 0.15 after 1.5 h, this steadily decreased to 4.74 ± 0.12 after 6 h with no significant change at later time points (**Figure 5.2B**). The pH decrease was accompanied by a narrowing in the distribution of pH inside the cell after 3 h (**Figure 5.2A**). The corresponding images show a punctate distribution of vesicles, indicating trafficking through endosomes and lysosomes. Over time, nanosensor containing vesicles appear to cluster around the nuclear periphery suggesting transfer from early endosomes to lysosomes. This is in marked contrast to other studies where nanoparticle-based pH sensors, have been utilised to perform measurements in HeLa cells, following delivery by endocytosis. A study by Peng *et al*[136] reports a pH value of 7.2 following a 4 hour incubation of 50 nm silica-based sensors. However in another study using positively charged mesoporus silica based nanoparticles sensors, with similar physicochemical properties to the study by Peng *et al* by Chen *et al*[276] shows pH values were measured as ~ 6.0 over the same period. The source of these differences are likely to be due to differences in methodology for measurement, because the particles used have similar physicochemical characteristics. However the possibility that silica is trafficked by an alternative pathway cannot be excluded. This demonstrates the difficulty in making comparisons of measurements between different cell types using different materials.

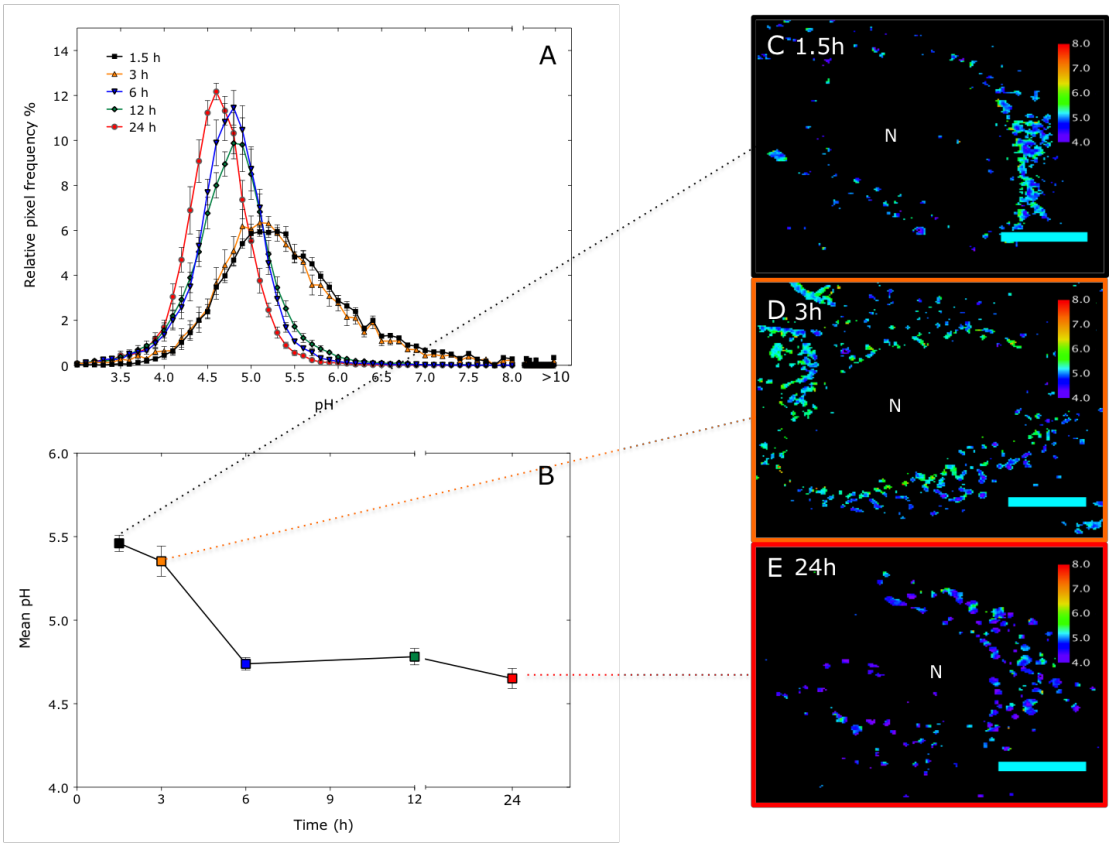

Figure 5.2 *Temporal pH measurement in HeLa cells.* (A) pH distribution in cells over different time points measured following exposure to nanosensors, pixels outside the calibration range are assigned pH > 10 (n =~ 50 cells from 3 independent experiments, error bars represent SD). (B) Corresponding mean pH. (n =~ 50 cells, error bars represent SD). (C,D,E) Representative colour mapped images at corresponding time points. Pixels outside the calibration range are represented as black pixels. Scale bar = 12 μm.

To make a standardised comparison of the differences in intracellular trafficking between different cell types, the experiment was repeated using the same methodology in 3T3 fibroblast cells. 3T3 cells were selected because this is another widely used cell line. Interestingly, 3T3 cells showed a different pH profile to HeLa cells (**Figure 5.3**) and (**Figure 5.4**). Although there was no significant difference in mean pH after 1 h exposure to nanosensors, pH was 0.4 pH units lower in 3T3 cells after 3 h. pH in 3T3 cells did not change significantly after 3 h whereas pH decreases in HeLa cells to a similar value to that seen in 3T3 cells after 24 h. For further comparison, the experiment was repeated in JAWS II cells. JAWS II cells are immature murine dendritic cells (DCs). DCs form an important component of the immune system; they are potent antigen presenting cells that play a key role in initiating T-Cell mediated immune responses and inducing immune tolerance[308,309]. In order to perform this function, DCs have a highly

regulated endocytic environment with elevated pH[310]. The pH measured in JAWS II cells showed the same progressive lowering of pH with time as HeLa and 3T3 cells, pH was elevated in these cells by ~ 0.31 pH units across the different time points.

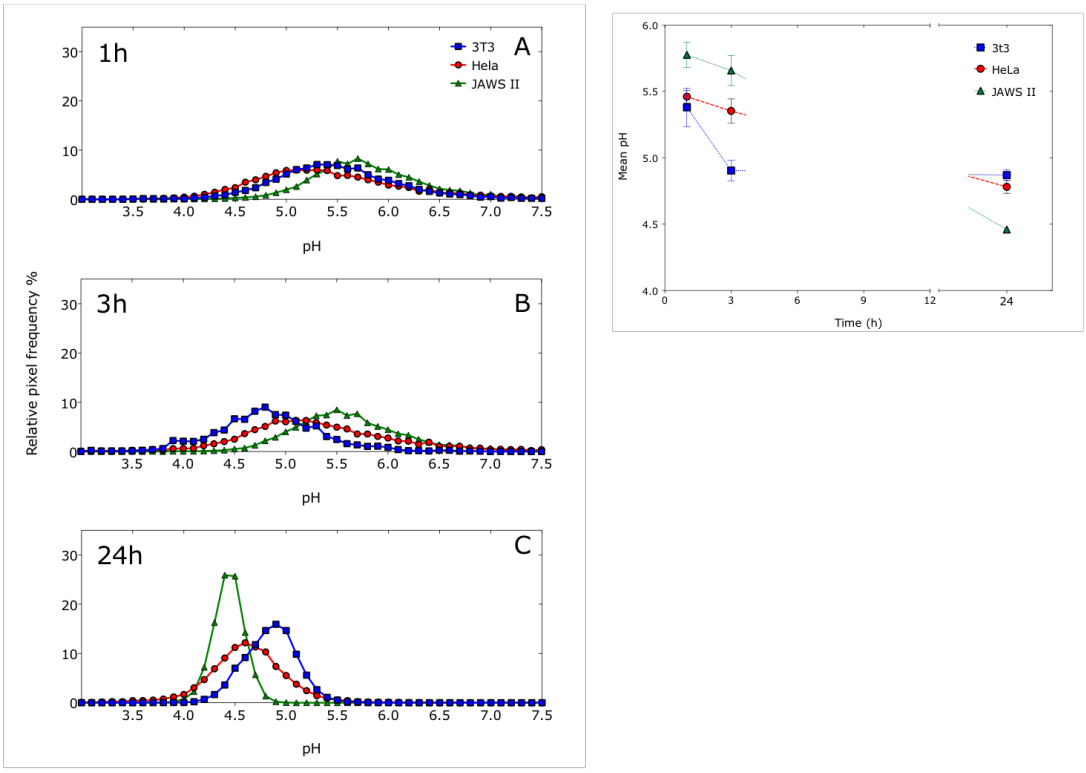

Figure 5.3 *Temporal pH measurements in different cell types.* (A,B,C) pH distribution in 3T3, HeLa and JAWS II cells measured following 24 h nanosensor exposure. < 0.5% of pixels were outside the calibration range for all images (n =~ 50 cells, error bars represent SD). (D) Mean pH in different cell types over 24 h (n =~ 50 cells from 3 independent experiments, error bars represent SD).

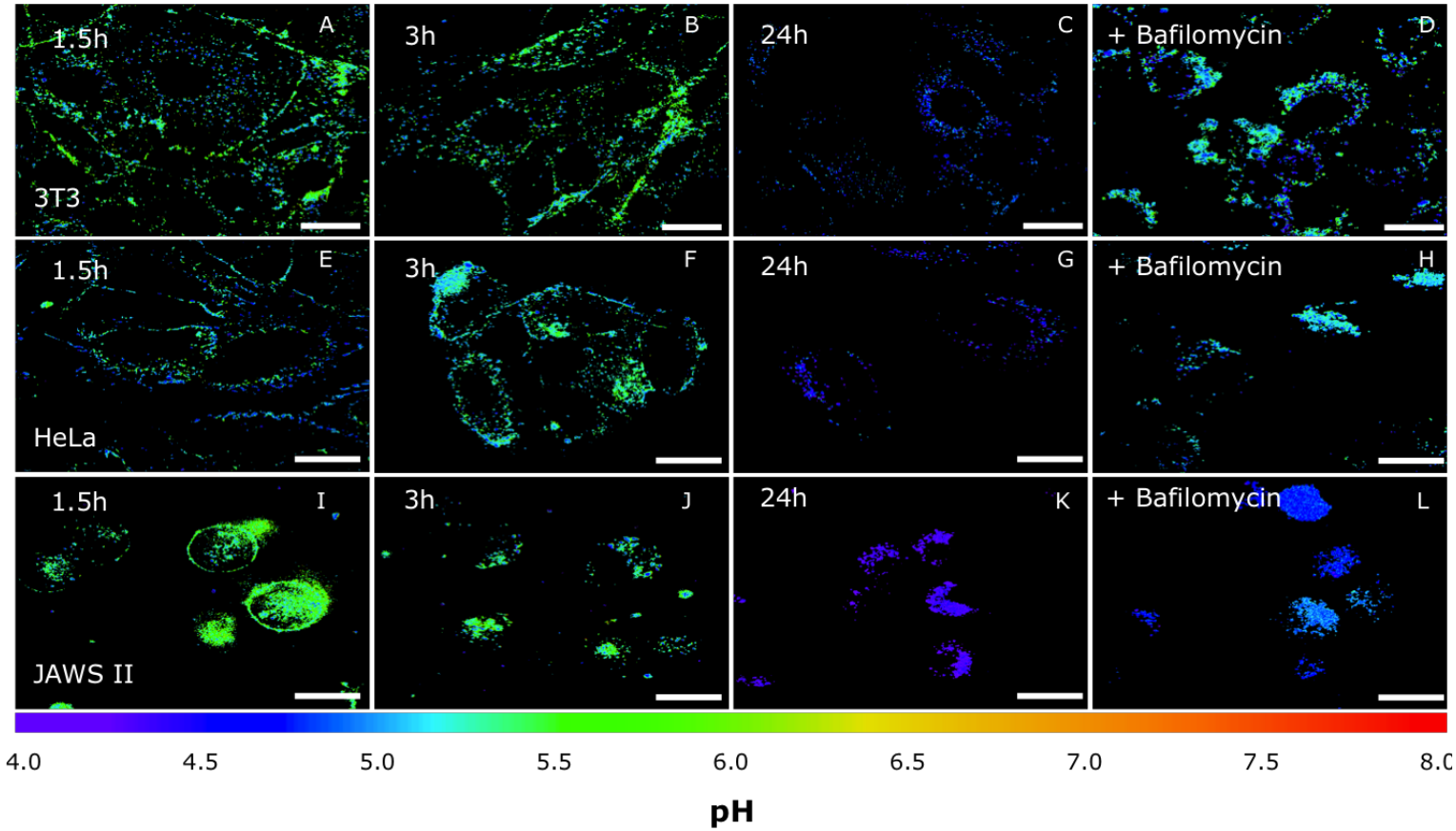

Figure 5.4 *Representative colour mapped images of temporal pH measurements in different cell types.* pH distributions were measured following nanosensor exposure at different time points (A,B,C) 3T3 cells. (D,E,F) HeLa cells. (I,J,K) JAWS II cells. (D,H,L) Cells after treatment with Bafilomycin A1. Pixels outside the calibration range are represented as black pixels. Scale bar = 18 μm.

There are several possible explanations for the differences in the pH profiles between different cell types. Firstly changes in pH in the endocytic pathway are closely related to intracellular location. Therefore the progressive decrease in pH could be from transport of nanosensors through early endosomes to lysosomes. This is reflected in colour-mapped images showing a characteristic punctate distribution at all time points. However measured mean pH values are all between ~ 5.0 and ~ 6.0 whereas endocytic vesicles in the earlier stages in the endocytic pathway have been seen to show pH values greater than 6.0[54]. An explanation for this is that the majority of sensors have already reached lysosomes and the progressive lowering of pH reflects a small proportion of nanosensors accumulating in lysosomes over time. Over time these nanosensors accumulate into the lysosomes resulting in the pH profile stabilising. Evidence for this can be seen in images shown in **Figure 5.4** where there is a change in the distribution of the colour mapped pixels. This would also correspond to other reports of pulse-chase experiments in the literature, which suggest material is rapidly transported in lysosomes within minutes[11].

Based on this premise, measurements from 3T3 and HeLa cells indicate nanosensors are trafficked into lysosomes faster in 3T3 cells. The reason for this could be that different cells employ different endocytic mechanisms to internalise the same materials as has been indicated previously[16]. There are other possible explanations for differences in pH between different cell types. For example, the increased pH in JAWS II cells may reflect endocytic regulatory mechanisms; alternatively elevated pH could be due to endosomal release. Further investigation is required to conclusively rule these out.

The insights from the pH profiles seen in this work are significant for the design of pH-sensitive nanomedicines. Many systems aim to release a drug before exposure to degraditive lysosomes[62]. In such cases the system needs to be tailored to the cell type, both in terms of the time taken for release and the pH were release must occur. For 3T3 cells, the trigger should occur within 3 hours, whereas for HeLa cells there is a longer time period for the release to occur before delivery in lysosomes, approximately 3 – 6 hours. For HeLa and 3T3 cells the pH trigger must be above pH 4.87 ± 0.13 and 4.782 ± 0.16 respectively. However as pH in the early stages of the endocytic pathway is higher in JAWS II cells hence the trigger must also be slightly higher to ensure release (pH 5.2 ± 0.01). This illustrates how these measurements could aid the design of delivery systems to specific cell types, however it is important to note that this is based

on the premise that polyacrylamide nanosensors are processed in the same way as the material under investigation. The validity of this premise is dependent on the type of nanomedicine under development.

5.4.2 Effect of surface charge on intracellular trafficking

In order to test the effect of charge on intracellular trafficking, differentially charged sensors were fabricated and used to perform measurements in 3T3 cells. Furthermore the effect of serum on the intracellular trafficking of differentially charged sensors was investigated.

5.4.2.1 Characterisation of charged nanosensors

Differentially charged nanosensors were synthesised by replacing acrylamide with different amounts of monomers containing positively and negatively charged groups (ACTA and NAS respectively), as shown in **Figure 5.5.**

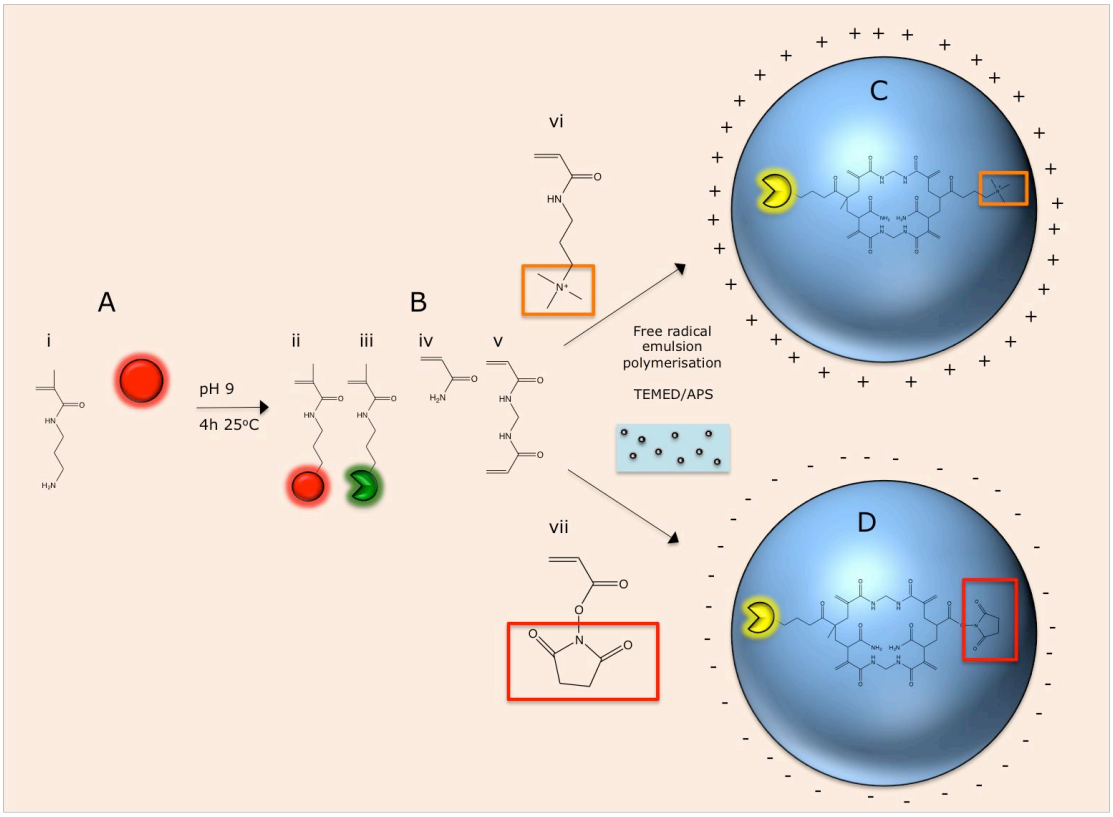

Figure 5.5 *Synthesis of differentially charged nanosensors.* (i) N-(3-Aminopropyl)methacrylamide hydrochloride (APMA), (ii) APMA conjugated to reference fluorophore (TAMRA), (iii) APMA conjugated to indicator fluorophores (Oregon Green, 5(6)-FAM), (iv) Acrylamide, (v) N, N methylenebisacrylamide, (vi) (3-acrylamidopropyl) trimethylammonium (ACTA), (vii) N-acryloxysuccinimide (NAS). (A) Conjugation of fluorophores to APMA. (B) Emulsion polymerisation of acrylamide monomers. (C) Positively charged nanosensor. (D) Negatively charged nanosensor. (Yellow represents a combination of reference and indicator fluorophores).

The amount of cross-linker was kept consistent, in an effort to maintain a uniform architecture and size in the particles. This resulted in a range of charged nanosensors from + 32.7 ± 0.93 to – 18.0 ± 0.81 (**Figure 5.6A**). Unexpectedly, a non-linear trend of increasing charge with increasing monomer concentration was seen for cationic nanosensors. Incorporating 2.5% to 10% w/w of ACTA into the nanosensor monomer mixture resulted in zeta potential of ~ +10 mV whereas increasing the concentration to 20% resulted in a large increase to +32.7 mV. There are two possible contributing factors, which are dictating this trend. Firstly, the amount of ACTA monomer incorporated into the particle, in which case there is a large increase in monomer incorporation from 10% to 20% ACTA but not between 2.5% and 10%. Secondly, changes to the overall polymeric architecture of the nanosensor. In this context, perhaps for low ACTA

composition nanosensors (< 10%), most charged monomers are located in the core, with relatively few exposed on the surface. But when the amount of charged monomer is increased to above a certain threshold, there is increased steric repulsion which forces groups to the surface of the sensor. This explanation seems more plausible as it is more likely to result in non-linear increase in surface charge with increasing monomer concentration. The exact composition of nanosensors could be determined to some extent by NMR spectroscopy as has been utilised previously[120], however investigating the architecture of the sensor is very difficult by standard techniques.

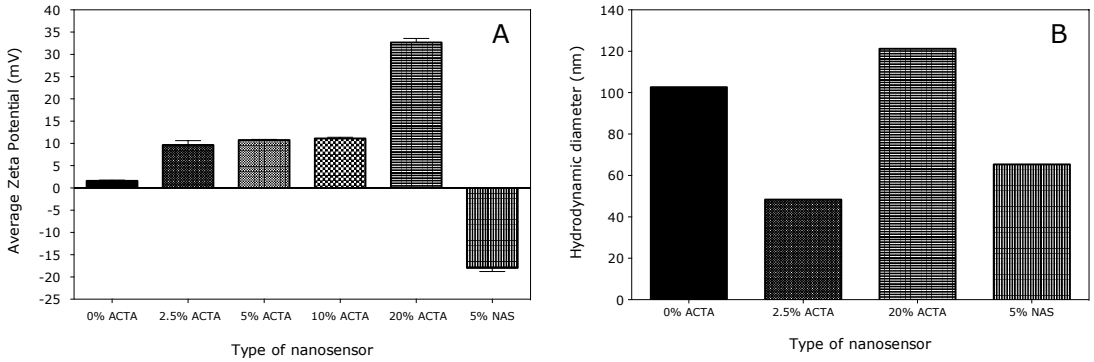

Type of nanosensor	Zeta Potential (mV)	Hydrodynamic diameter (nm)
0% ACTA	1.59 ± 0.18	102.7
2.5% ACTA	9.7 ± 0.97	48.37
5% ACTA	10.8 ± 0.15	-
10% ACTA	11.1 ± 0.30	-
20% ACTA	32.7 ± 0.93	121.2
5% NAS	18.0 ± 0.81	65.34

Figure 5.6 *Characterisation of differentially charged nanosensors.* (A) Zeta potential of nanosensors measured in PBS pH 7.4 (n = 3 measurements, error bars represent SD). (B) Hydrodynamic diameter of nanosensors measured in PBS. Table is a summary of results.

If there are changes to the polymeric architecture of nanosensors by incorporating different amounts of monomer these results show there is not an even distribution on the surface of the particle. This is important to consider for further applications, for example if sensors were to be functionalised with ligands to target a receptor mediated internalisation mechanism. For this study the polymeric architecture is not of great significance as small differences in the internal polymeric architecture are unlikely to affect cellular uptake.

Regardless of the architecture the particle size will play a role in uptake. The size of nanosensors was determined by DLS. All sensors were sized with a hydrodynamic diameter of less than 150 nm, however the strongly cationic sensors were larger than weakly cationic sensors (42 and 120 nm respectively) (**Figure 5.6B**). A possible reason for this difference is that the increased size may occur due to increased repulsion within the matrix resulting in less compact particle. For the purposes of this work, the ideal scenario would be to have all sensors of the same size. Although it is important to acknowledge the differences in the particle size of differentially charged sensors, previous literature utilising suggest that differences in size less than 200 nm do not have a radical impact on the endocytic route of uptake or the final intracellular location. In a study by Rejman *et al*[204] investigating the effect of size on uptake of fluorescent latex beads in B16 cells, sizes up to 50 nm particles were found to internalise much faster (30 minutes) compared to the corresponding 150 nm particles (several hours), however all particles were internalised by clathrin-mediated endocytosis, and were stably incorporated into late endosomal/lysosomal compartments after 12 h. This suggests a valid comparison can be made between differentially charged nanosensors providing intracellular location is assessed over long periods > 12 h.

5.4.2.2 pH measurements from differentially charged nanosensors

Intracellular trafficking was assessed by performing pH measurements using differentially pre-conjugated charged nanosensors in 3T3 fibroblast cells and following uptake in cells over a 24 h period in serum free conditions.

Firstly, the effect of differentially charged nanosensors on cell viability was tested using an MTS assay for cell proliferation (**Figure 5.7**)**.** All sensors showed a cell viability of greater than 85%, following 24 h exposure to nanosensors at a concentration of 100 μg ml^{-1}. This is in contrast to previous studies in HepG2 cells where cationic nanosensors (+23.9 mV) have been shown to demonstrate significant loss in cell viability at the same concentration[183], indicating good compatibility of 3T3 cells with polyacrylamide nanosensors.

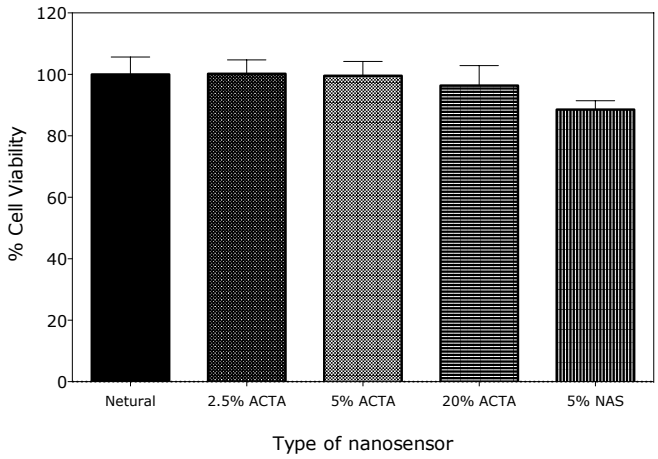

Figure 5.7 *Cell viability of differentially charged nanosensors.* Cell viability was measured by an MTS assay (absorbance measured at λ490 nm). Measurements are normalised against untreated cells. (n = 6, error bars represent SD).

Secondly, calibration curves were generated from differentially charged nanosensors (**Figure 5.8**)**.** Nanosensors were prepared using the same amount of fluorophores. Differentially charged nanosensors resulted in almost identical calibration curves. However anionic nanosensors (5% NAS) resulted in a less consistent calibration curve (**Figure 5.8C**). This could be due to fluorophores interacting with the monomer. As the overall response was similar, the sensor was deemed to be appropriate for measurement

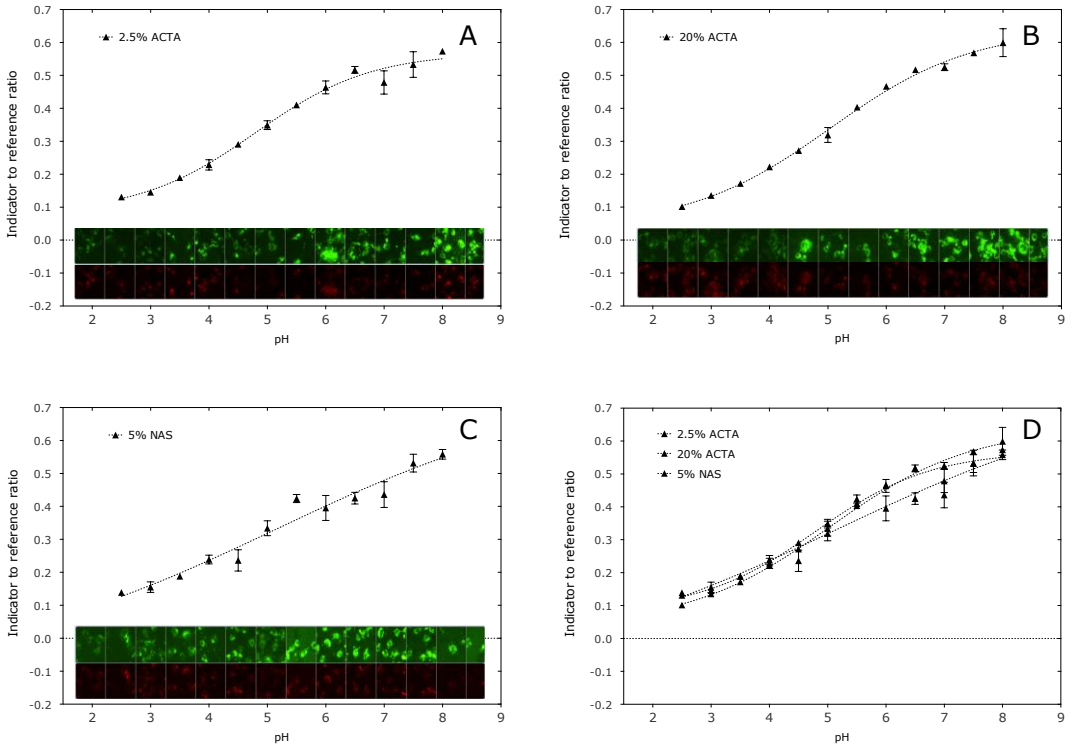

Figure 5.8 *Calibration of differentially charged nanosensors.* (A,B,C) Calibration of nanosensors synthesised with 2.5%, 20% w/w (3-acrylamidopropyl) trimethylammonium (ACTA) and 5% w/w N-acryloxysuccinimide (NAS) using deconvolution microscopy. (D) Collated calibration curves. (n = ~ 25, error bars represent SD). Images are representative images taken in the corresponding calibration condition.

Measurements were performed using weakly cationic (2.5% ACTA, +9.7 mV), strongly cationic (20% ACTA,+32.7 mV) and anionic (5% NAS, -18.0 mV) nanosensors (**Figure 5.9A**). Similar pH profiles were observed for all nanosensors, with large variation for weakly cationic nanosensors. The source of this variation is due to low overall uptake (**Figure 5.9D**). This resulted in few pixels above the threshold, increasing the likelihood of error in measurements. The lack of variation in measurements indicates that although there is greater uptake from strongly charged sensors perhaps by different uptake pathways, differentially charged sensors are trafficked to the same intracellular location. In contrast to this charge has been seen to effect intracellular location in similar study by Chen *et al*[276]. In this study ratiometric mesoporus silica nanosensors delivered by endocytosis were used to investigate the effect of charge on intracellular location in HeLa cells. Cationic and anionic sensors were synthesised with an average particle size of approximately 50 nm and Zeta Potential of – 40 mV and + 25 measured at pH 7.0. Following exposure to cells for 4 h pH was

measured in selected ROIs in cells using confocal microscopy, pH was found to be < 5.0 for negatively charged sensors and ~ 6.0 for the corresponding positively charged sensors. In further investigation cationic sensors were found to show less colocalisation with endosomal markers suggesting endosomal escape. Interestingly the monomers used to synthesise cationic nanosensors (N-trimethoxysilylpropyl-N,N,N-trimethylammonium chloride) has a weak buffering capacity, suggesting the main mechanism of release is more likely to be a membrane disruptive mechanism not the proton sponge effect. This could indicate that the role of charge in intracellular trafficking is dependent on the material and cell types, but also the membrane disrupting properties of the surface groups on the material. Further work is required is to clarify this.

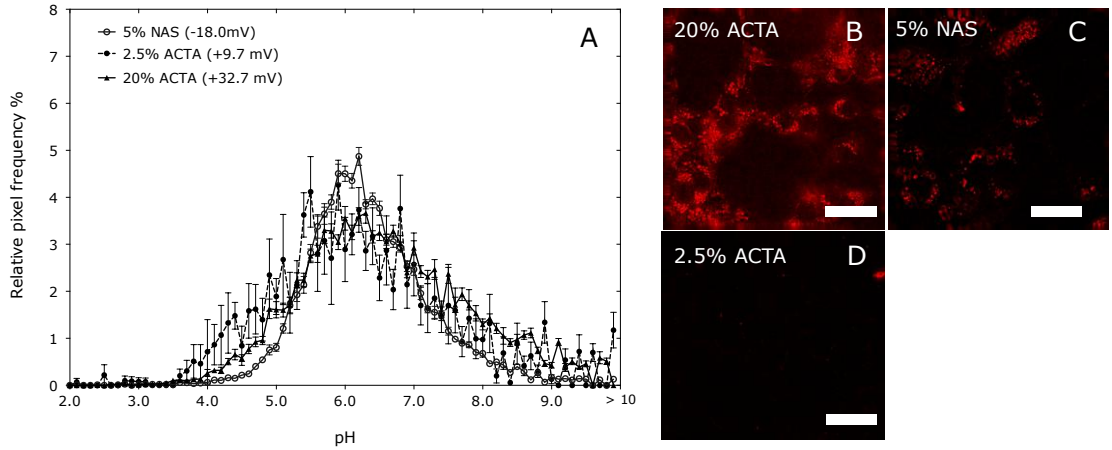

Figure 5.9 *Effect of charge on uptake and pH values in 3T3 cells. (*A) pH distribution following 24 h exposure to differentially charged nanosensors. Measurements outside the calibration range are presented as > 10 (n =~ 50 cells from 2 independent experiments, error bars represent SD). (B,C,D) Representative images showing uptake of nanosensors in 3T3 cells. Images of sensors are taken in the reference channel (TAMRA). Scale bar = 12 µm.

Although no difference was seen in measurements between differentially charged sensors, the average pH for all sensors was ~ 6.0, which is higher than observed for measurements performed in the previous section of this chapter (**Figure 5.3**) using post-conjugated sensors, where measurements were < 5.0 over the same time period using sensors of a similar charge (+ 16.7 mV). However in both cases nanosensors appear to be predominantly situated in lysosomes. This is shown by colocalisation of strongly cationic nanosensors with lysosomal markers (**Figure 5.10B,C**). Whereas for post-conjugated sensors this is confirmed by virtue of response to Bafilomycin A1 (**Figure 5.4D**). The difference could be attributed to

the surface groups on the sensors. For post conjugated sensors there are likely to be residual free amine groups on the surface of the sensor, which may alter the lysosomal environment of nanosensors manifesting as an increase in pH.

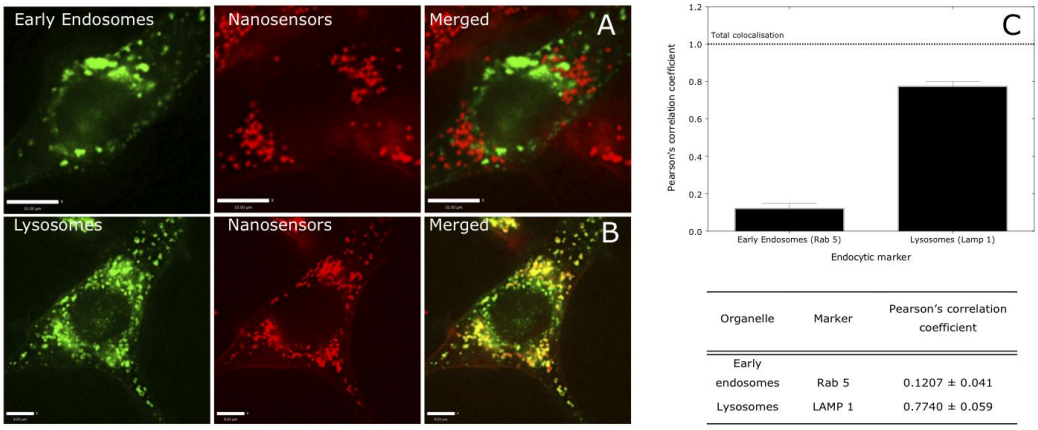

Organelle	Marker	Pearson's correlation coefficient
Early endosomes	Rab 5	0.1207 ± 0.041
Lysosomes	LAMP 1	0.7740 ± 0.059

Figure 5.10 *Colocalisation of cationic nanosensors with early endosomes and lysosomes in 3T3 fibroblasts.* (A,B) Representative images showing colocalisation of nanosensors with early endosomes after 24 h exposure. (C), measured Pearson's correlation coefficient from corresponding images (n = ~ 20 cells, error bars represent SD). Scale bar = 10 μm (top). Scale bar = 5 μm (bottom).

5.4.2.3 Effect of serum on pH measurements

To expand the investigation to more biorelevant conditions, the experiment was repeated in a serum containing media. The physicochemical characteristics of nanosensors were characterised in the presence of serum (**Figure 5.11**). This was found to have a substantial impact on the size and charge of nanosensors. For weakly and strongly cationic nanosensors the size was increased to 678.9 nm and > 1 μm respectively, whereas the size increase was only ~ 10 nm for negatively charged sensors (**Figure 5.11B**). The presence of serum also resulted in the neutralisation of the surface charge on the sensors (**Figure 5.11A**).

The change in physicochemical characteristics for positively charged nanosensors is presumably due to the formation of a protein corona around the nanoparticles. Conversely the lesser effect on the size of negatively charged nanosensors maybe due to charge repulsion of serum proteins. It is also possible the sizes of nanoparticles are artificially inflated due to the assumptions of the sizing method. DLS measurement is based on the assumption the particle behaves as a perfectly spherical object in a liquid of known viscosity. The presence of a protein corona may have an additional affect on how the particle diffuses through media.

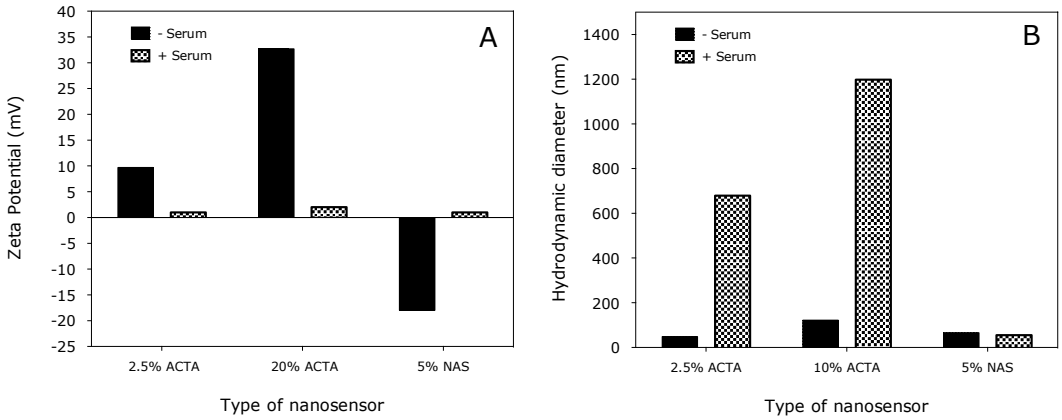

Figure 5.11 *Effect of serum on physicochemical properties of nanosensors. (*A) Zeta potential of nanosensors in the presence of 10% serum v/v pH 7.4. (B) Hydrodynamic diameter of nanosensors in the presence of 10% serum v/v pH 7.4.

One may expect the change in physicochemical characteristics to preclude uptake altogether, however sensors were taken up into 3T3 cells. Moreover there was little effect on pH measurements as shown in (**Figure 5.12.** A possible reason for this that there is a mixed population of sensors, the majority of which have are enclosed in a protein corona but critically a few are not. These few could be the sensors with the appropriate characteristics for cell uptake. Alternatively particles could be taken up with the protein corona but are trafficked to lysosomes regardless.

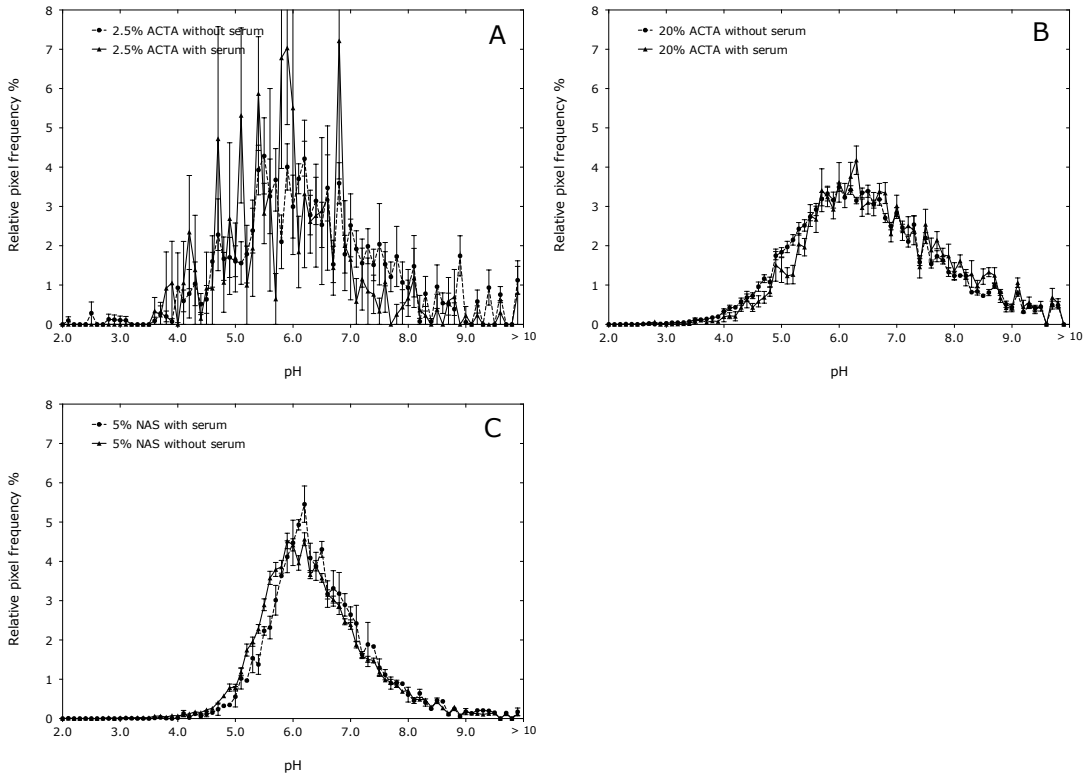

Figure 5.12 *Effect of serum on pH measurements from differentially charged nanosensors in 3T3 cells.* (A,B,C) Measurements performed following 24 h exposure of cells to nanosensors substituted with 2.5% ACTA, 20% ACTA and 5% NAS. (n =~ 50 cells from 3 independent experiments, error bars represent SD).

5.4.3 Investigation of intracellular trafficking of siRNA

In addition to understanding the effect of the fundamental physicochemical properties of nanoparticles on intracellular trafficking, nanosensors have the potential to yield biological insights into endosomal escape of drug formulations. As a proof-of-concept to show how this could be done, pH nanosensors were used to investigate trafficking of siRNA using commercially available transfection agents as 'test formulations'. Transfection agents used were Lipofectamine, siPORTAmine and HiPerFect. These were selected, because they are thought to facilitate delivery by different mechanisms. Although suppliers do not disclose the exact formulation of these agents, the type of formulation gives an indication of the mechanism of action. Lipofectamine and HiPerFect are cationic lipid based formulations thought to function by a lipid disruption mechanism, whilst siPORTAmine is polyamine based formulation, more likely to function by the proton-sponge mechanism.

An overview of the strategy taken to investigate intracellular trafficking of siRNA from test formulations is presented (**Figure 5.13**)**.** Essentially this approach involves the incorporation of nanosensors in lysosomes, which act as silent observers of the transfection process. Nanosensors report pH whilst, knockdown activity is recorded by a luciferase reporter assay, in which a reduction of luminescence indicates knockdown. The luciferase reporter system was generated in MCF-7 cells by transduction. In order for knockdown to occur siRNA is required to reach the cytoplasm, therefore knockdown is an indicator of intracellular location of siRNA. The key question to be answered is whether or not the trafficking of siRNA through endosomes and lysosomes correlates with a measured pH change from nanosensors.

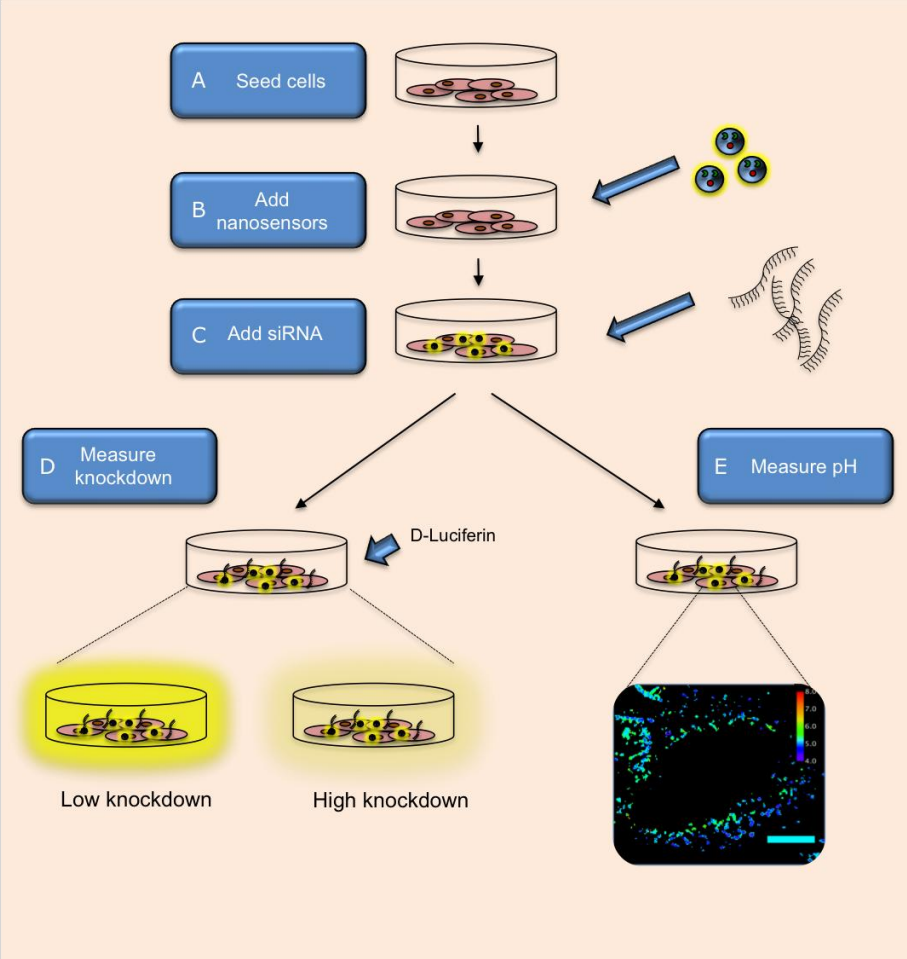

Figure 5.13 *Strategy for investigating intracellular trafficking of siRNA formulations using pH nanosensors.* (A) MCF-7 cells expressing luciferase seeded to result in 50% confluency at the start of the experiment. (B) Nanosensors added to deliver sensors to lysosomes. (C) siRNA targeted to luciferase is added, with the 'test formulation'. (D) Knockdown is measured. Substrate for luciferase is added (D-Luciferin) luminescence is measured. A reduction in luminescence indicates knockdown. (E) In a parallel experiment, pH is measured from nanosensors in lysosomes during transfection. Results are presented as a colour map or histogram.

5.4.3.1 Interference of nanosensors with intracellular trafficking of siRNA

In this strategy nanosensors are intended 'silent observers' of the trafficking process therefore it is important that the sensors do not affect the activity of the test formulations, and also do not affect cell viability. To test this, knockdown efficiency of test formulations, was compared in MCF-7 cells with and without nanosensors over 24 and 48 hours (**Figure 5.14A,B**). No significant differences in knockdown efficiency were observed for the different reagents after 48 h indicating nanosensors do not interfere with the transfection process. There was

some variation after 24 h particularly for Lipofectamine where cells with nanosensors showed a 24% increase in knockdown efficiency. As this trend was not seen at 48 h or in any other condition, this is likely to have arisen due to an experimental factor. One possibility is that differences in cell proliferation kinetics resulted in a lag phase, causing a reduction in luminescence at the early timepoint.

In order to test for nanosensor-associated toxicity under different transfection conditions, the overall luminescence of the cells was compared with an untreated control as shown in **Figure 5.14C.** Nanosensors delivered with siPORTAmine showed no change in luminescence indicating minimal toxicity, conversely HiPerFect and Lipofectamine showed a 28% and 47% reduction in luminescence respectively indicating significant toxicity. However nanosensors alone did not show any significant reduction in luminescence. From this we can deduce toxicity is linked to the test formulation. This confirms nanosensors do not interfere with the transfection process in MCF-7 cells.

5.4.3.2 Knockdown efficiency of transfection reagents

Knockdown efficiency of siPORTAmine (75.2%) and Lipofectamine (78.2%) is comparatively high. High knockdown efficiency is an indicator of delivery of siRNA to the cytoplasm. Conversely efficiency of HiPerFect is comparatively low (25%). This suggests only a small fraction of siRNA has reached the cytoplasmic site of action; consequently only siPORTAmine and Lipofectamine were considered for nanosensor measurements.

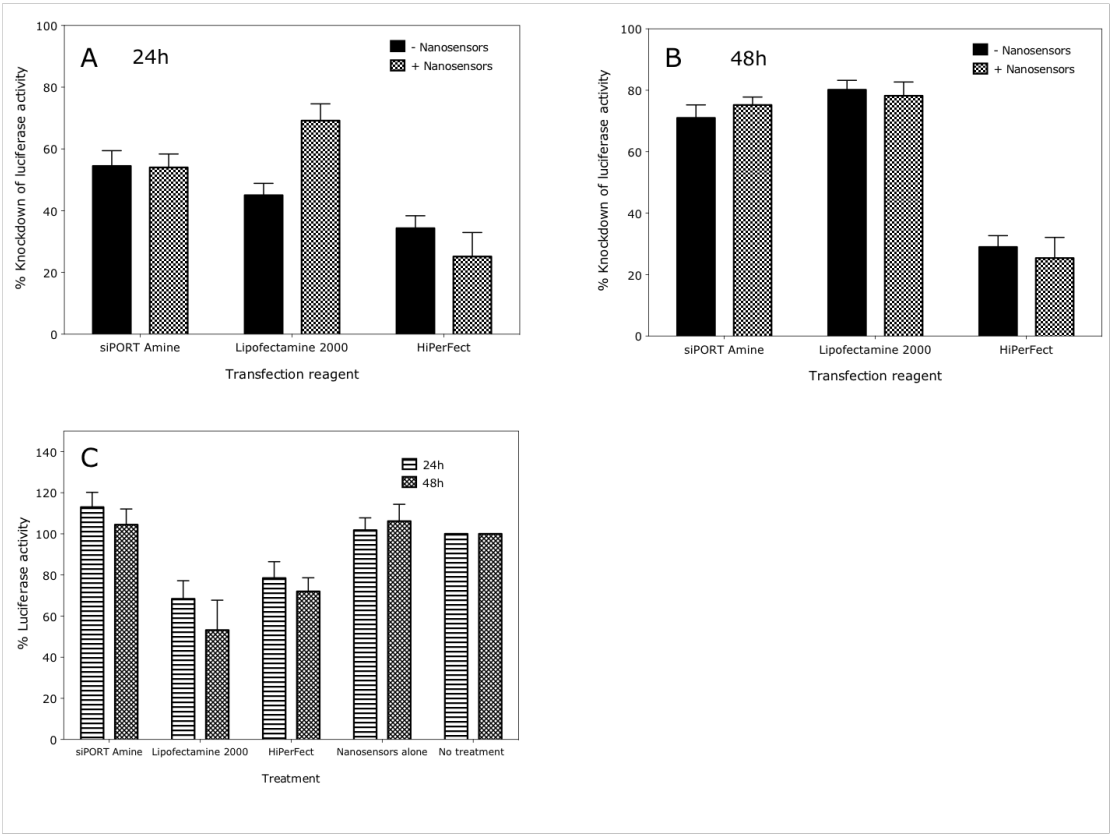

Figure 5.14 *Knockdown efficacy of transfection reagents measured by a luminescence assay in MCF-7 cells.* (A,B) Knockdown of luciferase activity by transfection reagents after 24 h and 48 h. Measurements are normalised against negative control siRNA. (N = 7 in 2 independent experiments, error bars represent SD). (C) Luciferase activity of cells following treatment with transfection agents. Luminescence is normalised against untreated cells. (n = 7, error bars represent SD).

5.4.3.3 Effect of transfection on pH measurements

pH measurement was performed in parallel to siRNA transfection utilising cationic and ionic nanosensors in separate experiments(**Figure 5.15A,B**).

Interestingly for untreated cells, elevated pH is reported from anionic nanosensors (~ 6.0) compared to cationic sensors (~ 4.7). This is in contrast to the measurements seen in 3T3 cells (**Figure 5.9**). This may indicate anionic sensors are delivered to an earlier stage of the endocytic pathway. However further work would be required to confirm this as similar values (~ 6.0) were measured in 3T3 cells, but colocalisation studies showed the majority of sensors were in lysosomes (**Figure 5.10B**)**.** There was little difference in pH profiles of cationic nanosensors during transfection mediated by the test formulations (**Figure 5.15A**). Whereas for anionic nanosensors a significant increase (~ 1 pH

unit), in measured pH for cells treated with Lipofectamine was observed compared to siPORTAmine and control cells (**Figure 5.15B**). Comparing the anionic and cationic sensors this suggests that the sensors are indeed delivered to different intracellular locations.

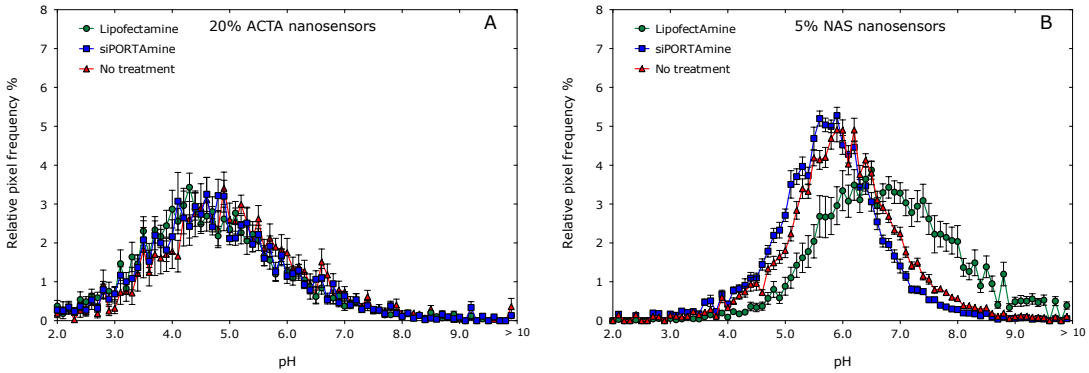

Figure 5.15 *Effect of siRNA transfection conditions on pH measurements after 24 h in MCF-7 cells.* (A) pH measurements from nanosensors with 20% ACTA w/w (+32.7 mV). (B) pH measurements from nanosensors with 5% NAS w/w (-18.0 mV). (n =~ 50 cells from 2 independent experiments, error bars represent SD).

Considering the anionic nanosensors, similar knockdown efficiency is observed for both siPORTAmine and Lipofectamine, from this we can deduce a similar amount of siRNA reaches the cytoplasmic site of action. The explanation for the change observed for different pH profiles is more ambiguous.

Measurements from untreated cells indicate nanosensors are delivered to endosomal and lysosomal compartments (pH < 6.0). Therefore, we can be confident Lipofectamine interferes with endosomes and lysosomes in some way during transfection. This interaction could result in an increase in pH in two ways, either Lipofectamine disrupts the lysosomes enough to cause rupture and release of nanosensors into the cytoplasm or Lipofectamine modulates pH inside endosomes and lysosomes without causing rupture. Considering the corresponding images in **Figure 5.16B**, it appears that there is a less punctate intracellular distribution of fluorescence indicating rupture of endosomes and lysosomes. Furthermore elevated pH would eventually lead to rupture of vesicles by the proton sponge-effect.

A compelling question is why no such change in pH is seen for siPORTAmine, when a similar amount of siRNA reaches the cytoplasm? Furthermore the images

in **Figure 5.16C** indicate a punctate distribution of fluorescence similar to control cells suggesting little endosomal disruption. This could occur either because siRNA transported by a different intracellular route or is released from endosomes and lysosomes by a different mechanism.

Considering the first explanation, siRNA delivered by siPORTAmine may be released in early stages of the endocytic pathway compared to Lipofectamine. A weakness in this explanation is that transfection efficiency increases from 24 h to 48 h in the same way as for Lipofectamine, however if there was rapid release, one might expect less of an increase over this time period. An alternative explanation is that siRNA which reaches the cytoplasm represents a small fraction of the internalised siRNA, which doesn't pass through the endosomes and lysosomes at all. siRNA has been shown in many studies to be deposited in lysosomes[3], however it is not clear how much siRNA is required to be in the cytoplasm to induce an effect, therefore this possibility cannot be excluded.

Considering the second explanation siPORTAmine may mediate endosomal release through a subtle interaction which causes minimal disruption to endosomes and lysosomes. There is evidence that lipoplexed drug delivery systems produce transient pores in the cell membranes which could provide passage for the concomitant release of nanoparticles[231,301,311]Whereas the polyplexes could facilitate transit through the cell membrane by a more subtle interaction with the membrane. This could be a reason why increased toxicity is seen from the Lipofectamine mediated transfection (**Figure 5.14C**).

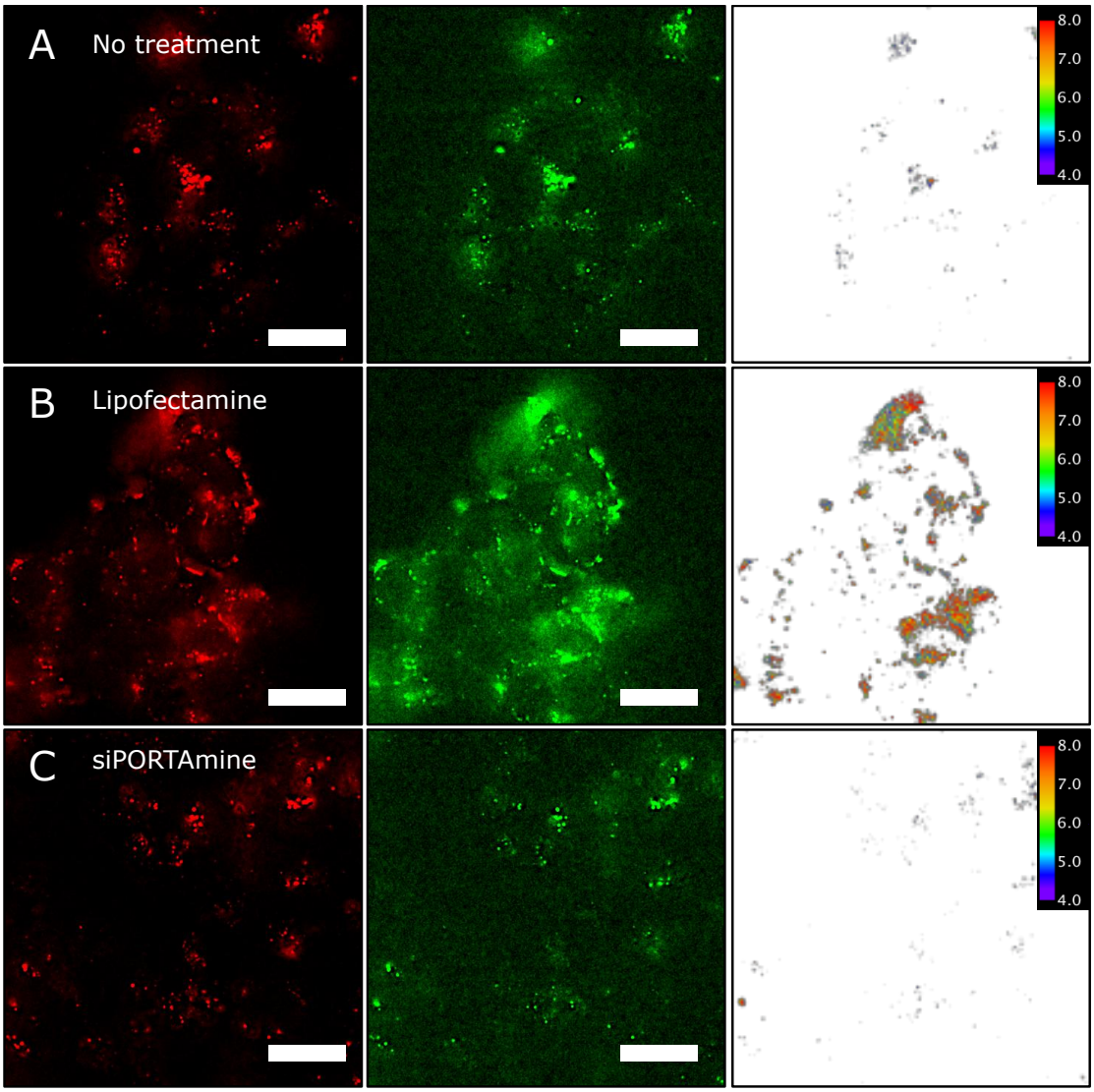

Figure 5.16 *Representative pH colour maps in MCF-7 cells following 24 h siRNA transfection*. Reference (left), indicator (centre), colour map (right). Measurements were taken following 24 h exposure to nanosensors followed by siRNA transfection (A,B,C) conditions for siRNA transfection. Black pixels in the colour maps are coloured white to improve visualisation. Scale bar = 15 μm.

5.5 Conclusions

The aim of this chapter was to evaluate potential applications of pH nanosensors for generating biological insights into the intracellular trafficking of nanomedicines. This was done with the view of using these insights to aid the rational design of nanomedicines. This work demonstrates potential applications of pH nanosensors for optimising pH-sensitive nanomedicines, investigating the effect of physicochemical characteristics on intracellular trafficking and for understanding the intracellular trafficking of siRNA formulations.

Considering the pH profiles of the cell lines closely we have seen significant differences in the extent of acidification in the endocytic pathways of these cells. 3T3 cells were seen to transfer nanosensors into lysosomes more rapidly than HeLa or JAWS II cells, whilst JAWS II cells showed an elevated pH profile, maintaining the same progressive lowering of pH and change in distribution seen with other cell types. From this we can conclude that there are differences in the acidification pathways of different cell types, which can be used to optimise delivery. Specifically we see that for 3T3 cells endosomal escape must occur more rapidly (< 3 hours) to avoid degradation in lysosomes and for JAWS II cells the pH-triggered release threshold must be set higher than other cells to avoid the same fate. The next stage of this work is to demonstrate tailored released systems release drugs more efficiently.

The potential for using pH nanosensors to investigate of the effect of physicochemical characteristics on intracellular trafficking was tested by performing measurements using differentially charged sensors in 3T3 cells. Cationic and anionic sensors resulted in similar pH profiles. From this we can conclude that for polyacrylamide particles, surface charge does not impact the final intracellular location of nanosensors in 3T3 cells. This was in contrast to pervious reports, which have demonstrated charge affects intracellular location. A key challenge for these studies was keeping other parameters, such as size of nanoparticles consistent whilst altering the surface charge. Further investigation is required to understand the role surface charge can play in controlling the location of nanoparticulate drug delivery systems.

Interestingly similar pH profiles for sensors in the presence and absence of serum were observed, although there was a significant change in the physicochemical

characteristics of the nanosensors when measured by light scattering techniques. From this we conclude that differences in the biological identity of a particle caused by the presence of serum may not affect its final intracellular location when internalised by endocytosis.

A novel method approach for determining the intracellular location of siRNA formulations based on pH nanosensors was investigated. By this method pH nanosensors were delivered to lysosomes in MCF-7 cells expressing luciferase. siRNA was then delivered to the cells using commercially available transfection reagents as 'test formulations'. Knockdown was measured by a luminescence assay and linked to the pH profile reported by the sensors during transfection. We found that nanosensors could be incorporated into the cells without any effect on cell viability or the activity of transfection reagents, shown by similar knockdown efficiencies in the presence and absence of nanosensors. pH measurements were conducted during transfection using cationic and anionic nanosensors. Anionic nanosensors reported an elevated pH compared to cationic nanosensors, suggesting localisation in the early part of the endocytic pathway. There was no change in the pH profile for cationic nanosensors during transfection under any condition, however there was a marked increase in pH when cells containing anionic nanosensors were transfected with siRNA mediated by Lipofectamine compared to siPORTAmine. The corresponding images show endosomal disruption for Lipofectamine mediated transfection, suggesting a different mechanism for release. Although further investigation is required to understand the mechanism of release, this demonstrates how pH nanosensors may be useful for investigating the extent of endosomal release from siRNA formulations.

Chapter 6 Conclusions and Future work

6.1 Conclusions

The overall aim of this thesis was to design and apply pH nanosensors in order to gain new biological insights into the fundamental aspects of the intracellular trafficking of nanoparticles, with the intention that these insights will aid the rational design of drug delivery systems. In order to do this a nanosensor was designed with optimal properties for measurement in the endocytic pathway (**Chapter 2**), methodology for performing intracellular measurements was then optimised and validated (**Chapter 3,4**). Finally the nanosensor was used to develop biological insights. The key conclusions from these investigations are summarised in the following sections.

6.1.1 Design of nanosensors for measurement of intracellular pH

Reliable measurement of intracellular pH requires a sensor with suitable optical and physical properties. Several designs for polyacrylamide nanosensors were explored based on commercially available fluorophores as the sensing elements. The optimal design in terms of range, sensitivity and stability was found to be a NS_{esc} sensor design incorporating two pH-sensitive fluorophores, OG and 5(6)-FAM with a reference fluorophore, TAMRA (**Figure 6.1**). This sensor was measured to have a dynamic range between 3.7 and 7.3 with accuracy of ± 0.2. In addition to this, different methods of incorporating fluorophores into the sensor were explored to create the most robust sensor. Conjugating fluorophores to a functionalised monomer prior to nanoparticle synthesis was found to be the most efficient way of incorporating fluorophores into the particle, in terms of brightness and stability.

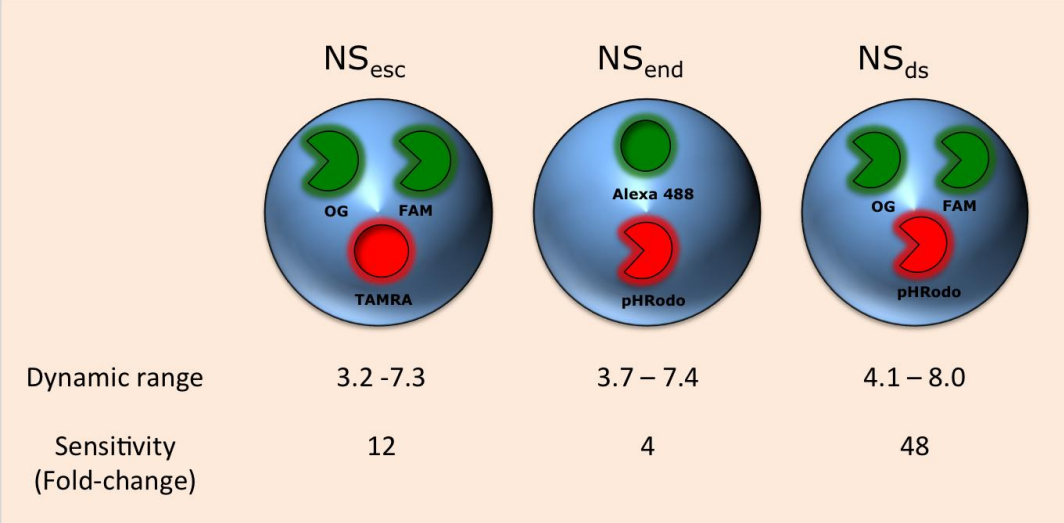

Figure 6.1 *Optimal sensor design for performing intracellular measurements.* The NS_{esc} was determined to be the optimal sensor design for intracellular measurements.

6.1.2 Optimisation of methodology for pH measurement

Any study seeking to apply nanosensors to yield insights into a biological process should be underpinned by reliable methodology. However there is a general lack of information in the literature on how to produce accurate measurements using nanosensors. Therefore a guide to performing ratiometric measurements was developed, based on several considerations that were found to affect measurements (instrument settings/experimental conditions, calibration conditions and image analysis) (**Table 6.1**). In general we found there are several pitfalls, which can bias a final measurement in all these areas. Hence measurement of pH requires meticulous experimental design. Image analysis in particular was found to result in large variations in data. However how this is addressed/carried out is not often reported in the literature and is likely to be the primary source of variations in measurements from similar studies. Utilising this methodology, pH measurements were performed in studies conducted at the University of Melbourne and the University of Nottingham using different instruments and materials, demonstrating the reproducibility of the method. In theory, the core principles and considerations are common for any ratiometric sensor utilised for performing intracellular measurements.

Process stage		Settings	Consideration	Design parameter
Nanosensor uptake	Image acquisition settings	Exposure and Gain	Minimise to avoid phototoxicity and photobleaching (<50 ms).	Maximum exposure used 10 ms
		Pixel size	Set below the resolution required with consideration to the Nyquist sampling theorem	Max pixel size used = 0.240 µm x 0.240 µm
		Deconvolution	Measure PSF experimentally, avoid algorithms which remove light	PSFs were measured and checked regularly, restorative algorithm was used
		Optical sectioning	Acquire multiple optical sections, for maximum information, set Z step size to within the axial resolution of the microscope. Take care to focus image	Optical sections of < 200 nm were used
		Alignment	Ensure adequate registration in channels used for the experiment	Alignment was check regularly using fluorescent beads
		Light source power	Ensure no fluctuations in the intensity of the light source during image acquisition	Fluctuations in lamp power checked by measuring intensity following repeated sample exposure
		Bleed through	Ensure no detectable bleed through is present. This can be minimised by using narrow band pass filters.	Checked experimentally
	Imaging conditions	Cell imaging chamber	Temperature, humidity and CO_2 need to be controlled.	Imaging chamber was modified to allow control atmospheric conditions
		Imaging time	Minimise imaging time to prevent affect on cell viability	Cells were imaged for a maximum of 2 hours at one time
Calibration	Image acquisition settings	As above	Should be kept identical to acquisition settings. Practically easier to determine image acquisition settings prior to calibration	Settings were kept identical
	Imaging conditions	Calibration conditions	Calibration conditions should match acquisition as closely as possible	Cells were calibrated in permeabilised cells
		Fitting calibration	Sigmoidal fit, R^2 should be more than 0.95	$R^2 > 0.95$ used for experiments
Image analysis	Variables	Background removal	Should be kept the same for calibration and nanosensor uptake if possible.	Measured using ROI based method and measurement of control cells
		Thresholding	Should be set to a level where there is minimal error	Set to where < 10% of pixels are outside the calibration range
	Other considerations	Optical sectioning	Consider central planes, take care to focus images	Only central planes considered for measurement
		Automation	Use software such as MATLAB or FIJI to automate image analysis. Should consider computational time as well	Scripts for batch processing were developed
		Weighting	Weighting gives information about the proportion of sensors reporting a pH as well as intracellular distribution	All images were weighted

Table 6.1 Summary of considerations for performing ratiometric intracellular measurements

6.1.3 Delivery of nanosensors to the endocytic pathway

In order to explore the application of nanosensors for yielding insights into intracellular trafficking, methods for delivering sensors to the endocytic pathway were explored. Increasing the surface charge (positive or negative) was found to promote the uptake of nanosensors into the endocytic pathway which is indicated by response of sensors to modulation of pH in endosomes and lysosomes (**Figure 6.2**)**.** The pH measurements following uptake correspond with localisation to lysosomes. However, further investigation of the intracellular location of nanosensors using fluorescence colocalisation microscopy, indicated partial colocalisation with early endosomes (widefield imaging). 3D-SIM super-resolution was used to definitively determine the intracellular location of nanosensors, this showed no colocalisation of sensors with early endosomes (**Figure 6.3**), this shows that pH measurements may be a more reliable indicator of intracellular location than widefield fluorescence colocalisation studies.

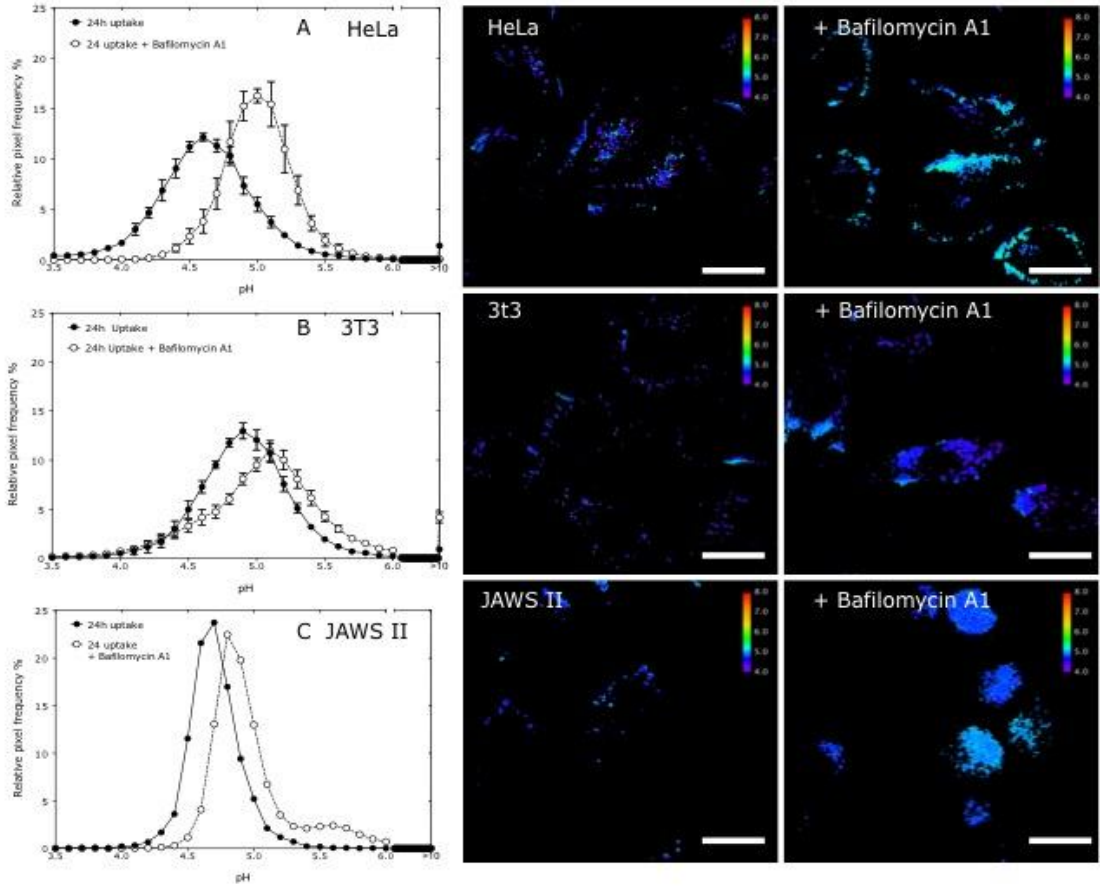

Figure 6.2 *Nanosensor response to inhibition of endosomal acidification.* This demonstrates responsiveness of sensors and delivery to the endocytic pathway. Scale bar = 15 μm.

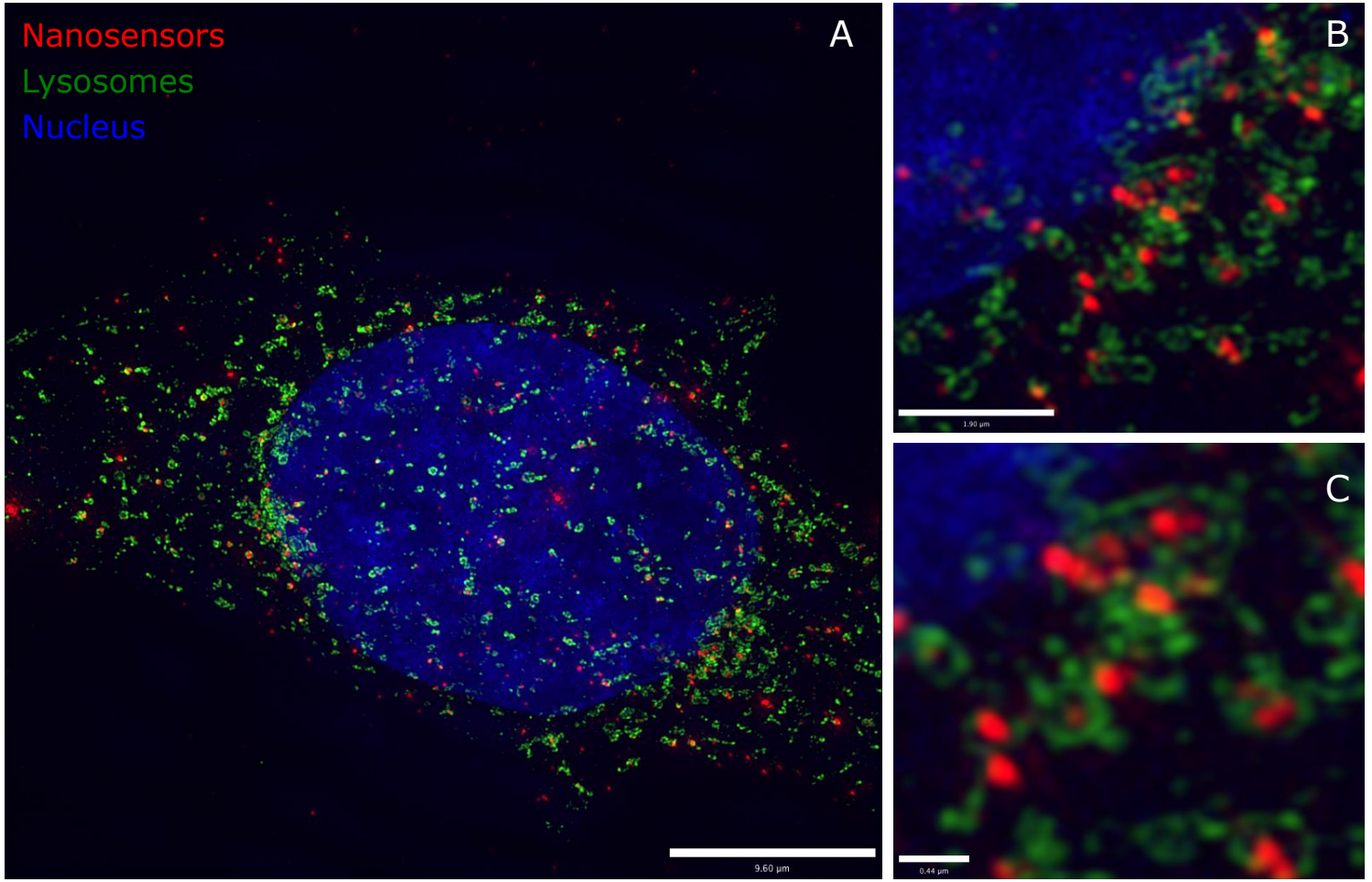

Figure 6.3 *Colocalisation of nanosensors with lysosomes in HeLa cells determined by 3D-SIM.* Lysosomes were labelled with CellLights markers for LAMP1 (green). Nanosensors (labelled with TAMRA only) (red) were exposed to cells for 24 h. (A) Scale bar = 9.6 µm. (B) Scale bar = 1.9 µm. (C) Scale bar = 0.44 µm.

6.1.4 Biological insights into intracellular trafficking from pH nanosensors

Nanosensors were used gain biological insights into intracellular trafficking in three investigations.

In the first of these, sensors were utilised to profile pH transitions occurring during intracellular trafficking in three common cell types used in drug delivery. Significant differences were found in terms of the rate at which pH transitions occur between different cell types (**Figure 6.4**). This insight has potential to be used to tailor the pH response of a nanomedicine to a specific cell type.

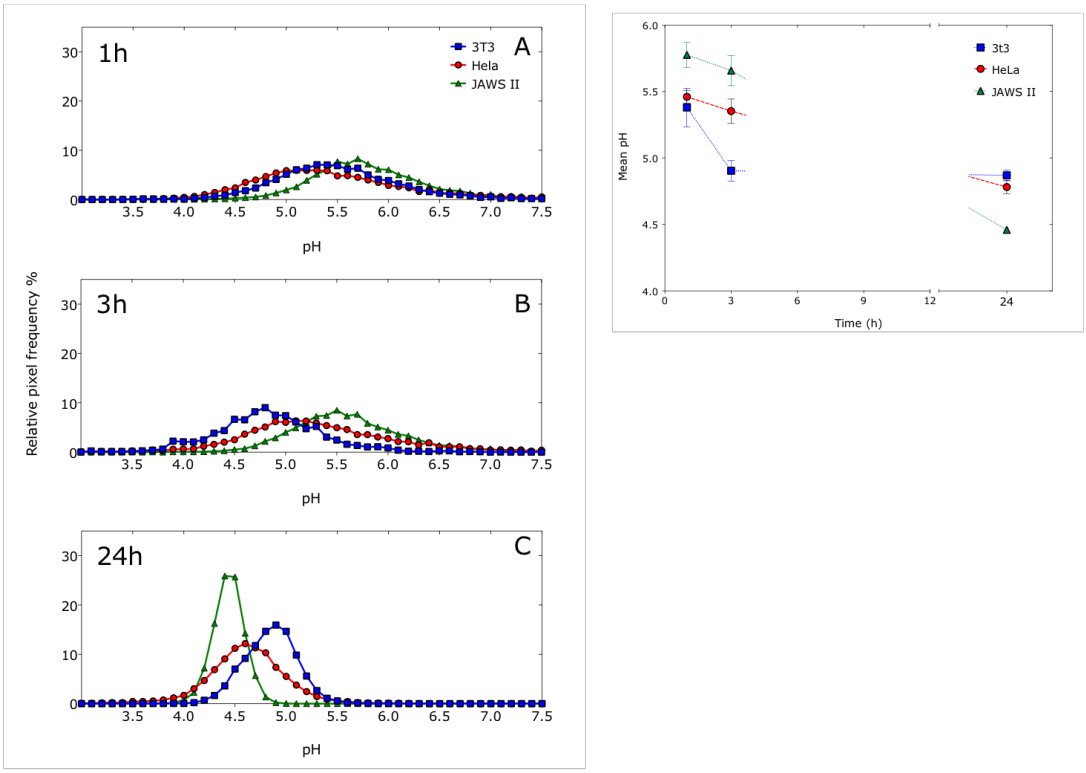

Figure 6.4 *Temporal pH measurements in different cell types.* (A,B,C) pH distribution in 3T3, HeLa and JAWS II cells over 24 h. < 0.5% of pixels were outside the calibration range for all images (n =~ 50 cells, error bars represent SD). (D) Mean pH in different cell types over 24 h (n =~ 50 cells from 3 independent experiments, error bars represent SD).

In the second investigation altering the effect of surface charge and serum conditions on intracellular trafficking was investigated. Surface charge and serum conditions had no effect on pH measurements, indicating particles of different charges are trafficked to the same intracellular location. This suggests altering surface charge alone is not a viable way of controlling the intracellular delivery of nanomedicines. Moreover this exemplifies the potential role of sensors in

understanding how the effect of the physicochemical characteristics of a material on intracellular trafficking can be investigated (**Figure 6.5**).

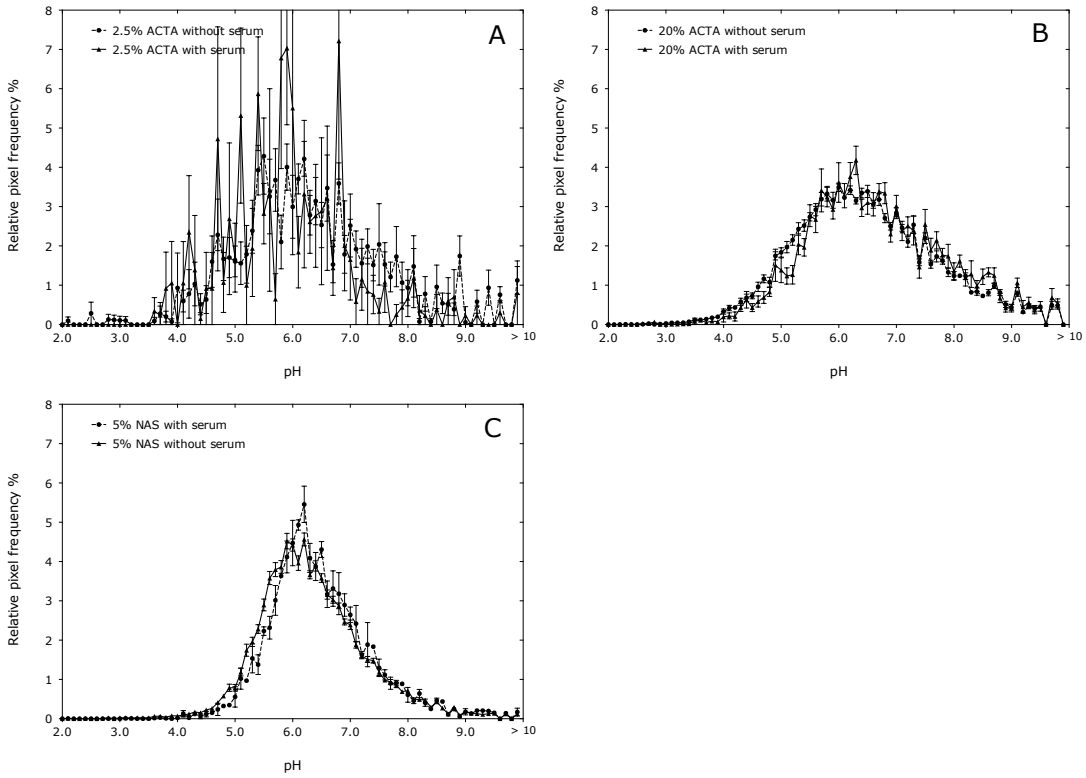

Figure 6.5 *Effect of serum on pH measurements from differentially charged nanosensors in 3T3 cells.* (A,B,C) Measurements performed using nanosensors substituted with 2.5% ACTA, 20% ACTA and 5% NAS. (n =~ 50 cells from 3 independent experiments, error bars represent SD).

In the final study, nanosensors were used to investigate the mechanism of endosomal release from siRNA formulations (**Figure 6.6**). A cationic lipid-based 'test formulation' (Lipofectamine) resulted in a large increase in measured pH whereas cationic polymer-based formulations did not, whilst providing similar levels of knockdown. This suggests Lipid-mediated transfection of siRNA is associated with a greater degree of lysosomal disruption compared to cationic polymer-mediated transfection, with the former observed to show increased toxicity. This insight gives information about mechanistic aspects of the delivery of siRNA, which has the potential to be used to optimize formulations. For example, in this case further studies could be done to optimize how Lipofectamine interacts with cell membranes via computer modelling.

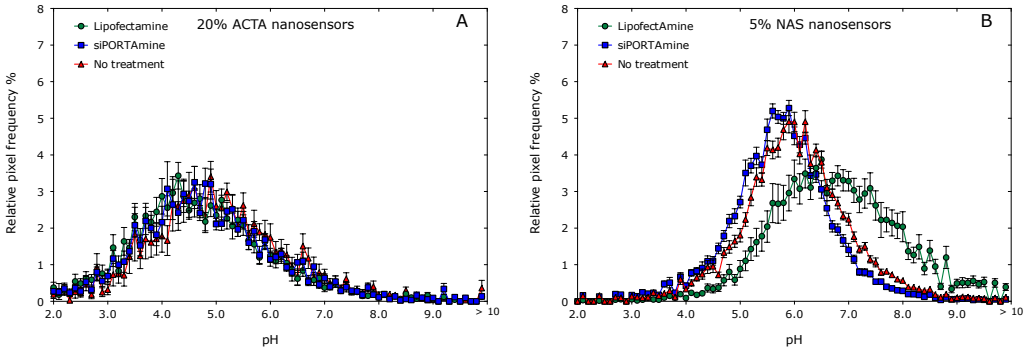

Figure 6.6 *Effect of siRNA transfection conditions on pH measurements after 24 h in MCF-7 cells.* (A) pH measurements from nanosensors with 20% ACTA w/w (+32.7 mV). (B) pH measurements from nanosensors with 5% NAS w/w (-18.0 mV). (n =~ 50 cells from 2 independent experiments, error bars represent SD).

6.2 Future perspectives

6.2.1 Improving the properties of optical nanosensors

In purely sensing terms, the development of these sensors will always be limited by the synthetic methods available to synthesise pH-responsive fluorophores. This represents a general limitation for the development of optical sensors, which utilise analyte-responsive fluorophores as the sole sensing and reporting component. Although this can be overcome by introduction of additional sensing components, such as enzymes[92,116,154] and ionophores[156-158], fluorescent probes still represent the most versatile approach. In an ideal situation it would be possible to synthesise fluorescent probes sensitive to any analyte, however methods for the *de novo* synthesis of fluorescent probes for many bio-relevant analytes are currently not available. Instead, high throughput screening based on combinatorial chemistry currently drives development in this field[312-314]. This approach involves the iterative interrogation of large structurally diverse libraries based on known molecular recognition structures to identify fluorescent molecules, which are sensitive to an analyte. The techniques, which are used to construct libraries, are much the same as those developed in the screening of compounds for drug discovery involving established organic methods such as click chemistry, Pd-catalysed couplings and condensation reactions[314]. Identifying suitable sensor molecules from these libraries requires careful design of assay platforms. In a typical process libraries are screened *in vitro* followed by more advance screens to determine cell permeability and localisation. This approach can be used to discover fluorescent probes sensitive to new analytes but also to optimise optical properties such as excitation coefficient and quantum yield[312]. These approaches are set to continue developing the field.

At present pH-sensitive probes are the best-developed probes available for biological measurement; indeed there is a greater array of fluorophores available for pH than for any other analyte. However there is not a single ratiometric fluorophore for measurement of the entire intracellular pH range, but as has been shown in this thesis, this can be achieved by selecting an appropriate combination of fluorophores. The photophysical properties of the fluorophores were also found to be adequate, although increasing the quantum yield would result in a more reliable measurement. Consequently in the wider context, a greater challenge now lies in the application of such sensors.

6.2.2 Future development of methodology for ratiometric measurements

The application of nanosensors for intracellular measurement is hampered by underdeveloped methodology for performing measurements[183]. Due to the sensitivity of measurements to variations in methods this makes the standardisation of methods to allow comparison between studies even more important. Aside from this, the further application of nanosensors is inexorably linked to the instruments available to detect fluorescence. This is a trade-off between the invasiveness of the technique, resolution and capability for high throughput. In this work widefield deconvolution microscopy was used, as a non-invasive high-resolution technique albeit one, which is less high throughput than other techniques such as fluorescent scanners or flow cytometry.

As our understanding grows in the field of nanomedicine, it has become apparent that in order to develop effective drug delivery strategies, the transport of the drug must be controlled inside the cell. Consequently, for sensors to be useful in this context a high-resolution approach becomes less of a trade-off and more of a necessity. Furthermore although widefield and confocal microscopes are the highest resolution widely available techniques for detecting intracellular fluorescence, these techniques are unable to resolve distances of less than ~ 250 nm, whereas many sub cellular structures are smaller than this. This makes it extremely challenging to ascertain whether a nanosensor is contained within a subcellular structure or merely in close proximity. Accordingly, opportunities for the field to develop will come from super-resolution technologies and high throughout approaches to fluorescence microscopy.

Super-resolution microscopy is a potential avenue by which the field of optical sensing can progress. The field of super-resolution microscopy encompasses a diverse range of techniques. Although these techniques aim to achieve the same objective, they are fundamentally different with implications in the context of sensing. The majority of these techniques require specialised photoswitchable fluorophores; these include STED[258], STORM/PALM[254] and associated derivatives. Exploiting these techniques will require the development of new fluorophores and sensing systems. Conversely other super-resolution techniques including SIM[255], 4Pi[259] and I^5M[260] essentially extend the resolution of conventional optical systems hence specialised fluorophores are not required. These techniques are also suitable for multicolour applications, which are needed for ratiometric sensing systems. An additional consideration for exploiting these systems is their suitability for live-cell imaging. Live-cell imaging requires non-invasive imaging as

well as adequate temporal resolution to monitor cellular dynamics. 4Pi and I^5M microscopies are essentially based upon conventional confocal and widefield setup respectively; hence both are theoretically suitable for live-cell imaging. A commercial version of the 4Pi microscope is available and has been used in several investigations of the uptake of nanoparticles in live cells including quantum dots[315] and zeolite nanocrystals[316]. As SIM is based on widefield microscopy, it is perhaps the least invasive super-resolution technique available. However SIM does require repeated light patterning to generate an image (typically 5 images are required to generate a single 2D image). This requires fluorophores to be relatively photostable. There are several examples of 3D SIM imaging of live cells using conventional fluorescent probes[317]. Furthermore imaging by SIM provides high frame rates up to 11 Hz enabling the almost real time tracking of cellular processes.

Super-resolution techniques have the potential to reveal new insights into biological process through optical nanosensors. At this point the growth in this area is only limited by the accessibility of these instruments.

However, a general limitation of using fluorescence microscopy techniques is that they low throughput compared to techniques such as flow cytometry and fluorescence scanning. During the course of this work, we have developed an automated system for image analysis but practically images of several hundreds of cells at high resolution can be acquired during an experiment at most, which is low compared to several thousands for other techniques, albeit at lower resolutions. The main reason for this that performing ratiometric measurements requires careful focusing which is time consuming, in addition to this imaging over long time periods increases the chances of photodamage and/or detrimental effects from suboptimal atmospheric conditions. Higher throughput techniques are required to answer broad questions such as what is the extent of endosomal entrapment in a cell population. High throughput or high content screening (HCS) microscopy techniques based on automated imaging systems have been in development for several years and have been used widely in systems biology[318], membrane trafficking studies[319] and for the automated determination of the subcellular location of proteins[320]. Conducting these studies require specialised robotic microscope systems with carefully determined instrument settings. Many of the considerations for development of these systems are the same as those for live-cell imaging, however there a few additional requirements. Perhaps most importantly the hardware must be set up for automated image acquisition. This requires automated stage movement, exposure control and focusing. Automatic

focusing is the limiting factor in most applications. Automatic focusing is currently achieved in two ways. Firstly, using software-based methods, which function by acquiring images in different planes and subsequently identifying the most in focus plane. The most in focus plane can be identified by measuring which plane has the most in focus objects or analysing signal variations. The second approach utilises infra red light to automatically position the focal point at certain distance from the imaging vessel. This distance can be determined by the operator or through an additional software-based procedure. Software-based procedures for automatic focusing are more accurate in general but require longer acquisition and exposure times. This can increase the chance of photodamage and limit the temporal resolution. The hardware-based approach is less time consuming, however it assumes there is little movement of the cells on the stage, which is rarely the case. For this reason software-based automatic focusing is most realistic for measurement using optical nanosensors. In addition to the automated aspects of image acquisition other conditions such as the excitation light source and atmospheric conditions must be kept stable during imaging.

Taking a high throughput approach to intracellular analyte measurement could result in new screens to assess to aid the rational design of drugs. For example pH measurements could be used to give quantitative information on the extent of endosomal entrapment. The success of these approaches will be primarily dependent on the precision of focusing mechanism.

6.2.3 Future applications of nanosensors for the study of intracellular trafficking

The field of optical nanosensors, and in particular pH nanosensors has developed to a level where a diverse range of sensors can be synthesised for intracellular measurement[104]. Moreover the capability of such sensors to provide robust measurements has been proven. This has laid a foundation from which researchers can ask diverse range of biological questions.

One area where this can be exploited further is in the field of targeted drug delivery. There are several examples where nanoparticle delivery systems are targeted to specific pathways to achieve subcellular localisation[27]. This is commonly achieved by the attachment of ligands to the surface of the nanoparticle, which correspond to a specific receptor. However it is difficult to ascertain the intracellular fate of these particles in comparison to those internalised by generic internalisation mechanisms. Of particular interest is whether or not the pathway by which a material is internalised results in different

extents of endosomal escape. Attachment of these ligands to a pH-nanosensors and concomitant measurement of pH is one way in which these questions can be answered. An example where this approach was pursued is a recent study by Sun *et al*[121]. In this study polyacrylamide pH nanosensors were targeted to CD44 receptors, which are overexpressed on the surface of cancer cells. Targeting was achieved by functionalising the polyacrylamide matrix with hyaluronic acid (HA), a ligand for the CD44 receptor. Although enhanced uptake was seen by HA functionalised nanosensors, pH profiles indicated lysosomal uptake after 24 h for both functionalised and unfuctionalised sensors. Although no difference was seen in this study there are broad range of other ligands and agents, which are uptaken by other pathways such as transferrin[321] and folate[322]. Additionally it would be interesting to investigate the effect of different endosomal escape agents when taken up into different pathways.

6.2.4 Using pH nanosensors for measurements in alternative biological environments

The work contained in this thesis is primarily concerned with intracellular measurement, however many of the methodologies and the sensors established here are applicable in other biological systems for example in different organisms and measurement of extracellular pH. An example of the former is a recent study by Chuahan *et al* where sensors were utilised to perform measurements in the nematode worm *Caenorhabditis elegans (C.elegans)*[220]*. C.elegans* has a highly regulated intestinal pH environment, which is important for the optimal function of digestive hydrolases. The digestion of material by the worm involves rapid transfer of material resulting in pH oscillations in the intestine, which were mapped using pH nanosensors. Another context where nanosensors are proving useful is for extracellular measurement[323]. This approach involves attaching nanosensors to a matrix, which supports cell growth. This has applications for the design of 3D cell models for *in-vitro* drug testing. From a general perspective, nanosensor technology has now developed to a stage where robust measurement methodologies have been demonstrated leading to a wide variety of potential applications, hence the growth in the number of studies where nanosensors are being used to gain biological insights is set to continue.

Chapter 7 References

1. Strebhardt, K. & Ullrich, A. Paul Ehrlich's magic bullet concept: 100 years of progress. *Nat Rev Cancer* **8,** 473–480 (2008).

2. Alexis, F., Pridgen, E., Molnar, L. K. & Farokhzad, O. C. Factors Affecting the Clearance and Biodistribution of Polymeric Nanoparticles. *Molecular Pharmaceutics* **5,** 505–515 (2008).

3. Whitehead, K. A., Langer, R. & Anderson, D. G. Knocking down barriers: advances in siRNA delivery. *Nature Reviews Drug Discovery* **8,** 129–138 (2009).

4. Zamecnik, J., Vargov, L., Homola, A., Kodet, R. & Sykov, E. Extracellular matrix glycoproteins and diffusion barriers in human astrocytic tumours. *Neuropathology and Applied Neurobiology* **30,** 338–350 (2004).

5. Jones, A. T., Gumbleton, M. & Duncan, R. Understanding endocytic pathways and intracellular trafficking: a prerequisite for effective design of advanced drug delivery systems. *Adv Drug Deliv Rev* **55,** 1353–1357 (2003).

6. Petros, R. A. R. & DeSimone, J. M. J. Strategies in the design of nanoparticles for therapeutic applications. *Nat Rev Drug Dis* **9,** 615–627 (2010).

7. Duncan, R. Polymer conjugates as anticancer nanomedicines. *Nat Rev Cancer* **6,** 688–701 (2006).

8. Berry, G. *et al.* The use of cardiac biopsy to demonstrate reduced cardiotoxicity in AIDS Kaposi's sarcoma patients treated with pegylated liposomal doxorubicin. *Annals of Oncology* **9,** 711–716 (1998).

9. Torchilin, V. P. Multifunctional nanocarriers. *Adv Drug Deliv Rev* **64,** 302–315 (2012).

10. Farokhzad, O. C. & Langer, R. Impact of Nanotechnology on Drug Delivery. *ACS Nano* **3,** 16–20 (2009).

11. Duncan, R. & Richardson, S. C. W. Endocytosis and Intracellular Trafficking as Gateways for Nanomedicine Delivery: Opportunities and Challenges. *Molecular Pharmaceutics* **9,** 2380–2402 (2012).

12. Duncan, R. & Gaspar, R. Nanomedicine(s) under the Microscope. *Molecular Pharmaceutics* **8,** 2101–2141 (2011).

13. Sahay, G., Alakhova, D. Y. & Kabanov, A. V. Endocytosis of nanomedicines. *J Control Release* **145,** 182–195 (2010).

14. Doherty, G. & McMahon, H. Mechanisms of endocytosis. *Annual review of biochemistry* **78,** 857–902 (2009).

15. Canton, I. & Battaglia, G. Endocytosis at the nanoscale. *Chemical Society Reviews* **41,** 2718 (2012).

16. Kumari, S., Mg, S. & Mayor, S. Endocytosis unplugged: multiple ways to enter the cell. *Cell Res.* **20,** 256–275 (2010).

17. Vercauteren, D. *et al.* On the cellular processing of non-viral nanomedicines for nucleic acid delivery: Mechanisms and methods. *J Control Release* **161,** 566–581 (2012).

18. Mousavi, S., Malerød, L., Berg, T. & Kjeken, R. Clathrin-dependent endocytosis. *Biochemical Journal* **377,** 1 (2004).

19. Mayor, S. & Pagano, R. E. Pathways of clathrin-independent endocytosis. *Nat Rev Mol Cell Biol* **8,** 603–612 (2007).

20. Simionescu, M., Popov, D. & Sima, A. Endothelial transcytosis in health and disease. *Cell and tissue research* **335,** 27–40 (2009).

21. Vercauteren, D. *et al.* The use of endocytic inhibitors to study uptake of gene carriers. *Journal of Controlled Release* **132,** e17–e18 (2008).

22. Zerial, M. & McBride, H. Rab proteins as membrane organizers. *Nat Rev Mol Cell Biol* **2,** 107–117 (2001).

23. Luzio, J. P., Parkinson, M. D. J., Gray, S. R. & Bright, N. A. The delivery of endocytosed cargo to lysosomes. *Biochemical Society Transactions* **37,** 1019–1021 (2009).

24. Pryor, P. R. *et al.* Combinatorial SNARE complexes with VAMP7 or VAMP8 define different late endocytic fusion events. *EMBO Rep* **5,** 590–595 (2004).

25. Luzio, J. P. *et al.* ESCRT proteins and the regulation of endocytic delivery to lysosomes. *Biochemical Society Transactions* **37** (**Pt 1**)**,** 178–180 (2009).

26. Maxfield, F. & McGraw, T. Endocytic recycling. *Nat Rev Mol Cell Biol* **5,** 121–132 (2004).

27. Rajendran, L., Knölker, H.-J. & Simons, K. Subcellular targeting strategies for drug design and delivery. *Nature Reviews Drug Discovery* **9,** 29–42 (2010).

28. Florence, A. T. & Hussain, N. Transcytosis of nanoparticle and dendrimer delivery systems: evolving vistas. *Adv Drug Deliv Rev* **50 Suppl 1,** S69–89 (2001).

29. de Duve, C. The lysosome turns fifty. *Nature cell biology* **7,** 847–849 (2005).

30. Varkouhi, A. K. A., Scholte, M. M., Storm, G. G. & Haisma, H. J. H. Endosomal escape pathways for delivery of biologicals. *Journal of Controlled Release* **151,** 220–228 (2011).

31. Hoekstra, D., Rejman, J., Wasungu, L., Shi, F. & Zuhorn, I. Gene delivery by cationic lipids: in and out of an endosome. *Biochemical Society Transactions* **35,** 68–71 (2007).

32. Dominska, M. & Dykxhoorn, D. M. Breaking down the barriers: siRNA delivery and endosome escape. *J. Cell. Sci.* **123,** 1183–1189 (2010).

33. Liang, W. & Lam, J. K. Endosomal escape pathways for non-viral nucleic acid delivery systems. *InTech* **17,** 421–467 (2012).

34. Prchla, E. Virus-mediated release of endosomal content in vitro: different behavior of adenovirus and rhinovirus serotype 2. *The Journal of cell biology* **131,** 111–123 (1995).

35. Simeoni, F. Insight into the mechanism of the peptide-based gene delivery system MPG: implications for delivery of siRNA into mammalian cells. *Nucleic acids research* **31,** 2717–2724 (2003).

36. Chernomordik, L. V., Melikyan, G. B. & Chizmadzhev, Y. A. Biomembrane fusion: a new concept derived from model studies using two interacting

planar lipid bilayers. *Biochim. Biophys. Acta* **906,** 309–352 (1987).

37. Browne, K. A. *et al.* Cytosolic delivery of granzyme B by bacterial toxins: evidence that endosomal disruption, in addition to transmembrane pore formation, is an important function of perforin. *Mol. Cell. Biol.* **19,** 8604–8615 (1999).

38. Plank, C., Oberhauser, B., Mechtler, K., Koch, C. & Wagner, E. The influence of endosome-disruptive peptides on gene transfer using synthetic virus-like gene transfer systems. *J. Biol. Chem.* **269,** 12918–12924 (1994).

39. Lear, J. D. & DeGrado, W. F. Membrane binding and conformational properties of peptides representing the NH2 terminus of influenza HA-2. *J. Biol. Chem.* **262,** 6500–6505 (1987).

40. Subramanian, A., Ma, H., Dahl, K. N., Zhu, J. & Diamond, S. L. Adenovirus or HA-2 fusogenic peptide-assisted lipofection increases cytoplasmic levels of plasmid in nondividing endothelium with little enhancement of transgene expression. *J Gene Med* **4,** 75–83 (2002).

41. Wagner, E. E., Plank, C. C., Zatloukal, K. K., Cotten, M. M. & Birnstiel, M. L. M. Influenza virus hemagglutinin HA-2 N-terminal fusogenic peptides augment gene transfer by transferrin-polylysine-DNA complexes: toward a synthetic virus-like gene-transfer vehicle. *Proceedings of the National Academy of Sciences of the United States of America* **89,** 7934–7938 (1992).

42. Oliveira, S., van Rooy, I., Kranenburg, O., Storm, G. & Schiffelers, R. Fusogenic peptides enhance endosomal escape improving siRNA-induced silencing of oncogenes. *International journal of pharmaceutics* **331,** 211–214 (2007).

43. Mastrobattista, E. *et al.* Functional characterization of an endosome-disruptive peptide and its application in cytosolic delivery of immunoliposome-entrapped proteins. *J. Biol. Chem.* **277,** 27135–27143 (2002).

44. Funhoff, A. M. A. *et al.* Poly(3-guanidinopropyl methacrylate): a novel cationic polymer for gene delivery. *Bioconjugate Chemistry* **15,** 1212–1220 (2004).

45. Funhoff, A. M. A. *et al.* Polymer side-chain degradation as a tool to control the destabilization of polyplexes. *Pharmaceutical research* **21,** 170–176 (2004).

46. Jiang, X., Lok, M. C. & Hennink, W. E. Degradable-brushed pHEMA-pDMAEMA synthesized via ATRP and click chemistry for gene delivery. *Bioconjugate Chemistry* **18,** 2077–2084 (2007).

47. Boussif, O. *et al.* A versatile vector for gene and oligonucleotide transfer into cells in culture and in vivo: polyethylenimine. *Proceedings of the National Academy of Sciences of the United States of America* **92,** 7297 (1995).

48. Pattrick, N. G., Richardson, S. C. W., Casolaro, M., Ferruti, P. & Duncan, R. Poly(amidoamine)-mediated intracytoplasmic delivery of ricin A-chain and gelonin. *Journal of Controlled Release* **77,** 225–232 (2001).

49. Lin, C. C. *et al.* Novel bioreducible poly(amido amine)s for highly efficient gene delivery. *Bioconjugate Chemistry* **18,** 138–145 (2007).

50. Mateos-Timoneda, M. A. M., Lok, M. C. M., Hennink, W. E. W., Feijen, J. J. & Engbersen, J. F. J. J. Poly(amido amine)s as gene delivery vectors: effects of quaternary nicotinamide moieties in the side chains. *Audio, Transactions of the IRE Professional Group on* **3,** 478–486 (2008).

51. Cheung, C. Y., Murthy, N., Stayton, P. S. & Hoffman, A. S. A pH-sensitive polymer that enhances cationic lipid-mediated gene transfer. *Bioconjugate Chemistry* **12,** 906–910 (2001).

52. Berg, K. K. *et al.* Photochemical internalization: a novel technology for delivery of macromolecules into cytosol. *Cancer research* **59,** 1180–1183 (1999).

53. Oliveira, S., Fretz, M. M., Hogset, A., Storm, G. & Schiffelers, R. M. Photochemical internalization enhances silencing of epidermal growth factor receptor through improved endosomal escape of siRNA. *Biochim. Biophys. Acta* **1768,** 1211–1217 (2007).

54. Casey, J. R., Grinstein, S. & Orlowski, J. Sensors and regulators of intracellular pH. *Nat Rev Mol Cell Biol* **11,** 50–61 (2010).

55. Llopis, J., McCaffery, J. M., Miyawaki, A., Farquhar, M. G. & Tsien, R. Y. Measurement of cytosolic, mitochondrial, and Golgi pH in single living cells with green fluorescent proteins. *Proceedings of the National Academy of Sciences of the United States of America* **95,** 6803–6808 (1998).

56. Stevens, T. H. & Forgac, M. Structure, function and regulation of the vacuolar (H^+)-ATPase. *Annu. Rev. Cell Dev. Biol.* **13,** 779–808 (1997).

57. Forgac, M. M. Vacuolar ATPases: rotary proton pumps in physiology and pathophysiology. *Nat Rev Mol Cell Biol* **8,** 917–929 (2007).

58. Asokan, A. & Cho, M. J. Exploitation of intracellular pH gradients in the cellular delivery of macromolecules. *J. Pharm. Sci.* **91,** 903–913 (2002).

59. Alarc n, C. de L. H., Pennadam, S. & Alexander, C. Stimuli responsive polymers for biomedical applications. *Chemical Society Reviews* **34,** 276 (2005).

60. Hoffman, A. S. Stimuli-responsive polymers: biomedical applications and challenges for clinical translation. *Adv Drug Deliv Rev* **65,** 10–16 (2013).

61. Shim, M. S. & Kwon, Y. J. Stimuli-responsive polymers and nanomaterials for gene delivery and imaging applications. *Adv Drug Deliv Rev* **64,** 1046–1059 (2012).

62. Gao, W., Chan, J. M. & Farokhzad, O. C. pH-Responsive Nanoparticles for Drug Delivery. *Molecular Pharmaceutics* **7,** 1913–1920 (2010).

63. Gerweck, L. E. L. & Seetharaman, K. K. Cellular pH gradient in tumor versus normal tissue: potential exploitation for the treatment of cancer. *Cancer research* **56,** 1194–1198 (1996).

64. Tannock, I. F. & Rotin, D. Acid pH in tumors and its potential for therapeutic exploitation. *Cancer research* **49,** 4373–4384 (1989).

65. Schmaljohann,D. Thermo- and pH-responsive polymers in drug delivery☆. **58,** 1655–1670 (2006).

66. Colombo, P., Sonvico, F., Colombo, G. & Bettini, R. Novel Platforms for

Oral Drug Delivery. *Pharmaceutical research* **26,** 601–611 (2009).

67. Peppas, N. A. Devices based on intelligent biopolymers for oral protein delivery. *International journal of pharmaceutics* **277,** 11–17 (2004).

68. Dai, S., Tam, K. C. & Jenkins, R. D. Aggregation behavior of methacrylic acid/ethyl acrylate copolymer in dilute solutions. *European Polymer Journal* **36,** 2671–2677 (2000).

69. Dai, J. *et al.* pH-sensitive nanoparticles for improving the oral bioavailability of cyclosporine A. *International journal of pharmaceutics* **280,** 229–240 (2004).

70. Griset, A. P. *et al.* Expansile Nanoparticles: Synthesis, Characterization, and in VivoEfficacy of an Acid-Responsive Polymeric Drug Delivery System. *J Am Chem Soc* **131,** 2469–2471 (2009).

71. Wu, X. L. *et al.* Tumor-Targeting Peptide Conjugated pH-Responsive Micelles as a Potential Drug Carrier for Cancer Therapy. *Bioconjugate Chemistry* **21,** 208–213 (2010).

72. Criscione, J. M. *et al.* Self-assembly of pH-responsive fluorinated dendrimer-based particulates for drug delivery and noninvasive imaging. *Biomaterials* **30,** 3946–3955 (2009).

73. Kneen, M., Farinas, J., Li, Y. & Verkman, A. S. Green Fluorescent Protein as a Noninvasive Intracellular pH Indicator. *Biophysical journal* (1998).

74. Lee, C.-H., Lo, L.-W., Mou, C.-Y. & Yang, C.-S. Synthesis and Characterization of Positive-Charge Functionalized Mesoporous Silica Nanoparticles for Oral Drug Delivery of an Anti-Inflammatory Drug. *Adv Funct Mater* **18,** 3283–3292 (2008).

75. Paige, J. S., Nguyen-Duc, T., Song, W. & Jaffrey, S. R. Fluorescence Imaging of Cellular Metabolites with RNA. *Science* **335,** 1194–1194 (2012).

76. Lin, Y.-H. *et al.* Multi-ion-crosslinked nanoparticles with pH-responsive characteristics for oral delivery of protein drugs. *Journal of Controlled Release* **132,** 141–149 (2008).

77. Chang, C.-H. *et al.* Nanoparticles Incorporated in pH-Sensitive Hydrogels as Amoxicillin Delivery for Eradication of Helicobacter pylori. *Biomacromolecules* **11,** 133–142 (2010).

78. Aryal, S., Hu, C.-M. J. & Zhang, L. Polymer−Cisplatin Conjugate Nanoparticles for Acid-Responsive Drug Delivery. *ACS Nano* **4,** 251–258 (2010).

79. Wang, B., Xu, C., Xie, J., Yang, Z. & Sun, S. pH Controlled Release of Chromone from Chromone-Fe 3O 4Nanoparticles. *J Am Chem Soc* **130,** 14436–14437 (2008).

80. Shen, Y. *et al.* Prodrugs Forming High Drug Loading Multifunctional Nanocapsules for Intracellular Cancer Drug Delivery. *J Am Chem Soc* **132,** 4259–4265 (2010).

81. Bruyère, H., Westwell, A. D. & Jones, A. T. Tuning the pH sensitivities of orthoester based compounds for drug delivery applications by simple chemical modification. *Bioorg. Med. Chem. Lett.* **20,** 2200–2203 (2010).

82. Resch-Genger, U., Grabolle, M., Cavaliere-Jaricot, S., Nitschke, R. & Nann, T. Quantum dots versus organic dyes as fluorescent labels. *Nature methods* **5,** 763–775 (2008).

83. Romberg, B., Hennink, W. E. & Storm, G. Sheddable Coatings for Long-Circulating Nanoparticles. *Pharmaceutical research* **25,** 55–71 (2007).

84. Cerritelli, S., Velluto, D. & Hubbell, J. A. PEG-SS-PPS: Reduction-Sensitive Disulfide Block Copolymer Vesicles for Intracellular Drug Delivery. *Biomacromolecules* **8,** 1966–1972 (2007).

85. Takae, S. *et al.* PEG-Detachable Polyplex Micelles Based on Disulfide-Linked Block Catiomers as Bioresponsive Nonviral Gene Vectors. *J Am Chem Soc* **130,** 6001–6009 (2008).

86. Webster, A. A., Coupland, P. P., Houghton, F. D. F., Leese, H. J. H. & Aylott, J. W. J. The delivery of PEBBLE nanosensors to measure the intracellular environment. *Biochemical Society Transactions* **35,** 538–543 (2007).

87. Lundberg, M. Cell surface adherence and endocytosis of protein transduction domains. *Molecular Therapy* **8,** 143–150 (2003).

88. Lindgren, M., Hällbrink, M., Prochiantz, A. & Langel, Ü. Cell-penetrating peptides. *Trends in pharmacological sciences* **21,** 99–103 (2000).

89. Gupta, B., Levchencko, T. & Torchilin, V. P. Intracellular delivery of large molecules and small particles by cell-penetrating proteins and peptides. *Adv Drug Deliv Rev* **57,** 637–651 (2005).

90. Meade, B. R. & Dowdy, S. F. Enhancing the cellular uptake of siRNA duplexes following noncovalent packaging with protein transduction domain peptides. *Adv Drug Deliv Rev* **60,** 530–536 (2008).

91. Sugahara, K. N. *et al.* Coadministration of a Tumor-Penetrating Peptide Enhances the Efficacy of Cancer Drugs. *Science* **328,** 1031–1035 (2010).

92. Xu, H., Aylott, J. W. & Kopelman, R. Fluorescent nano-PEBBLE sensors designed for intracellular glucose imaging. *Analyst* **127,** 1471–1477 (2002).

93. Han, J. & Burgess, K. Fluorescent Indicators for Intracellular pH. *Chemical reviews* **110,** 2709–2728 (2009).

94. Behr, J.-P. The proton sponge: a trick to enter cells the viruses did not exploit. *CHIMIA International Journal for Chemistry* **51,** 1–2 (1997).

95. Graber, M. L., DiLillo, D. C., Friedman, B. L. & Pastoriza-Munoz, E. Characteristics of fluoroprobes for measuring intracellular pH. *Analytical Biochemistry* **156,** 202–212 (1986).

96. Mellman, I., Fuchs, R. & Helenius, A. Acidification of the Endocytic and Exocytic Pathways. *Biochemistry* **55,** 663–700 (1986).

97. Ohkuma, S. & Poole, B. Fluorescence probe measurement of the intralysosomal pH in living cells and the perturbation of pH by various agents. *Proceedings of the National Academy of Sciences of the United States of America* **75,** 3327–3331 (1978).

98. Tycko, B. & Maxfield, F. R. Rapid acidification of endocytic vesicles containing alpha 2-macroglobulin. *Cell* **28,** 643–651 (1982).

99. Marsh, M., Bolzau, E. & Helenius, A. Penetration of Semliki Forest virus from acidic prelysosomal vacuoles. *Cell* **32,** 931–940 (1983).

100. Chazotte, B. Labeling lysosomes in live cells with LysoTracker. *Cold Spring Harb Protoc* **2011,** pdb.prot5571 (2011).

101. Vo-Dinh, T. Nanobiosensors: Probing the sanctuary of individual living cells. *J. Cell. Biochem.* **87,** 154–161 (2003).

102. Vo-Dinh, T., Kasili, P. & Wabuyele, M. Nanoprobes and nanobiosensors for monitoring and imaging individual living cells. *Nanomedicine: Nanotechnology, Biology and Medicine* **2,** 22–30 (2006).

103. Kurkdjian, A. & Guern, J. Intracellular pH: Measurement and Importance in Cell Activity. *Annu. Rev. Plant. Physiol. Plant. Mol. Biol.* **40,** 271–303 (1989).

104. Lee, Y.-E. K. & Kopelman, R. Nanoparticle PEBBLE sensors in live cells. *Meth. Enzymol.* **504,** 419–470 (2012).

105. Jares-Erijman, E. A. & Jovin, T. M. FRET imaging. *Nature biotechnology* **21,** 1387–1395 (2003).

106. Hille, C. & Walz, B. Characterisation of neurotransmitter-induced electrolyte transport in cockroach salivary glands by intracellular Ca2+, Na+ and pH measurements in duct cells. *J. Exp. Biol.* **211,** 568–576 (2008).

107. Nakabayashi, T., Wang, H.-P., Kinjo, M. & Ohta, N. Application of fluorescence lifetime imaging of enhanced green fluorescent protein to intracellular pH measurements. *Photochem Photobiol Sci* **7,** 668–670 (2008).

108. Sasaki, K., Shi, Z. Y., Kopelman, R. & Masuhara, H. Three-dimensional pH microprobing with an optically-manipulated fluorescent particle. *Chem. Lett., No. 2. (1996), pp. 141-142* **2,** 141–142 (1996).

109. Clark, H. A. *et al.* Subcellular optochemical nanobiosensors: probes encapsulated by biologically localised embedding (PEBBLEs). *Sensors and Actuators B: Chemical* **51,** 12–16 (1998).

110. Clark, H. A., Hoyer, M., Philbert, M. A. & Kopelman, R. Optical nanosensors for chemical analysis inside single living cells. 1. Fabrication, characterization, and methods for intracellular delivery of PEBBLE sensors. *Anal. Chem* **71,** 4831–4836 (1999).

111. Clark, H. A., Hoyer, M., Parus, S., Philbert, M. A. & Kopelman, R. Optochemical Nanosensors and Subcellular Applications in Living Cells. *Microchimica Acta* **131,** 121–128 (1999).

112. Coogan, M. P. Probing intracellular oxygen by quenched phosphorescence lifetimes of nanoparticles containing polyacrylamide-embedded $[Ru(dpp(SO_3Na_2)_3]Cl_2$. *Photochem Photobiol Sci* **9,** 103–109 (2010).

113. Graefe, A. *et al.* Development and critical evaluation of fluorescent chloride nanosensors. *Anal. Chem* **80,** 6526–6531 (2008).

114. Josefsen, L. B. L. *et al.* Porphyrin-nanosensor conjugates. New tools for the measurement of intracellular response to reactive oxygen species. *Photochemical & Photobiological Sciences* **9,** 801–811 (2010).

115. Kim, G., Lee, Y.-E. K., Xu, H., Philbert, M. A. & Kopelman, R. Nanoencapsulation method for high selectivity sensing of hydrogen peroxide inside live cells. *Anal. Chem* **82,** 2165–2169 (2010).

116. Poulsen, A. K., Scharff-Poulsen, A. M. & Olsen, L. F. Horseradish peroxidase embedded in polyacrylamide nanoparticles enables optical detection of reactive oxygen species. *Analytical Biochemistry* **366,** 29–36 (2007).

117. Schulz, A., Wotschadlo, J., Heinze, T. & Mohr, G. J. Fluorescent nanoparticles for ratiometric pH-monitoring in the neutral range. *J Mater Chem* **20,** 1475–1482 (2010).

118. Sumner, J. P. & Kopelman, R. Alexa Fluor 488 as an iron sensing molecule and its application in PEBBLE nanosensors. *The Analyst* **130,** 528–533 (2005).

119. Sumner, J. P. J., Aylott, J. W. J., Monson, E. E. & Kopelman, R. R. A fluorescent PEBBLE nanosensor for intracellular free zinc. *Analyst* **127,** 11–16 (2002).

120. Sun, H., Andresen, T. L., Benjaminsen, R. V. & Almdal, K. Polymeric Nanosensors for Measuring the Full Dynamic pH Range of Endosomes and Lysosomes in Mammalian Cells. *j biomed nanotechnol* **5,** 676–682 (2009).

121. Sun, H., Benjaminsen, R. V., Almdal, K. & Andresen, T. L. Hyaluronic Acid Immobilized Polyacrylamide Nanoparticle Sensors for CD44 Receptor Targeting and pH Measurement in Cells. *Bioconjugate Chemistry* **23,** 2247–2255 (2012).

122. Sun, H. *et al.* Phosphate sensing by fluorescent reporter proteins embedded in polyacrylamide nanoparticles. *ACS Nano* **2,** 19–24 (2008).

123. Benjaminsen, R. V. Design and application of optical nanosensors for pH imaging in cell compartments. *Phd Thesis* (2012).

124. Nielsen, L. J., Olsen, L. F. & Ozalp, V. C. Aptamers embedded in polyacrylamide nanoparticles: a tool for in vivo metabolite sensing. *ACS Nano* **4,** 4361–4370 (2010).

125. Cao, Y., Koo, Y.-E. L. & Kopelman, R. Poly(decyl methacrylate)-based fluorescent PEBBLE swarm nanosensors for measuring dissolved oxygen in biosamples. *Analyst* **129,** 745–750 (2004).

126. Borisov, S. M. & Klimant, I. Luminescent nanobeads for optical sensing and imaging of dissolved oxygen. *Mikrochim Acta* **164,** 7–15 (2009).

127. Borisov, S. M., Mayr, T. & Klimant, I. Poly(styrene-block-vinylpyrrolidone) beads as a versatile material for simple fabrication of optical nanosensors. *Anal. Chem* **80,** 573–582 (2008).

128. Brown, J. Q. & McShane, M. J. Core-referenced ratiometric fluorescent potassium ion sensors using self-assembled ultrathin films on europium nanoparticles. *IEEE Sens J* **5,** 1197–1205 (2005).

129. Guice, K. B. K., Caldorera, M. E. M. & McShane, M. J. M. Nanoscale internally referenced oxygen sensors produced from self-assembled nanofilms on fluorescent nanoparticles. *J. Biomed. Opt* **10,** 064031–064031 (2005).

130. Schmälzlin, E. *et al.* An Optical Multifrequency Phase-Modulation Method Using Microbeads for Measuring Intracellular Oxygen Concentrations in Plants. *Biophysical journal* **89,** 7–7 (2005).

131. Arduini, M., Mancin, F., Tecilla, P. & Tonellato, U. Self-organized fluorescent nanosensors for ratiometric Pb2+ detection. *Langmuir : the ACS journal of surfaces and colloids* **23,** 8632–8636 (2007).

132. Burns, A. A., Sengupta, P. P., Zedayko, T. T., Baird, B. B. & Wiesner, U. U. Core/Shell fluorescent silica nanoparticles for chemical sensing: towards single-particle laboratories. *Small* **2,** 723–726 (2006).

133. Cao, Y., Koo, Y.-E. L., Koo, S. M. & Kopelman, R. Ratiometric singlet oxygen nano-optodes and their use for monitoring photodynamic therapy nanoplatforms. *Photochemistry and photobiology* **81,** 1489–1498 (2005).

134. Hammond, V. J. V. *et al.* An optical sensor for reactive oxygen species: encapsulation of functionalised silica nanoparticles into silicate nanoprobes to reduce fluorophore leaching. *Analyst* **133,** 71–75 (2008).

135. Koo, Y.-E. L. *et al.* Real-time measurements of dissolved oxygen inside live cells by Ormosil (organically modified silicate) fluorescent PEBBLE nanosensors. *Anal. Chem* **76,** 2498–2505 (2004).

136. Peng, J. *et al.* Noninvasive monitoring of intracellular pH change induced by drug stimulation using silica nanoparticle sensors. *Anal Bioanal Chem* **388,** 645–654 (2007).

137. Seo, S. *et al.* Fluorescein-Functionalized Silica Nanoparticles as a Selective Fluorogenic Chemosensor for Cu2+ in Living Cells. *Eur J Inorg Chem* **2010,** 843–847 (2010).

138. Teolato, P. P. *et al.* Silica nanoparticles for fluorescence sensing of Zn(II): exploring the covalent strategy. *Chemistry* **13,** 2238–2245 (2007).

139. Wang, S., Bin Li, Zhang, L., Liu, L. & Wang, Y. Photoluminescent and oxygen sensing properties of core-shell nanospheres based on a covalently grafted ruthenium(II) complex. *Appl Organomet Chem* **25,** 21–26 (2011).

140. Xu, H. H., Aylott, J. W. J., Kopelman, R. R., Miller, T. J. T. & Philbert, M. A. M. A real-time ratiometric method for the determination of molecular oxygen inside living cells using sol-gel-based spherical optical nanosensors with applications to rat C6 glioma. *Anal. Chem* **73,** 4124–4133 (2001).

141. Son, H. H. *et al.* A highly sensitive and selective turn-on fluorogenic and chromogenic sensor based on BODIPY-functionalized magnetic nanoparticles for detecting lead in living cells. *Chemistry* **16,** 11549–11553 (2010).

142. Schulz, A., woolley, R., tabarin, T. & mcdonagh, C. M. Dextran-coated silica nanoparticles for calcium-sensing. *Analyst* **8,** 1722–1727

143. Hornig, S. *et al.* Biocompatible fluorescent nanoparticles for pH-sensoring. *Soft Matter* **4,** 1169–1172 (2008).

144. Stanca, S. E., Nietzsche, S., Fritzsche, W., Cranfield, C. G. & Biskup, C. Intracellular ion monitoring using a gold-core polymer-shell nanosensor architecture. *Nanotechnology* **21,** 055501–55501 (2010).

145. Nakayama-Ratchford, N., Bangsaruntip, S., Sun, X., Welsher, K. & Dai, H. Noncovalent Functionalization of Carbon Nanotubes by Fluorescein−Polyethylene Glycol: Supramolecular Conjugates with pH-Dependent Absorbance and Fluorescence. *J Am Chem Soc* **129,** 2448–2449 (2007).

146. Myc, A., Majoros, I. J., Thomas, T. P. & Baker, J. R. Dendrimer-based targeted delivery of an apoptotic sensor in cancer cells. *Biomacromolecules* **8,** 13–18 (2007).

147. Cheng, Z. Z. & Aspinwall, C. A. C. Nanometre-sized molecular oxygen sensors prepared from polymer stabilized phospholipid vesicles. *Analyst* **131,** 236–243 (2006).

148. Tyner, K. M., Kopelman, R. & Philbert, M. A. ''Nanosized Voltmeter'' Enables Cellular-Wide Electric Field Mapping. *Biophysical journal* **93,** 12–12 (2007).

149. Wang, B., Zhang, L., Bae, S. C. & Granick, S. Nanoparticle-induced surface reconstruction of phospholipid membranes. *Proceedings of the National Academy of Sciences* **105,** 18171–18175 (2008).

150. Chen, Y. Y. & Rosenzweig, Z. Z. Luminescent CdS quantum dots as selective ion probes. *Anal. Chem* **74,** 5132–5138 (2002).

151. Cordes, D. B. D., Gamsey, S. S. & Singaram, B. B. Fluorescent quantum dots with boronic acid substituted viologens to sense glucose in aqueous solution. *Angew Chem Int Ed Engl* **45,** 3829–3832 (2006).

152. Medintz, I. L. I. *et al.* Quantum-dot/dopamine bioconjugates function as redox coupled assemblies for in vitro and intracellular pH sensing. *Nat Mater* **9,** 676–684 (2010).

153. Peptide-coated CdS quantum dots for the optical detection of copper(II) and silver(I). *Chem Commun* **21,**

154. Gill, R., Bahshi, L., Freeman, R. & Willner, I. Optical detection of glucose and acetylcholine esterase inhibitors by H2O2-sensitive CdSe/ZnS quantum dots. *Angew Chem Int Ed Engl* **47,** 1676–1679 (2008).

155. Krooswyk, J. D., Tyrakowski, C. M. & Snee, P. T. Multivariable Response of Semiconductor Nanocrystal-Dye Sensors: The Case of pH. *J. Phys. Chem. C* **114,** 21348–21352 (2010).

156. Brasuel, M., Kopelman, R., Miller, T. J., Tjalkens, R. & Philbert, M. A. Fluorescent Nanosensors for Intracellular Chemical Analysis: Decyl Methacrylate Liquid Polymer Matrix and Ion-Exchange-Based Potassium PEBBLE Sensors with Real-Time Application to Viable Rat C6 Glioma Cells. *Anal. Chem* **73,** 2221–2228 (2001).

157. Dubach, J. M., Harjes, D. I. & Clark, H. A. Fluorescent ion-selective nanosensors for intracellular analysis with improved lifetime and size. *Nano Lett.* **7,** 1827–1831 (2007).

158. Ruedas-Rama, M. J. & Hall, E. K^+-selective nanospheres: maximising response range and minimising response time. *Analyst* **12,** (2006).

159. Kim, S.-H. S., Kim, B. B., Yadavalli, V. K. V. & Pishko, M. V. M. Encapsulation of enzymes within polymer spheres to create optical nanosensors for oxidative stress. *Anal. Chem* **77,** 6828–6833 (2005).

160. Lee, D. D. *et al.* In vivo imaging of hydrogen peroxide with chemiluminescent nanoparticles. *Nat Mater* **6,** 765–769 (2007).

161. Lim, C.-K. *et al.* Chemiluminescence-Generating Nanoreactor Formulation for Near-Infrared Imaging of Hydrogen Peroxide and Glucose Level in vivo. *Adv Funct Mater* **20,** 2644–2648 (2010).

162. Lee, D. *et al.* Detection of hydrogen peroxide with chemiluminescent micelles. *Int J Nanomedicine* **3,** 471–476 (2008).

163. Gota, C. C., Okabe, K. K., Funatsu, T. T., Harada, Y. Y. & Uchiyama, S. S. Hydrophilic fluorescent nanogel thermometer for intracellular thermometry. *J Am Chem Soc* **131,** 2766–2767 (2009).

164. Liu, T. & Liu, S. Responsive polymers-based dual fluorescent chemosensors for Zn2+ ions and temperatures working in purely aqueous media. *Anal. Chem* **83,** 2775–2785 (2011).

165. SHIMOMURA, O. O., JOHNSON, F. H. F. & SAIGA, Y. Y. Extraction, purification and properties of aequorin, a bioluminescent protein from the luminous hydromedusan, Aequorea. *J Cell Comp Physiol* **59,** 223–239 (1962).

166. Prasher, D. C. D., Eckenrode, V. K. V., Ward, W. W. W., Prendergast, F. G. F. & Cormier, M. J. M. Primary structure of the Aequorea victoria green-fluorescent protein. *Gene* **111,** 229–233 (1992).

167. Misteli, T. & Spector, D. L. Applications of the green fluorescent protein in cell biology and biotechnology. *Nature biotechnology* **15,** 961–964 (1997).

168. Zhang, J., Campbell, R. E., Ting, A. Y. & Tsien, R. Y. Creating New Fluorescent Probes for Cell Biology. *Nat Rev Mol Cell Biol* **3,** 906–918 (2002).

169. Pollok, B. A. & Heim, R. Using GFP in FRET-based applications. *Trends Cell Biol.* **9,** 57–60 (1999).

170. McCombs, J. E. & Palmer, A. E. Measuring calcium dynamics in living cells with genetically encodable calcium indicators. *Methods* **46,** 152–159 (2008).

171. Mank, M. & Griesbeck, O. Genetically encoded calcium indicators. *Chemical reviews* **108,** 1550–1564 (2008).

172. Berg, J., Hung, Y. P. & Yellen, G. A genetically encoded fluorescent reporter of ATP:ADP ratio. *Nature methods* **6,** 161–166 (2009).

173. Mizuno, T., Murao, K., Tanabe, Y., Oda, M. & Tanaka, T. Metal-ion-dependent GFP emission in vivo by combining a circularly permutated green fluorescent protein with an engineered metal-ion-binding coiled-coil. *J Am Chem Soc* **129,** 11378–11383 (2007).

174. Baird, G. S., Zacharias, D. A. & Tsien, R. Y. Circular permutation and receptor insertion within green fluorescent proteins. *Proceedings of the National Academy of Sciences of the United States of America* **96,** 11241–11246 (1999).

175. Strack, R. L. & Jaffrey, S. R. New approaches for sensing metabolites and proteins in live cells using RNA. *Curr Opin Chem Biol* **17,** 651–655 (2013).

176. Paige, J. S., Wu, K. Y. & Jaffrey, S. R. RNA Mimics of Green Fluorescent Protein. *Science* **333,** 642–646 (2011).

177. Kneipp, J., Kneipp, H., Wittig, B. & Kneipp, K. Following the Dynamics of pH in Endosomes of Live Cells with SERS Nanosensors †. *J. Phys. Chem. C* **114,** 7421–7426 (2010).

178. Sun, H., Scharff-Poulsen, A. M., Gu, H. & Almdal, K. Synthesis and characterization of ratiometric, pH sensing nanoparticles with covalently attached fluorescent dyes. *Chem Mater* **18,** 3381–3384 (2006).

179. Chauhan, V. M., Burnett, G. R. & Aylott, J. W. Dual-fluorophore ratiometric pH nanosensor with tuneable pKa and extended dynamic range. *The Analyst* **136,** 1799–1801 (2011).

180. Ray, A., Koo Lee, Y.-E., Epstein, T., Kim, G. & Kopelman, R. Two-photon nano-PEBBLE sensors: subcellular pH measurements. *The Analyst* **136,** 3616–3622 (2011).

181. Peng, J. *et al.* Noninvasive monitoring of intracellular pH change induced by drug stimulation using silica nanoparticle sensors. *Anal Bioanal Chem* **388,** 645–654 (2007).

182. Allard, E. & Larpent, C. Core- shell type dually fluorescent polymer nanoparticles for ratiometric pH- sensing. *… of Polymer Science Part A: Polymer …* **46,** 6206–6213 (2008).

183. Benjaminsen, R. V. *et al.* Evaluating nanoparticle sensor design for intracellular pH measurements. *ACS Nano* **5,** 5864–5873 (2011).

184. Buck, S., Xu, H., Brasuel, M., Philbert, M. & Kopelman, R. Nanoscale probes encapsulated by biologically localized embedding (PEBBLEs) for ion sensing and imaging in live cells. *Talanta* **63,** 41–59 (2004).

185. Welser, K., Perera, M. D. A., Aylott, J. W. & Chan, W. C. A facile method to clickable sensing polymeric nanoparticles. *Chem Commun* **43,** 6601–6603 (2009).

186. Coupland, P. G., Fisher, K. A., Jones, D. R. E. & Aylott, J. W. Internalisation of polymeric nanosensors in mesenchymal stem cells: analysis by flow cytometry and confocal microscopy. *J Control Release* **130,** 115–120 (2008).

187. Rink, T. J., Tsien, R. Y. & Pozzan, T. Cytoplasmic pH and free Mg2+ in lymphocytes. *The Journal of cell biology* **95,** 189–196 (1982).

188. Gottlieb, R. A., Nordberg, J., Skowronski, E. & Babior, B. M. Apoptosis induced in Jurkat cells by several agents is preceded by intracellular acidification. *Proceedings of the National Academy of Sciences of the United States of America* **93,** 654–658 (1996).

189. Nedergaard, M., Desai, S. & Pulsinelli, W. Dicarboxy-dichlorofluorescein: a new fluorescent probe for measuring acidic intracellular pH. *Analytical Biochemistry* **187,** 109–114 (1990).

190. Sun, W.-C., Gee, K. R., Klaubert, D. H. & Haugland, R. P. Synthesis of Fluorinated Fluoresceins. *J. Org. Chem.* **62,** 6469–6475 (1997).

191. Cooper, M., Gregory, S., Adie, E. & Kalinka, S. pH-sensitive cyanine dyes for biological applications. *Journal of Fluorescence* (2002).

192. Miksa, M., Komura, H., Wu, R., Shah, K. & Wang, P. A novel method to determine the engulfment of apoptotic cells by macrophages using pHrodo succinimidyl ester. *J Immunol Methods* **342,** 71–77 (2009).

193. Klonis, N. & Sawyer, W. H. Spectral properties of the prototropic forms of fluorescein in aqueous solution. *Journal of Fluorescence* **6,** 147–157 (1996).

194. Sun, H., Almdal, K. & Andresen, T. L. Expanding the dynamic measurement range for polymeric nanoparticle pH sensors. *Chemical Communications* **47,** 5268–5270 (2011).

195. Instruments, M. Tech Note: Dynamic Light Scattering: An Introduction in 30 Minutes. 1–8 (2005).

196. Adsley, R. Visulaisation of the cellular uptake of nanoparticles. *Phd Thesis* (2013).

197. Rezende, C. A., Lee, L.-T. & Galembeck, F. Surface mechanical properties of thin polymer films investigated by AFM in pulsed force mode. *Langmuir : the ACS journal of surfaces and colloids* **25,** 9938–9946 (2009).

198. Hansma, H. G. H. *et al.* Properties of Biomolecules Measured from Atomic Force Microscope Images: A Review. *J Struct Biol* **119,** 10–10 (1997).

199. Danilatos, G. D. G. Bibliography of environmental scanning electron microscopy. *Microsc Res Tech* **25,** 529–534 (1993).

200. Malvern. Zeta Potential - An introduction in 30 minutes. (2005).

201. Miksa, M., Komura, H., Wu, R., Shah, K. G. & Wang, P. A novel method to determine the engulfment of apoptotic cells by macrophages using pHrodo succinimidyl ester. *J Immunol Methods* **342,** 71–77 (2009).

202. Beletskii, A. *et al.* High-throughput phagocytosis assay utilizing a pH-sensitive fluorescent dye. *Biotechniques* **39,** 894–897 (2005).

203. Benjaminsen, R. V., Mattebjerg, M. A., Henriksen, J. R., Moghimi, S. M. & Andresen, T. L. The possible 'proton sponge' effect of polyethylenimine (PEI) does not include change in lysosomal pH. *Molecular Therapy* **21,** 149–157 (2012).

204. Rejman, J., Oberle, V., Zuhorn, I. & Hoekstra, D. Size-dependent internalization of particles via the pathways of clathrin-and caveolae-mediated endocytosis. *Biochemical Journal* **377,** 159 (2004).

205. Lee, Y.-E. K., Smith, R. & Kopelman, R. Nanoparticle PEBBLE sensors in live cells and in vivo. *Annu Rev Anal Chem (Palo Alto Calif)* **2,** 57–76 (2009).

206. Bradley, M. *et al.* pH sensing in living cells using fluorescent microspheres. *Bioorg. Med. Chem. Lett.* **18,** 313–317 (2008).

207. Schreiber, R., Zhang, F. & Häussinger, D. Regulation of vesicular pH in liver macrophages and parenchymal cells by ammonia and anisotonicity as assessed by fluorescein isothiocyanate-dextran fluorescence. *Biochem J* **315** (**Pt 2**)**,** 385–392 (1996).

208. Coupland, P. G., Briddon, S. J. & Aylott, J. W. Using fluorescent pH-sensitive nanosensors to report their intracellular location after Tat-mediated delivery. *Integr Biol (Camb)* **1,** 318–318 (2009).

209. Piston, D. W. & Swedlow, J. R. The impact of technology on light microscopy. *Nature cell biology* **11,** S23–S24 (2009).

210. Minsky, M. Memoir on inventing the confocal scanning microscope. *Scanning* **10,** 128–138 (1988).

211. Toomre, D. & Bewersdorf, J. A New Wave of Cellular Imaging. *Annu. Rev. Cell Dev. Biol.* **26,** 285–314 (2010).

212. Nikon. http://www.microscopyu.com/articles/fluorescence/fluorescenceintro.html . Accessed 31/08/13

213. Pawley, J. Handbook of biological confocal microscopy. (2006).

214. Olympus. http://www.olympusmicro.com/primer/digitalimaging/deconvolution/deconvolutionhome.html. Accessed 31/08/13.

215. Swedlow, J. R. in **72,** 349–367 (Methods in Cell Biology, 2003).

216. Hoebe, R. A. *et al.* Controlled light-exposure microscopy reduces photobleaching and phototoxicity in fluorescence live-cell imaging. *Nature biotechnology* **25,** 249–253 (2007).

217. Young, I. T. Quantitative microscopy. *IEEE Eng. Med. Biol. Mag.* **15,** 59–66 (1996).

218. Schermelleh, L., Heintzmann, R. & Leonhardt, H. A guide to super-resolution fluorescence microscopy. *The Journal of cell biology* **190,** 165–175 (2010).

219. Watson, P. P., Jones, A. T. A. & Stephens, D. J. D. Intracellular trafficking pathways and drug delivery: fluorescence imaging of living and fixed cells. *Adv Drug Deliv Rev* **57,** 19–19 (2005).

220. Chauhan, V. M., Orsi, G., Brown, A., Pritchard, D. I. & Aylott, J. W. Mapping the pharyngeal and intestinal pH of Caenorhabditis elegans and real-time luminal pH oscillations using extended dynamic range pH-sensitive nanosensors. *ACS Nano* **7,** 5577–5587 (2013).

221. Thomas, J. A., Buchsbaum, R. N., Zimniak, A. & Racker, E. Intracellular pH measurements in Ehrlich ascites tumor cells utilizing spectroscopic probes generated in situ. *Biochemistry* **18,** 2210–2218 (1979).

222. Boyarsky, G. G., Hanssen, C. C. & Clyne, L. A. L. Inadequacy of high K+/nigericin for calibrating BCECF. I. Estimating steady-state intracellular pH. *Am J Physiol* **271,** C1131–C1145 (1996).

223. Wolfbeis, O. S. Fiber-optic chemical sensors and biosensors. *Anal. Chem* **76,** 3269–3283 (2004).

224. Sonawane, N. D., Thiagarajah, J. R. & Verkman, A. S. Chloride concentration in endosomes measured using a ratioable fluorescent Cl- indicator: evidence for chloride accumulation during acidification. *Journal of Biological Chemistry* **277,** 5506–5513 (2002).

225. Christensen, K. A., Myers, J. T. & Swanson, J. A. pH-dependent regulation of lysosomal calcium in macrophages. *J. Cell. Sci.* **115,** 599–607 (2002).

226. Sonawane, N. D. N., Szoka, F. C. F. & Verkman, A. S. A. Chloride accumulation and swelling in endosomes enhances DNA transfer by

polyamine-DNA polyplexes. *J. Biol. Chem.* **278,** 44826–44831 (2003).

227. Euliss, L. E., DuPont, J. A., Gratton, S. & DeSimone, J. Imparting size, shape, and composition control of materials for nanomedicine. *Chemical Society Reviews* **35,** 1095–1104 (2006).

228. Chithrani, B. D., Ghazani, A. A. & Chan, W. C. W. Determining the Size and Shape Dependence of Gold Nanoparticle Uptake into Mammalian Cells. *Nano Lett* **6,** 662–668 (2006).

229. Gratton, S. E. A. *et al.* The effect of particle design on cellular internalization pathways. *Proceedings of the National Academy of Sciences* **105,** 11613–11618 (2008).

230. Mislick, K. A. K. & Baldeschwieler, J. D. J. Evidence for the role of proteoglycans in cation-mediated gene transfer. *Proceedings of the National Academy of Sciences of the United States of America* **93,** 12349–12354 (1996).

231. Soliman, M. *et al.* Interaction of reducible polypeptide gene delivery vectors with supported lipid bilayers: pore formation and structure–function relationships. *Soft Matter* **6,** 2517 (2010).

232. Vasir, J. K. & Labhasetwar, V. Quantification of the force of nanoparticle-cell membrane interactions and its influence on intracellular trafficking of nanoparticles. *Biomaterials* **29,** 4244–4252 (2008).

233. Huang, M., Ma, Z., Khor, E. & Lim, L.-Y. Uptake of FITC-chitosan nanoparticles by A549 cells. *Pharmaceutical research* **19,** 1488–1494 (2002).

234. Jäger, M., Schubert, S., Ochrimenko, S., Fischer, D. & Schubert, U. S. Branched and linear poly(ethylene imine)-based conjugates: synthetic modification, characterization, and application. *Chemical Society Reviews* **41,** 4755–4767 (2012).

235. Dausend, J. *et al.* Uptake mechanism of oppositely charged fluorescent nanoparticles in HeLa cells. *Small* **7,** 1322–1337 (2011).

236. Röcker, C., Pötzl, M., Zhang, F., Parak, W. J. & Nienhaus, G. U. A quantitative fluorescence study of protein monolayer formation on colloidal nanoparticles. *Nat Nanotechnol* **4,** 577–580 (2009).

237. Best, J. P., Yan, Y. & Caruso, F. The role of particle geometry and mechanics in the biological domain. *Advanced healthcare materials* **1,** 35–47 (2012).

238. Brannon-Peppas, L. & Blanchette, J. O. Nanoparticle and targeted systems for cancer therapy. *Adv Drug Deliv Rev* (2012).

239. Jones, A. T. & Sayers, E. J. Cell entry of cell penetrating peptides: tales of tails wagging dogs. *J Control Release* **161,** 582–591 (2012).

240. Ibuki, Y. & Toyooka, T. in *Nanotoxicity* **926,** 157–166 (Humana Press, 2012).

241. Richardson, S. C. W. *et al.* The use of fluorescence microscopy to define polymer localisation to the late endocytic compartments in cells that are targets for drug delivery. *Journal of Controlled Release* **127,** 1–11 (2008).

242. Costes, S. V. *et al.* Automatic and quantitative measurement of protein-protein colocalization in live cells. *Biophysical journal* **86,** 3993–4003 (2004).

243. Manders, E. M. M., Verbeek, F. & Aten, J. A. Measurement of co-localization of objects in dual-colour confocal images. *J Microsc* **169,** 375–382 (2011).

244. Rink, J., Ghigo, E., Kalaidzidis, Y. & Zerial, M. Rab conversion as a mechanism of progression from early to late endosomes. *Cell* (2005).

245. Luzio, J. P., Pryor, P. R. & Bright, N. A. Lysosomes: fusion and function. *Nat Rev Mol Cell Biol* **8,** 622–632 (2007).

246. Kost, T. A. T., Condreay, J. P. J., Ames, R. S. R., Rees, S. S. & Romanos, M. A. M. Implementation of BacMam virus gene delivery technology in a drug discovery setting. *Drug Discov Today* **12,** 8–8 (2007).

247. Schermelleh, L., Heintzmann, R. & Leonhardt, H. A guide to super-resolution fluorescence microscopy. *The Journal of cell biology* **190,** 165–175 (2010).

248. Huang, B., Bates, M. & Zhuang, X. Super-Resolution Fluorescence Microscopy. *Annual review of biochemistry* **78,** 993–1016 (2009).

249. van de Linde, S., Heilemann, M. & Sauer, M. Live-cell super-resolution imaging with synthetic fluorophores. *Annu Rev Phys Chem* **63,** 519–540 (2012).

250. Ball, G., Parton, R. M., Hamilton, R. S. & Davis, I. A cell biologist's guide to high resolution imaging. *Meth. Enzymol.* **504,** 29–55 (2012).

251. Abbe, E. Beiträge zur Theorie des Mikroskops und der mikroskopischen Wahrnehmung. *Archiv f. mikrosk. Anatomie* **9,** 413–418 (1873).

252. Rayleigh. On the theory of optical images, with special reference to the microscope. *Journal of the Royal Microscopical Society* **23,** 474–482 (1903).

253. de Lange, F. F. *et al.* Cell biology beyond the diffraction limit: near-field scanning optical microscopy. *J. Cell. Sci.* **114,** 4153–4160 (2001).

254. Rust, M. J., Bates, M. & Zhuang, X. Sub-diffraction-limit imaging by stochastic optical reconstruction microscopy (STORM). *Nature methods* **3,** 793–796 (2006).

255. Gustafsson, M. G. L. Surpassing the lateral resolution limit by a factor of two using structured illumination microscopy. SHORT COMMUNICATION. *J Microsc* **198,** 82–87 (2000).

256. Kner, P., Chhun, B. B., Griffis, E. R., Winoto, L. & Gustafsson, M. G. L. Super-resolution video microscopy of live cells by structured illumination. *Nature methods* **6,** 339–342 (2009).

257. Schermelleh, L. *et al.* Subdiffraction Multicolor Imaging of the Nuclear Periphery with 3D Structured Illumination Microscopy. *Science* **320,** 1332–1336 (2008).

258. Hell, S. W. S. & Wichmann, J. J. Breaking the diffraction resolution limit by stimulated emission: stimulated-emission-depletion fluorescence microscopy. *Opt Lett* **19,** 780–782 (1994).

259. Hell, S. & Stelzer, E. H. K. Fundamental improvement of resolution with a 4Pi-confocal fluorescence microscope using two-photon excitation. *Optics Communications* **93,** 277–282 (1992).

260. Gustafsson, Agard & Sedat. I5M: 3D widefield light microscopy with better than 100 nm axial resolution. *J Microsc* **195,** 10–16 (1999).

261. Manunta, M., Izzo, L., Duncan, R. & Jones, A. T. Establishment of subcellular fractionation techniques to monitor the intracellular fate of polymer therapeutics II. Identification of endosomal and lysosomal compartments in HepG2 cells combining single-step subcellular fractionation with fluorescent imaging. *J Drug Target* **15,** 37–50 (2007).

262. Fares, H. & van der Bliek, A. M. Analysis of membrane-bound organelles. *Methods Cell Biol.* **107,** 239–263 (2012).

263. Kaiser, C. A., Chen, E. J. & Losko, S. Subcellular fractionation of secretory organelles. *Meth. Enzymol.* **351,** 325–338 (2002).

264. Cotten, M. *et al.* Transferrin-polycation-mediated introduction of DNA into human leukemic cells: stimulation by agents that affect the survival of transfected DNA or modulate transferrin receptor levels. *Proceedings of the National Academy of Sciences* **87,** 4033–4037 (1990).

265. Huth, U. S., Schubert, R. & Peschka-Süss, R. Investigating the uptake and intracellular fate of pH-sensitive liposomes by flow cytometry and spectral bio-imaging. *J Control Release* **110,** 490–504 (2006).

266. Douglas, K. L., piccirillo, C. A. & Tabrizian, M. Cell line-dependent internalization pathways and intracellular trafficking determine transfection efficiency of nanoparticle vectors. *European Journal of Pharmaceutics and Biopharmaceutics* **68,** 676–687 (2008).

267. Gabrielson, N. P. & Pack, D. W. Efficient polyethylenimine-mediated gene delivery proceeds via a caveolar pathway in HeLa cells. *Journal of Controlled Release* **136,** 8–8 (2009).

268. Perumal, O. P. O., Inapagolla, R. R., Kannan, S. S. & Kannan, R. M. R. The effect of surface functionality on cellular trafficking of dendrimers. *Biomaterials* **29,** 3469–3476 (2008).

269. Gonçalves, C. Macropinocytosis of Polyplexes and Recycling of Plasmid via the Clathrin-Dependent Pathway Impair the Transfection Efficiency of Human Hepatocarcinoma Cells*1. *Molecular Therapy* **10,** 373–385 (2004).

270. Simões, S. S. *et al.* Human serum albumin enhances DNA transfection by lipoplexes and confers resistance to inhibition by serum. *ACTA-BIOENERG* **1463,** 459–469 (2000).

271. Kichler, A., Leborgne, C., Coeytaux, E. & Danos, O. Polyethylenimine-mediated gene delivery: a mechanistic study. *J Gene Med* **3,** 135–144 (2001).

272. Dröse, S. & Altendorf, K. Bafilomycins and concanamycins as inhibitors of V-ATPases and P-ATPases. (1997).

273. http://www.promega.co.uk/resources/protocols/technical-bulletins/0/celltiter-96-aqueous-nonradioactive-cell-proliferation-assay-protocol/.

274. Malich, G., Markovic, B. & Winder, C. The sensitivity and specificity of the MTS tetrazolium assay for detecting the in vitro cytotoxicity of 20 chemicals using human cell lines. *Toxicology* (1997).

275. Chan, Y.-H. *et al.* Development of ultrabright semiconducting polymer dots for ratiometric pH sensing. *Anal. Chem* **83,** 1448–1455 (2011).

276. Chen, Y.-P. *et al.* Surface charge effect in intracellular localization of mesoporous silica nanoparticles as probed by fluorescent ratiometric pH imaging. *RSC Advances* **2,** 968–973 (2012).

277. Kulkarni, S. A. & Feng, S.-S. Effects of Particle Size and Surface Modification on Cellular Uptake and Biodistribution of Polymeric Nanoparticles for Drug Delivery. *Pharmaceutical research* **30,** 2512–2522 (2013).

278. Yue, Z.-G. *et al.* Surface charge affects cellular uptake and intracellular trafficking of chitosan-based nanoparticles. *Biomacromolecules* **12,** 2440–2446 (2011).

279. Harush-Frenkel, O., Rozentur, E., Benita, S. & Altschuler, Y. Surface Charge of Nanoparticles Determines Their Endocytic and Transcytotic Pathway in Polarized MDCK Cells. *Biomacromolecules* **9,** 435–443 (2008).

280. Leroueil, P. R. *et al.* Wide varieties of cationic nanoparticles induce defects in supported lipid bilayers. *Nano Lett.* **8,** 420–424 (2008).

281. Mecke, A. A. *et al.* Lipid bilayer disruption by polycationic polymers: the roles of size and chemical functional group. *Langmuir* **21,** 10348–10354 (2005).

282. Verma, A. & Stellacci, F. Effect of surface properties on nanoparticle–cell interactions. *Small* **6,** 12–21 (2010).

283. Walczyk, D., Bombelli, F. B., Monopoli, M. P., Lynch, I. & Dawson, K. A. What the Cell 'Sees' in Bionanoscience. *J Am Chem Soc* **132,** 5761–5768 (2010).

284. Cedervall, T. *et al.* Understanding the nanoparticle–protein corona using methods to quantify exchange rates and affinities of proteins for nanoparticles. *Proceedings of the National Academy of Sciences* **104,** 2050–2055 (2007).

285. Monopoli, M. P. M. *et al.* Physical-chemical aspects of protein corona: relevance to in vitro and in vivo biological impacts of nanoparticles. *J Am Chem Soc* **133,** 2525–2534 (2011).

286. Casals, E., Pfaller, T., Duschl, A., Oostingh, G. J. & Puntes, V. Time Evolution of the Nanoparticle Protein Corona. *ACS Nano* **4,** 3623–3632 (2010).

287. Lundqvist, M. *et al.* Nanoparticle size and surface properties determine the protein corona with possible implications for biological impacts. *Proceedings of the National Academy of Sciences of the United States of America* **105,** 14265–14270 (2008).

288. Winter, J., Jung, S., Keller, S., Gregory, R. I. & Diederichs, S. Many roads to maturity: microRNA biogenesis pathways and their regulation. *Nature cell biology* **11,** 228–234 (2009).

289. Fire, A. A. *et al.* Potent and specific genetic interference by double-

stranded RNA in Caenorhabditis elegans. *Nature* **391,** 806–811 (1998).

290. Elbashir, S. M. *et al.* Duplexes of 21-nucleotide RNAs mediate RNA interference in cultured mammalian cells. *Nature* **411,** 494–498 (2001).

291. Elbashir, S. M., Lendeckel, W. & Tuschl, T. RNA interference is mediated by 21- and 22-nucleotide RNAs. *Genes Dev* **15,** 188–200 (2001).

292. Bernstein, E., Caudy, A. A., Hammond, S. M. & Hannon, G. J. Role for a bidentate ribonuclease in the initiation step of RNA interference. *Nature* **409,** 363–366 (2001).

293. Matranga, C. C., Tomari, Y. Y., Shin, C. C., Bartel, D. P. D. & Zamore, P. D. P. Passenger-Strand Cleavage Facilitates Assembly of siRNA into Ago2-Containing RNAi Enzyme Complexes. *Cell* **123,** 14–14 (2005).

294. Rand, T. A., Ginalski, K., Grishin, N. V. & Wang, X. Biochemical identification of Argonaute 2 as the sole protein required for RNA-induced silencing complex activity. *Proceedings of the National Academy of Sciences of the United States of America* **101,** 14385–14389 (2004).

295. Ameres, S. L., Martinez, J. & Schroeder, R. Molecular Basis for Target RNA Recognition and Cleavage by Human RISC. *Cell* **130,** 101–112 (2007).

296. Bartlett, D. W. Insights into the kinetics of siRNA-mediated gene silencing from live-cell and live-animal bioluminescent imaging. *Nucleic acids research* **34,** 322–333 (2006).

297. Gallas, A., Alexander, C., Davies, M. C., Puri, S. & Allen, S. Chemistry and formulations for siRNA therapeutics. *Chemical Society Reviews* (2013). doi:10.1039/c3cs35520a

298. Wattiaux, R., Laurent, N., Wattiaux-De Coninck, S. & Jadot, M. Endosomes, lysosomes: their implication in gene transfer. *Adv Drug Deliv Rev* **41,** 201–208 (2000).

299. Grimm, D. *et al.* Fatality in mice due to oversaturation of cellular microRNA/short hairpin RNA pathways. *Nature* **441,** 537–541 (2006).

300. Judge, A. *et al.* Sequence-dependent stimulation of the mammalian innate immune response by synthetic siRNA. *Nature biotechnology* **23,** 457–462 (2005).

301. Koltover, I. I., Salditt, T. T., Rädler, J. O. J. & Safinya, C. R. C. An inverted hexagonal phase of cationic liposome-DNA complexes related to DNA release and delivery. *Science* **281,** 78–81 (1998).

302. Heyes, J. J., Palmer, L. L., Bremner, K. K. & MacLachlan, I. I. Cationic lipid saturation influences intracellular delivery of encapsulated nucleic acids. *Journal of Controlled Release* **107,** 12–12 (2005).

303. Stegmann, T. Membrane Fusion Mechanisms: The Influenza Hemagglutinin Paradigm and its Implications for Intracellular Fusion. *Traffic* **1,** 598–604 (2000).

304. Gonzalez, M. E. M. & Carrasco, L. L. Viroporins. *FEBS Lett* **552,** 7–7 (2003).

305. Kwon, E. J., Bergen, J. M. & Pun, S. H. Application of an HIV gp41-derived peptide for enhanced intracellular trafficking of synthetic gene

and siRNA delivery vehicles. *Bioconjugate Chemistry* **19,** 920–927 (2008).

306. Berg, K. *et al.* Photochemical Internalization: A New Tool for Drug Delivery. *curr pharm biotechnol* **8,** 362–372 (2007).

307. Bartz, R. R. *et al.* Effective siRNA delivery and target mRNA degradation using an amphipathic peptide to facilitate pH-dependent endosomal escape. *Biochem J* **435,** 475–487 (2011).

308. Banchereau, J. & Steinman, R. M. Dendritic cells and the control of immunity : Abstract : Nature. *Nature* **392,** 245–252 (1998).

309. Banchereau, J. *et al.* Immunobiology of dendritic cells. *Immunology* **18,** 767–811 (2000).

310. Trombetta, E. S., Ebersold, M., Garrett, W., Pypaert, M. & Mellman, I. Activation of lysosomal function during dendritic cell maturation. *Science* **299,** 1400–1403 (2003).

311. Ting, C. L. & Wang, Z.-G. Interactions of a charged nanoparticle with a lipid membrane: implications for gene delivery. *Biophysical journal* **100,** 1288–1297 (2011).

312. Ljosa, V. & Carpenter, A. E. High-throughput screens for fluorescent dye discovery. *Trends Biotechnol.* **26,** 527–530 (2008).

313. Vendrell, M., Lee, J.-S. & Chang, Y.-T. Diversity-oriented fluorescence library approaches for probe discovery and development. *Curr Opin Chem Biol* **14,** 383–389 (2010).

314. Vendrell, M., Zhai, D., Er, J. C. & Chang, Y.-T. Combinatorial strategies in fluorescent probe development. *Chemical reviews* **112,** 4391–4420 (2012).

315. Jiang, X. *et al.* Endo- and Exocytosis of Zwitterionic Quantum Dot Nanoparticles by Live HeLa Cells. *ACS Nano* **4,** 6787–6797 (2010).

316. Li, Z. *et al.* Internalization Pathways of Anisotropic Disc-Shaped Zeolite L Nanocrystals with Different Surface Properties in HeLa Cancer Cells. *Small* **9,** 1809–1820 (2013).

317. Shao, L., Kner, P., Rego, E. H. & Gustafsson, M. G. Super-resolution 3D microscopy of live whole cells using structured illumination. *Nature methods* **8,** 1044–1046 (2011).

318. Pepperkok, R. & Ellenberg, J. High-throughput fluorescence microscopy for systems biology. *Nat Rev Mol Cell Biol* **7,** 690–696 (2006).

319. Pepperkok, R. R. *et al.* Imaging Platforms for Measurement of Membrane Trafficking. *Meth. Enzymol.* **404,** 11–11 (2005).

320. Glory, E. & Murphy, R. F. Automated Subcellular Location Determination and High-Throughput Microscopy. *Dev Cell* **12,** 10–10 (2007).

321. Li, H. H. & Qian, Z. M. Z. Transferrin/transferrin receptor-mediated drug delivery. *Med Res Rev* **22,** 225–250 (2002).

322. Lu, Y. & Low, P. S. Folate-mediated delivery of macromolecular anticancer therapeutic agents. *Adv Drug Deliv Rev* **64,** 342–352 (2012).

323. Harrington, H. C. *et al.* Electrospun PLGA fibre sheets incorporating

fluorescent nanosensors: self-reporting scaffolds for application in tissue engineering. *Analytical Methods* **5,** 68–71 (2013).